Development of innovative magnetic field sensors with tuning features for a wide operative range

Eng. Valentina Maria Sinatra

Supervisor: Prof. Eng. Salvatore Baglio

Coordinator: Prof. Eng. Paolo Arena

Department of Electric, Electronic and Computer Engineering

University of Catania

Doctor of Philosophy in System, Energy, Computer and Telecommunication Engineering – XXXII Cycle

March 2020

Το μυαλό δεν είναι ένα βάζο που πρέπει να γεμίσει,

αλλά ένα ξύλο για να κάνει το κάψιμο έτσι

ώστε η γεύση της έρευνας

και η αγάπη της αλήθειας είναι φλεγμονή .....

Πλούταρχος

(The mind is not a vase to be filled

but a wood to make burn so that

the taste of research and the love of truth may be inflamed .....

Plutarch)

To my family and to my love Simone

Acknowledgements

This research activity has been supported by the European Organization for Nuclear Research (CERN), in Geneva, Switzerland, and by the Paradox Engineering, in Novazzano, Switzerland. It is important to emphasize that these institutions have enhanced the quality of the manuscript presented.

A special recognition is reserved to my supervisor, Prof. Eng. Salvatore Baglio, who encouraged my work with precious suggestions and relentless research ideas. He was an incomparable mentor, able to feed my thirst for research without delay.

In addition, I would like to thank my supervisor at CERN, Dott. Eng. Stephan Russenschuck, who helped my research with his analytic and mathematical approach on electromagnetic fields. His point of view was invaluable for performing the measurements at CERN using dipoles, quadrupoles and sextuples.

My gratitude is also addressed to the Paradox Engineering to have supported my research activity and, in a special way, I would like to thank my supervisor, Dott. Gaetano Calabrò, who has scrupulously followed the progress of my activity and he has always provided interesting causes for reflection.

Furthermore, I would like to thank my colleagues of Electric and Electronic Measurements Laboratory at DIEEI in University of Catania, Eng. Vincenzo Marletta, Eng. Salvatore Castorina,

Eng. Ruben Crispino and Eng. Santhosh Kurukunda, with whom I have shared so many beautiful moments of work and friendship.

An important mention has to be addressed to all members of MM (Magnetic Measurement) section at CERN, in Geneva, who allowed to bring merit and quality to the time spent there: in particular, I would like to thank Eng. Marco Buzio, who followed my research activity with interest and curiosity and he helped me integrate into the MM group. Moreover, a special acknowledgement is reserved to some engineers working at CERN, such as Eng. Maria Amodeo, Eng. Federico Gargiulo, Eng. Michela Pirozzi, Eng. Mariano Pentella, Eng. Vincenzo Di Capua, Eng. Kevin Maccaron, Eng. Andreas Windischhofer and Eng. Joseph Vella Wallbank, who warmly welcomed me and supported my PhD activity.

At last, I would like to thank Dott. Adi R. Bulsara, an illustrious and friendly physicist to the SPAWAR (Space and Naval Warfare Systems Command), in San Diego, California, USA, with whom I had the honor of comparing myself in these years in the context of the magnetic field sensors: Dott. Bulsara provided precious suggestions and he encouraged my work.

Abstract

The research activity discussed in the following manuscript is based on the implementation, fabrication and characterization of an integrated magnetic field sensor in PiezoMUMPs technology, to use in two alternative applicative contexts, such as the mapping of the magnetic field dispersed in a particle accelerator and "smart cities parking". The duality of application is correlated to the typology of the mentioned PhD project which the Ministry of Education, University and Research (MIUR) has subsidized with the clause to spend a time period abroad, in a research entity, and a time period in a company. In detail, the two institutions involved in the project are the European Organization for Nuclear Research (CERN), in Geneva, and Paradox Engineering company, in Novazzano, respectively for the dispersion of the magnetic field in an accelerator particle and for "smart cities" application. Therefore, taking into account that the detection of magnetic fields to be measured is completely unalike in both cases, the aim to be reached has been the realization of a tunable integrated micromechanical device having a wide operative range, that is [1 μT – 2 T]. As explained later, the operative range has been selected considering the alteration of the geomagnetic field generated by a car for the lower extreme, whereas the high magnetic fields (B ~ 2 T), used in Large Hadron Collider (LHC) tunnel to deflect bunches of proton particles, for the upper extreme. The challenge has been correlated to the opportunity of using the same microelectromechanical system (MEMS) to detect and to measure completely different static or quasi-static magnetic fields. Another important feature in terms of realization has been connected to the readout strategy; indeed, in relation to this point, several solutions have been investigated (resistive, capacitive, optic and piezoelectric output) in order to pursue the goal of a magnetic field sensor having low

consumption, reduced conditioning circuit and capable of being self-generating. Therefore, the following manuscript has been split into four chapters:

- ✓ in Chapter I, the magnetometers actuated by Lorentz force have been described in order to examine the actuation mechanism;
- ✓ in Chapter II, a specific category of Lorentz force magnetometers, U-shaped beam cantilever, have been analysed, paying attention to several fabrication technologies and readout strategies (resistive, capacitive, optic and piezoelectric); in details, the PiezoMUMPs technology has been estimated as the most promising;
- ✓ in Chapter III, the research activity has been focused on a new architecture of U-shaped beam cantilever, Meander MEMS device, that has been examined in terms of static and dynamic model (through Matlab-Simulink) and FEM analysis to evaluate stress, displacement and modal analysis (using Comsol Multiphysics); in addition, the MEMSPro CAD has been used in order to realize the layouts;
- ✓ in Chapter IV, the last one, the phases of testing and characterization of the integrated MEMS device, at first as accelerometer and later as magnetic field sensor, has been illustrated; preliminary results, coming from measurements implemented at CERN, in Geneva, have been discussed and the fabrication of a second run of MEMS prototypes with the realization of a suitable conditioning circuit in order to perform experimental measurements in Paradox Engineering company, in Novazzano, is presented. Unfortunately, the pandemic due to COVID-19 virus imposed suddenly to interrupt the following research activity.

Table of contents

Chapter 1

Introduction

1.1 Magnetic field sensors

Magnetic field sensors have a great potential for important applications in different sectors, like magnetic storage, automotive [1], navigation systems [2], non-destructive material testing, structural stability, military instruments [3], medical sensing [4] and others. For example, in the automotive these sensors are employed in wheel speed detection of ABS (Antilock Braking System) [5]; in addition, new cell phones include an electronic compass using field sensors for their GPS [6]. For all these applications, magnetic field sensors need often such characteristics as small dimensions, light weight, low power consumption, low cost, high resolution and sensitivity. It is interesting to note that microelectromechanical systems (MEMS) technology allowed the integration of magnetic field sensors with electronic components on a single chip and contained all previous listed characteristics. For these reasons MEMS magnetic field sensors represent a potential alternative for numerous applications, including the automotive industry [7,8], military, medical, telecommunications, spatial, environment science and etc.

1.1.1 Classification

There are different kinds of magnetic field sensors with unique characteristics, therefore a preliminary classification is believed essential in order to understand the argumentation that leads to using a magnetic field sensor instead of another. Although all devices measuring magnetic field are frequently called "Magnetometer", a rigorous categorization should provide for the partition of these sensors in two macro-areas, as can be observed in Fig. 1.1, depending on whether the magnetic flux density (**B**), to be measured, is higher or lower than 1 mT; in detail, it is possible to distinguish "Magnetometers" if B < 1 mT and "Gaussmeters" if B > 1 mT.

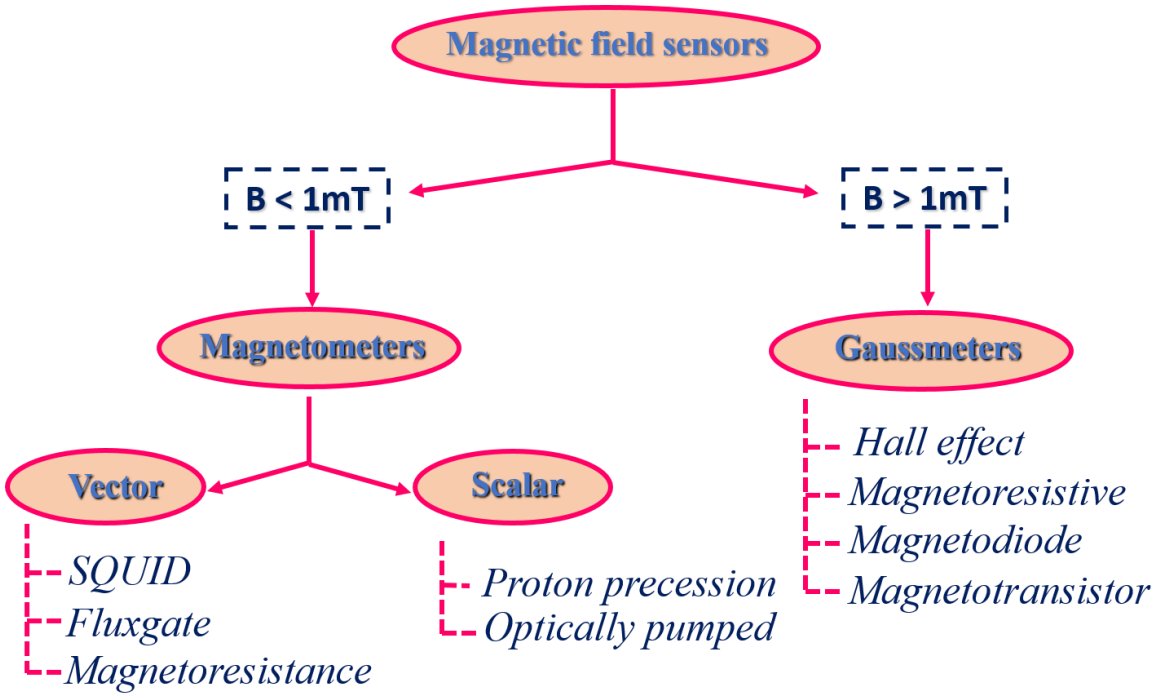

Fig. 1.1: Magnetic field sensors classification.

Furthermore, magnetometers can be split in vector or scalar in accordance with the following feature:

- Vector magnetometer measures the magnetic flux density value in a specific direction in 3 D space.
- Scalar magnetometer which measures only the magnitude of the vector passing through the sensor regardless of the direction.

A brief description related to the working principle and the peculiar characteristics of each magnetic field sensor listed in Fig. 1.1 is considered essential to contextualize the topic presented in this manuscript.

1.1.2 SQUID

The Superconducting Quantum Interference Device (SQUID) is a vector magnetometer and it is the most sensitive magnetic field sensor with a resolution on the order of several fT [9,10]. This sensor is noise sensitive, has a power consumption of numerous watts and its operation is based on two effects: flux quantization and Josephson effects (observable only in the presence of superconductivity) [9]. Structurally, it is composed of two Josephson junctions, as shown in Fig. 1.2 [11], and its working principle is based on the conversion of the magnetic flux (Φ) or any physical property that can be transformed into magnetic flux, into a voltage across the device. Due to the strongly nonlinear, periodic voltage vs flux (V-Φ) the magnetometer must be operated in a flux-locked loop. Unfortunately, instruments based upon SQUIDs require cooling down to liquid helium temperatures (4.2 K) [12] and, as a consequence, their applications are still limited e.g., in geophysics and in other niche applications, such as the investigation of brain activity [13,14], because it has a high price and it needs to operate at low temperatures.

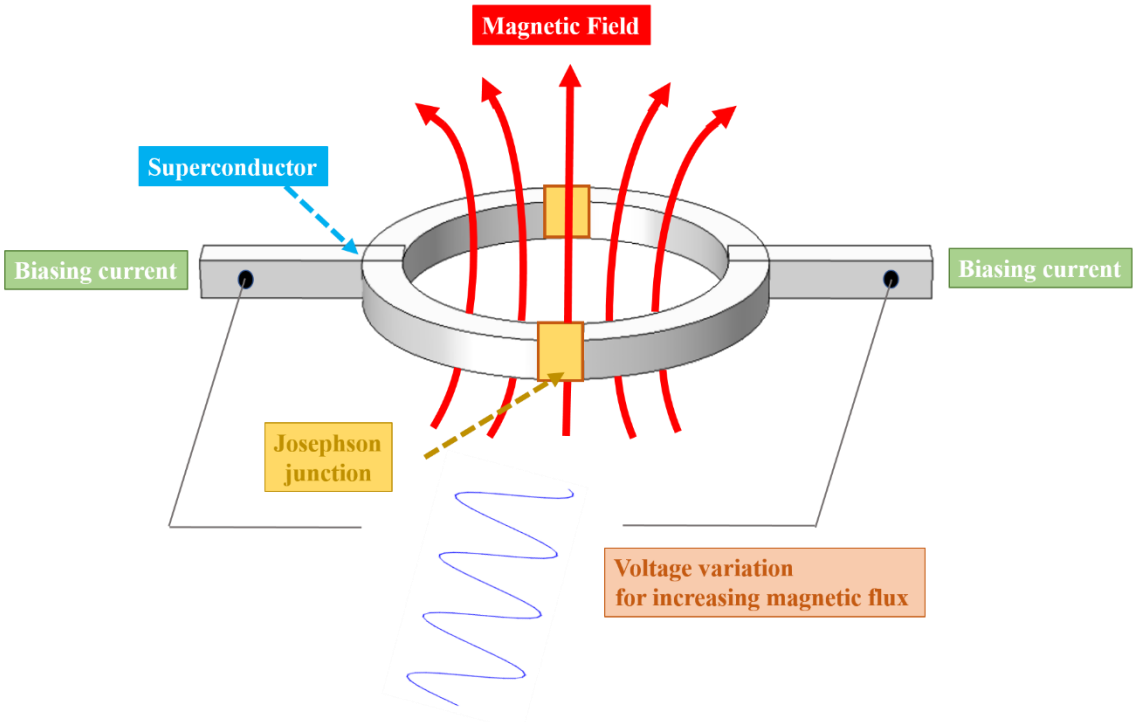

Fig. 1.2: Working principle of the SQUID magnetometer.

In addition, it is interesting to note that since the SQUID is noise sensitive a magnetically shielded room (MSR) is used in order to reduce the noise; however, this room is expensive and heavy, and, for this reason, the environments in which it can be used are restricted. In [15] authors proposed a new SQUID magnetometer system that has combined the direct-feedback gradiometer method and FQC method (Flux-Quanta Counting) for MCG (magnetocardiogram) measurement without MSR, obtaining a noise cancellation factor ranged from 10 dB to 20 dB. Several studies have been found in literature to improve the field resolution of a magnetometer for use in the Earth's field: in particular, a multi-turn input coil has been inserted between a directly-coupled SQUID and a pickup coil in series [16] developing a "hybrid" SQUID with a field noise as low as 18 $fT/Hz^{1/2}$ (white).

1.1.3 Fluxgate

The Fluxgate magnetometer is a simple, room-temperature sensor used to measure static or quasi-static magnetic field targets and it has promising performance in terms of resolution (~ 100 pT) and sensitivity. Various topologies have been found in literature, planar (in PCB technology) [17,18] or cylindrical, in single or coupled [19] configuration. Although, a fluxgate magnetometer having an amorphous ribbon core (Metglas 2714A) has been analysed in [20], determining a noise level at 1 Hz that is comparable or lower than the noise level (6 pT/Hz$^{1/2}$) of one of the best commercially available fluxgate magnetometers, typically, the basic architecture is composed of a ferromagnetic core, that has very high permeability (~ 80000) and a hysteretic input-output characteristic, and two coils wound around the ferromagnetic core [21] (IEEE copyright line © 2011 IEEE), as illustrated in Fig 1.3 a-b.

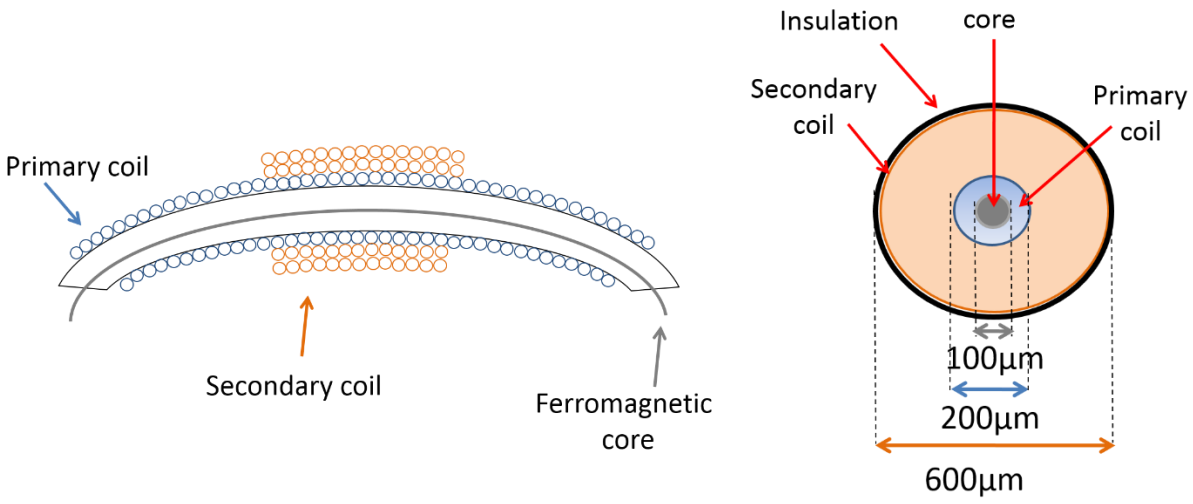

(a) (b)

Fig. 1.3: (a) Fluxgate architecture [21]; (b) Cross section of magnetic sensor [21]

(IEEE copyright line © 2017 IEEE).

In [21] we have investigated the performance of a totally flexible Fluxgate magnetometer (see Fig. 1.4) in which primary and secondary coils are directly wound around the ferromagnetic core, composed of CoFeSiB (80% Co-Fe, 20% Si, B) and having a diameter of 100 μm; as a consequence, the magnetic coupling, compared with previous versions [22], is increased, a sensitivity of about 7.3×10−2 μs/nT and a noise level (variance) of about 8.0912×10−6 V^2 have been obtained. Its versatility allowed to be used in several applicative contexts that can be notably different from each other, such as in geophysics [23], in providing non-invasive solutions for the measurement of very low-frequency currents in electron cyclotron resonance ion source (ECRIS) beamline [24,25], or still in monitoring brain iron contents in neurodegenerative diseases [26,27]. Related to the last aspect, we have examined the opportunity of using a flexible core fluxgate to measure the increase of iron contents in a specific brain area, basal ganglia, correlated to the development of Parkinson's and Alzheimer's disease [26,27].

Fig. 1.4: Flexible Fluxgate magnetometer [21] (IEEE copyright line © 2017 IEEE).

In addition, it is interesting to note that two different readout strategies can be adopted, that are the second harmonic and the Residence Times Difference (RTD). In the first case, since the pick up voltage consists of even-numbered harmonics of the excitation frequency, the second harmonic, proportional to the external magnetic field, is extracted and rectified; in the second case, the unknown magnetic field is correlated to a time measurement, coming from the "spike train response" of the secondary coil output voltage, which is the first derivative of the magnetization core.

1.1.4 Magnetoresitance or Magnetoresistive

In Magnetoresistance magnetometers (MR) a resistance variation, ΔR, is obtained in accordance with the strength of an unknown applied magnetic field and the specific direction. They are especially indicated for low cost applications because they are simply energized by applying a constant current and measuring the output voltage that is correlated to the magnetic field [7]. One characteristic in MR is given by $\Delta R = R - R_0$, where R_0 is the nominal value of the resistance corresponding to $H = 0$, therefore, the value for MR is usually expressed as the percentage change in resistance per oersted (Oe). Typically, since ΔR is small, a bridge circuit or other methods must be used in order to estimate the DC voltage change and to minimize the DC offset. Several magnetoresistance sensors, having totally different mechanisms, can be mentioned, such as AMR (Anisotropic MR), GMR (Giant MR) and TMR (Tunnel MR); in the AMR devices, materials, known as permalloy, exhibit a resistance which is a function of the angle between the magnetization of the material and the electrical current direction (as shown in Fig. 1.5).

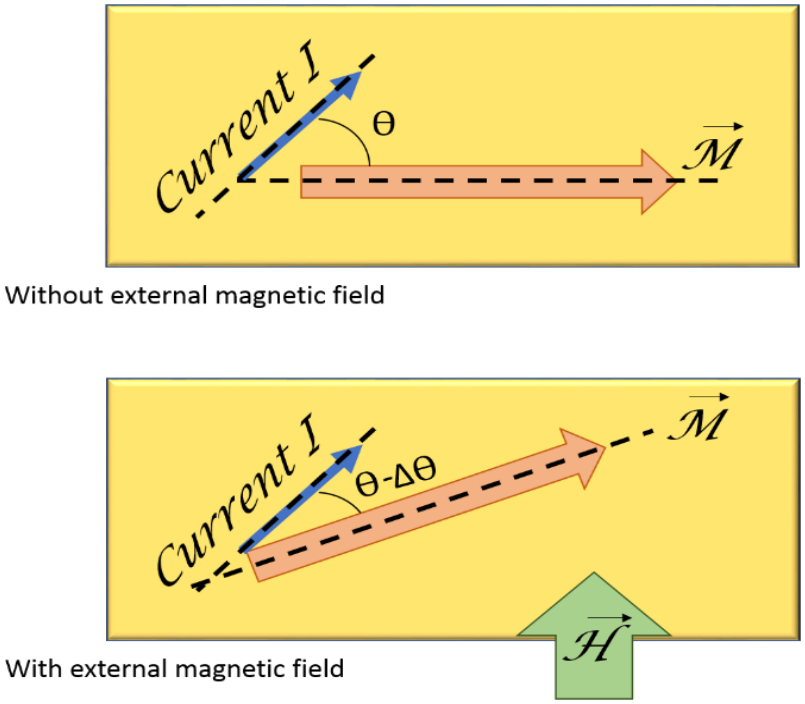

Fig. 1.5: Working principle of AMR sensor.

Taking into account that the resistance varies as the element of angle between the current direction and the field direction, in accordance with the following eq. (1.1) [28]:

$$R = R_0 + \Delta R \cos^2 \theta \tag{1.1}$$

as a consequence, the resistance change amount (ΔR), which is shown in Fig. 1.6, becomes maximum when the current direction is vertical with the filed direction (θ = 90° or θ = 270°) and it becomes minimum when the current direction is horizontal with the filed direction (θ = 0° or θ = 180°).

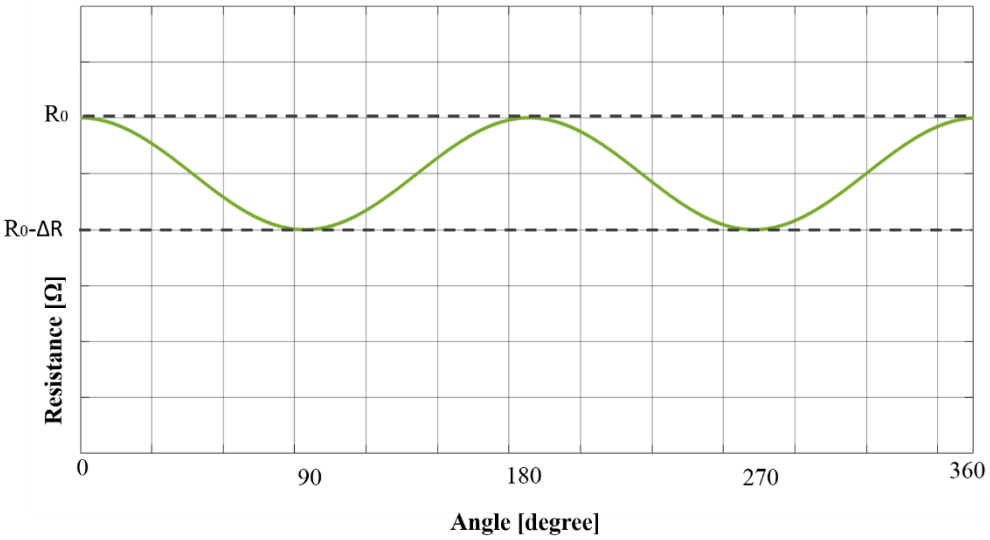

Fig. 1.6: Resistance variation VS magnetic field direction.

Typical applicative contexts for these magnetometers are automotive [29], industry [30] or magnetic object localization [31]. In detail, in [31] authors used HMC1001 and HMC1002 MR sensors, which are extremely sensitive for measuring magnetic field in a sensitive axis direction. As results, they estimated a spatial resolution of 11.4 nT and when the magnet of surface magnetic field, generated by a Helmholtz coil, is 0.9 T, the location error is not more than 10% from 50 cm to 140 cm. Other interesting advantages of AMR sensors to be mentioned are low power consumption (between 0.1 mW and 0.5 mW), large temperature range (55 ˚C and 200 ˚C), lightness and small dimensions.

As concerns the GMR magnetometers, the giant magnetoresistance effect is a very basic phenomenon that occurs in magnetic materials ranging from nanoparticles over multi-layered thin films to permanent magnets and it was discovered by Grünberg and Fert in 1988 [32]. In thin metallic film systems, they observed that the magnetization of adjacent ferromagnetic films, separated by a thin non-magnetic conductive layer, as can be Cu [33], spontaneously aligns parallel or antiparallel, depending on the thickness of the interlayer. The orientation of the magnetization in the ferromagnetic layers strongly influences the resistance of the system. A

parallel orientation is characterized by an electrical state of low resistance (R_P), while an antiparallel orientation is a state of high resistance (R_{AP}) [30], as illustrated in Fig. 1.7.

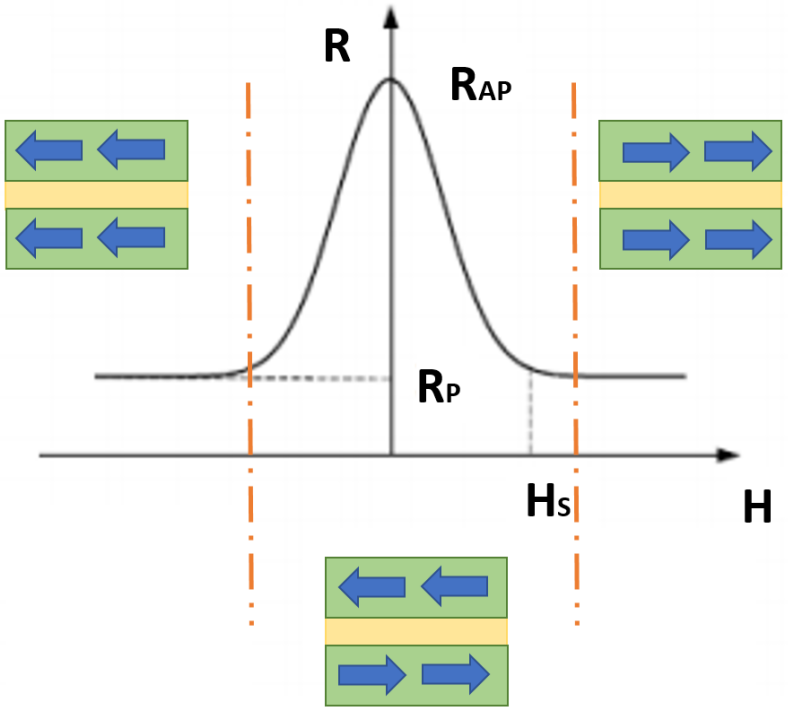

Fig. 1.7: Schematic representation of GMR effect.

GMR sensors have greater output than conventional anisotropic magnetoresistive (AMR) sensors or Hall Effect sensors and they are able to operate at fields well above the range of AMR sensors. Nowadays the spectrum of successful applications of GMR technology is impressively broad, ranging from applications in the air- and space or automotive industry [34], non-destructive material testing, biomedical techniques [35] and biosensors [36]. Another important aspect is correlated to the temperature: since, for instance, a lot of automotive magnetic sensors are implemented into security-relevant functions, it is essential that the magnetic behavior of the GMR sensors be stable under the applied conditions [37].

As regards the TMR magnetometers, they are constructed as a magnetic multilayer film material. TMR magnetic field sensing elements exhibit a greater change in resistivity, as a function of

applied magnetic field induction, than that of the previously developed magnetoresistance technologies, AMR and GMR. As can be observed in Fig. 1.8, the magnetic structure of a TMR element is almost the same as that of a GMR element, however, in a TMR element, the current flows perpendicular to the film surface, while it flows horizontally to the film surface in a GMR element.

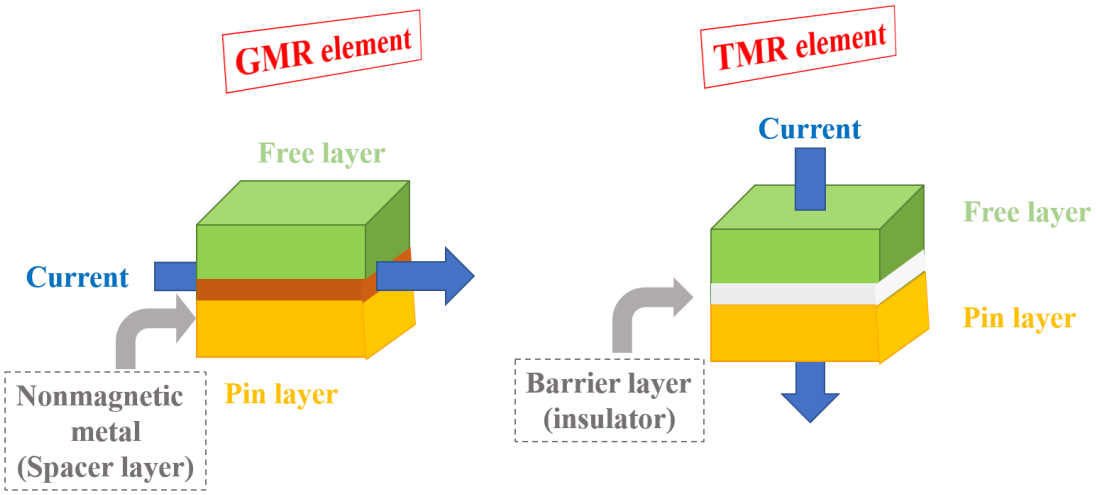

Fig. 1.8: Schematic of the TMR structure.

Furthermore, a TMR element is a thin-film having a structure in which a barrier layer composed of a thin insulator of 1 nm to 2 nm is sandwiched between two ferromagnetic layers (free layer and pin layer) having a thickness in the range [0.1 – 10] nm [38]. Although the magnetization direction of the pin layer is fixed, the magnetization direction of the free layer changes according to the external magnetic field direction. The electrical resistance of the TMR element changes along with this change in the free layer. The electrical resistance becomes the smallest when the magnetization directions of the pin layer and free layer are parallel, causing a large current to flow into the barrier layer. When the magnetization directions are antiparallel, the resistance becomes extremely large, and almost no current flows into the barrier layer (as illustrated in Fig. 1.9).

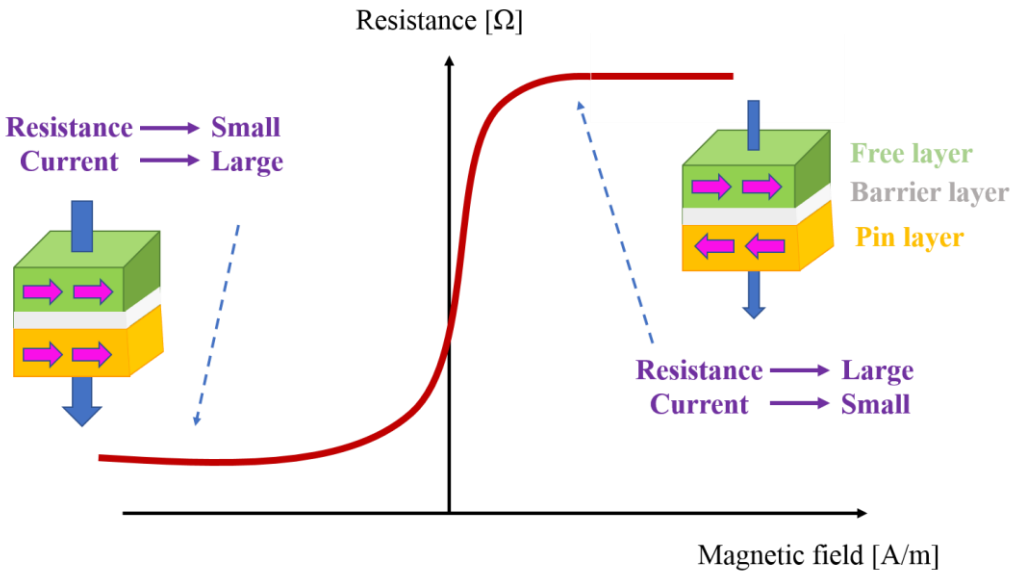

Fig. 1.9: Resistance VS magnetic field in TMR magnetometers.

Nevertheless, although the TMR sensor has a higher sensitivity and a wider linear range compared with the previous two magnetometers, the noise problem limits its sensitivity for ultra-low magnetic field application. Several studies have been found in literature in order to reduce the noise disturbance, such as flux concentrator [39], flux chopper [40] and TMR arrays [41]; in particular, in [42] the authors have reduced the *1/f* noise by a factor of 12 with a shielding type magnetic flux chopper. At last, the TMR magnetometers are widely used in space application [43] and biomedical imaging such as magnetocardiography [44]. In conclusion, the potential of magnetoresistive technology seems to be far from being exhausted.

1.1.5 Proton precession

The proton precession magnetometer (PPM) uses NMR (nuclear magnetic resonance) methods to measure the geomagnetic field [45] and it can be considered the oldest instrument in the history of quantum weak magnetic measurement instruments. In quantum physics, since protons

possess electric charge and spin, they have an intrinsic magnetic dipole moment; therefore, if a particle

with non-zero magnetic dipole moment is placed in an external magnetic field it will start to precess around the magnetic field in accordance with Larmor equation, eq. (1.2):

$$\vec{\omega} = \gamma \vec{B} \tag{1.2}$$

where $\vec{\omega}$ is the angular frequency of precession, γ is the gyromagnetic constant that is higher for electron than proton, and, at last, $\vec{B}$ is the magnetic induction. The proton precession magnetometer consists of a proton-rich fluid (commonly hydrogen or kerosene) in a container, surrounded by a coil (as described in Fig. 1.10). When the current is passed through the coil, a magnetic field is induced and the protons in the liquid sample align themselves with the magnetic field, whereas, when the current is turned off, the protons try to align themselves with the Earth's magnetic field.

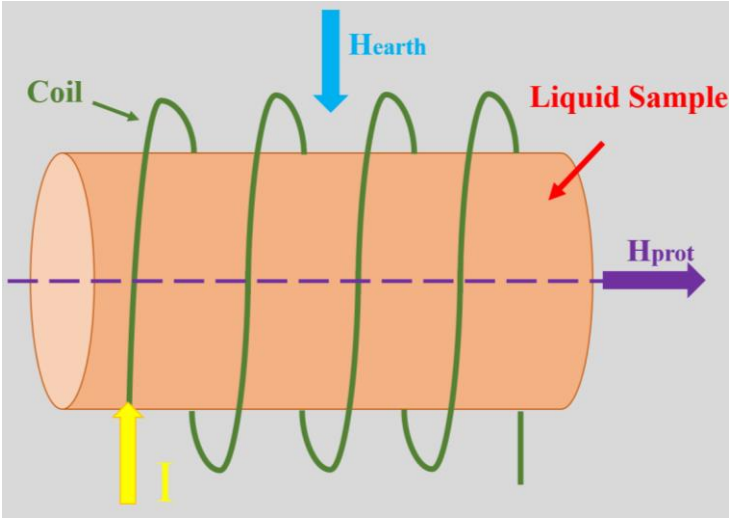

Fig. 1.10: Proton Precession Magnetometer (PPM): working principle.

It is important to highlight that the proton precesses can generate a free induction decay (FID) signal in the sensing coil, whose frequency is proportional to the magnetic field strength [46]. Hence, the measurement performance of a PPM is mainly determined by the signal-to-noise ratio (SNR) of the induced FID signal. In order to solve this problem, numerous solutions have been found in literature, in particular: in [47] an equivalent circuit of ATCN-LCBF (AdjustableTuning Capacitor Network – LC Band-pass Filter) has been investigated, demonstrating that it cannot only enhance the strength of the FID signal but also suppress the external noises, improving the measurement accuracy of the PPM by approximately 2 times; in [48] is a new algorithm based on the combination of principal component analysis (PCA) and singular value decomposition (SVD), called C-PCASVD method, has been developed for high-precision tuning of FID signals; in [49] a novel real-time processing algorithm, called LRC – GDRO, based on a new efficient framework, dubbed Low-Rank Constraint-based Geomagnetic Data Readout Optimizer has been implemented, improving the performance of the PPM with a measurement accuracy of ± 0.2 nT. Typically, the proton precession magnetometer has a resolution of 0.1 nT and accuracies of 0.5 nT are achievable in the field.

1.1.6 Optically pumped

Optically pumped magnetometers (OPMs) have been developed since the 1960s and have seen rapid progress over the last decade in terms of performance and technology development. The OPMs use an ionizing light beam to manipulate one of several elements from a specific chemical Group within a sample volume for the purpose of observing their reaction to external magnetic forces [50] (IEEE copyright line © 2011 IEEE). By manipulating and monitoring the nuclei of any one of the Periodic Element Table Group 1 or alkali metals (Li, Na, K, Rb, Cs, Fr), measurements can be made of magnetic forces (see Fig. 1.11). Alkali metals are very reactive to certain external forces and will easily lose an electron such as when ionizing light energy is

applied. However, magnetic forces have a stabilizing effect on alkali metals that have lost an electron and tend to force any losing electron back to its stable neutral state, thus counteracting the ionizing light energy or optically pumped energy.

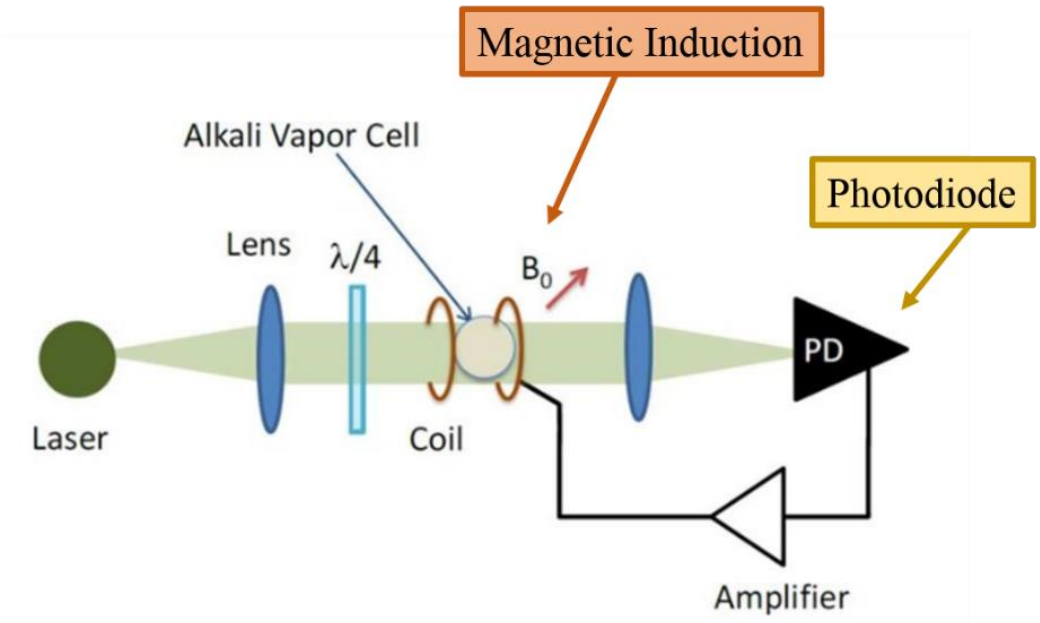

Fig. 1.11: Optically Pumped Magnetometer (OPM): working principle [50] (IEEE copyright line © 2011 IEEE).

An alkali vapor, such as cesium (Cs) or potassium (K), is sealed within a temperature controlled vacuum chamber where ionizing light is emitted or "pumped" into the chamber through various optical filters. The ionizing light energizes the molecules in the sample volume and ejects electrons from the outermost orbit of individual electrons. A photocell at the end of the vacuum chamber measures the amount of light given off. Greater light intensity means that a strong magnetic field is quickly forcing electrons back to a normal state within the sample volume. Weaker magnetic fields will not cause the electrons to return to normal as rapidly, thus producing less light in the sample volume. Several improvements have been introduced into the basic structure of an OPM in order to increase the performance: for instance, in [51] authors implemented a miniaturized cesium cell using the light-narrowing effect and impressing a spin-

exchange relaxation suppression and they have estimated a shot-noise-limited sensitivity of 42 fT/Hz$^{1/2}$. Taking into account the OPMs are highly sensitive at room-temperature without requiring cryogenic cooling, they are capable of replacing superconducting quantum interference device (SQUID) in several imaging systems, such as magnetoencephalography (MEG) [52,53], that measures the magnetic fields from neural currents by placing sensors on the scalp of the subject. Due to the curvature of the head, rigid helmets do not allow for close proximity of sensors for every head size. Furthermore, it has been possible to record magneto cardiograms (MCG) by placing several sensors over the chest of a healthy subject [54] and also the fetal MCG with an array of 25 magnetometers and extracting the maternal and fetal heart signals [55].

1.1.7 Hall Effect

Magnetic sensors using the Hall effect as their principle of transduction are commonly fabricated on standard Complementary Metal-Oxide Semiconductor (CMOS) technology [56]. Hall effect sensors have low cost and are used for measuring linear and angular position [57], velocity, rotational speed and in current sensing applications [58]. They are based on the Hall effect principle that can be explained as follows and described in Fig. 1.12 a-b [59]: a current (I) is passed through a thin sheet of semiconducting material (Hall element), whose output connections are perpendicular to the direction of current. If an external magnetic field is absent the current distribution will be uniform, and no potential difference will be seen across the output (see Fig. 1.12 a), whereas, if an external magnetic field is present the Lorentz Force will disturb the current distribution, resulting in a potential difference across the output (V_H), as shown in Fig. 1.12 b. It is noteworthy to underline that the Lorentz force can be described by eq. (1.3):

$$\vec{F} = q \cdot \left(\vec{E} + \vec{v}\, x\, \vec{B}\right) \tag{1.3}$$

in which, the Lorentz force $\vec{F}$ is perpendicular to both the velocity v of the charge q, $\vec{E}$ is the electric field and the magnetic induction $\vec{B}$. The output voltage, called Hall voltage and indicated with V_H, is proportional to the vector cross product of the current (I) and the magnetic induction (B).

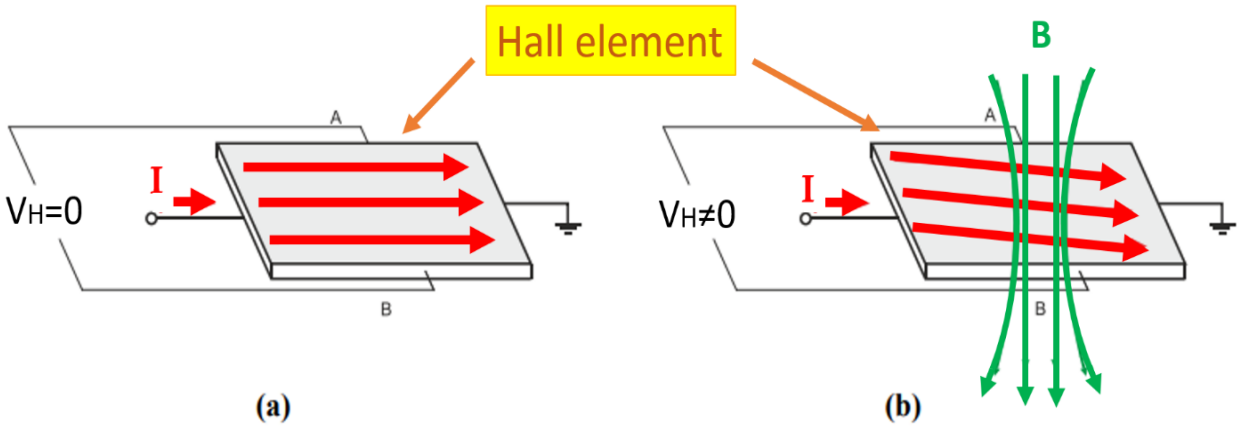

Fig. 1.12: Hall effect principle (a) Without magnetic field; (b) With magnetic field applied [59].

Typically, the Hall voltage is quite small, only a few microvolts even when subjected to strong magnetic fields so most commercially available Hall effect devices are manufactured with built-in DC amplifiers and voltage regulators to improve the sensors sensitivity, hysteresis and output voltage (as illustrated in Fig. 1.13).

In general, Hall sensors are applicable for measuring magnetic field in the range [1 – 100] mT, have a power consumption between 100 mW and 200 mW, and an offset of several mT. These sensors can measure either constant or varying magnetic field: the upper frequency limit is about 1 MHz and operate well in the temperature range from –100 ºC to +100 ºC, although they need temperature compensation circuits that can include temperature sensor and operational amplifiers. Regarding the improvement of the performance, several solutions have been found in literature: in [60] a n-type Hall sensor has been developed in GLOBALFOUNDRIES on

0.13 µm BCD (bipolar/CMOS/DMOS) technology exhibiting a sensitivity of 418 V/AT and a small offset voltage ranging in ± 1.05 mV; in [61] authors estimated a sensitivity of 964 V/AT concerning an horizontal Hall sensor in 0.35 µm BCD technology.

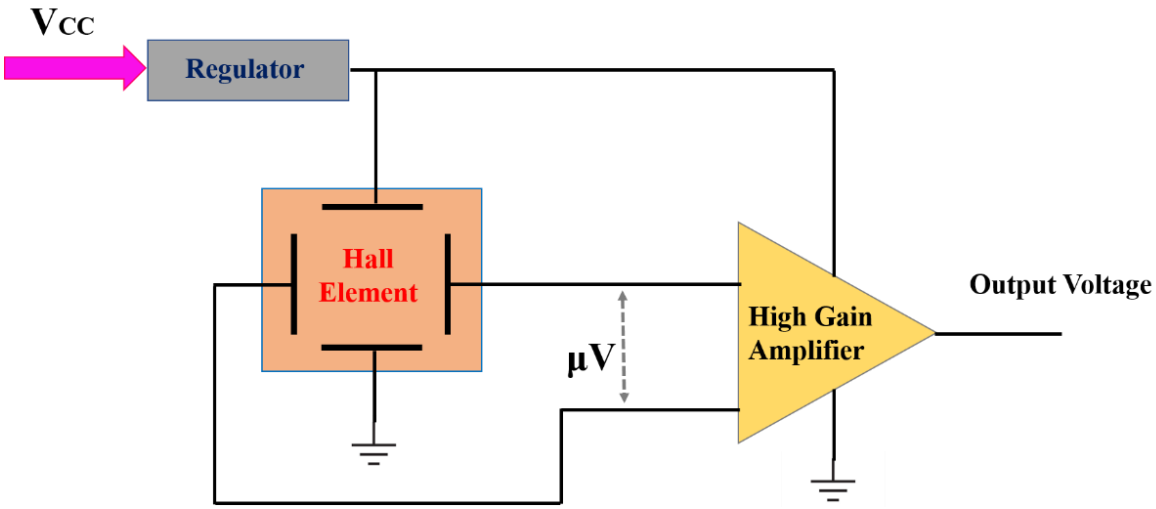

Fig. 1.13: Basic Hall effect sensor.

1.1.8 Magnetodiode

A magnetodiode is conceived as an intrinsic semiconductor slab subject to double injection and a transverse magnetic field, in other terms it combines Lorentz force and injection effects [62]. The classical magnetodiode is a two-terminal semiconductor device capable of detecting the magnetic field in the order of mT and whose operation is based on the superposition of high carriers' injection by one or two (a p^+-n and an n^+-n) junctions, magneto concentration and surface recombination. It operates by the difference in recombination rate between two interfaces depending on the direction of the magnetic induction. In [63] (IEEE copyright line © 2011 IEEE) authors developed a dual Schottky magnetodiode, shown in Fig. 1.14, in which the common anode terminal is aluminum (p-type), whereas the symmetrical separated cathodes are n-type

substrate with the n^+ diffusion window for ohmic contact with aluminum (Al). In relation to Fig. 1.14 it is interesting to specify that $W = 10$ μm is the gap between cathode terminals, whereas L = 15 μm is the spacing between anode and cathode terminal.

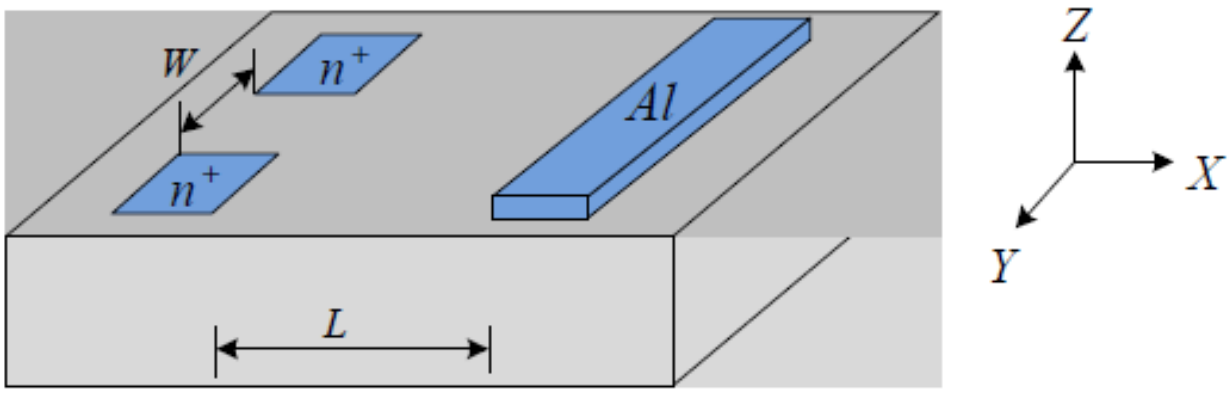

Fig. 1.14: The top view of the dual Schottky magnetodiode structure [63] (IEEE copyright line © 2012 IEEE).

Eventually, the simulated results demonstrated that the device is able to detect magnetic field in vertical direction and it relies on the carrier deflection mechanism causing the current difference between cathode 1 and cathode 2.

In addition, a no-touch flux-meter solution, illustrated in Fig. 1.15, has been found in literature in order to monitor the flux of a liquid in specific circumstances, for example oil pipes that contain many combustible gases; it is based on a series connection magneto-diode [64], whose V-I characteristics as a function of the magnetic induction are described in Fig. 1.16.

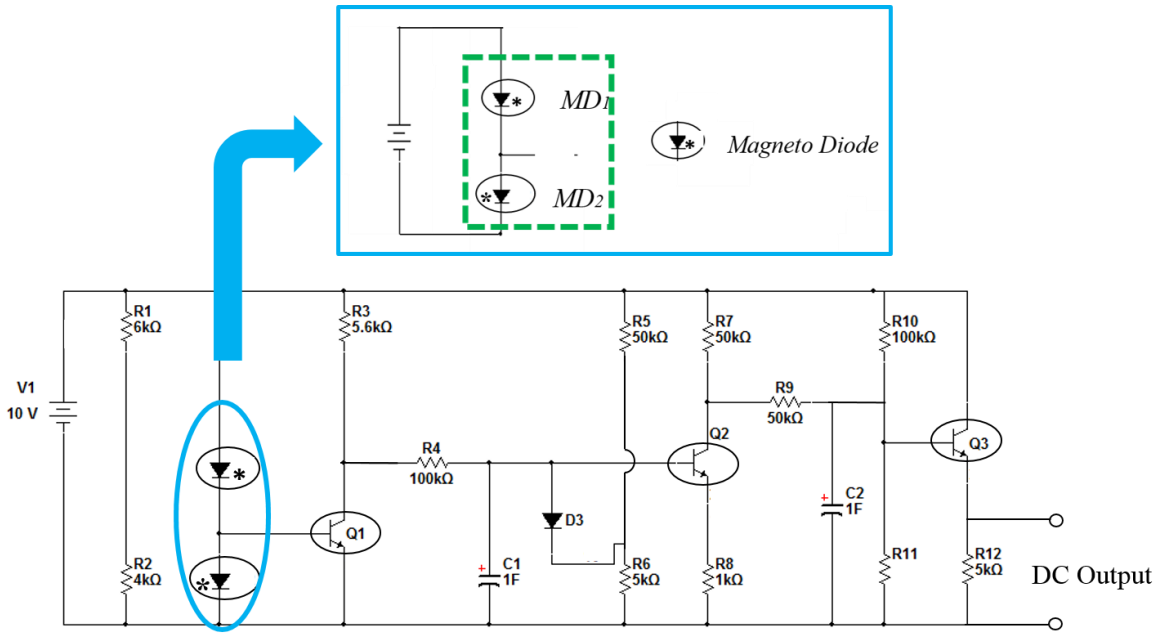

Fig. 1.15: Tachometer Circuit based on Series Magneto-diode [64].

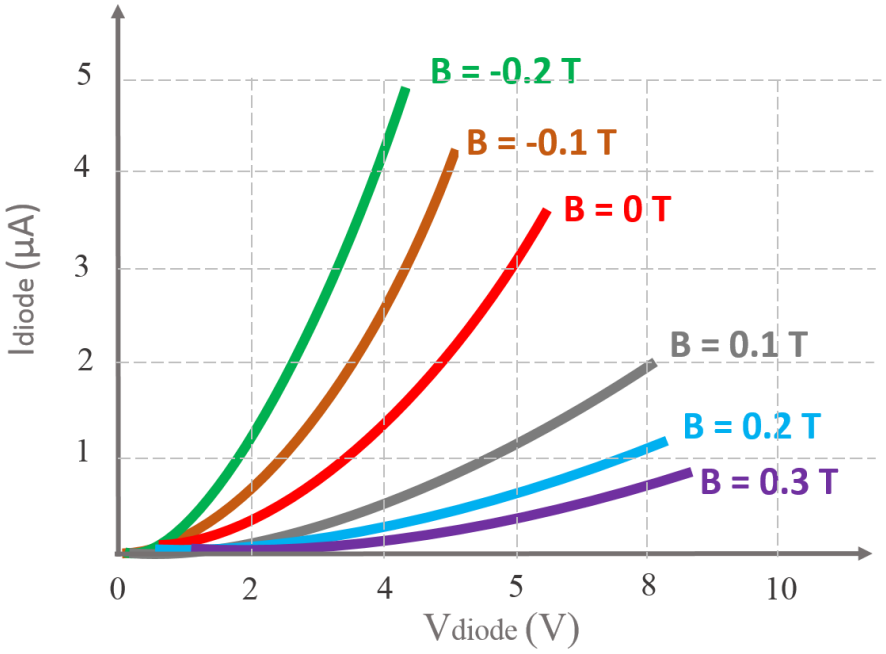

Fig. 1.16: I-V characteristics of magneto-diode [64].

1.1.9 Magnetotransistor

The magnetotransistor is a magnetic sensor device, which has the structure similar to a bipolar transistor. In general, it is composed of three terminals which are emitter, base and collector on a silicon substrate, and it is a useful sensor for magnetic field applied to vertical direction of the chip. The main mechanism for magnetic sensitivity of these devices is the deflection and recombination of minority carriers in the neutral base region by Lorentz force. The carrier deflection influences the difference between base and collector current (ΔI_{BC}) which is directly proportional to magnetic field that is expressed in terms of magnetic induction (B) applied. In Fig. 1.17 an NPN magnetotransistor fabricated in a standard CMOS technology is presented [65] (IEEE copyright line © 2011 IEEE), in which a LOCOS oxide (local oxidation of silicon) has been inserted around emitter area to reduce the leakage current by limit its carrier injection area.

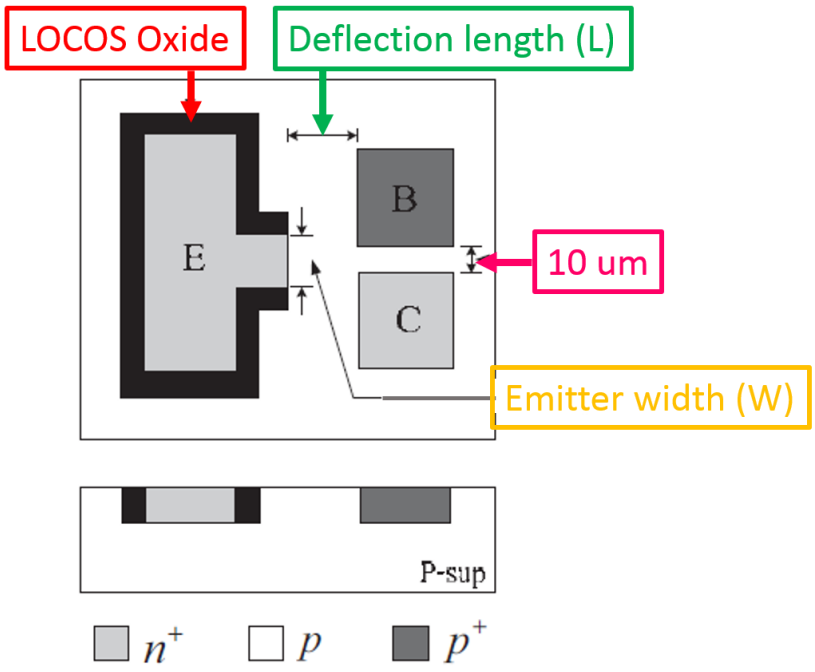

Fig. 1.17: Magnetotransistor structure [65] (IEEE copyright line © 2011 IEEE).

The best sensitivity has been estimated about 10.75 mV/T in correspondence with emitter width (W) of 4 μm, emitter current of 4 mA and a deflection length (L) of 10 μm. In order to detect magnetic field in perpendicular and lateral directions a magnetotransistor, having one emitter I, 4 collectors (C1, C2, C3, C4) and 4 bases (B1, B2, B3, B4), has been designed and fabricated using CMOS technology (see Fig. 1.18) [66] (IEEE copyright line © 2011 IEEE), and the experimental results showed that, imposing 10 mA of biasing current, the B_Y and B_Z direction sensitivity to magnetic field within the range [0 – 400] mT are 0.7 and 1.35 %/T, respectively.

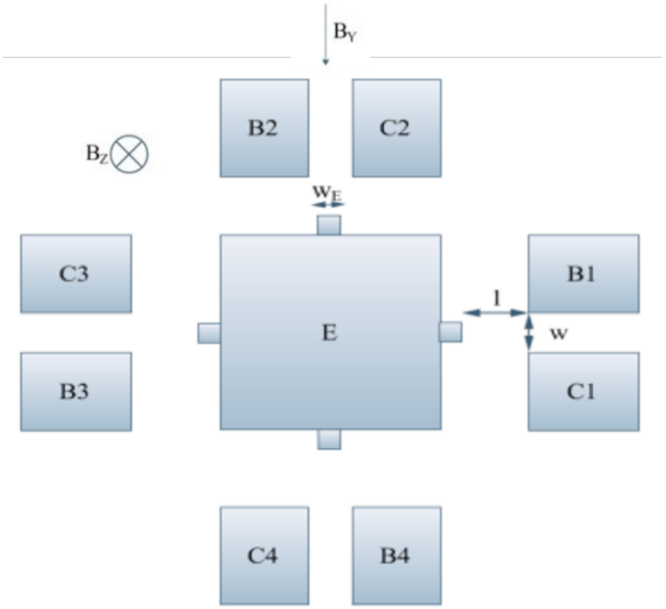

Fig. 1.18: Top view of magnetotransistor structure [66] (IEEE copyright line © 2015 IEEE).

For in-plane magnetic field sensing, bipolar npn Lateral MagnetoTransistors (LMTs) are often used, although they suffer from a large offset; for this reason, in order to implement a 360° angular sensor, in [67] (IEEE copyright line © 2011 IEEE) authors presented a MOS-gate Bipolar MagnetoTransistor, fabricated in CMOS-SOI technology and having two central emitters (E_1, E_2) for smaller offset, and emitter E, base (B), and collector (C) contact definition by MOS-gate structures (see Fig. 1.19).

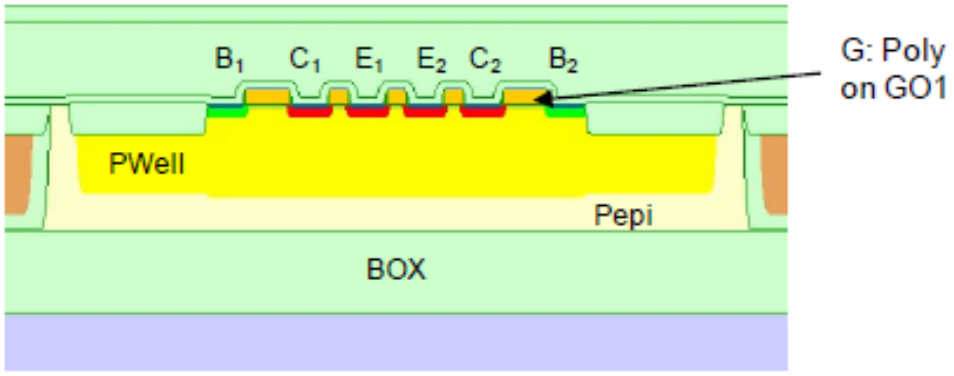

Fig. 1.19: Cross-sections of SOI-LMTs with poly gates on GO1 (top) between E (n^+), C (n^+) and B (p^+) regions [67] (IEEE copyright line © 2014 IEEE).

1.2 MEMS magnetometer

The miniaturization has allowed the fabrication of numerous elements on the same chip, such as sensors, actuators, electronics, computation, signal processing and control [68]. The chip can be developed using the batch production of micro fabrication processes, which can reduce its cost. The miniaturization is key to produce chips with important characteristics, such as multiple functions, small size, low-energy consumption and high performance and it has achieved faster devices with considerable cost/performance advantages and the integration of mechanical and fluidic parts with electronics. Thus, these devices can increase their functionality, resolution and sensibility. Microelectromechanical systems (MEMS) have enabled the development of devices composed of electrical and mechanical components with size in the micrometer-scale, which can include signal acquisition, signal processing, actuation and control. These devices offer several advantages such as small size, reduced power consumption, high sensitivity and low-cost batch fabrication. Recently, several MEMS devices have been fabricated such as micromirrors, accelerometers [69], gyroscopes [70], magnetometers, pressure sensors [71] and micropumps [72] and they can be employed in biomedical and chemical analyses, automobile

and military industries, telecommunications, consumer electronic and navigation. Furthermore, MEMS devices can be classified in three groups: sensors, actuators and micromechanical structures: the first one, sensors, detect chemical and physical signals, which are converted into electrical signals; the actuators transform magnetic or electrical input signals to motions, and, eventually, the micromechanical structures are represented by beams, plates or microchannels. Taking account into this research activity is founded on the realization, fabrication and testing of a MEMS magnetometer in a specific technology, PiezoMUMPs, it is believed essential to mention and describe some procedural aspects, such as fabrication and packaging processes. In relation to the first point, MEMS devices can be manufactured using surface and bulk micromachining techniques, which take advantage of both mechanical and electrical properties of the silicon. Just to mention, silicon mechanical properties have a higher strength than the steel and a minimum mechanical hysteresis. Surface micromachining is based on patterning layers deposited on the silicon surface and it allows to integrate MEMS devices with microelectronics on the same substrate. The thickness of the structural layer is determined by the thickness of the deposited layer through, typically, the low-pressure chemical vapor deposition (LPCVD) technique. As concerns bulk micromachining, it selectively removes a silicon substrate to fabricate three-dimensional microstructures, for example beams, membranes, holes and microchannels, using etching techniques that eliminate materials in desired areas through physical (Plasma etching) or chemical (KOH) processes. Related to the second point, the packaging process is very important to protect the MEMS device from environmental parameters such as moisture, liquid or gaseous chemicals; during this phase the device die is bonded to a package (die-attach) and, afterwards, the electrical contacts (pads) of the die surface are connected to package pads by wire bonds, guaranteeing the electrical connections between the device and external components. Finally, it is important to underline that MEMS devices require reliability tests to verify their performance under different environmental and operating

conditions. These tests can involve operational life, temperature cycling, mechanical shock, humidity variations, high temperature, and vibrations.

1.3 Lorentz force Magnetometer

MEMS-based Lorentz force magnetometers represent an option for monitoring magnetic field with important advantages such as small size, light weight, low power consumption, high sensitivity, good resolution, wide dynamic range, and low cost by using batch fabrication. However, MEMS magnetometers need more reliability studies to ensure a safe performance under different environmental conditions. MEMS Lorentz force magnetometers can operate with silicon-based structures, in which the interaction between an external magnetic field and an electrical current is exploited to generate a Lorentz force on the structures. This force, which is expressed in general form in eq. (1.4), is perpendicular to the direction of both magnetic field and electrical current and it causes a deformation of the magnetometer structure that can be measured by using a capacitive, piezoresistive, or optical sensing technique.

$$\vec{F} = q\left(\vec{E} + \vec{v}\, x\ \vec{B}\right) \tag{1.4}$$

Taking into account a resonant structure exhibits an amplified response to an excitation source applied with a frequency equal to the resonant frequency(ies) of the structure itself, it is recommended to operate at resonance. For this reason, electrical current is applied with a frequency equal to the resonant frequency of the magnetometer structure, increasing its sensitivity up to a parameter equal to its quality factor (Q). As concerns the quality factor, Q, it is correlated to the damping factor for a second order system in accordance with the eq. (1.5) [73] and illustrated in Fig. 1.20:

$$Q=\frac{1}{2*\xi}=\frac{f_n}{\Delta f}=\frac{f_n}{f_2-f_1} \tag{1.5}$$

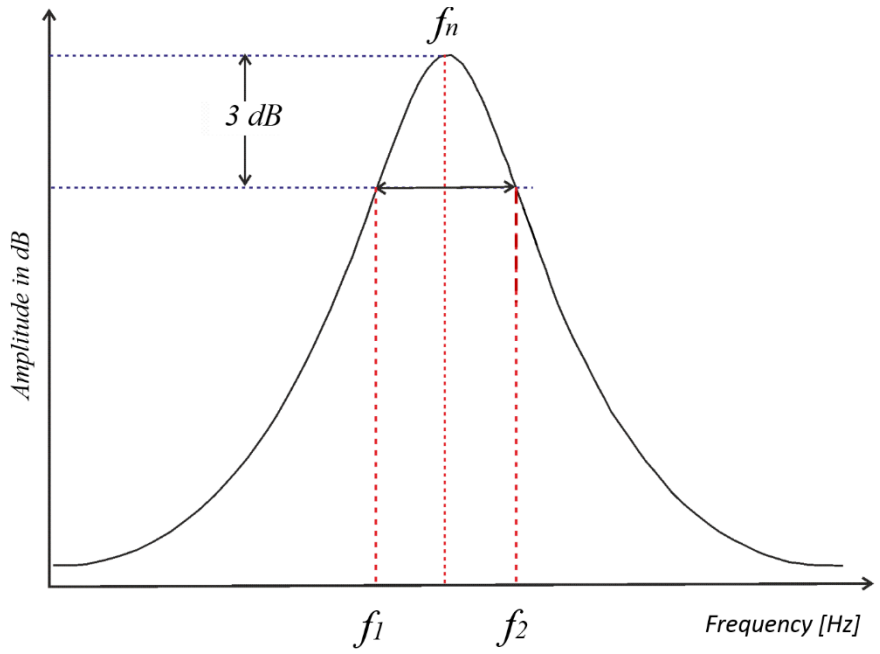

Fig. 1.20: Amplitude in dB of a second order system as a function of the frequency.

In which f_n is the natural frequency, $\Delta f = f_2 - f_1$ is the bandwidth at -3 dB and, at last, ξ is the damping factor that can be expressed as:

$$\xi=\frac{d}{2*\sqrt{k*m}} \tag{1.6}$$

where d is the dynamic damping of the mass movement and k and m are the stiffness and the mass of the structure, respectively. Therefore, the quality factor also describes the accuracy at the resonance peak: the higher the Q, the narrower the band. The eq. (1.5) and (1.6) suggest the most common method to measure Q or the damping factor by measuring the frequency of resonance and bandwidth.

It is interesting to note that these resonant structures commonly are integrated by clamped-free/clamped-clamped beams, torsion/flexion plates or an array of them, as discussed below. The application of external magnetic fields alters the deflections of the resonant structure, which can be detected through piezoresistive, capacitive and optical sensing techniques.

1.4 Sensing Techniques

Just for completeness, a brief mention related the working principle of several sensing techniques is considered essential in order to discuss, afterwards, various MEMS devices.

1.4.1 Piezoresistive transduction

In the piezoresistive sensing approach, a Wheatstone bridge having two active (placed on the microbeams, R_1 and R_4) and two passive piezoresistors (deposited on the substrate, R_2 and R_3) is used (as shown in Fig. 1.21). The active piezoresistors can shift their resistance magnitudes, whereas, the passive piezoresistors have fixed-value resistances.

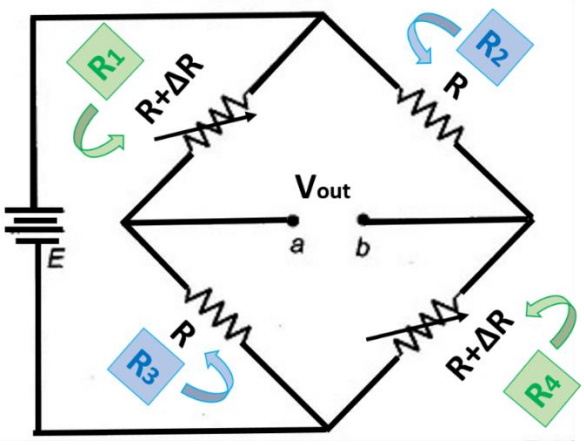

Fig. 1.21: Wheatstone bridge.

Typically, an excitation AC current (*I*) is supplied with a frequency equal to the resonant frequency of the microbeams through an aluminium loop. When the structure is exposed to an external magnetic field the generated Lorentz force determines a longitudinal strain (ε) on the two active piezoresistors changing their resistance values, as indicated in eq. (1.7):

$$\Delta R = G * \varepsilon * R \tag{1.7}$$

where ΔR is the piezoresistive variation in each piezoresistor, *G* is the gauge factor and *R* is the nominal resistance value. As a consequence, in accordance with eq. (1.8), an output voltage shift (V_{out}) is produced due to the resistive variation:

$$V_{out} = \frac{\Delta R}{2R + \Delta R} \cdot E \tag{1.8}$$

in which *E* is the bias voltage of the Wheatstone bridge. The sensor sensitivity (*S*) is defined as the ratio between output voltage variation and the range of the external magnetic field, as expressed in eq. (1.9):

$$S = \frac{\Delta V_{out}}{\Delta B} \tag{1.9}$$

It is essential to underline that piezoresistive sensing approach is simple and easy to use in resonant magnetic field sensors based on MEMS technology.

1.4.2 Capacitive transduction

Any MEMS sensor with capacitive sensing approach is composed of a mobile part (called "rotor") and a fixed part (called "stator") in its simplest form. The rotor consists of a mobile mass suspended with respect to the substrate and anchored by a system of springs, in order to allow the movement on one or more axes. The stator is instead composed of rigid structures, anchored to the substrate, on which the readout electrodes are created. In general, it is possible to estimate a current signal which changes in accordance with the position of the rotor respect to the stator (as shown in Fig. 1.22) [74].

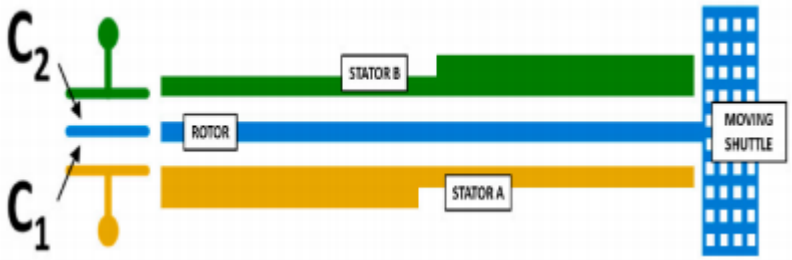

Fig. 1.22: Differential capacitive sensing cell for a MEMS structure [74].

The number, shape and size of the electrodes on the stators, as well as of the moving mass, depend on the technological possibilities of the production process, the project specifications and the choices in the implementations. When the MEMS device is actuated by Lorentz force this force is then used to move an armature of a capacitor, held at a constant voltage, generating a charge displacement that is subsequently acquired by a front-end circuit. Several front-end circuits have been found in literature in order to convert the capacitance variation in a useful signal: in [74] authors used a switched-capacitor (SC) preamplifier in order to induce the capacitive to voltage (C-V) conversion, and, afterwards, a self-oscillated noise-shaping integrating dual-slope (DS) converter is used to digitize this magnitude. Another solution is

described in [75] (IEEE copyright line © 2011 IEEE), where a capacitance-to-voltage converter and an amplitude detector are used (as shown in Fig. 1.23).

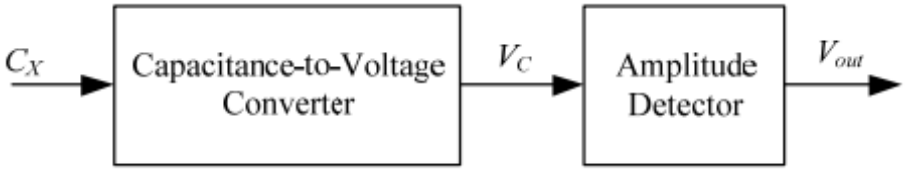

Fig. 1.23: Block diagram of the proposed interfacing circuit technique [75] (IEEE copyright line © 2015 IEEE).

In detail, the C-V converter is based on a charge amplifier, in which the sinusoidal voltage V_{ex} is the excitation signal applied into charge detector, whereas the second block is founded on a sample-and-hold circuit S/H, two monostable multivibrators MN1 – MN2 and comparator CP_1, as illustrated in Fig. 1.24.

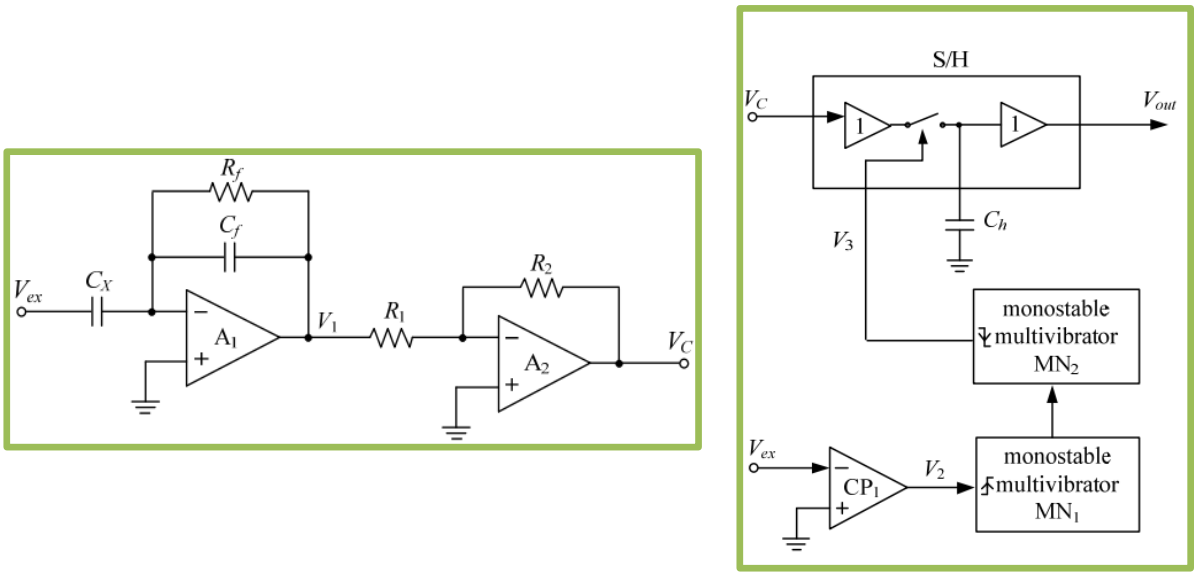

(a) (b)

Fig. 1.24: (a) C-V converter based on charge amplifier; (b) Amplitude detector [75] (IEEE copyright line © 2015 IEEE).

Furthermore, typically, in order to redouble the performance, the central plate of a differential capacitor is moved, with the proof mass moving from the centre towards one of the two external plates, moving away from the other (see Fig. 1.25).

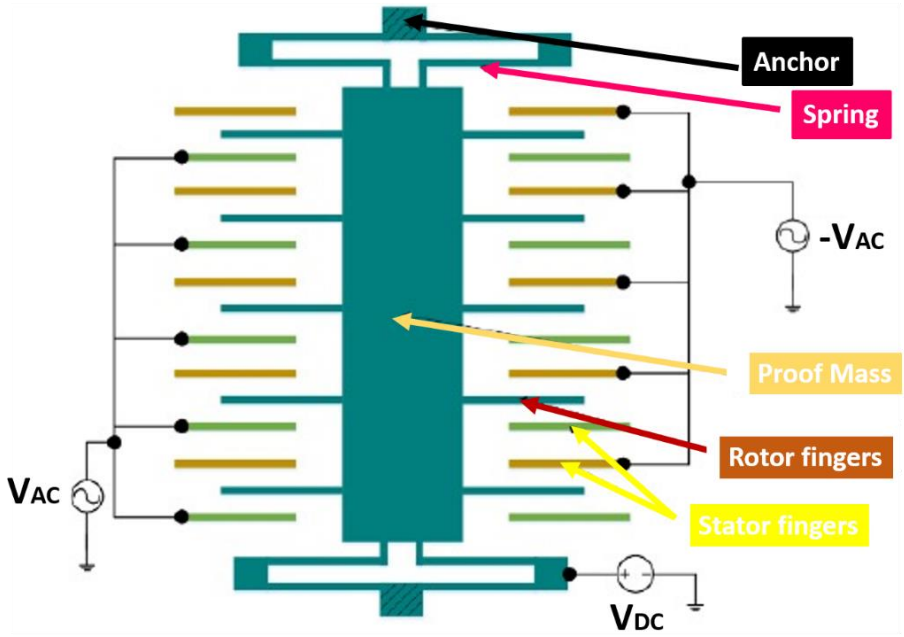

Fig. 1.25: Differential configuration of a capacitive accelerometer © Sinha, Mukhiya, Pant / CC-BY-SA-4.0.

1.4.3 Optical transduction

In the optical sensing approach, an optical fiber [76] or a miniature laser, that can be a laser diode beam with position sensitive detector [77], are used to detect the deflection on the MEMS device. It is interesting to underline that magnetometers with optical readout systems exhibit, as advantage, the opportunity to reduce their electronic circuitries and weights, nevertheless they require an almost perfect vertical front side of the cantilevers, in order to avoid the interfering reflected light. In detail, in [76] authors have developed two U-shaped beam cantilever magnetometers, that have dimensions 1100 μm × 100 μm × 10 μm, with an optical detection

system (as can be observed in Fig. 1.26). These magnetometers are appropriate to detect magnetic field from 10 mT to 50 T in electromagnetically noisy environments. It is essential to notice that temperature shifts can alter the fundamental resonant frequencies of the cantilevers, modifying the deflections and output signals of the magnetometers.

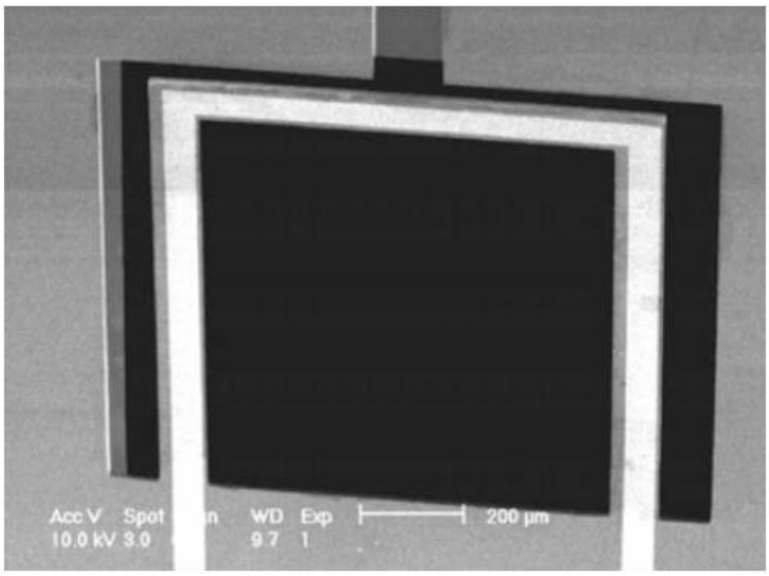

Fig. 1.26: SEM image of a magnetometer integrated by a resonant silicon structure with optical sensing [76].

Another solution has been found in [78], where a magnetic field sensor, composed of a shuttle which is designed to resonate in the lateral direction (first mode of resonance) is described and showed in Fig. 1.27.

In the presence of an external magnetic field, the Lorentz force actuates the shuttle in the lateral direction and the differential change in the amplitude of the resonating shuttle is correlated to the strength of the external magnetic field to be measured. The resonance frequency of the shuttle is determined to be 8164 Hz experimentally and the quality factor and damping ratio have been estimated in an open environment 51.34 and 0.00973, respectively. The sensitivity of the sensor has been estimated 0.034 µm/mT when a current of 10 mA is generated into the shuttle, although

a sensitivity of 1.35 µm/mT has been determined at the resonance with a current of 8 mA. Finally, the resolution of the sensor has been evaluated 370.37 µT.

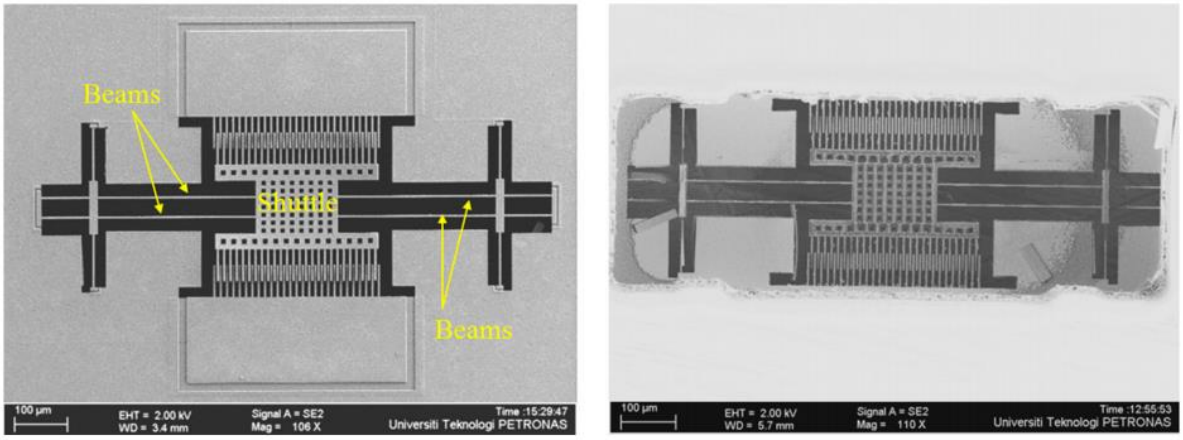

(a) (b)

Fig. 1.27: FESEM image of fully released device [78]; (a) Front side view; (b) Back side view.

1.4.4 Piezoelectric transduction

In the piezoelectric sensing approach, the piezoelectric effect is used. Taking account into the MEMS magnetometer presented in this manuscript exhibits a piezoelectric readout strategy, it is considered favourable to describe the peculiar aspects of piezoelectric materials.

Piezoelectricity was discovered by two French scientists, Jacques and Pierre Curie, in 1880 and the term comes from the Greek word piezo which means squeeze or press. The piezoelectric effect is the ability of certain materials to generate an electric charge in response to applied mechanical stress and it is reversable process. In other terms, when a mechanical stress is applied to a piezoelectric material, a shifting of the positive and negative charge centres in the material takes place, with the consequent generation of an external electrical field (called *direct* piezoelectric effect, see Fig. 1.28a). On the contrary, an outer electrical field applied to a

piezoelectric material introduces stretches or compresses in it (called *inverse* piezoelectric effect, see Fig. 1.28b).

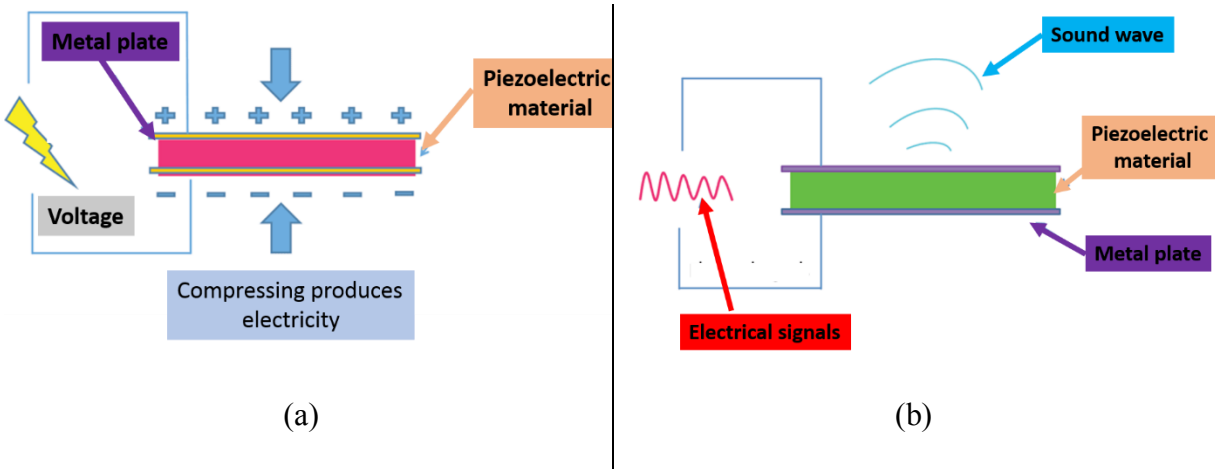

Fig. 1.28: Piezoelectric Effect: (a) Direct; (b) Inverse.

Therefore, piezoelectric materials are materials that can produce electricity due to mechanical stress, such as compression and they can also deform when voltage (electricity) is applied. Some examples of piezoelectric materials are PZT (also known as lead zirconate titanate), barium titanate, lithium niobite, aluminium nitride and piezoelectric fluoropolymer films. Typically, piezoelectric materials are used in the realization of actuators, sensors and transducers. Just to mention, in [79] we have presented a movable strategy to measure static or quasi-static magnetic field by using a RTD-Fluxgate magnetometer and a bimorph artificial whisker used as actuator. In detail, a piezoelectric bimorph, composed of two piezoelectric fluoropolymer film sheets and produced by Images SI Inc. [80], has been implemented in parallel mode in order to actuate a flexible RTD-Fluxgate magnetometer and to test its capability to “sense” the presence of a magnetic target in different positions during its actuation. In conclusion, the actuation foil has been characterized in absence of the sensor and in presence of the sensor, obtaining a sensitivity of 9.12×10-3 °/V and resolution of 0.22 ° in the first case, whereas a sensitivity of 7.96×10-3 °/V and resolution of 0.17 ° are carried out in the second one.

As concerns the piezoelectric sensing approach in MEMS magnetometers, few studies have been found in literature; in [81] (IEEE copyright line © 2011 IEEE) Ghosh *et al.* demonstrated the sensing of lateral magnetic fields using the piezoelectric effect in a resonant MEMS thin-film piezoelectric-on-silicon (TpoS) CMOS compatible magnetometer (as illustrated in Fig. 1.29b). The magnetometer is based on an 800 µm wide suspended square plate which works as the resonator to be mechanically actuated by Lorentz forces resulting from the cross product of a line current passing along the sides of the plate and a lateral magnetic field. It is important to highlight that an AC current is applied around the resonance frequency of the MEMS device in order to maximize its displacement amplitude as determined by the quality (Q) factor. As can be observed in Fig. 1.29a, an output patch electrode of a piezoelectric transducer stack is placed at the centre of the square plate, while the input tracks are routed along the perimeter of the square plate. Authors have experimentally estimated a resonance frequency and a responsivity of 159.35 kHz and of 12156 ppm/T, respectively.

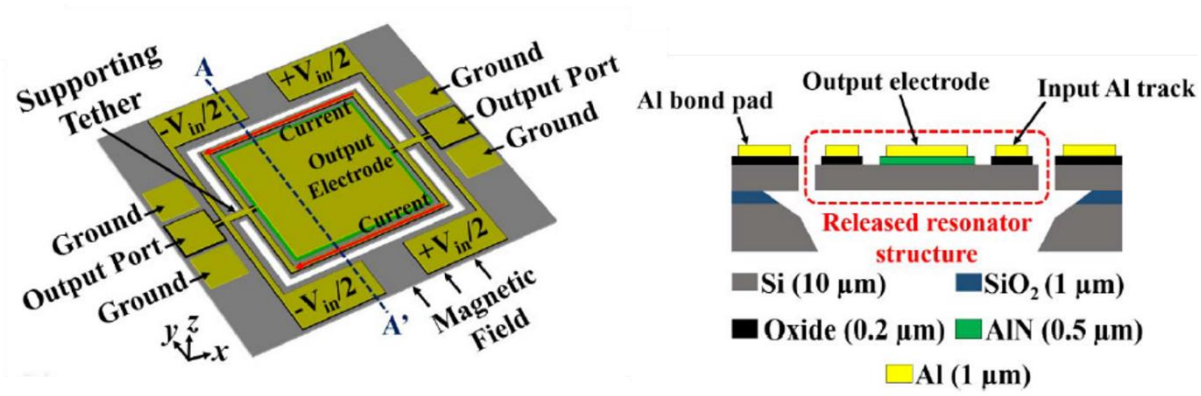

(a) (b)

Fig. 1.29: (a) Schematic of TpoS magnetometer with required biasing configuration; (b) Cross-sectional view [81] (IEEE copyright line © 2017 IEEE).

1.5 MEMS torsional resonant magnetometers based on Lorentz force

This section is dedicated to a peculiar sub-class of MEMS resonant magnetometers based on Lorentz force, that are torsional structures. Although the MEMS architecture analysed in this manuscript is focused on a U-shaped beam cantilever, that is characterized by a linear deflection, in order to provide a thorough overview, it is believed necessary to describe briefly some examples of torsional architectures and their performance. Just to mention, Ren *et al.* have developed a MEMS magnetometer actuated by Lorentz force, which is suitable for spacecraft and it is composed of torsional structures, torsional beams, metal plates, a coil and a glass substrate (as shown in Fig. 1.30a) [82] (IEEE copyright line © 2011 IEEE); in detail, they have designed a novel structure of folded torsional beams and a double-layer excitation coil to increase the sensitivity of the sensor. The Lorentz force, generated by the interaction of a current in the MEMS coil and an external horizontal magnetic field, determines a displacement of the torsional structure, which can be detected by two sensing capacitors in accordance with the differential change.

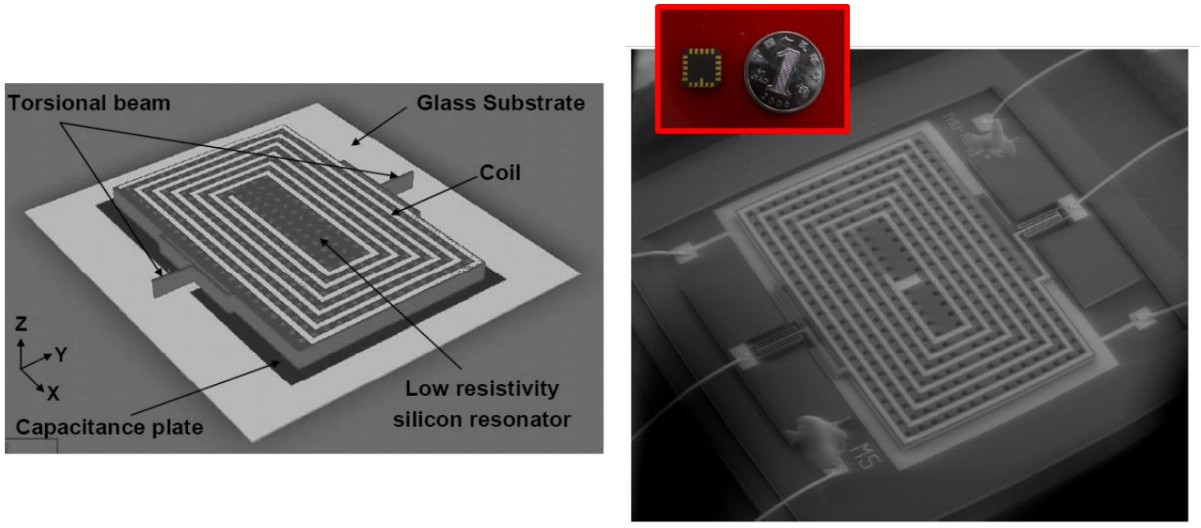

(a) (b)

Fig. 1.30: MEMS torsional resonant magnetometer [82] (IEEE copyright line © 2013 IEEE): (a) Structure and principle; (b) Prototype.

The device has been packaged and bonded (see Fig. 1.30b) with are six gold wires needed for the connections among the gold poles of the shell package and the MEMS structures. The sensing technique is capacitive, and the results have demonstrated a resonance frequency of 1100 Hz, a capacitance variation around 100 fF when an external 50 μT magnetic field is applied and a resolution of 30 nT has been estimated.

As previously mentioned, MEMS devices find utilization in several contexts, such as compass applications and not always they work at the resonance; in particular, a MEMS magnetometer, capable of measuring magnetic fields along an in-plane direction and operating off-resonance, has been developed in ThELMA technology (from STMicroelectronics) and it is based on four torsional springs sustaining a 1095 μm × 282 μm suspended plate [83] (as described in Fig. 1.31a-b).

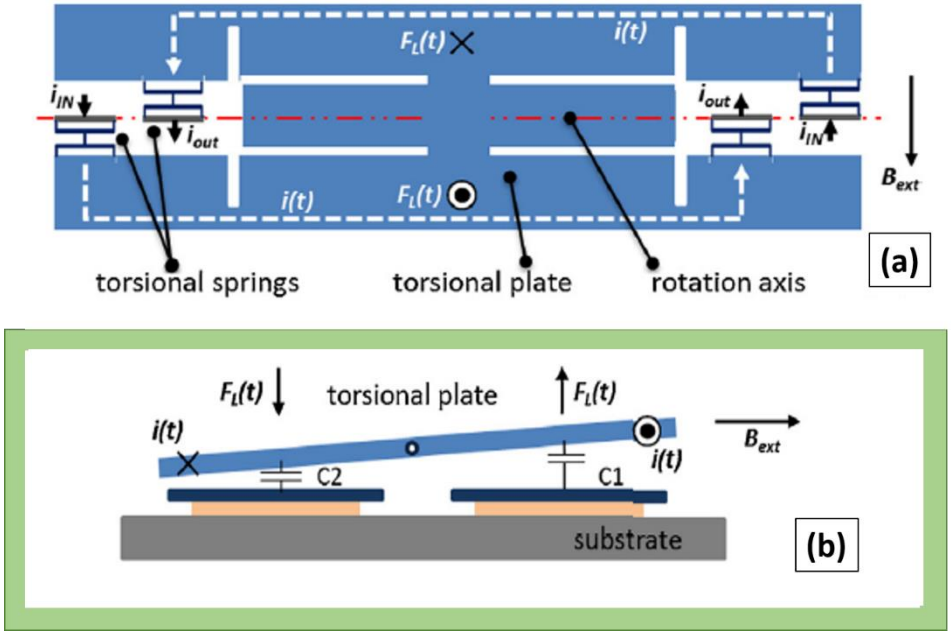

Fig. 1.31: Working principle [83]: (a) Top view; (b) Cross-section.

The device is designed in order to have the first mechanical mode at a nominal frequency of 20 kHz (FEM analysis is shown in Fig. 1.32) and the motion is detected by the parallel-plate capacitors having an area of 7.9 μm × 104 μm, suitably designed 1.8 μm below the frame.

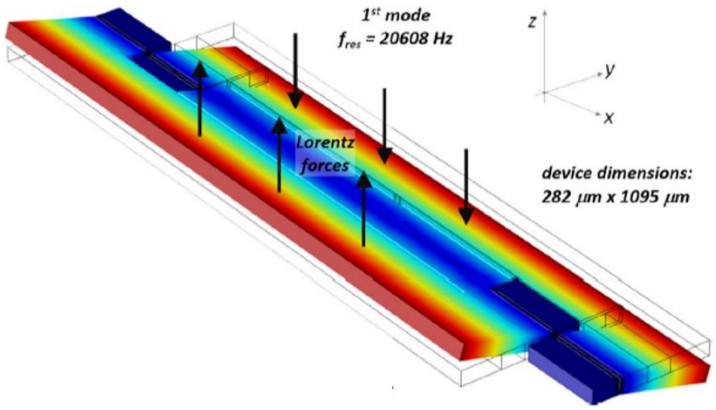

Fig. 1.32: FEM analysis of the first resonant mode [83].

As experimental results, the resonance frequency has been estimated at 19953 Hz and, generating a quasi-static ramp of magnetic fields around ± 5 mT, a sensitivity of 0.85 V/mT has been evaluated. Afterwards, the device is then operated off-resonance by changing the frequency of the drive signal, and, considering a mismatch of 50 Hz, a sensitivity of 0.068 V/mT is obtained. Thanks to the much better immunity to small changes of the resonance frequency, which may be induced by poor stability of the biasing voltages or by temperature changes, off-resonance operation demonstrates a 100-fold better long-term stability at 100 s observation time.

As last example, another interesting study case is presented in [84] (IEEE copyright line © 2011 IEEE) where a torsional MEMS magnetometer has been implemented using the MEMSCAP SOI process and it is composed of beams, combs, rotor and stator (as illustrated in Fig. 1.33a-b).

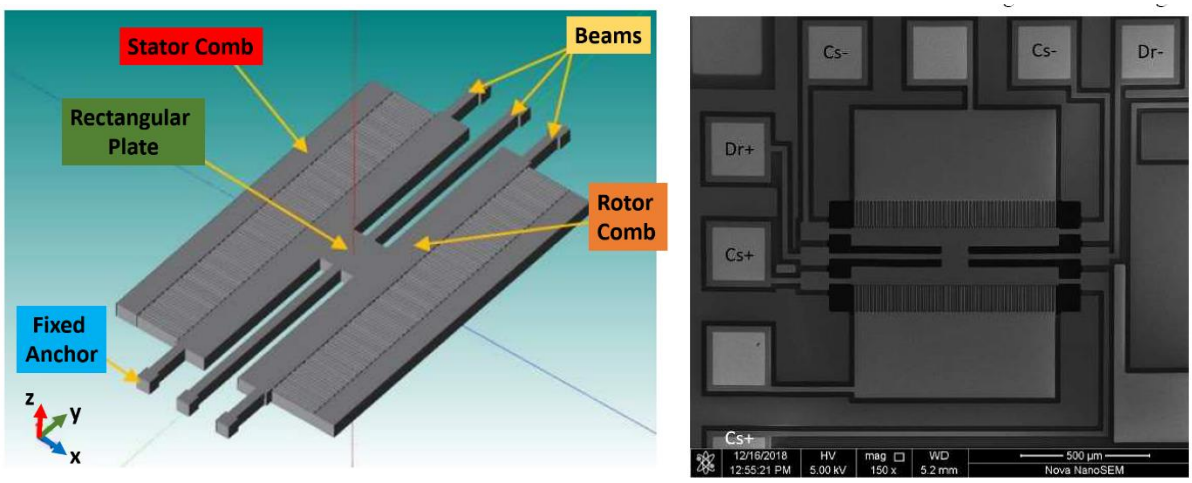

(a) (b)

Fig. 1.33: MEMSCAP SOI magnetometer: (a) 3D model; (b) SEM image [84]

The difference in capacitance and displacement are measured through the overlapping motion in the x direction of the comb fingers at the resonance frequency. During its motion, the gap between fingers changes, thus impacting the differential capacitance. Regarding geometrical parameters it is important to mention that the beam width is 20 µm and its spacing from the rotor plate is 30 µm, the fingers are 100 µm long, 5 µm wide and two adjacent fingers have a gap of 2 µm. Authors have simulated the MEMS device performance considering several beam's lengths in the range [85 – 250] µm and several beam's widths in range [5 – 20] µm at the same Q value (Q = 100000): as expected, the sensitivity improves if the length increases and higher displacements are obtained when the width decreases and therefore higher sensitivities. In order to actuate the magnetometer a current is generated from the application of voltage across the driving elements of the device (Dr+ and Dr-) and this current, combined with the surrounding magnetic field, generates the Lorentz force, which produces the displacement of the sensing

element, Cs+ and Cs- (see Fig. 1.33b).The results show that the proposed device is appropriate for navigational applications close to the Earth's surface.

1.6 Summary

In conclusion, in order to contextualize the research activity presented in this thesis a table summarizing the main characteristics of discussed magnetic field sensors has been implemented (see Table 1), in which the operative range (T), the accuracy (ppm), benifts (Pros) and limitations (Cons) are listed.

Magnetic Sensor	***Operative Range (T)***	***Accuracy (ppm)***	***Pros***	***Cons***
SQUID	$10^{-15} \div 10^{-9}$	8000	• High sensitivity • Magnetically "clean" • Linear with feedback	• Cryogenic temperature • High cost • High power • Complexity • Bandwidth limited by feedback
Fluxgate	$10^{-10} \div 10^{-4}$	900	• Good low field performance	• Point measurement • Large physical size • Limited bandwidth
Magnetoresistance	$10^{-8} \div 10^{-3}$	5000	• Good low field performance • Good bandwidth	• *1/f* noise • Unipolar • Point measurement
Proton Precession	$10^{-11} \div 10^{-7}$	~ 5	• Sensitive to 1 nT • Small, rugged and reliable	• Sensitive to high gradients • Low sampling rates

			• Not sensitive to orientation	• High power consumption
Optically Pumped	$10^{-12} \div 10^{-5}$	30000	• High sensitivity room temperature • Short distance between the sensor and the sample	• Complex Setup • Heating
Hall Effect	$> 10^{-5}$	100 ÷ 300	• Robustness • Low Cost • Fast Response • Contactless	• Require separate magnet for its operation • Influence of the Temperature • Drift, require compensation
Magnetodiode	$10^{-5} \div 10^{2}$	20	• Sensitive to longitudinal and transverse field	• Nonlinear output and decrease device yield
Magnetotransistor	$10^{-6} \div 10^{2}$	30000	• High sensitivity • Nearly linear response • Integration of sensor element and circuitry • Wide calibration range • Low cost	• *1/f* noise and shot noise • Large offset • Instability of device surface • Reduced carrier mobility in the channel
MEMS Lorentz Force	$10^{-9} \div 1$	20000	• small size, low power consumption, good resolution, low cost, wide dynamic range light weight, high sensitivity.	• Reliability studies • Offset and associated Drifts • Sensitivity long term stability

Table 1: Main characteristics of the magnetic field sensors presented.

After this brief nevertheless fundamental introduction a specific category of MEMS magnetometers actuated by Lorentz force are on the point of being described, taking into account the MEMS magnetic field sensor proposed in this manuscript, is a modification of this class, represented by the U-shaped beam cantilever.

Chapter 2

U-shaped beam cantilevers

A U-shaped beam cantilever is a beam anchored at two extremes having greater length as compared to its width and thickness. The main characteristic of a cantilever is related to its property to respond mechanically when a variation in external parameters, such as temperature, molecule absorption, magnetic field and so on, is present. As microelectromechanical system the architecture of a U-shaped beam cantilever is quite simple and it can be realized in numerous integrated technologies, such as CMOS, MEMSCAP SOI, MEMSCAP PiezoMUMPs, and with various readout strategies, such as piezoresistive, capacitive, optical and piezoelectric. In this chapter several prototypes of U-shaped beam cantilever will be examined in terms of performance, taking into account different technologies and readout approaches.

2.1 Working Principle and Modeling

In order to describe the working principle of a U-shaped beam cantilever a general schematic is presented in Fig. 2.1. It is interesting to underline that this category of MEMS devices is typically used as current sensor, magnetic field sensor or accelerometer.

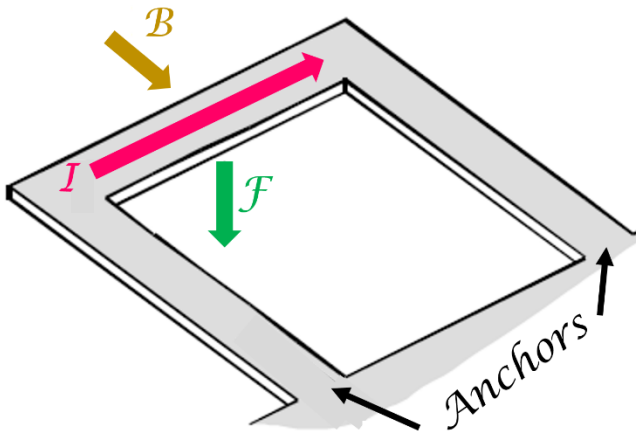

Fig. 2.1: General schematic of U-shaped beam cantilever.

Acting as current or magnetic field sensor, the U-shaped beam cantilever exploits Lorentz force exerted by magnetic induction on a charged moving particle, and this behaviour is modeled by the following equation, as explained in [85]:

$$\overrightarrow{F_L} = q \cdot (\vec{E} + \vec{v} \times \vec{B}) \tag{2.1}$$

where q is the charge of the particle, $\vec{E}$ is the electric field, $\vec{v}$ is the velocity of the particle and $\vec{B}$ is the magnetic induction. Here we assume that $\vec{E}$ is absent and an electrical current I is driven into an electrical wire. Taking also into account that the current I can be described as

$$\vec{I} = \lambda \vec{v} \tag{2.2}$$

in which λ is a free charge having velocity$\vec{v}$, in a section dl the total charge dq, can be expressed as

$$dq = \lambda \, dl \tag{2.3}$$

and hence the expression of Lorentz force becomes:

$$d\vec{F} = dq \, \vec{v} \times \vec{B} = \lambda \, dl \, \vec{v} \times \vec{B} \tag{2.4}$$

The net force can be found by integrating (2.4):

$$F = \int dl \, \vec{I} \times \vec{B} = ILB \tag{2.5}$$

where L is the length in which $\vec{I}$ and $\vec{B}$ are perpendicular.

It is noteworthy to highlight that this electromagnetic force is used to deform the mechanical structure. When supplied by a calibrated current the structure deformation directly depends on the external magnetic field intensity and the following deformation is then translated into an electrical signal by several readout strategies.

Moreover, the U-Shaped beam cantilever exhibits a dynamic behaviour which can be depicted using the well-known equivalent mass-spring system equation [86]: in detail, this system, that is shown in Fig. 2.2, can be depicted with the second-order differential equation:

$$m\ddot{x} + d\dot{x} + kx = F_L(t) \tag{2.7}$$

in which m is the inertial mass of the microelectromechanical structure, d represents the damping coefficient and k is the mechanical stiffness. Furthermore, $F_L(t)$ represents the Lorentz force, whereas $\ddot{x}, \dot{x}$ and x are the acceleration, the velocity and the displacement of the cantilever tip, respectively. In relation to the inertial mass it is interesting to specify that the m term should include two components which are the structure mass (m_s) and the mass on the tip (m_{tip}); however, in general, in order to increase the sensitivity of the MEMS sensor m_{tip} is greater than m_s and it is legitimate to assume:

$$m = m_{structure} + m_{tip} \approx m_{tip} \tag{2.8}$$

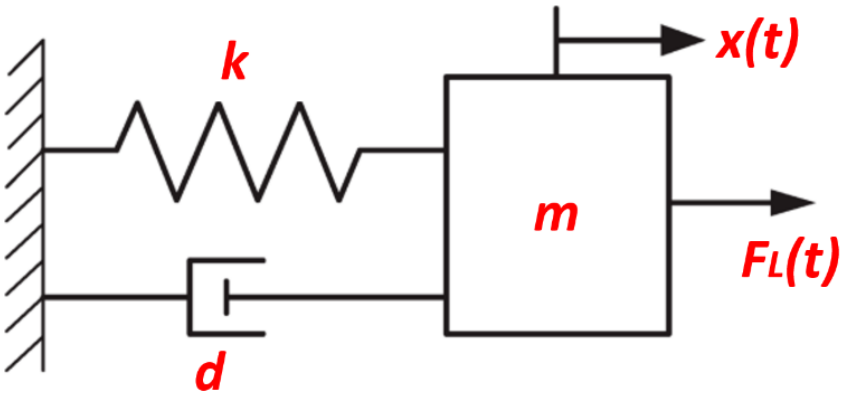

Fig. 2.2: Schematic of mass-spring-damper system.

In relation to the class of magnetometers actuated by Lorentz force it is interesting to underline that they are capable to tune their operative range: taking into account the displacement of the tip is a function of the Lorentz force applied and this force is regulated by eq. (2.5) it is possible to detect several magnetic fields modifying the current which is driven into the sensor. Related to this aspect, it is necessary to specify the current range is limited by the capability of the driving

circuit as concerns the lower extreme, whereas the higher extreme is correlated to geometrical parameters of the layer where the current passes.

2.2 State of Art about U-shaped beam cantilevers

In this sub-section a detailed description of several prototypes, found in literature, of U-shaped beam cantilever which have been fabricated in different technologies and having several readout strategies is illustrated. In [87] Beroulle *et al.* have developed an electromechanical magnetic field sensor monolithically integrated together with CMOS electronics (see Fig. 2.3b). The sensor exhibits length (L_c), width (W_c) and single beam width (W_b) as indicated in Fig. 2.3a. It is important to note that the microbeams contain a planar aluminium coil of 80 turns (not represented in the picture) and two piezoresistive strain gauges of polysilicon connected to a Wheatstone bridge.

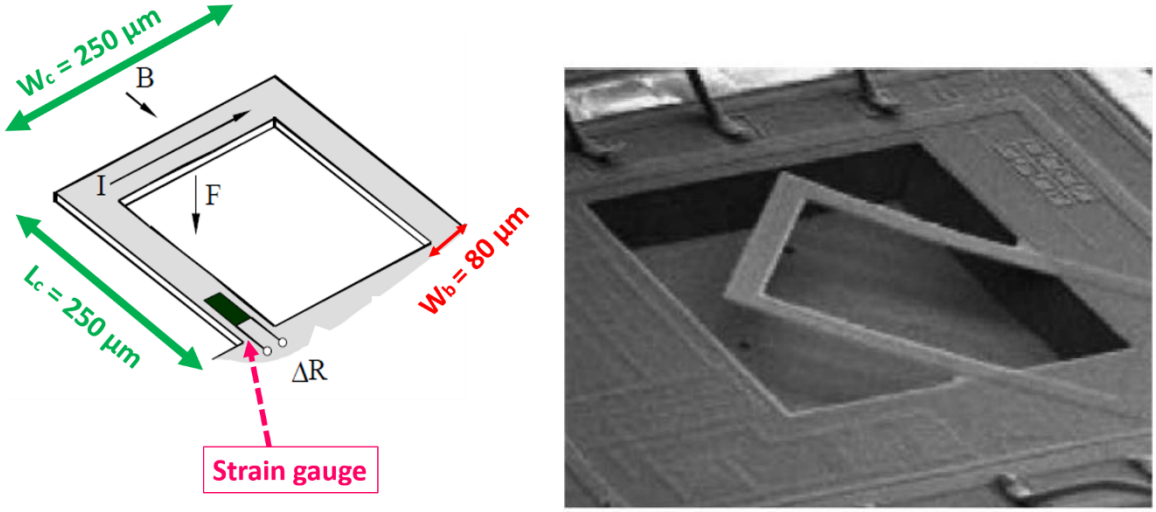

(a) (b)

Fig. 2.3: Bernoulli *et al.* device: (a) Dimensions; (b) SEM image of the fabricated sensor [87].

The coil is applied by an electrical current I, that can be either DC or AC in order to excite various actuation modes. When an external magnetic field B is present, the cantilever beam is therefore deflected due to the Lorentz force F, whose magnitude is given by

$$F = (nI) \cdot BW_c \tag{2.6}$$

where W_c represents the length of the cantilever free standing edge and n the number of turns in the integrated coil. As mentioned, the sensor is fabricated using an industrial CMOS process (1.2 μm CMOS by AMS (Austria Mikro Systeme)), as illustrated in Fig. 2.4a, which is followed by a post-process to release its microbeams. Experimental results have demonstrated that the resonance frequency is 8.97 kHz, the mass is 750 ng, the quality factor is 59 and about the performance in terms of sensitivity and resolution the MEMS magnetometer exhibits a sensitivity of 530 mV/T and a resolution of 10 μT.

In another paper, referenced [88] (IEEE copyright line © 2011 IEEE), almost all previous authors have realized in the same technology two matryoshka prototypes: the external one, named Cantilever F, with uniform beam width and another one, smaller, with a sharp reduction in the beam width, named Cantilever D (as can be observed in Fig. 2.4b). They have confirmed that both sensitivity and linearity are improved via the sharp reduction in the beam width realized in the D structure, and, in addition, D sensor results approximately twice faster than the F device.

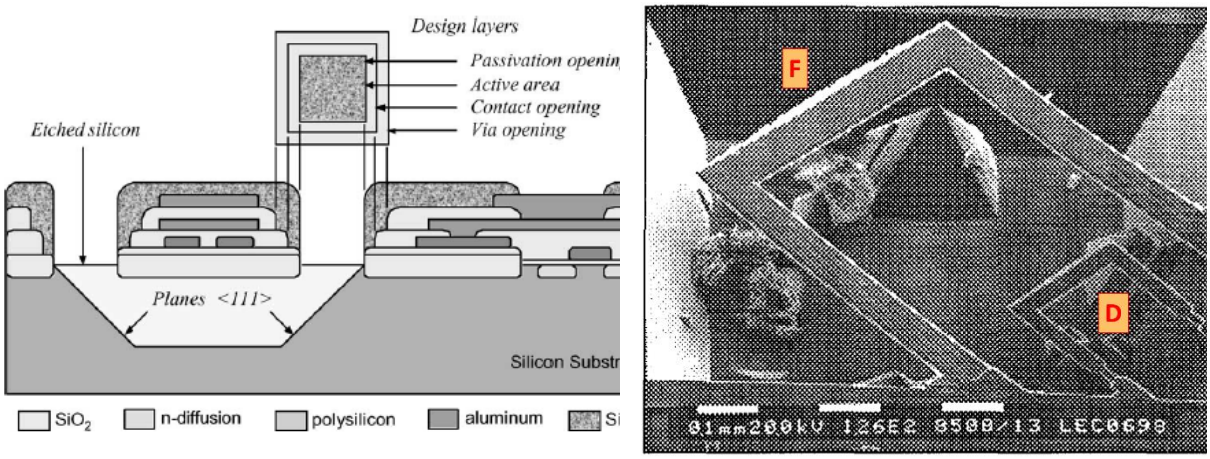

(a) (b)

Fig. 2.4: S. Baglio *et al.* device: (a) Realization through Standard CMOS process; (b) SEM image of MEMS sensors [88] (IEEE copyright line © 1999 IEEE).

Keplinger *et al.* [76,89] (IEEE copyright line © 2011 IEEE) have used the bending of a U-shaped Si cantilever as actuator principle for measuring the magnetic fields and an optical fiber as readout strategy. The magnetic flux density is converted into a movement of a micro machined U-shaped cantilever, which poses as a deflecting mirror in an optical readout system. The ratio of the intensity of the light reflected by the front side of the cantilever to the intensity of the incident light is analyzed. The cantilevers have a length of 1100 μm, a width of 100 μm, a thickness of 10 μm, an overall width of 1000 μm, and a gold loop having a thickness of 0.5 μm (see Fig. 2.5). The sensor has a large dynamic range and is principally used for applications with high magnetic fields [10 m – 50] T, corresponding to a current range [10 m – 40 μ] A; in detail, adopting a FEM analysis in ANSYS 6.0 authors have simulated a magnetic flux density of 40 T, a current of 2 mA, a length of the electrical lead of 1 mm, and they have determined a Lorentz force on the cantilever of 80 μN. Unfortunately, high current magnitudes (around 50 mA) are necessary in order to measure very low magnetic fields. The resonance frequency and the resolution have been evaluated 5 kHz and 10 mT, respectively.

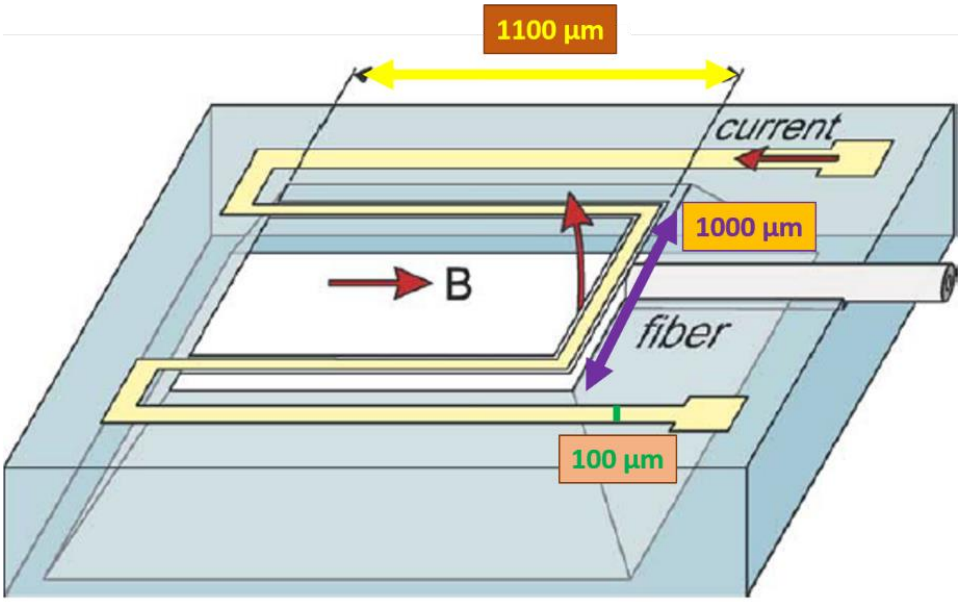

Fig. 2.5: Schematic and dimensions of MEMS magnetometer with optical readout [89] (IEEE copyright line © 2003 IEEE).

In addition, a Lorentz force magnetometer, having a micro leverage mechanism and a capacitive sensing approach, is presented in [90] (IEEE copyright line © 2011 IEEE), where Li *et al.* have realized a flexural beam resonator coupled to current-carrying silicon beams via a mechanical amplification. The device exhibits a length of 1.2 mm and an active length of 0.68 mm, as explicated in Fig. 2.6a; it is fabricated out of 40 µm-thick single crystalline silicon (as illustrated by SEM image in Fig. 2.6b).

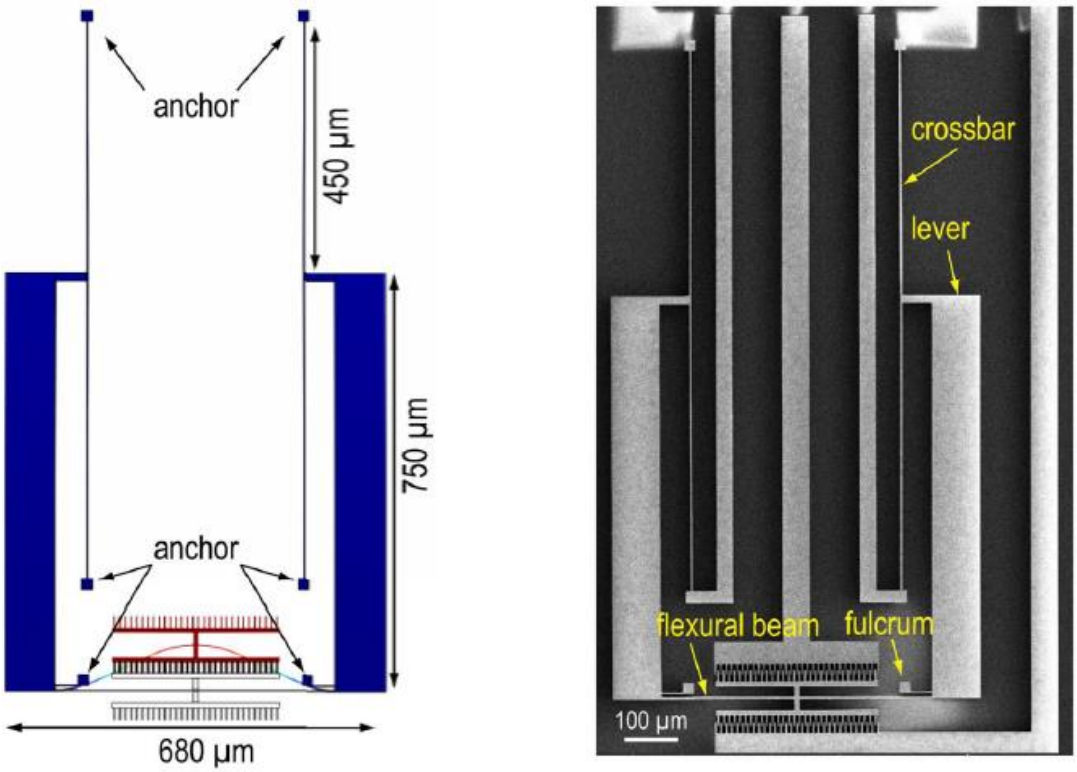

(a) (b)

Fig. 2.6: M. Li *et al.* magnetometer: (a) Structure and geometrical parameters; (b) SEM image [90] (IEEE copyright line © 2015 IEEE).

The working principle is presented in Fig. 2.7, in which the Lorentz force is generated by the presence of an external magnetic field and a DC current, I_B, passing through the 542 Ω device resistance, R_{LFS}.

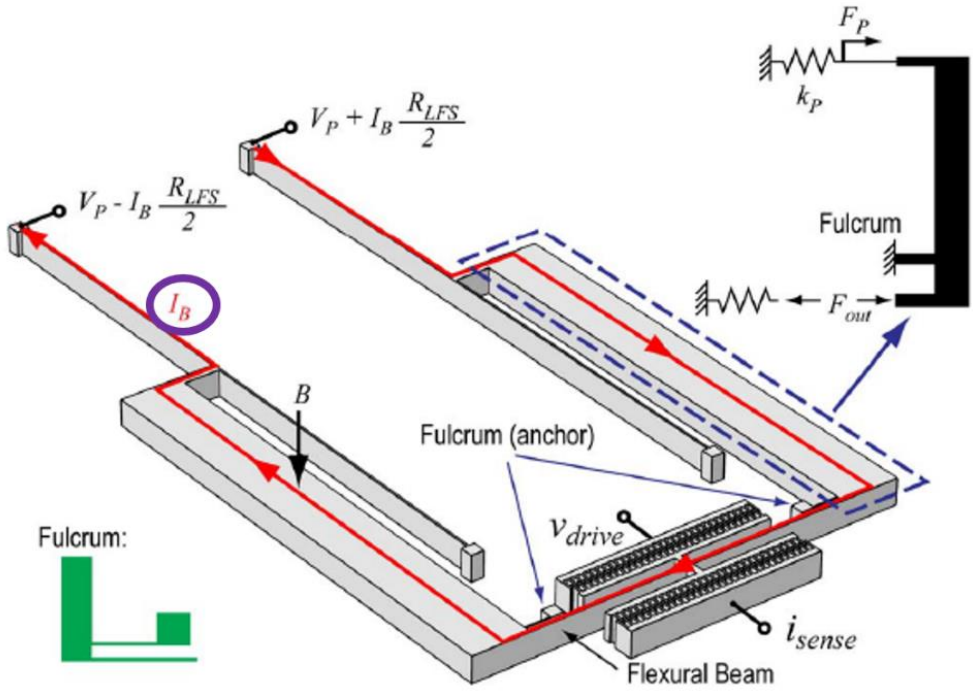

Fig. 2.7: M. Li *et al.* magnetometer: working principle [90] (IEEE copyright line © 2015 IEEE).

In order to maximize the sensitivity of the whole system a suitable distance of 7 μm from the fulcrum to the flexural beam has been selected to be about 100X smaller than the distance from the fulcrum to the lever input. The COMSOL simulation at a resonance frequency of 23.8 kHz confirmed that the mechanical amplification improves the sensitivity of the magnetometer by a factor of 42. During the characterization phase a Hall-effect gaussmeter is used to calibrate the magnetic field applied; in absence of the bias current, the measured resonant frequency is 22.6 kHz with Q of 540, nevertheless this frequency is reduced to 21.92 kHz when a current of 4 mA is applied. Eventually, the device has a measured sensitivity of 6687 ppm/(mA·T).

Another interesting prototype of Lorentz force magnetic field sensor, which provides a frequency output signal, is discussed in [91] (IEEE copyright line © 2011 IEEE): a cantilever structure is embedded as the frequency-determining element in an electrical oscillator and it is fabricated

using an industrial 0.8 µm CMOS process provided by *austriamicrosystems*, Unterpremstätten, Austria. The whole device is composed of a resonant silicon structure, a planar aluminum coil, two heating resistors, and P-channel Metal Oxide Semiconductor (PMOS) transistors (as illustrated Fig. 2.8). The Si-cantilever resonates at its resonant frequency because of the thermal actuation of two heating resistors and the oscillation is detected using PMOS transistors connected in a Wheatstone bridge.

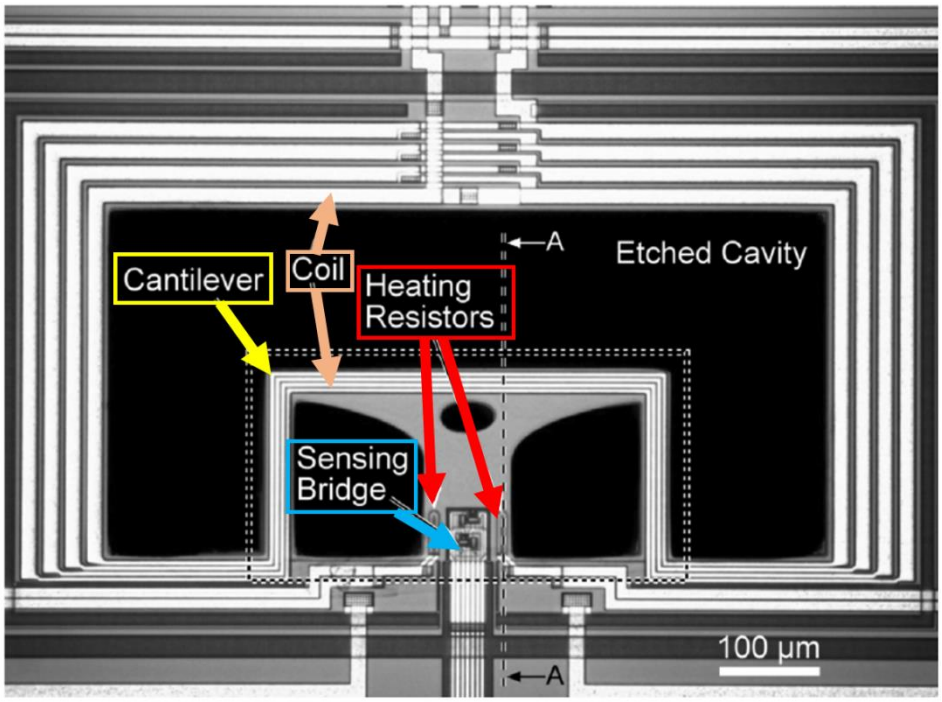

Fig. 2.8: Microphotograph of resonant MEMS sensor [91] (IEEE copyright line © 2006 IEEE).

Since the interaction between an electrical current, driven into the coil, and an external magnetic field, to be measured, enables the actuation due to the Lorentz force, the total spring constant of the resonant structure changes and, as a consequence, a frequency variation can be estimated because it is a function of the microbeams equivalent mass and spring constant. Therefore, the

resonant frequency shift is correlated to the magnitude of the external magnetic field, as explained by eq. (2.7) [91]:

$$\Delta f = \frac{1}{2\pi} \cdot \sqrt{\frac{k - {}^{F_L}/_{x}}{m}} \tag{2.7}$$

where k is the equivalent spring constant (stiffness) of the microbeams, m is the effective microbeams mass, x is the resonator displacement (deflection) and F_L is the Lorentz force. Lastly, the sensitivity can be expressed as the ratio between the variation of the resonant frequency (Δf) and the range of the magnetic induction (ΔB) correlated to magnetic field applied:

$$S = \frac{\Delta f}{\Delta B} \tag{2.8}$$

In addition, this microsensor has an efficient continuous offset cancelation, high robustness and low cross sensitivity. Finally, in terms of performance the following characteristics can be listed: a sensitivity of 60 kHz/T, a resolution of 1 μT, a resonant frequency of 175 kHz, a quality factor of 600, and a power consumption close to 5 mW.

It is very important to highlight that all previous prototypes of U-shaped beam cantilever, presented in this sub-section, have been fabricated in the same technology, that is CMOS, although they manifested numerous sensing approaches. For this reason, considering that the MEMS magnetometer discussed in this manuscript has been realized in a different technology, it has been deemed necessary to examine separately and in detail the design and the performance

of a U-shaped beam cantilever implemented using the same technology, which is the PiezoMUMPs process.

2.3 Study case: U-shaped beam cantilever in PiezoMUMPs technology

In this study case [85] (IEEE copyright line © 2011 IEEE), we have analyzed a novel integrated piezoelectric microsensor based on PiezoMUMPs technology, that is referenced in [92] and described in Appendix A. The novelty introduced in this fabrication process is the presence of a piezoelectric layer in Aluminum Nitride (AlN) that is used to generate an electric output.

The MEMS device has been designed and fabricated with applications to the field of resonant sensors for contactless measurements of electrical currents. As expected, the magnetometer is actuated by Lorentz force which is induced by interaction between an unknown electrical current I that produces the magnetic induction B and a known current I_{cant} driven through a silicon cantilever beam (see Fig. 2.9), as expressed in eq. (2.9):

$$F_L = \left(\vec{I}_{cant} \times \vec{B}\right) \cdot L = \left(\vec{I}_{cant} \times \left(\frac{\mu_0}{2\pi} \cdot \frac{\vec{I}}{r}\right)\right) \cdot L = \frac{\mu_0}{2\pi r} \cdot I_{cant} \cdot I \cdot L \cdot \sin\theta \qquad (2.9)$$

where r is the distance between the cantilever tip and the wire with the unknown current.

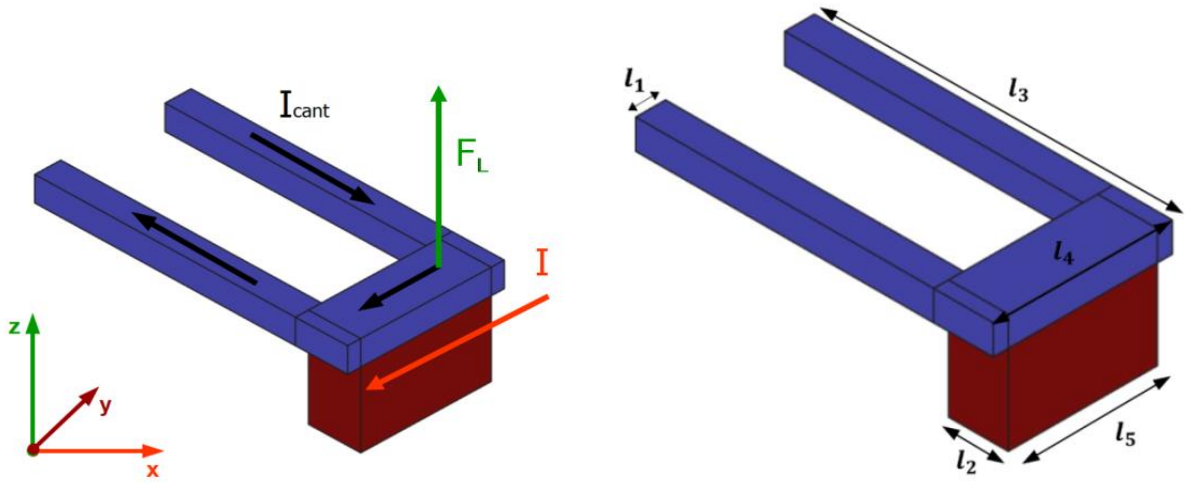

(a) (b)

Fig. 2.9: (a) Working principle; (b) Geometrical parameters [85] (IEEE copyright line © 2019 IEEE).

It is essential to highlight here that the electrical current to be evaluated is converted in a force (F_L), then into a displacement (z) of the cantilever beam free end through eq. (2.7) transformed in eq. (2.10) due to the Λ damping term caused by the piezoelectric transduction:

$$m\ddot{z} + d\dot{z} + \Lambda V(t) + kz = F_L(t) \tag{2.10}$$

Finally, the displacement is converted into a voltage through the use of a piezoelectric material composing the MEMS device:

$$V(t) = \int (\prod \dot{z} - V(t)/RC) \tag{2.11}$$

where Π is the coupling constant and RC is the load of the piezoelectric stack. In addition, $V(t)$ and $\dot{V}(t)$ represent the voltage and its first derivative in the output of the piezoelectric layer. In detail, all parameters describing the previous equations are listed in Table 2.

Parameter	*Unit*	*Value*
μ_0	H/m	$4*\pi*10^{-7}$
r	m	$1*10^{-3}$
I_{cant}	A	$30*10^{-3}$
I	A	6.4
L	m	$800*10^{-6}$
m	kg	$74.5*10^{-9}$
d	kg/s	$1*10^{-4}$
Λ	N/V	$1*10^{-9}$
k	N/m	5.74
$\prod$	V/m	$-1*10^{7}$
R	Ω	$1*10^{6}$
C	F	$200*10^{-12}$

Table 2: List of parameters used in [85] (IEEE copyright line © 2019 IEEE).

The layout of the sensor has been realized by using MEMSPro as CAD design tool; the die, that is illustrated in Fig. 2.10, has dimensions 11.15 mm × 11.15 mm, although the active area is 9.65 mm × 9.65 mm: in this work we have focused our attention to the device circled, whose parameters are indicated in Fig. 2.9b and listed in Table 3.

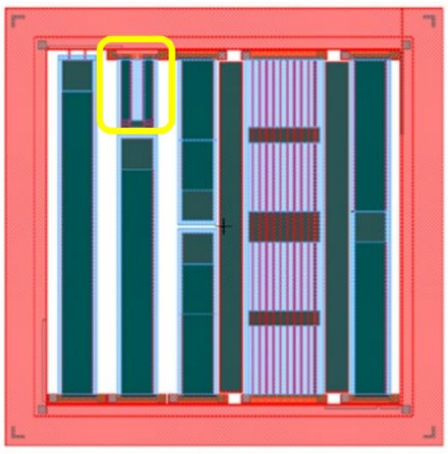

Fig. 2.10: Layout of MEMS device [85] (IEEE copyright line © 2019 IEEE).

Parameter	***Value***
l_1	250 μm
l_2	200 μm
l_3	1740 μm
l_4	800 μm
l_5	400 μm
t_{Si}	10 μm
t_{AlN}	0.5 μm
t_{Al}	1 μm
t_{Si_bulk}	400 μm
E_{Si}	170 Gpa
E_{AlN}	310 Gpa
E_{Al}	70 Gpa

Table 3: Device parameters [85] (IEEE copyright line © 2019 IEEE).

By using the equivalent section method [93,94] the elastic constant k and afterwards the natural frequency f_n have been calculated as k = 5.74 N/m and f_n = 1.39 kHz, respectively. In addition, the theoretical resistance beam, R_{beam} of 0.87 Ω, has been estimated taking account into $R\square$ = 0.055 Ω/Sq.

In order to provide a complete overview of the microelectromechanical system in terms of displacement and stress a FEM analysis has been carried out using COMSOL Multiphysics environment. The device geometry has been reproduced considering layers of thin silicon, aluminum nitride and aluminum for the suspend structure and thick silicon for the proof mass. An analysis in frequency domain and an eigen frequency analysis have been implemented in order to estimate the natural frequency and the oscillation modes: this last analysis acquired a relevant significance since the performance of a piezoelectric material is correlated to the velocity. The eigen frequency analysis has returned the following frequencies: f_1 = 1.38 kHz for

the first mode, f_3 = 11.8 kHz for the third mode and at last f_5 = 43 kHz for the fifth mode, whereas oscillation modes of even order have been neglectful because the structure is symmetric. In detail, in Fig. 2.11a-b-c the displacements as a function of the three oscillation modes are presented: it is interesting to underline that, since the output voltage in a piezoelectric material is correlated to the frequency, a trade-off with the displacement is essential.

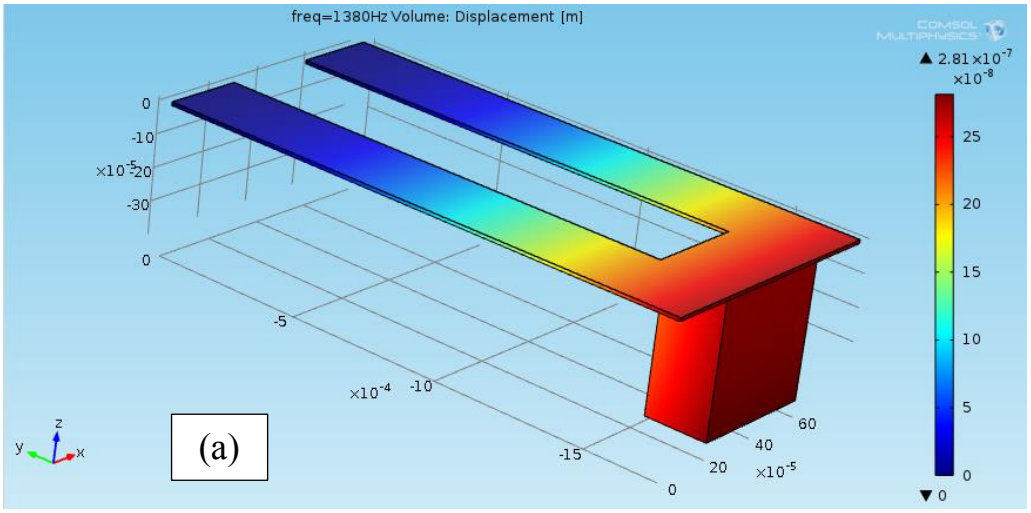

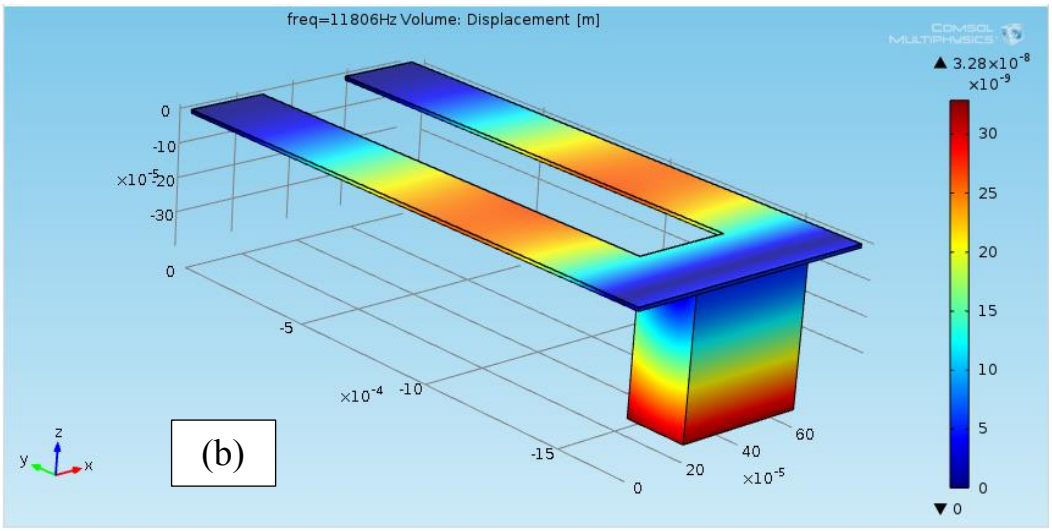

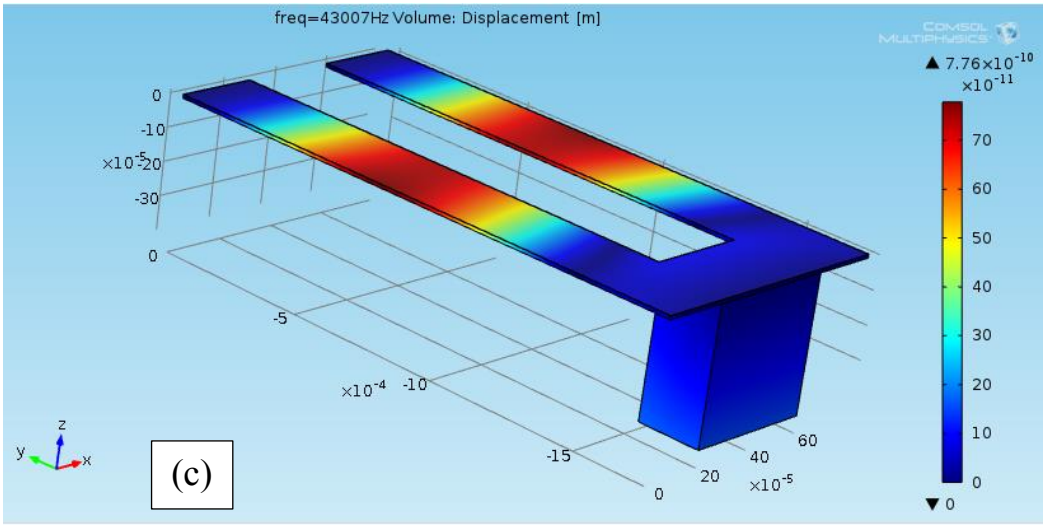

Fig. 2.11: Displacements in FEM analysis: (a) At f_1 = 1.38 kHz; (b) At f_3 = 11.8 kHz; (c) At f_5 = 43 kHz [85] (IEEE copyright line © 2019 IEEE).

For this reason, judging the displacement in the fifth oscillation mode comparable with a noise level the authors have decided to neglect, definitely, the last case and to characterize the microelectromechanical structure considering only the first two modes. Therefore, in order to characterize the MEMS device as current sensor, the die has been packaged and bonded, and afterwards an electrical wire, having a diameter of 0.15 mm, has been located at the distance of r = 1 mm from the device and the DC current to be measured is passed through it (see Fig. 2.12a). The whole experimental setup is shown in Fig. 2.12b, in which an Agilent 33220A function waveform is used to drive a sinusoidal current into the device and an Infiniium MSO9064A oscilloscope is needed to monitor the output signal (V_{out}). A DC current has to be measured, hence a power supply, specifically K.E.R.T. System 420 Professional, is employed to force a known DC current into an electrical wire.

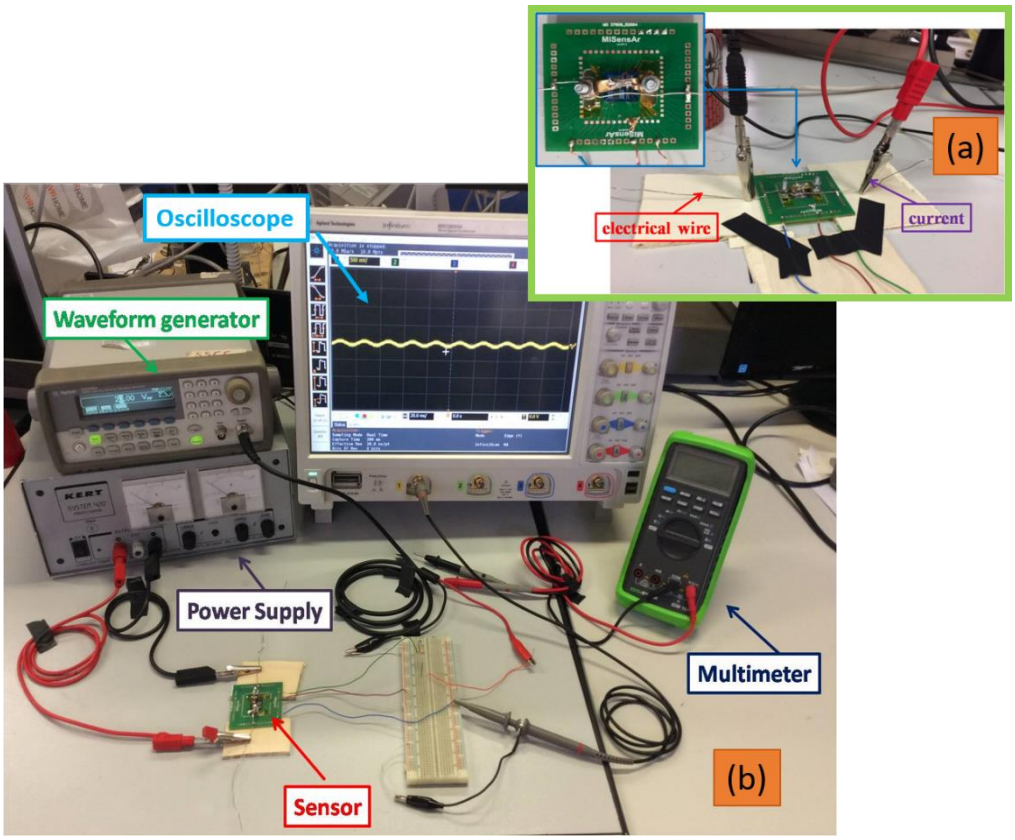

Fig. 2.12: Experimental setup [85] (IEEE copyright line © 2019 IEEE).

At first, the two experimental mechanical frequencies have been identified at f_1 = 1.4 kHz for the first mode and at f_3 = 10.3 kHz for the third mode. The next step is concerned about the experimental comparison between two oscillation modes evaluating the voltage in the output of the piezoelectric layer, for this reason the same operative conditions have been repeated, or rather, a sinusoidal current driven into the MEMS device having an amplitude of 30 mA_{PP} and a DC electrical current into the electrical wire with a range [0 A - 8 A]. In Fig. 2.13 the output voltage as a function of the current passing through the electrical wire and varying into the range [0 A – 8 A] is shown for each excitation frequency with the result that the third oscillation mode (in green) exhibits a better response in terms of sensitivity than the first one (in red). This comparison allowed to explain and to verify experimentally that, although the first oscillation

mode produces the highest displacement, the output voltage of the piezoelectric stack is correlated to the velocity too.

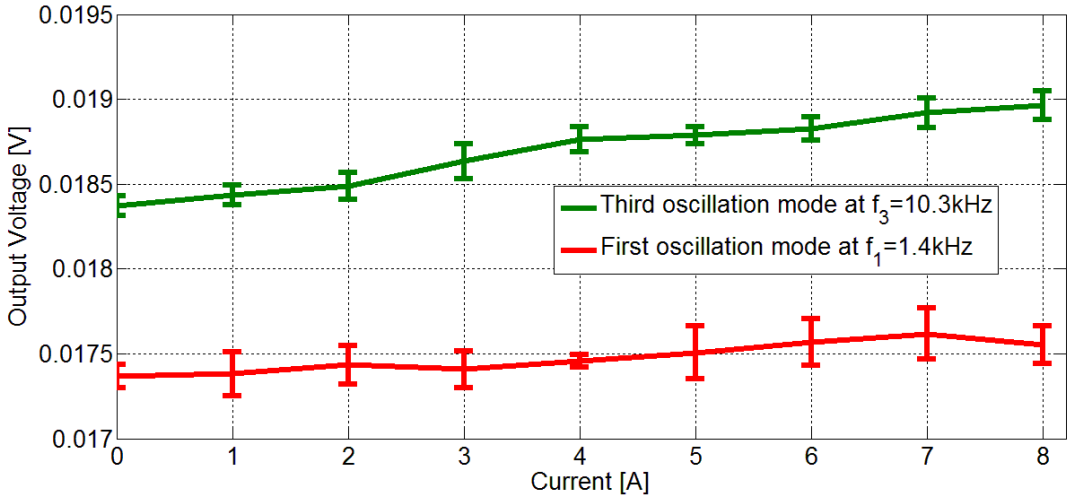

Fig. 2.13: Experimental comparison between the first and the third oscillation modes [85] (IEEE copyright line © 2019 IEEE).

Therefore, in order to characterize the working region of the device with the highest responsivity of the MEMS sensor a sinusoidal current, with amplitude of 30 mA_{PP} and a frequency of 10.3 kHz, is applied to the U-Shaped beam cantilever, while a DC current in [0 A – 8 A] range is imposed in the electrical wire (*I*). It is interesting to highlight that for each DC current value ten measurements are collected and, later, the mean value is determined. The transduction diagram is illustrated having a linear trend in all the range [0 A – 8 A] in Fig. 2.14, where the σ value has been estimated 42.88×10-6 V and a responsivity of 80.8×10-6 V/A has been evaluated. In addition, a noise level specified in standard deviation and expressed in volt has been estimated experimentally and a value of 22.6 μV has been carried out. Therefore, it has been possible to determine the resolution in ampere considering the ratio between the noise level [V] and the

responsivity [A/V] and obtaining a resolution value of 0.279 A. Eventually, the fitting with the model is presented in green, confirming its validity.

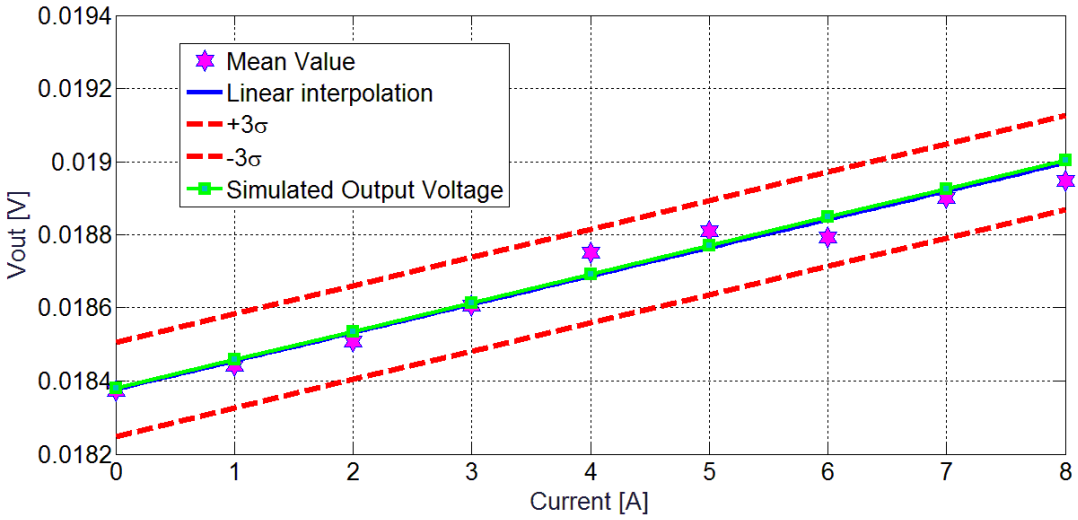

Fig. 2.14: The Transduction diagram in linear region [85] (IEEE copyright line © 2019 IEEE).

Definitively, it is intriguing to note that the MEMS device has been characterized, *in primis*, as current sensor, however, it would have been possible to characterize as magnetic field sensor considering that a current-carrying conductor generates a magnetic field.

In conclusion, the Chapter 2 represented an essential dissertation about U-shaped beam cantilever history in order to contextualize the topic of this manuscript, providing an overview on different prototypes and readout approaches.

Chapter 3

Meander device in PiezoMUMPs Technology

As previously mentioned, the goal pursued in this research activity has been prototyping an integrated magnetic field sensor capable to include tuning features for a wide operative range, that is [1 μT – 2 T], in order to satisfy specifications required by two partners involved in the project. It is interesting to note that two different applicative contexts have been investigated due to different goals pursued in Paradox Engineering Company and in CERN; in particular the detection of geomagnetic field alteration produced by the presence of a car, that is around 1 μT, proves extremely beneficial in the smart city parking application, whereas the dispersion of the magnetic field is an extremely important aspect in a particle accelerator since high magnetic fields have the assignment to deflect the particle bunches in dipoles and to focus them in quadrupoles. For this reason, as already furnished proof, taking into account the versatility of the U-shaped beam cantilever architecture in tuning the operative range of the magnetic field through the applied Lorentz force and therefore the variation of the current supplied into MEMS sensor, this type of design has been selected as basic structure in this research activity.

Another relevant issue concerned the integrated technology to be adopted in order to realize the device and to arrange the readout strategy. It is essential to underline that initial design steps,

which are related to the simulation of the structure behavior in terms of static and dynamic model in Matlab & Simulink environment and FEM analysis in COMSOL Multiphysics, are strictly influenced by the physical and geometrical properties of the layers composing the structure. Furthermore, the possibility of implementing a magnetic field sensor capable of supplying by itself, in other terms being self-generating, represented an intriguing challenge to be investigated and pursued. For this reason, although in the first phase of this research activity several fabrication processes have been examined in terms of layers, masks and characteristics, such as, in detail, MeltalMUMPs, SOIMUMPs and PiezoMUMPs technologies, in the end the choice fell on the latter due to the presence of a piezoelectric stack, which, as is known, has the capability to generate an electric field if it is subjected to a mechanical deformation. In relation to this aspect, it is important to highlight that anywhere the MEMS sensor is located it will be always influenced by the environmental noise, that is a white noise having a bandwidth around 400 Hz; as a consequence, regardless of the presence of an external magnetic field to be detected, the integrated device, that works at the resonance, will tend to deform due to the effect of environmental noise and therefore to develop a voltage that can be stored and used to supply, for example, itself conditioning circuit. In addition, the AlN layer is used to generate an electric output: this aspect represents the most important advantage in this process, because an electric signal is directly available in the output of the sensor. In this manner, the sensor output is not correlated to variation of resistance (resistive output) or capacitance (capacitive output).

In order to provide a complete and exhaustive overview it has been deemed appropriate to structure the 3rd Chapter in the following sub-sections:

- Analysis of static and dynamic model in Matlab & Simulink environment;
- FEM analysis in COMSOL Multiphysics environment;
- Realization of layout using the MEMSPro CAD;

- Optimization of MEMS device through a second fabrication run and the implementation of a differential architecture.

3.1 Static and Dynamic model in Matlab & Simulink environment

Static and dynamic model allowed to analyze the performance of numerous architectures of U-shaped beam cantilever in order to satisfy the specification of a unique MEMS device having a wide operative range; for this reason, the focus has been directed to the search for the most flexible structure, comparing it with the basic architecture of a U-shaped beam cantilever. As previously mentioned, the well-known equivalent mass-spring system [86] can be used to depict the dynamic behaviour of the reported structure, whereas, as regard the piezoelectric output, the behaviour of the piezoelectric layer respects the model indicated by Fedder in his PhD thesis [95]; therefore, the whole system of equations which has been implemented in Matlab & Simulink environment is described by eqs. (3.1) and (3.2):

$$\begin{cases} m\ddot{x} + d\dot{x} + \frac{dU(x)}{dx} + d_{piezo}V = F_{Lorentz} & (3.1) \\ \dot{V} = K_{piezo}\dot{\dot{x}} - \gamma V & (3.2) \end{cases}$$

where $\frac{dU(x)}{dx}$ is the first derivative of the potential energy function correlated to the mechanical stiffness; therefore, considering that the potential energy can be expressed by eq. (3.3)

$$U(x) = \frac{1}{2}kx^2 \quad (3.3)$$

the equations system can be written as indicated in eqs. (3.4) and (3.5):

$$\begin{cases} \boldsymbol{m\ddot{x} + d\dot{x} + kx + d_{piezo}V = F_{Lorentz}} & (3.4) \\ \boldsymbol{\dot{V} = K_{piezo}\dot{x} - \gamma V} & (3.5) \end{cases}$$

where:

- $\boldsymbol{m}$ is the inertial mass of the microelectromechanical structure [kg];
- $\boldsymbol{d}$ represents the damping coefficient [Ns/m];
- $\boldsymbol{k}$ is the mechanical stiffness [N/m];
- $\boldsymbol{d_{piezo}}$ is the damping term caused by the piezoelectric transduction [N/V];
- $\boldsymbol{K_{piezo}}$ is the coupling constant of the piezoelectric stack [V/m];
- $\boldsymbol{\gamma}$ which is equal to inverse of product RC represents the load of the piezoelectric stack [Hz];
- $\boldsymbol{F_{Lorentz}}$ represents the Lorentz force [N];
- $\boldsymbol{V}$ and $\boldsymbol{\dot{V}}$ represent the voltage and its first derivative in the output of the piezoelectric layer;
- $\boldsymbol{\ddot{x}}$, $\boldsymbol{\dot{x}}$ and $\boldsymbol{x}$ are the acceleration, the velocity and the displacement of the cantilever tip, respectively [m/s^2], [m/s], [m].

Just a notation, the d_{piezo} term corresponds to the term indicated in the 2nd Chapter with Λ.

It is important to underline that a study about the elastic constant and about parameters which influence its value has been implemented since the flexibility is strictly correlated to k and, in particular, in an inversely proportional manner; as a consequence, a reduction of k translates into an increase of flexibility.

In addition, taking into account the mechanical stiffness is inversely proportional to the physical length of the MEMS structure, in accordance with eq. (3.6)

$$k \propto \frac{EI}{L^3} \tag{3.6}$$

which is in detail described in Appendix B in Matlab scripts, several architectures having different physical lengths have been considered. In relation to eq. (3.6) it is important to mention that E is the Young's modulus, I is the inertia moment and L is the length of the material. Furthermore, the eq. (3.6) is still valid even if the microelectromechanical system is not composed of a single material but it is a multi-layer structure; in this last case, which represents all structures examined in this manuscript since the PiezoMUMPs technology is a multi-layer process, the equivalent section method [93,94] is applied. In addition, it is intriguing to highlight that the maximum length of the MEMS sensor permitted is correlated to the die dimension, that exhibits an active area equal to 9.65 mm × 9.65 mm.

In the following sub-sections, the comparison between the simple architecture of U-shaped beam cantilever and the new structures in the same operative conditions is presented.

3.1.1 Simple U-shaped VS Topology 1

In accordance with eq. (3.6) in order to reduce the mechanical stiffness k, thus increasing the flexibility, a new topology of U-shaped beam cantilever has been implemented extending total length L; as a consequence, a comparison in terms of static and dynamic analysis between the simple structure (in Figs. 3.1a-b) and the new architecture (Topology 1, that is illustrated in Figs. 3.1c-d) has been carried out. In relation to two designs it is essential to specify that they are not in scale and a 2D schematic is presented just to provide an idea of the design, whereas all layers have been considered for the implementation of the model. For the same reason, the

inertial mass on the cantilever tip is neglected, although it has been introduced in Matlab & Simulink model.

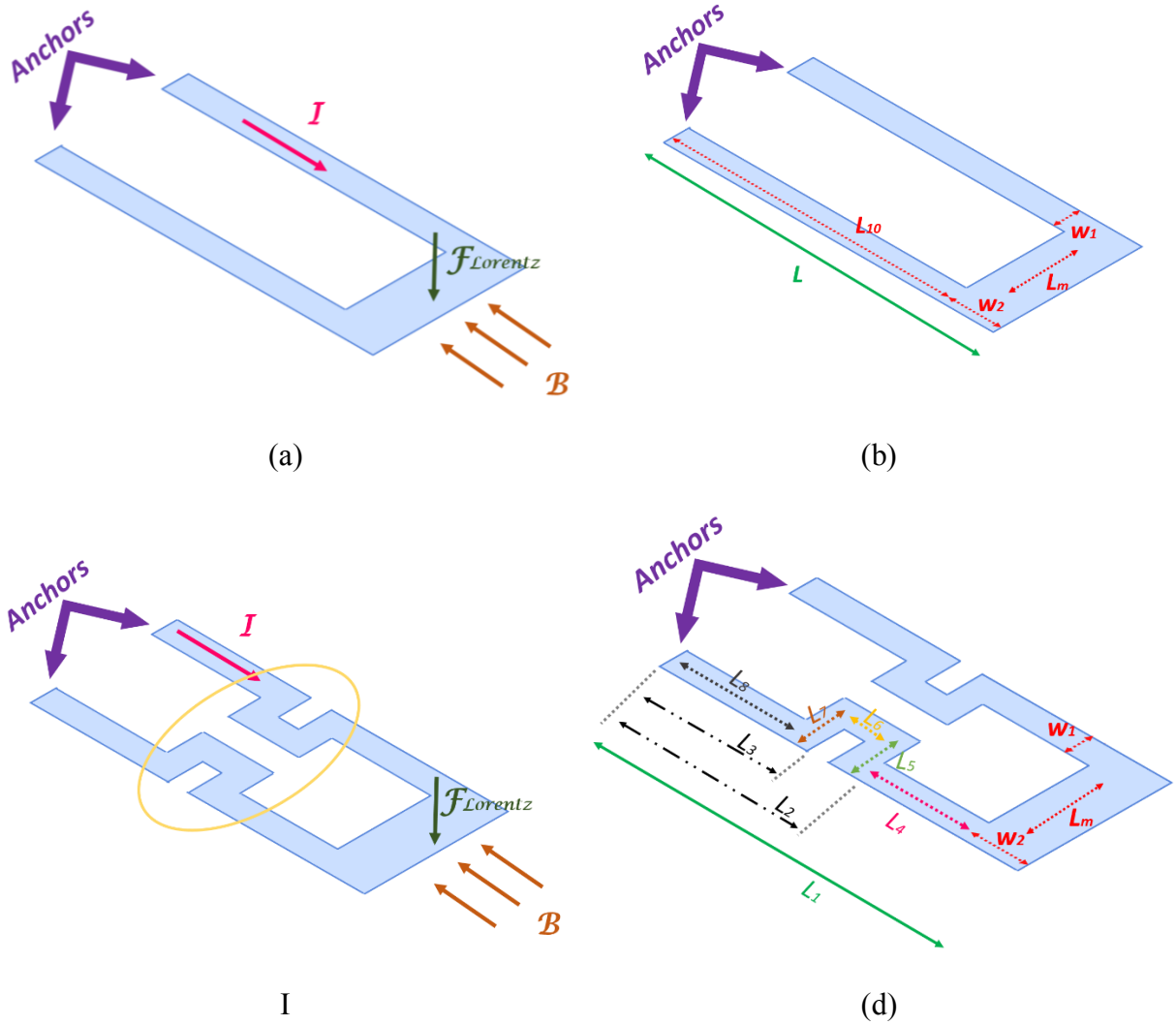

Fig. 3.1: Simple U-shaped beam cantilever: (a) Working principle; (b) Geometrical parameters; Topology 1: (c) Working principle; (d) Geometrical parameters.

It is believed important to focus the attention on Fig. 3.1c and to analyze what the presence of the meander (indicated in yellow) determines: as expressed in eq. (2.1) the Lorentz force is correlated to the vector product between the current into the sensor (I) and the magnetic induction (B), and, therefore, this force operates in all sections of the structure in which I and B are perpendicular (as clarified in Fig. 3.2).

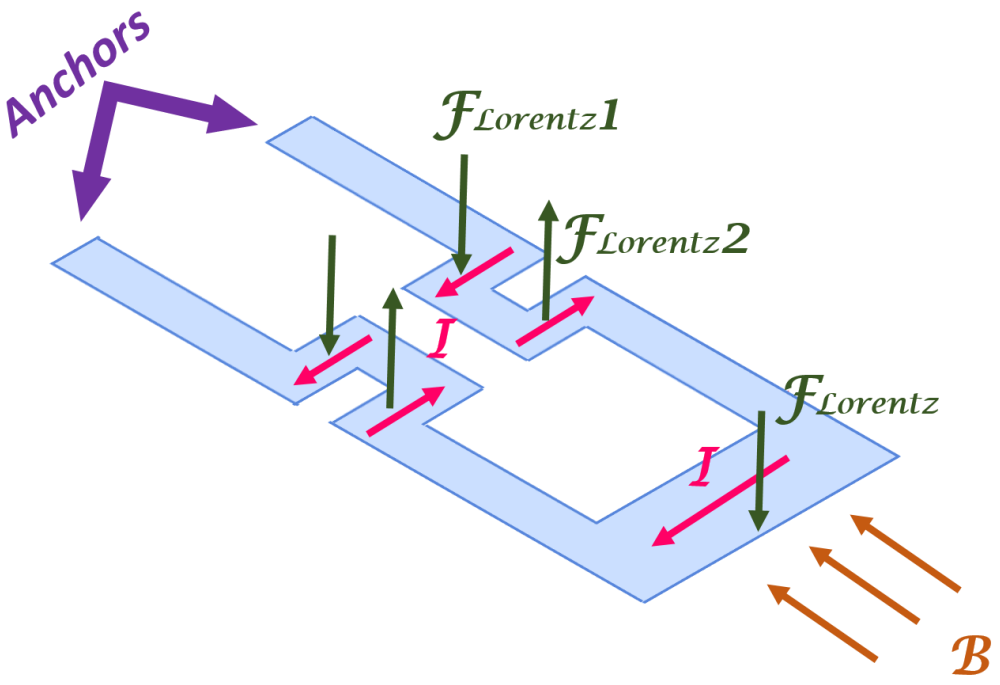

Fig. 3.2: Detail on working principle of Topology 1.

The Lorentz force direction is a function of the driving current direction; hence, it is intriguing to note opposite directions of the Lorentz force which introduce not only a deflection of the structure but also a torsional moment. As a consequence, in the static and dynamic model other two contributions should be inserted, nevertheless, taking into account the initial moment can be assumed equal to zero, the torsional moment can be neglected, whereas the contribution related to the application of a concentrated load at any point which is not the cantilever tip must be included [96,97]. In relation to Fig. 3.2 it is essential to highlight that the Lorentz forces $F_{Lorentz1}$ and $F_{Lorentz2}$ assume the same value because the arm length is equal, nevertheless they are different to $F_{Lorentz}$ because the active lengths are dissimilar. In addition, for the Topology 1 the principle of effects superposition is applied, considering the individual contributions unrelated. Eventually, in order to analyze the static and dynamic model the following equations systems have been implemented for two architectures:

$$\begin{cases} m\ddot{x} + d\dot{x} + kx + d_{piezo}V = F_{Lorentz} & (3.7) \\ \dot{V} = K_{piezo}\dot{x} - \gamma V & (3.8) \end{cases}$$

$$\begin{cases} m\ddot{x_F} + d\dot{x_F} + kx_F + d_{piezo}V = F_{Lorentz} & (3.9) \\ m\ddot{x_{F1}} + d\dot{x_{F1}} + \left(\frac{12EI}{(3L_1 - L_3)\cdot L_3^2}\right)x_{F1} + d_{piezo}V = F_{Lorentz1} & (3.10) \\ m\ddot{x_{F2}} + d\dot{x_{F2}} + \left(\frac{12EI}{(3L_1 - L_2)\cdot L_2^2}\right)x_{F2} + d_{piezo}V = F_{Lorentz2} & (3.11) \\ \dot{V} = K_{piezo}\dot{x} - \gamma V & (3.12) \end{cases}$$

Just to clarify, eqs. (3.7) and (3.8) are related to the simple U-shaped beam cantilever whereas eqs. (3.9), (3.10), (3.11) and (3.12) are used to describe the behavior of the Topology 1. The static and dynamic model has been implemented in Simulink environment whereas a suitable Matlab code has been written to order to formulate a parametric system; in particular, some parameters related to different layers have been estimated by the technological specifications used to fabricate the MEMS device, such as Young's modulus, thickness and density (see Table 4). Although the complete fabrication process is described in detail in Appendix A it is supposed essential to provide the following Fig. 3.3 which exhibits the layers sequence and their thickness. In relation to geometrical parameters, that are indicate in Table 4, the limit has been imposed by the die dimension, which is 11.15 mm × 11.15 mm, however the active area is just 9.65 mm × 9.65 mm. Furthermore, the equivalent section method [93,94] has been applied in order to estimate the mechanical stiffness for a multi-layer structure and it is illustrated in Appendix B. Finally, the mechanical damping, d = 0.0001 kg/s, has been estimated by

literature [98], where the whole characterization of an integrated MEMS sensor having similar dimensions has been carried out.

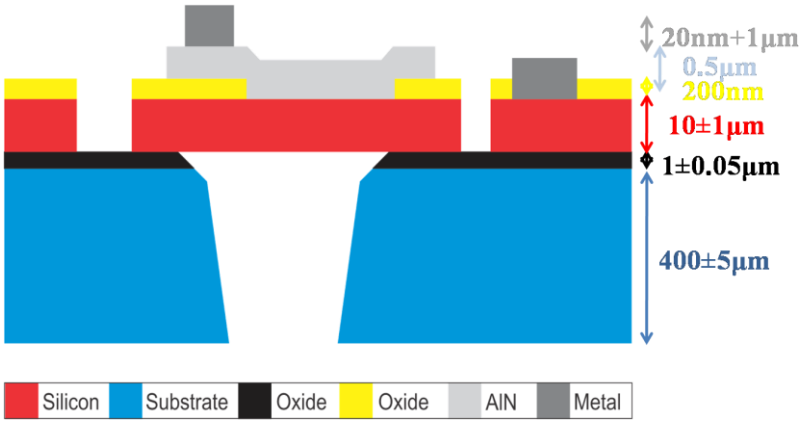

Fig. 3.3: Cross sectional view of PiezoMUMPs technology [92] (not in scale).

Simple U-shaped beam cantilever	
t_{Si}	10 µm
t_{AlN}	0.5 µm
t_{Al}	1 µm
t_{Si_bulk}	400 µm
E_{Si}	170 Gpa
E_{AlN}	310 Gpa
E_{Al}	70 Gpa
w_1	100 µm
w_2	100 µm
L_m	4500 µm
L_{10}	6400 µm

Topology 1	
t_{Si}	10 µm
t_{AlN}	0.5 µm
t_{Al}	1 µm
t_{Si_bulk}	400 µm
E_{Si}	170 Gpa
E_{AlN}	310 Gpa
E_{Al}	70 Gpa
w_1	100 µm
w_2	100 µm
L_m	4500 µm
L_4	900 µm
L_5	1500 µm
L_6	100 µm
L_7	1500 µm
L_8	5200 µm

Table 4: List of parameters related to Simple U-shaped beam cantilever and Topology 1.

where t_{Si}, t_{AlN}, t_{Al} and t_{Si_bulk} are the thicknesses of Silicon, Aluminum Nitride, Aluminum and Silicon bulk layers, respectively; E_{Si}, E_{AlN}, and E_{Al} are the Young's moduli for Silicon, Aluminum Nitride and Aluminum layers, respectively. As regards w_1 and w_2, they represent the widths related to the arm of the MEMS sensor and to the cantilever tip, in that order; L_m is the length correlated to the inertial mass, in accordance with the layout rules. In addition, the quantities L_1, L_2 and L_3, that are related to the Topology 1, are shown in Fig. 3.1d and are indicated in eqs. (3.10) and (3.11), assume the following expressions:

$$L_1 = L_8 + 2 \cdot w_1 + L_6 + L_4 + w_2 \tag{3.13}$$

$$L_2 = L_8 + 2 \cdot w_1 + L_6 \tag{3.14}$$

$$L_3 = L_8 + w_1 \tag{3.15}$$

Eventually, the total lengths, that are necessary to estimate the elastic constant for each structure have the following expressions:

$$L = L_{10} + w_2 \tag{3.16}$$

$$L_{TOT} = L_8 + L_7 + L_6 + 2 \cdot w_1 + L_5 + L_4 + w_2 \tag{3.17}$$

Using the equivalent section method for the simple U-shaped beam cantilever a mechanical stiffness of 0.0260 N/m and a natural frequency of 230 Hz have been estimated, whereas for the Topology 1 a mechanical stiffness of 0.0083 N/m and a natural frequency of 131 Hz have been evaluated. Just to mention, analyzing the value of two elastic constants it is emerged that the Topology 1 is more flexible and therefore higher displacements should be estimated.

It is intriguing to mention that the model implemented in Matlab & Simulink is not exactly the same described in the previous equations, due to the absence of the term correlated to the piezoelectric damping (d_{piezo}) that has been neglected because it introduces an irrelevant contribution.

In order to analyze the static and dynamic model the Simulink simulation environment has been used (as illustrated in Appendix B, 2.1 section); in particular, it is believed essential to specify that in static analysis the driving current (I) and the magnetic induction (B) assume a constant value, whereas in dynamic analysis the magnetic induction is the same, but the driving current is a sinusoidal signal, having an excitation frequency equal to the natural frequency of the examined architecture. For this reason, in static analysis the magnetic induction has been fixed at minimum value required in this work (B = 1 μT), the amplitude of the current driven into the MEMS sensor has been set to 20 mA, therefore, a Lorentz force, in module, of 94 pN has been applied. As can be observed in Fig. 3.4 the Topology 1 exhibits a tip displacement (~ 11 nm) which is greater than the displacement of the simple U-shaped beam cantilever (~ 3.61 nm). A similar behavior has been determined analyzing the dynamic model, in which the magnetic induction (B) is maintained constant and equal to 1 μT, the driving current is a sinusoidal signal having an amplitude of 20 mA_{PP} and a frequency of 230 Hz for the simple architecture and of 131 Hz for the Topology 1, and as a consequence, the Lorentz force is a sinusoidal signal too (see Fig. 3.5). It is important to note that two architectures have been compared at own resonance when they produce the maximum output signal; in relation to this aspect it is absolutely necessary to underline that making the device works on the resonance allows to obtain greater displacements in the same operative conditions.

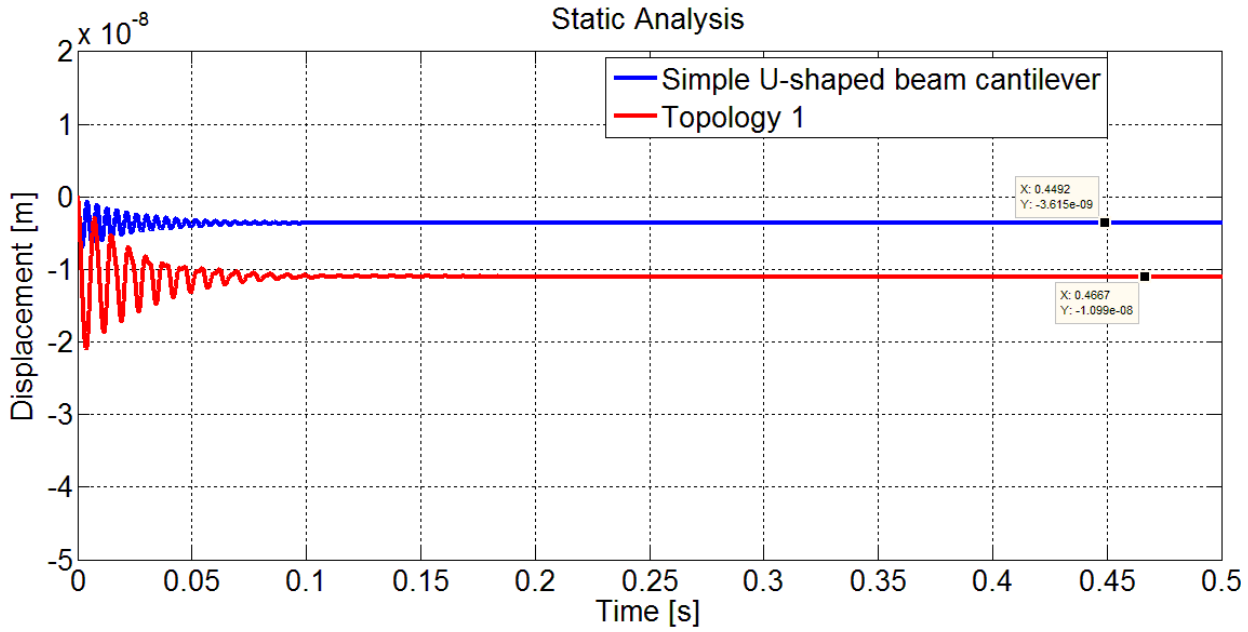

Fig. 3.4: Static analysis: Simple U-shaped beam cantilever VS Topology 1.

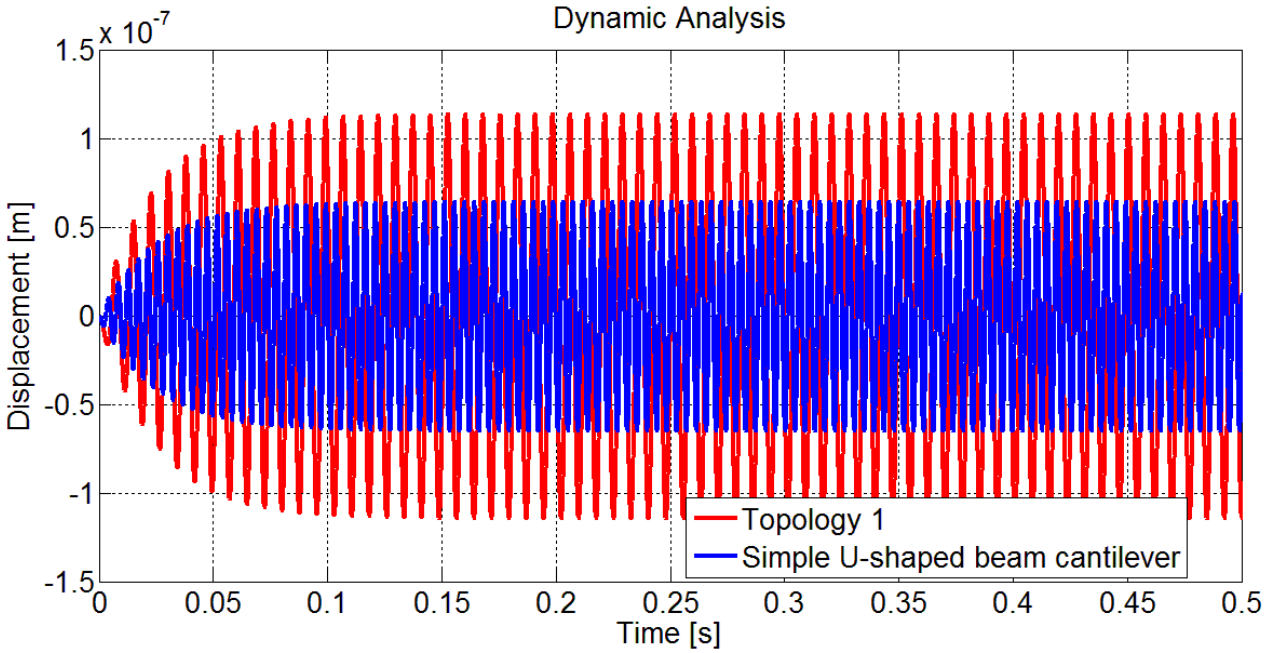

Fig. 3.5: Dynamic analysis: Simple U-shaped beam cantilever VS Topology 1.

In conclusion, Topology 1 manifests better performance in terms of displacement than the simple U-shaped beam cantilever.

3.1.2 Simple U-shaped VS Topology 2

In order to satisfy the feature of a wide operative range another architecture of U-shaped beam cantilever has been investigated and compared with the simple structure (see Figs. 3.6a-b). In this case, since the Lorentz force assumes maximum amplitude in all points in which the current driven into the device (I) and the magnetic induction (B) are perpendicular, the Topology 2 has been implemented considering other three arms parallel to the arm where the tip is located (as shown in Figs. 3.6c-d). It is important to underline that for each arm an identical inertial mass is supposed in static and dynamic analyses, although it is not displayed in Figs. 3.6c-d.

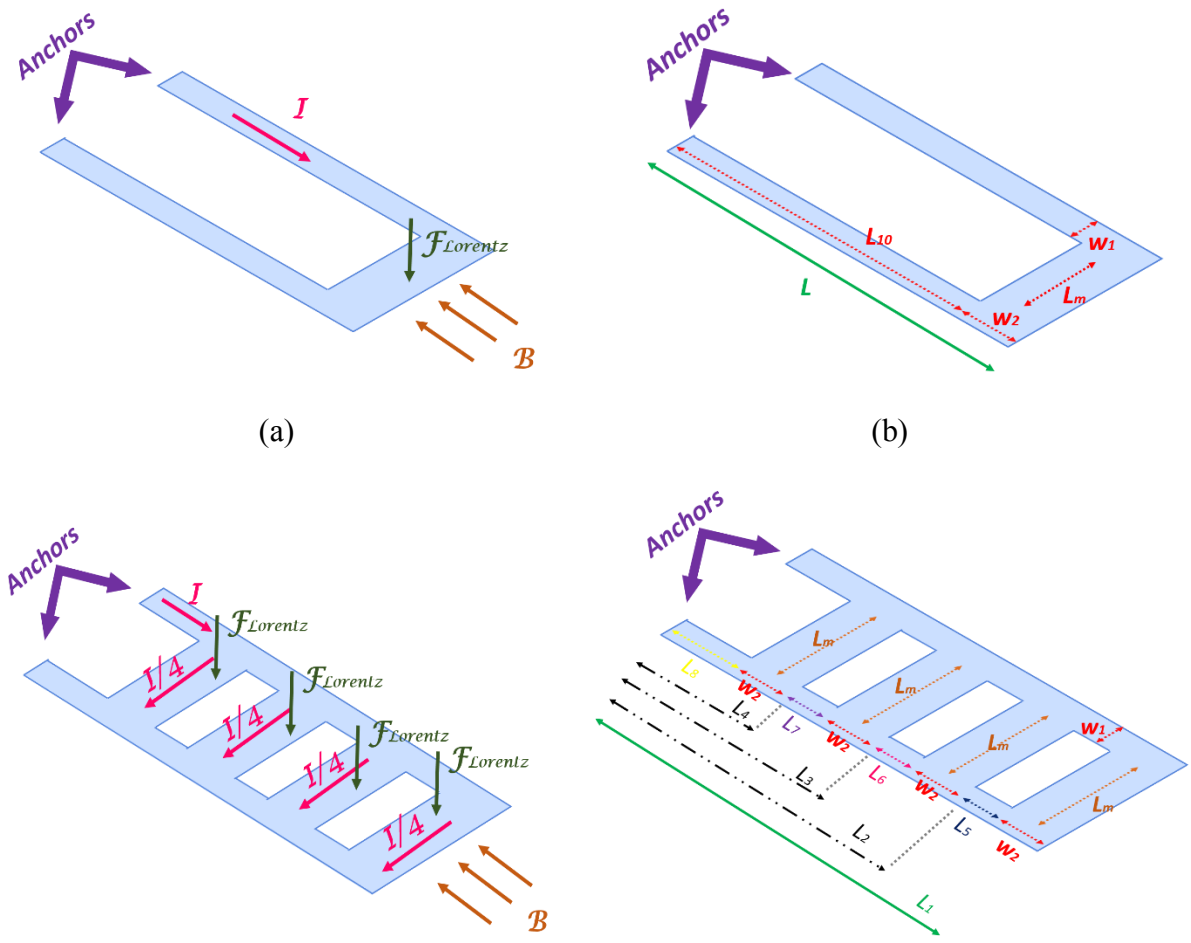

Fig. 3.6: Simple U-shaped beam cantilever: (a) Working principle; (b) Geometrical parameters; Topology 2: (c) Working principle; (d) Geometrical parameters.

It is essential to specify that in order to compare two architectures in the same operative conditions the current applied to the MEMS structures has to keep the same amplitude; for this reason, in Topology 2 the driving current is split in four arms, as indicate in Fig. 3.6c, and therefore, the Lorentz force imposed is reduced by a factor equal to four in each arm. In order to analyze the static and dynamic model the following equations systems have been implemented for two architectures:

$$\begin{cases} m\ddot{x} + d\dot{x} + kx + d_{piezo}V = F_{Lorentz} & (3.18) \\ \dot{V} = K_{piezo}\dot{x} - \gamma V & (3.19) \end{cases}$$

$$\begin{cases} m\ddot{x_F} + d\dot{x_F} + kx_F + d_{piezo}V = \frac{F_{Lorentz}}{4} & (3.20) \\ m\ddot{x_{F1}} + d\dot{x_{F1}} + \left(\frac{12EI}{(3L_1 - L_2)\cdot L_2^2}\right)x_{F1} + d_{piezo}V = \frac{F_{Lorentz}}{4} & (3.21) \\ m\ddot{x_{F2}} + d\dot{x_{F2}} + \left(\frac{12EI}{(3L_1 - L_3)\cdot L_3^2}\right)x_{F2} + d_{piezo}V = \frac{F_{Lorentz}}{4} & (3.22) \\ m\ddot{x_{F3}} + d\dot{x_{F3}} + \left(\frac{12EI}{(3L_1 - L_4)\cdot L_4^2}\right)x_{F3} + d_{piezo}V = \frac{F_{Lorentz}}{4} & (3.23) \\ \dot{V} = K_{piezo}\dot{x} - \gamma V & (3.24) \end{cases}$$

Just to specify, eqs. (3.18) and (3.19) describe the simple U-shaped beam cantilever whereas eqs. (3.20), (3.21), (3.22), (3.23) and (3.24) are used to describe the behavior of the Topology 2. In relation to the technological parameters (Young's modulus and thickness) they are the same listed in Table 4, whereas the geometrical ones are tabulated in Table 5.

Simple U-shaped beam cantilever	
w_1	100 µm
w_2	100 µm
L_m	4500 µm
L_{10}	6400 µm

Topology 2	
w_1	100 µm
w_2	100 µm
L_m	4500 µm
L_5	300 µm
L_6	300 µm
L_7	300 µm
L_8	5200 µm

Table 5: List of geometrical parameters related to Simple U-shaped beam cantilever and Topology 2.

As previously mentioned, w_1 and w_2 represent the widths related to the arm of the MEMS sensor and to the cantilever tip, in that order; L_m is the length correlated to the inertial mass, in accordance with the layout rules. In addition, the quantities L_1, L_2, L_3 and L_4 that are related to the Topology 2 (see Fig. 3.6d) assume the following expressions:

$$L_1 = L_8 + 4 \cdot w_2 + L_5 + L_6 + L_7 \tag{3.25}$$

$$L_2 = L_8 + 3 \cdot w_2 + L_6 + L_7 \tag{3.26}$$

$$L_3 = L_8 + 2 \cdot w_2 + L_7 \tag{3.27}$$

$$L_4 = L_8 + w_2 \tag{3.28}$$

Finally, in order to evaluate the mechanical stiffness, the total lengths have been considered with the following expressions:

$$L = L_{10} + w_2 \tag{3.29}$$

$$L_{TOT} = L_1 \tag{3.30}$$

It is interesting to note that in this case $L = L_{TOT}$ because the arms are linear. For this reason, applying the equivalent section method for both architectures the identical values in terms of elastic constant and natural frequency have been determined: in particular, k = 0.0260 N/m and f_n = 230 Hz. Also in this case, the term inherent to the piezoelectric damping (d_{piezo}) has been neglected in the model implemented in Matlab & Simulink because it introduces an irrelevant contribution. The Simulink simulation environment has been used (as explained in Appendix B, 2.2 section) to investigate the static and dynamic model; in particular, the magnetic induction has been fixed at minimum value required in this work (B = 1 μT), the amplitude of the current driven into the MEMS sensor has been set to 80 mA in the static analysis and to 80 mA_{PP} in the dynamic one, therefore, a Lorentz force, in module, of 376 pN has been applied in the simple U-shaped beam cantilever, whereas in the Topology 2 a Lorentz force of 94 pN operates in each arm because the driving current is equal to 20 mA on them. Just to remember, in Topology 2 the principle of effects superposition is applied, considering the individual contributions unrelated and at the end single displacements are added. In relation to the static analysis, as can be observed in Fig. 3.7, the displacement related to the simple U-shaped beam cantilever (~ 14.4 nm) is greater than the total displacement coming from the sum of single displacement contributions in Topology 2 (~ 12.4 nm). The same trend can be found examining the dynamic model where a larger gap in terms of displacement is estimated due to the resonance working for both architectures (see Fig. 3.8). In this case, a sinusoidal current, having an amplitude of 80 mA_{PP} and a frequency of 230 Hz, has been applied. It is important to underline that these results were expected because, in Topology 2, the distribution of the driving current determined the distribution of the same Lorentz force, which is applied in a unique point in the simple U-shape beam cantilever, in four points with consequent fewer displacements.

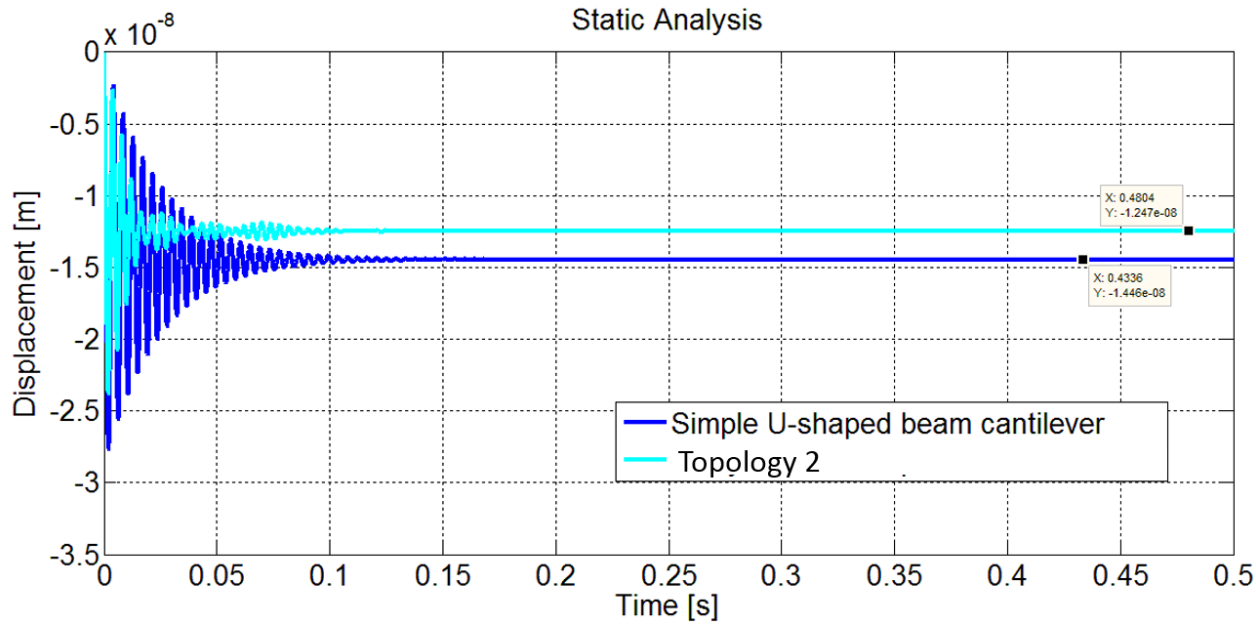

Fig. 3.7: Static analysis: simple U-shaped beam cantilever VS Topology 2.

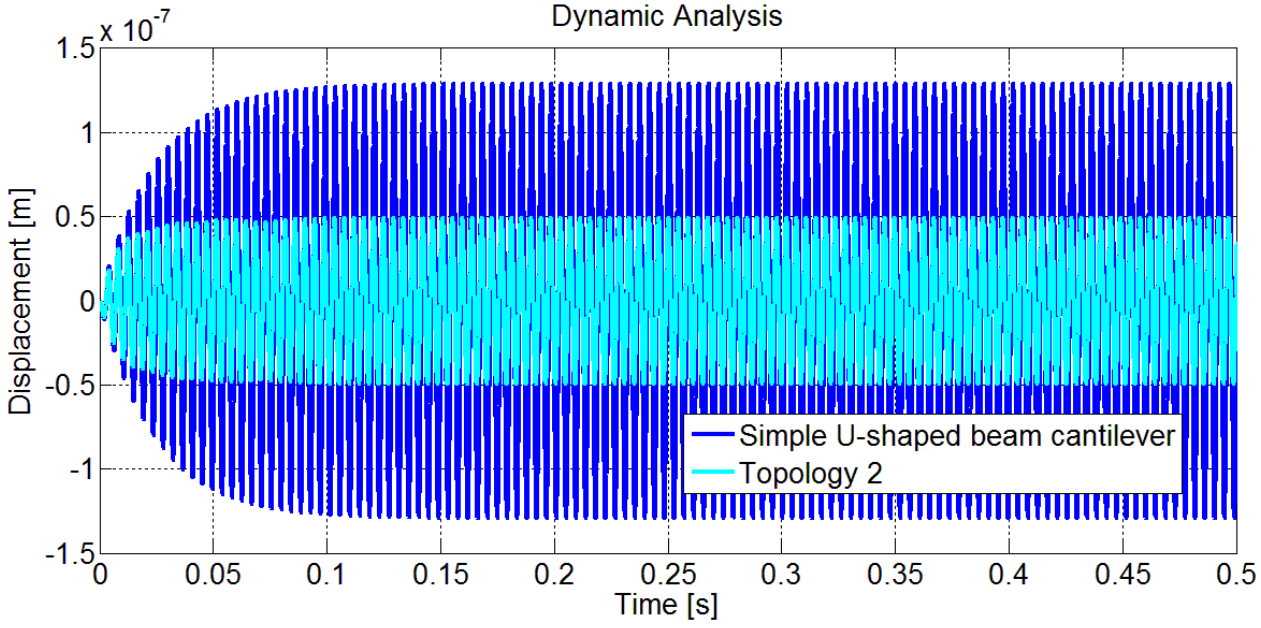

Fig. 3.8: Dynamic analysis: Simple U-shaped beam cantilever VS Topology 2.

In conclusion, this new modification of U-shaped beam cantilever (Topology 2) is not indicated to realize a MEMS device with relevant flexibility because its performance is poorer compared with the simple architecture, as demonstrated by static and dynamic analysis.

3.1.3 Simple U-shaped VS Topology 3

Since the previous architecture did not satisfy the requirement to reach greater displacements than the simple U-shaped beam cantilever, it has been believed appropriate to investigate another similar one before definitively shelving this structure. The Topology 3 has been implemented considering different widths of the arms (as can be observed in Figs. 3.9c-d) and different inertial masses and it has been compared with a simple architecture having a unique width equal to the maximum width, w_4, (as shown in Figs. 3.9a-b).

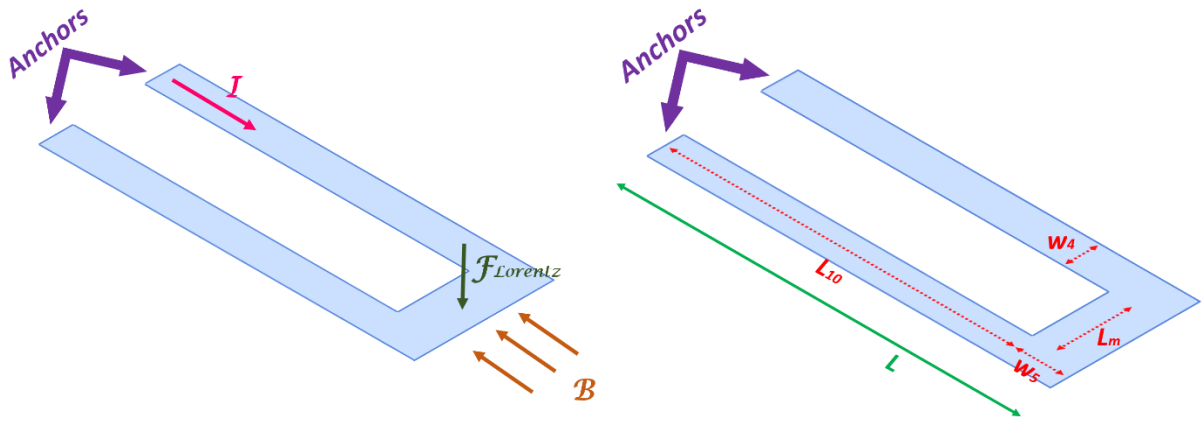

(a) (b)

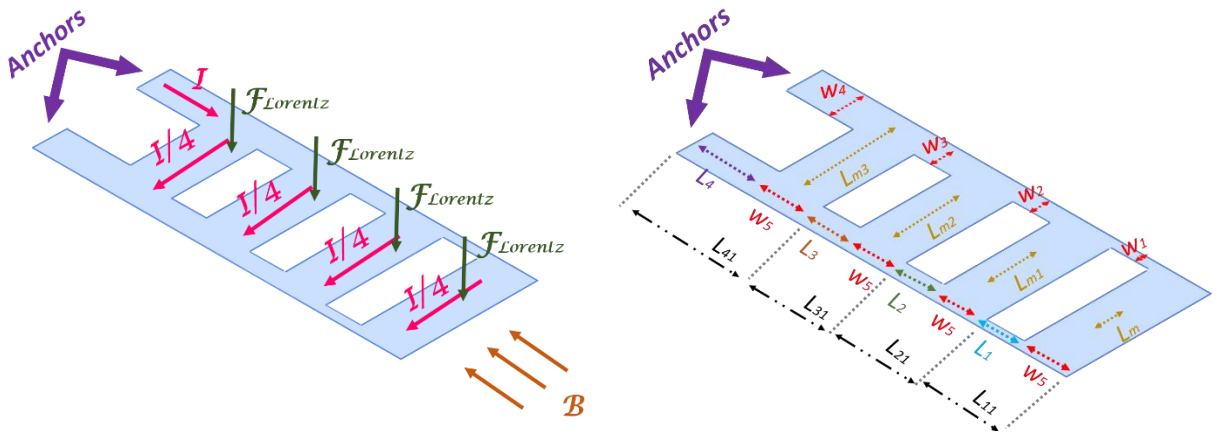

(c) (d)

Fig. 3.9: Simple U-shaped beam cantilever: (a) Working principle; (b) Geometrical parameters; Topology 3: (c) Working principle; (d) Geometrical parameters.

It is interesting to specify that different inertial masses have been considered because various lengths, linked together by a multiplicative factor, have been conceived; in particular, the relationship between length and mass is shown below, in eq. (3.31):

$$m = L_m * w_5 * (dens_{Si} * t_{Si} + dens_{Al} * t_{Al} + dens_{AlN} + t_{AlN}) \quad (3.31)$$

hence, taking into account the following connection among lengths in each sub-structure of Topology 3:

$$L_m = \frac{L_{m1}}{2} = \frac{L_{m2}}{3} = \frac{L_{m3}}{4} \quad (3.32)$$

thus, as a consequence, in eq. (3.33) the relationship among several masses is explained:

$$m = \frac{m_1}{2} = \frac{m_2}{3} = \frac{m_3}{4} \quad (3.33)$$

Also in this case, in Topology 3 the driving current is split in four arms, as illustrated in Fig. 3.9c, and therefore, the Lorentz force imposed is reduced by a factor equal to four in each arm. In order to analyze the static and dynamic model the following equations systems have been implemented for two architectures:

$$\begin{cases} m\ddot{x} + d\dot{x} + kx + d_{piezo}V = F_{Lorentz} & (3.34) \\ \dot{V} = K_{piezo}\dot{x} - \gamma V & (3.35) \end{cases}$$

$$\begin{cases} m\ddot{x_F} + d\dot{x_F} + kx_F + d_{piezo}V = \frac{F_{Lorentz}}{4} & (3.36) \\ m_1\ddot{x_{F1}} + d\dot{x_{F1}} + k_1x_{F1} + d_{piezo}V = \frac{F_{Lorentz}}{4} & (3.37) \\ m_2\ddot{x_{F2}} + d\dot{x_{F2}} + k_2x_{F2} + d_{piezo}V = \frac{F_{Lorentz}}{4} & (3.38) \\ m_3\ddot{x_{F3}} + d\dot{x_{F3}} + k_3x_{F3} + d_{piezo}V = \frac{F_{Lorentz}}{4} & (3.39) \\ \dot{V} = K_{piezo}\dot{x} - \gamma V & (3.40) \end{cases}$$

Just to clarify, the first two equations are related to the simple U-shaped beam cantilever whereas eqs. (3.36), (3.37), (3.38), (3.39) and (3.40) are used to describe the behavior of the Topology 3. In relation to the technological parameters (Young's modulus and thickness) they are the same listed in Table 4, whereas the geometrical ones are tabulated in Table 6.

Simple U-shaped beam cantilever	
w_4	400 µm
w_5	100 µm
L_m	1500 µm
L_{10}	6400 µm

Topology 3	
w_4	400 µm
w_5	100 µm
L_m	1500 µm
L_1	1500 µm
L_2	1500 µm
L_3	1500 µm
L_4	1600 µm
w_1	100 µm
w_2	200 µm
w_3	300 µm

Table 6: List of geometrical parameters related to Simple U-shaped beam cantilever and Topology 3.

It is important to remember that w_4 and w_5 represent the widths related to the arm of the MEMS sensor and to the cantilever tip, in that order; L_m is the length correlated to the inertial mass of both the simple U-shaped beam cantilever and the most external sub-structure in Topology 3. In addition, the widths w_1, w_2 and w_3 are related to the Topology 3 (see Fig. 3.9d) and they assume the following expressions:

$$w_1 = \frac{w_2}{2} = \frac{w_3}{3} = \frac{w_4}{4} \tag{3.41}$$

Using the equivalent section method for the simple U-shaped beam cantilever an elastic constant and natural frequency of 1.74 N/m and 801 Hz have been determined, respectively; in relation of Topology 3 a mechanical stiffness k = 3.48 N/m and a natural frequency f_n = 3.28 kHz have been estimated. In the model implemented in Matlab & Simulink, where a Matlab code and Simulink blocks have been used to investigate the static and dynamic behavior (as described in Appendix B, 2.3 section), the piezoelectric damping (d_{piezo}) has been neglected; furthermore, the

magnetic induction has been fixed at minimum value required in this work (B = 1 μT), the amplitude of the current driven into the MEMS sensor has been set to 80 mA in the static analysis and to 80 mA_{PP} in the dynamic one, therefore, a Lorentz force, in module, of 376 pN has been applied in the simple U-shaped beam cantilever, whereas in the Topology 3 a Lorentz force of 94 pN operates in each arm because the driving current is equal to 20 mA on them. In addition, in Topology 3 the principle of effects superposition is applied, considering the individual contributions unrelated and at the end single displacements are added. As can be observed in Fig. 3.10 the simple architecture exhibits a relevant displacement (~ 1.3 nm) compared to the total displacement of Topology 3 (~ 41.6 pm); this result was expected because the new architecture is less flexible due to reduction of the arm length in each sub-structure, although more contributions in terms of displacement are added at the end. Furthermore, the elastic constants in this last study case are greater in both structures, therefore the overall displacement is lower than the previous architectures. For the same reason, the dynamic behavior presents the same trend, as shown in Fig. 3.11.

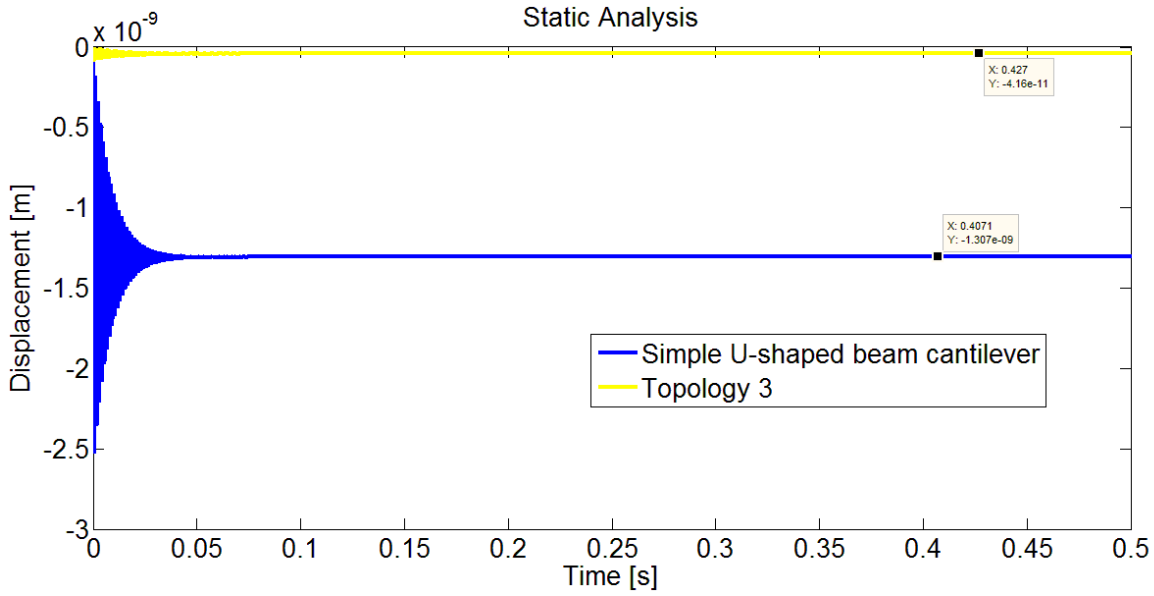

Fig. 3.10: Static analysis: Simple U-shaped beam cantilever VS Topology 3.

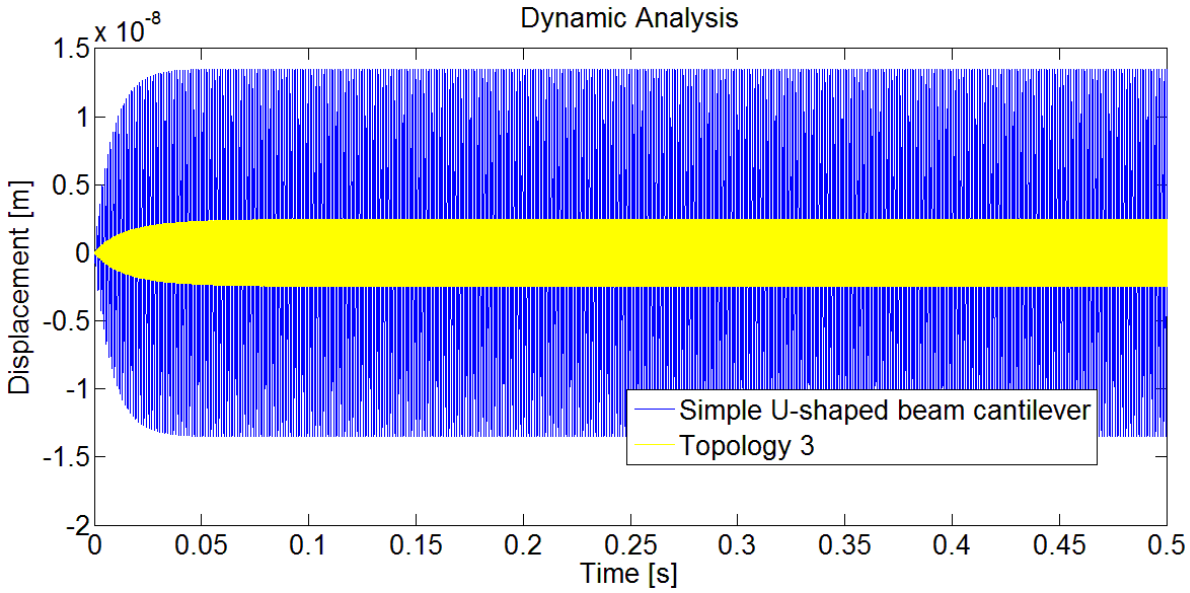

Fig. 3.11: Dynamic analysis: Simple U-shaped beam cantilever VS Topology 3.

In conclusion, Topologies 2 and 3 did not satisfy the expectation to perform the flexibility in order to implement a new architecture of U-shaped beam cantilever having features of a wide operative range. For this reason, it has been decided to shelve the investigation on Topology 2 and Topology 3 and to deepen possible variations of Topology 1.

3.1.4 Simple U-shaped VS Topology 4

Topology 4 has been thought to investigate possible modifications of the Topology 1 which provided better performance than the simple architecture of U-shaped beam cantilever. For this reason, Topology 1 has been proposed again and called Topology 4A (see Figs. 3.12c-d); its two variations, having different meander gaps (indicated with L_9), have been implemented and indicated with Topology 4B and Topology 4C (as shown in Figs. 3.12e-f-g-h); an architecture

with double meander has been introduced and called Topology 4D (as can be observed in Figs. 3.12i-l); finally, all solutions have been compared in the same operative conditions to the simple U-shaped beam cantilever (presented in Figs. 3.12a-b). Also in this case, all designs are not in scale and a 2D schematic is presented just to provide an idea of the structure, whereas all layers have been considered for the implementation of the model. For the same reason, the inertial mass on the cantilever tip is neglected, although it has been introduced in Matlab & Simulink model.

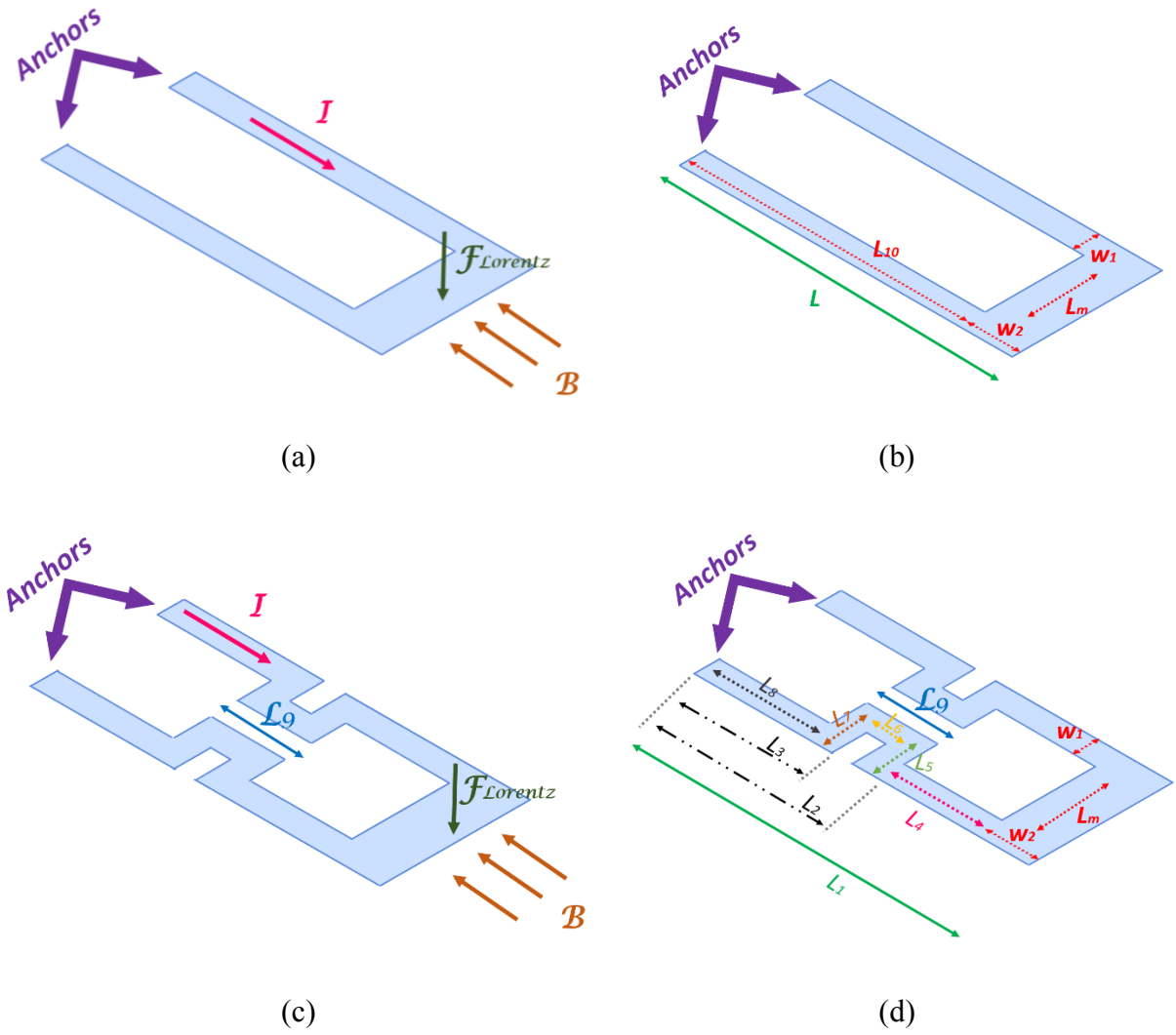

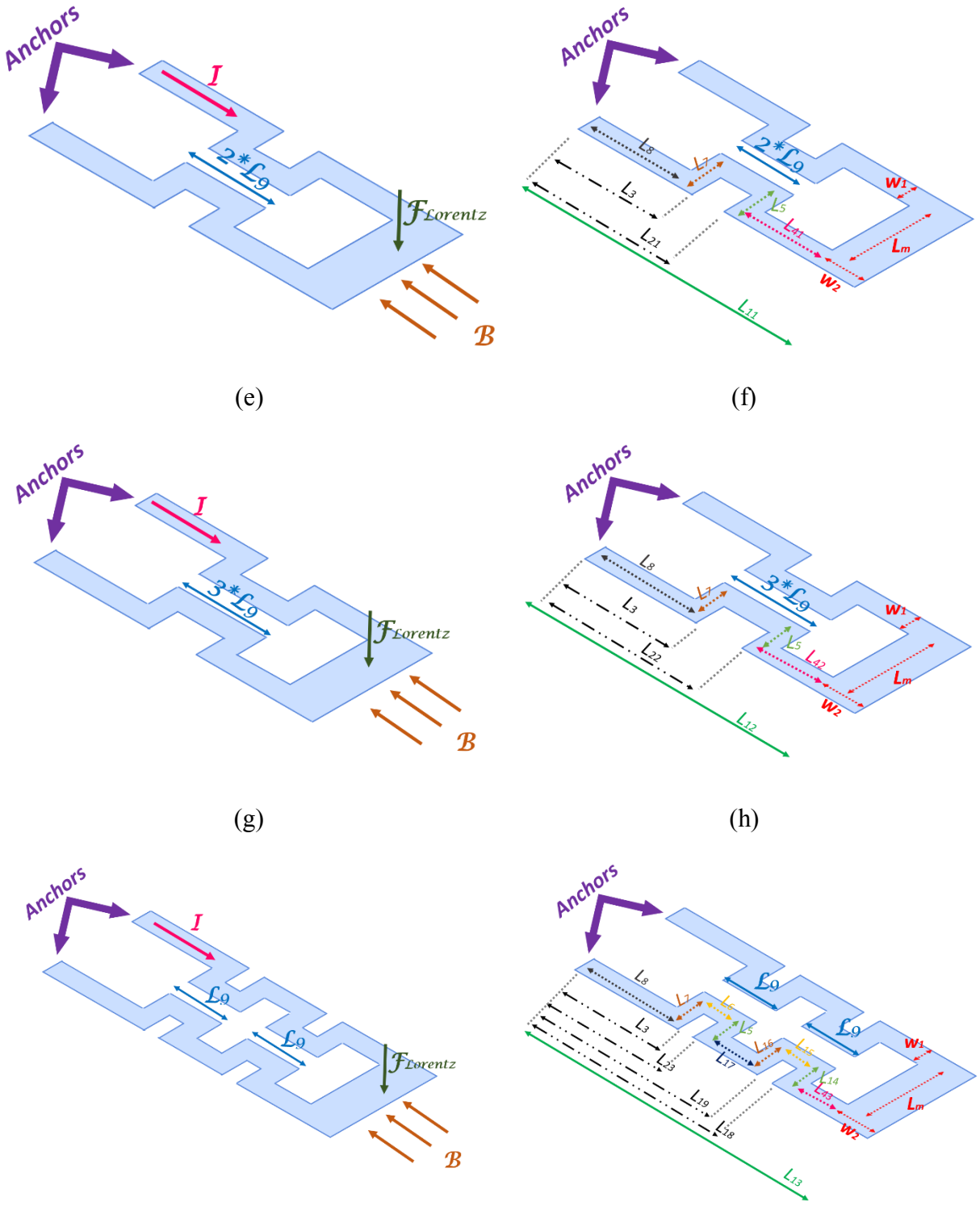

Fig. 3.12: Simple U-shaped beam cantilever: (a) Working principle; (b) Geometrical parameters; Topology 4A: (c) Working principle; (d) Geometrical parameters; Topology 4B: (e) Working principle; (f) Geometrical parameters; Topology 4C: (g) Working principle; (h) Geometrical parameters; Topology 4D: (i) Working principle; (l) Geometrical parameters.

It is intriguing to underline that Topologies 4A, 4B and 4C are exactly the same for the purpose of the mechanical stiffness since the total linear length of these architectures is kept constant, as denoted by eq. (3.74). Identical observations drown attention to previous Topology 1 are still valid as concerns the Lorentz forces: $F_{Lorentz1}$ and $F_{Lorentz2}$ have doubled and they assume the same value because the arm length is equal, nevertheless they are different to $F_{Lorentz}$ because the active lengths are dissimilar. Furthermore, it is interesting to mention that the presence of double meander in Topology 4D implicates the introduction of other two equations because the Lorentz force operates on other two arms with opposite direction, as shown in Fig. 3.13.

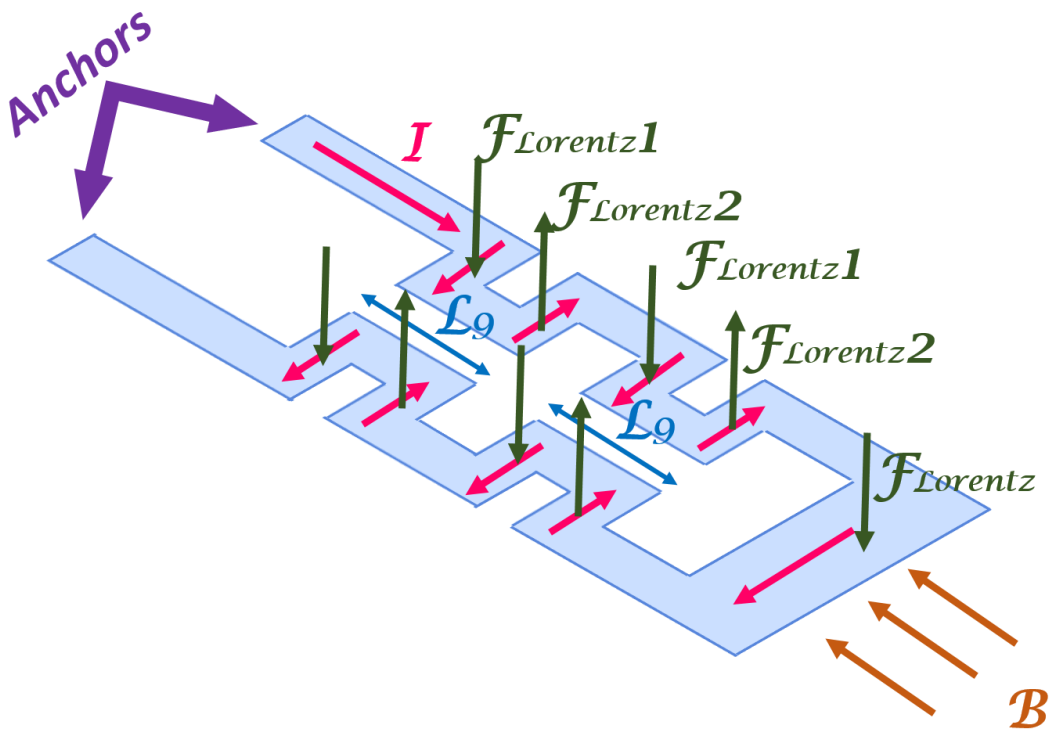

Fig. 3.13: Detail on working principle of Topology 4D.

As concerns the Topology 4 and its variations the principle of effects superposition is applied, considering the individual contributions unrelated. Eventually, in order to analyze the static and dynamic model the following equations systems have been implemented for two architectures:

$$m\ddot{x} + d\dot{x} + kx + d_{piezo}V = F_{Lorentz} \tag{3.42}$$

$$\dot{V} = K_{piezo}\dot{x} - \gamma V \tag{3.43}$$

$$m\ddot{x_F} + d\dot{x_F} + k_F x_F + d_{piezo}V = F_{Lorentz} \tag{3.44}$$

$$m\ddot{x_{F1}} + d\dot{x_{F1}} + \left(\frac{12EI}{(3L_1 - L_3)\cdot L_3^2}\right)x_{F1} + d_{piezo}V = F_{Lorentz1} \tag{3.45}$$

$$m\ddot{x_{F2}} + d\dot{x_{F2}} + \left(\frac{12EI}{(3L_1 - L_2)\cdot L_2^2}\right)x_{F2} + d_{piezo}V = F_{Lorentz2} \tag{3.46}$$

$$\dot{V} = K_{piezo}\dot{x} - \gamma V \tag{3.47}$$

$$m\ddot{x_{F3}} + d\dot{x_{F3}} + k_{F3}x_{F3} + d_{piezo}V = F_{Lorentz} \tag{3.48}$$

$$m\ddot{x_{F4}} + d\dot{x_{F4}} + \left(\frac{12EI}{(3L_{11} - L_3)\cdot L_3^2}\right)x_{F4} + d_{piezo}V = F_{Lorentz1} \tag{3.49}$$

$$m\ddot{x_{F5}} + d\dot{x_{F5}} + \left(\frac{12EI}{(3L_{11} - L_{21})\cdot L_{21}^2}\right)x_{F5} + d_{piezo}V = F_{Lorentz2} \tag{3.50}$$

$$\dot{V} = K_{piezo}\dot{x} - \gamma V \tag{3.51}$$

$$m\ddot{x}_{F6} + d\dot{x}_{F6} + k_{F6}x_{F6} + d_{piezo}V = F_{Lorentz} \tag{3.52}$$

$$m\ddot{x}_{F7} + d\dot{x}_{F7} + \left(\frac{12EI}{(3L_{12}-L_3)\cdot L_3^2}\right)x_{F7} + d_{piezo}V = F_{Lorentz1} \tag{3.53}$$

$$m\ddot{x}_{F8} + d\dot{x}_{F8} + \left(\frac{12EI}{(3L_{12}-L_{22})\cdot L_{22}^2}\right)x_{F8} + d_{piezo}V = F_{Lorentz2} \tag{3.54}$$

$$\dot{V} = K_{piezo}\dot{x} - \gamma V \tag{3.55}$$

$$m\ddot{x}_{F9} + d\dot{x}_{F9} + k_{F9}x_{F9} + d_{piezo}V = F_{Lorentz} \tag{3.56}$$

$$m\ddot{x}_{F10} + d\dot{x}_{F10} + \left(\frac{12EI}{(3L_{13}-L_3)\cdot L_3^2}\right)x_{F10} + d_{piezo}V = F_{Lorentz1} \tag{3.57}$$

$$m\ddot{x}_{F11} + d\dot{x}_{F11} + \left(\frac{12EI}{(3L_{13}-L_{23})\cdot L_{23}^2}\right)x_{F11} + d_{piezo}V = F_{Lorentz2} \tag{3.58}$$

$$m\ddot{x}_{F12} + d\dot{x}_{F12} + \left(\frac{12EI}{(3L_{13}-L_{19})\cdot L_{19}^2}\right)x_{F12} + d_{piezo}V = F_{Lorentz1} \tag{3.59}$$

$$m\ddot{x}_{F13} + d\dot{x}_{F13} + \left(\frac{12EI}{(3L_{13}-L_{18})\cdot L_{18}^2}\right)x_{F13} + d_{piezo}V = F_{Lorentz2} \tag{3.60}$$

$$\dot{V} = K_{piezo}\dot{x} - \gamma V \tag{3.61}$$

Just to elucidate, the first two equations, eqs. (3.42) and (3.43), are related to the simple U-shaped beam cantilever whereas eqs. (3.44), (3.45), (3.46) and (3.47) are used to describe the behavior of the Topology 4A; in addition, eqs. (3.48), (3.49), (3.50) and (3.51) regard Topology 4B, whereas eqs. (3.52), (3.53), (3.54) and (3.55) represent Topology 4C. Finally, Topology 4D is described by equations from (3.56) to (3.61). In relation to the technological

parameters (Young's modulus and thickness) they are the same listed in Table 4, whereas the geometrical ones are tabulated in Table 7.

Simple U-shaped		***Topology 4A***		***Topology 4B***		***Topology 4C***		***Topology 4D***	
w_1	100 µm	w_1	100 µm	w_1	100 µm	w_1	100 µm	w_1	100 µm
w_2	100 µm	w_2	100 µm	w_2	100 µm	w_2	100 µm	w_2	100 µm
L_m	4500 µm	L_m	4500 µm	L_m	4500 µm	L_m	4500 µm	L_m	4500 µm
L_{10}	6400 µm	L_5	1500 µm	L_5	1500 µm	L_5	1500 µm	L_5	1500 µm
		L_7	1500 µm	L_7	1500 µm	L_7	1500 µm	L_7	1500 µm
		L_8	5200 µm	L_8	5200 µm	L_8	5200 µm	L_8	5200 µm
		L_4	900 µm	L_{41}	600 µm	L_{42}	300 µm	L_{43}	300 µm
		L_6	100 µm					L_{14}	1500 µm
								L_{15}	100 µm
								L_{16}	1500 µm
								L_{17}	300 µm

Table 7: List of geometrical parameters related to Simple U-shaped beam cantilever and Topologies 4A, 4B, 4C and 4D.

As regards w_1 and w_2, they represent the widths related to the arm of the MEMS sensor and to the cantilever tip, in that order; L_m is the length correlated to the inertial mass, in accordance with the layout rules. In addition, the quantities L_9, L_1, L_2, and L_3 that are related to the Topology 4A, L_{11}, and L_{21} that are related to the Topology 4B, L_{12}, and L_{22} that are related to the Topology 4C, and eventually L_{13}, L_{18}, L_{19} and L_{23} that are related to the Topology 4D, assume the following expressions:

$$L_9 = L_6 + 2 \cdot w_1 \tag{3.62}$$

$$L_1 = L_8 + L_9 + L_4 + w_2 \tag{3.63}$$

$$L_2 = L_8 + L_9 \tag{3.64}$$

$$L_3 = L_8 + w_1 \tag{3.65}$$

$$L_{11} = L_8 + 2 \cdot L_9 + L_{41} + w_2 \tag{3.66}$$

$$L_{21} = L_8 + 2 \cdot L_9 \tag{3.67}$$

$$L_{12} = L_8 + 3 \cdot L_9 + L_{42} + w_2 \tag{3.68}$$

$$L_{22} = L_8 + 3 \cdot L_9 \tag{3.69}$$

$$L_{13} = L_8 + 2 \cdot L_9 + L_{17} + L_{43} + w_2 \tag{3.70}$$

$$L_{23} = L_8 + L_9 \tag{3.71}$$

$$L_{18} = L_8 + 2 \cdot L_9 + L_{17} \tag{3.72}$$

$$L_{19} = L_8 + L_9 + L_{17} \tag{3.73}$$

Just to specify, the linear lengths must preserve the same quantity, in other terms:

$$L = L_1 = L_{11} = L_{12} = L_{13} \tag{3.74}$$

Finally, the total lengths, that are necessary to estimate the elastic constant for each structure and that are indicated with L_{TOT}, L_{TOT1}, L_{TOT2}, and L_{TOT3} for Topologies 4A, 4B, 4C and 4D, respectively, and L for the simple U-shaped beam cantilever, have the following expressions:

$$L = L_{10} + w_2 \tag{3.75}$$

$$L_{TOT} = L_8 + L_7 + L_9 + L_5 + L_4 + w_2 \tag{3.76}$$

$$L_{TOT1} = L_8 + L_7 + 2 \cdot L_9 + L_5 + L_{41} + w_2 \tag{3.77}$$

$$L_{TOT2} = L_8 + L_7 + 3 \cdot L_9 + L_5 + L_{42} + w_2 \tag{3.78}$$

$$L_{TOT3} = L_8 + L_7 + 2 \cdot L_9 + L_{17} + L_{16} + L_{14} + L_{43} + L_5 + w_2 \tag{3.79}$$

Applying the equivalent section method for the simple U-shaped beam cantilever a mechanical stiffness of 0.0260 N/m and a natural frequency of 230 Hz have been estimated, whereas for Topologies 4A, 4B and 4C a mechanical stiffness of 0.0083 N/m and a natural frequency of 131 Hz have been evaluated. Lastly, Topology 4D exhibits a mechanical stiffness of 0.0037 N/m and a natural frequency of 86 Hz. Taking into account results in terms of elastic constants Topology 4D is expected to be the most performing for the flexibility.

It is intriguing to mention that the model implemented in Matlab & Simulink is not exactly the same described in the previous equations, due to the absence of the term correlated to the piezoelectric damping (d_{piezo}) that has been neglected because it introduces an irrelevant contribution.

In order to analyze the static and dynamic model the Simulink simulation environment has been used (as illustrated in Appendix B, 2.4 section); in detail, in static analysis the magnetic induction has been fixed at minimum value required in this work (B = 1 μT), the amplitude of the current driven into the MEMS sensor has been set to 20 mA, therefore, a Lorentz force, in module, of 94 pN has been applied. As can be observed in Fig. 3.14a the Topology 4A exhibits a tip displacement (~ 11 nm) which is comparable with the displacement found in Topology 1. In relation to the Topologies 4B and 4C the tip displacements are 10.5 nm and 9.88 nm respectively, whereas the Topology 4D presents the greatest tip movement, that is 24.8 nm; in

any case, they are greater than the displacement of the simple U-shaped beam cantilever (~ 3.61 nm). It is believed essential to mention that different meander gaps did not influence in a significate way the total tip displacement, as can be observed in Fig. 3.14b, where a focus on displacement in Topologies 4A, 4B and 4C is presented. A similar behavior (as shown in Fig. 3.15) has been determined analyzing the dynamic model, in which the magnetic induction (B) is maintained constant and equal to 1 μT, the driving current is a sinusoidal signal having an amplitude of 20 mA_{PP} and a frequency of 230 Hz for the simple architecture, of 131 Hz for the Topologies 4A, 4B and 4C and of 86 Hz for Topology 4D. All architectures have been compared at own resonance when they produce the maximum output signal; in relation to this aspect it is absolutely necessary to underline that making the device works on the resonance allows to obtain greater displacements in the same operative conditions.

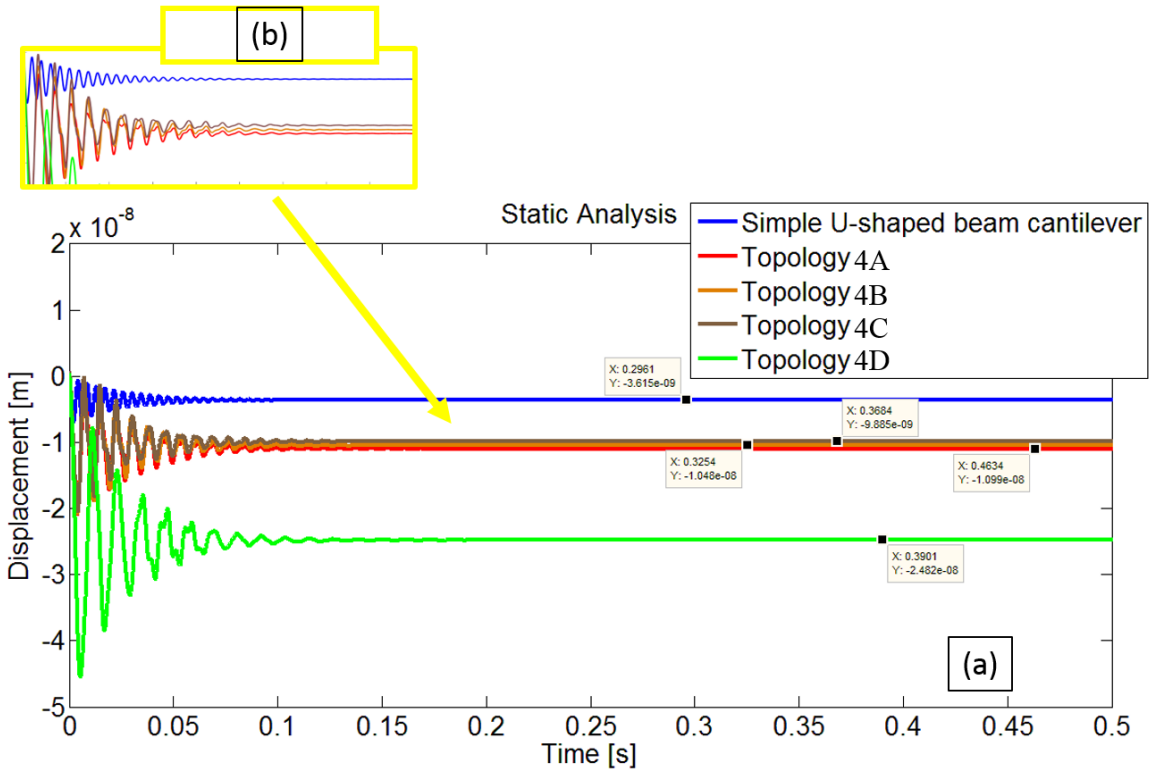

Fig. 3.14: Static analysis: (a) Simple U-shaped beam cantilever VS Topologies 4; (b) Focus on Topologies 4A, 4B and 4C.

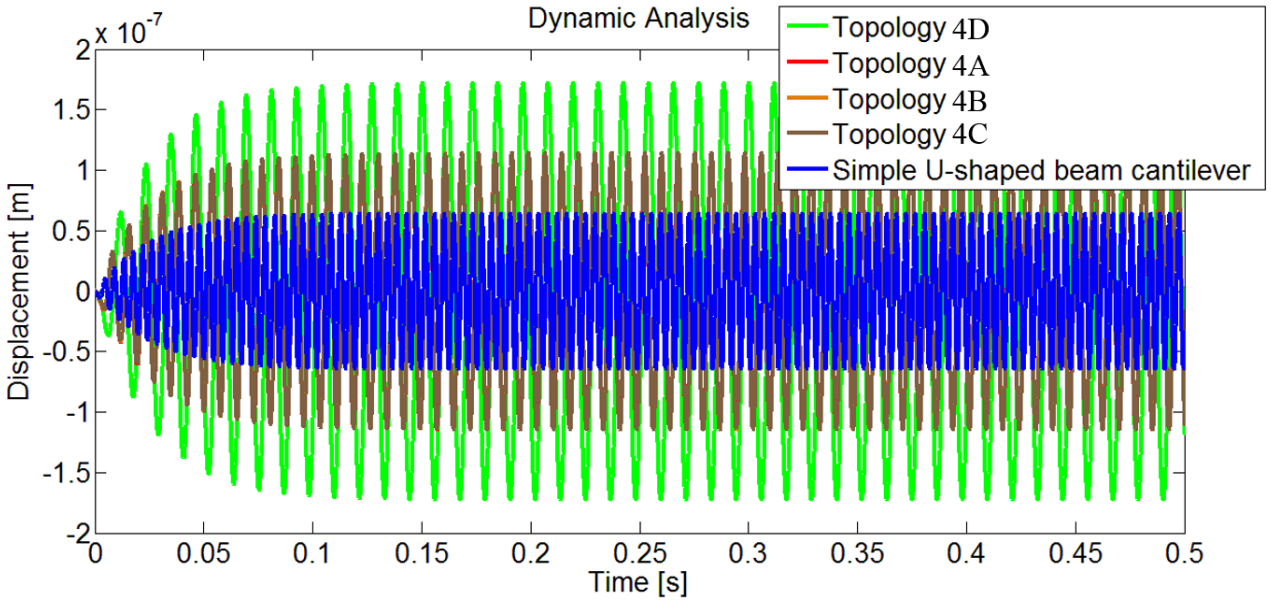

Fig. 3.15: Dynamic analysis: Simple U-shaped beam cantilever VS Topologies 4.

In conclusion, a variation of the meander gap did not introduce an improvement in terms of tip displacement, therefore Topologies 4A, 4B and 4C are equivalent; instead, the most relevant result is presented by Topology 4D where a double meander has been inserted in order to improve the flexibility; for this reason, it has been decided to investigate the static and dynamic behavior of a new structure having more meanders.

3.1.5 Simple U-shaped VS Topology 5

The research of a very flexible architecture, capable of tuning features for a wide operative range, encouraged to investigate structures where the mechanical stiffness can be significantly reduced while preserving the typology of magnetic field sensor actuated by Lorentz force (U-shaped beam cantilever). For this reason, after having examined two macro-architectures of MEMS device the focus fell on a particular topology, that has been defined “meander”, that demonstrated an improvement of flexibility and hence displacement in the same operative conditions, if it is

compared to a simple U-shaped beam cantilever. Taking into account results obtained analyzing the static and dynamic model of Topology 4D it has been thought to implement another architecture increasing the meander numbers; as a consequence, a comparison between the simple U-shaped beam cantilever (in Figs. 3.16a-b) and the new architecture (Topology 5, that is shown in Figs. 3.16c-d) has been carried out. Again, two designs are not in scale and a 2D schematic is presented just to provide an idea of the design, whereas all layers have been considered for the implementation of the model. For the same reason, the inertial mass on the cantilever tip is neglected, although it has been introduced in Matlab & Simulink model.

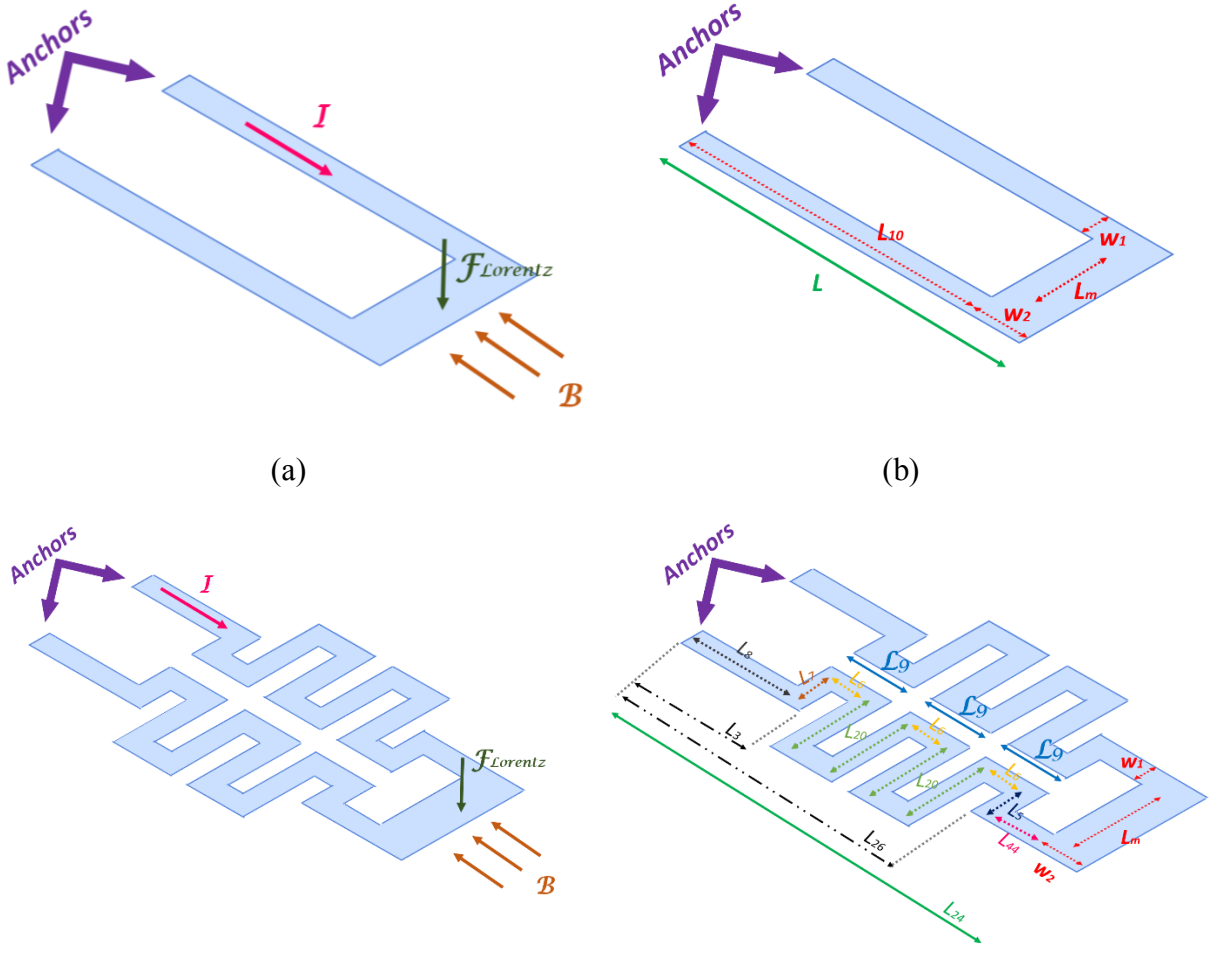

Fig. 3.16: Simple U-shaped beam cantilever: (a) Working principle; (b) Geometrical parameters; Topology 5: (c) Working principle; (d) Geometrical parameters.

It is important to underline that, since the Lorentz force operates in all sections of the structure in which *I* and *B* are perpendicular with different directions, which are determined by the rule of the right hand, in Topology 5 several arms are subjected to this force, as described in Fig. 3.17; in particular, $F_{Lorentz1}$ and $F_{Lorentz2}$ have a similar amplitude in module because the arm length is equal although they are dissimilar to the force on the tip, $F_{Lorentz}$, and, for the same reason, $F_{Lorentz3}$ and $F_{Lorentz4}$ are identical. In addition, previous simulations correlated to Topologies 1, 4B, 4C and 4D demonstrated that contributions in terms of displacement relative to very close arms are completely negligible; for this reason, in order to investigate the static and dynamic behavior of Topology 5 contributions which are function of the Lorentz forces, $F_{Lorentz3}$ and $F_{Lorentz4}$, have been procrastinated in Matlab & Simulink model.

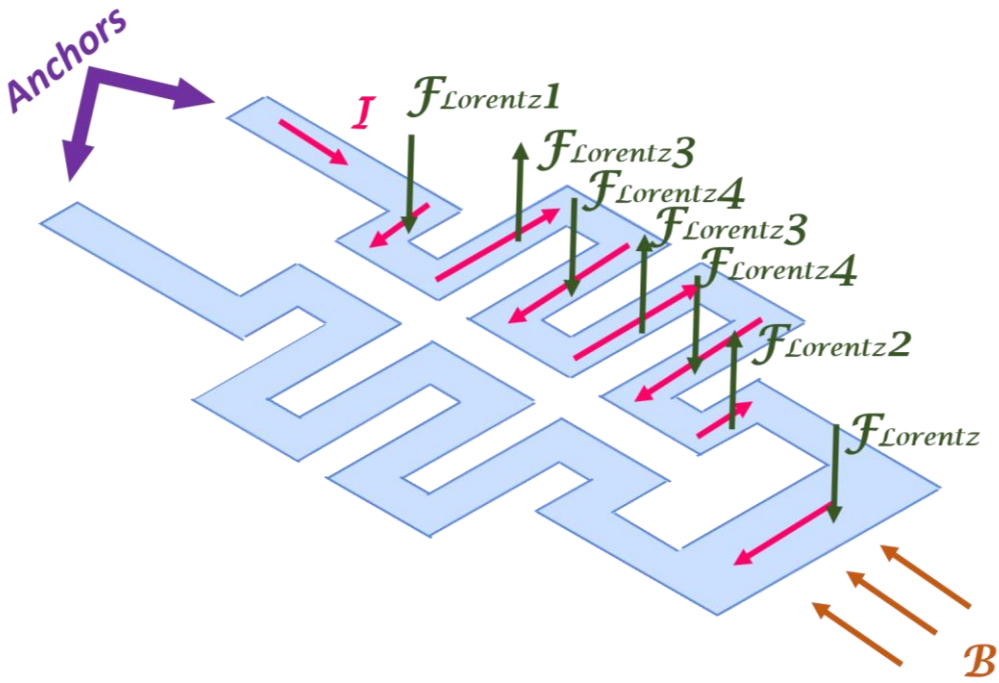

Fig. 3.17: Detail on working principle of Topology 5.

Also in this case, for the Topology 5 the principle of effects superposition is applied, considering the individual contributions unrelated. Eventually, in order to analyze the static and dynamic model the following equations systems have been implemented for two architectures:

$$\begin{cases} m\ddot{x} + d\dot{x} + kx + d_{piezo}V = F_{Lorentz} & (3.80) \\ \dot{V} = K_{piezo}\dot{x} - \gamma V & (3.81) \end{cases}$$

$$\begin{cases} m\ddot{x}_{F14} + d\dot{x}_{F14} + k_{F14}x_{F14} + d_{piezo}V = F_{Lorentz} & (3.82) \\ m\ddot{x}_{F15} + d\dot{x}_{F15} + \left(\frac{12EI}{(3L_{24}-L_3)\cdot L_3^2}\right)x_{F15} + d_{piezo}V = F_{Lorentz1} & (3.83) \\ m\ddot{x}_{F16} + d\dot{x}_{F16} + \left(\frac{12EI}{(3L_{24}-L_{26})\cdot L_{26}^2}\right)x_{F16} + d_{piezo}V = F_{Lorentz2} & (3.84) \\ \dot{V} = K_{piezo}\dot{x} - \gamma V & (3.85) \end{cases}$$

Just to clarify, eqs. (3.80) and (3.81) are related to the simple U-shaped beam cantilever whereas eqs. (3.82), (3.83), (3.84) and (3.85) are used to describe the behavior of the Topology 5. In relation to the technological parameters (Young's modulus and thickness) they are the same listed in Table 4, whereas the geometrical ones are tabulated in Table 8.

Simple U-shaped beam cantilever	
w_1	100 μm
w_2	100 μm
L_m	5300 μm
L_{10}	8500 μm

Topology 5	
w_1	100 μm
w_2	100 μm
L_m	5300 μm
L_5	1500 μm
L_6	100 μm

L_7	1500 µm
L_8	5200 µm
L_{44}	2200 µm
L_{20}	2900 µm

Table 8: List of geometrical parameters related to Simple U-shaped beam cantilever and Topology 5.

As concerns w_1 and w_2, they represent the widths related to the arm of the MEMS sensor and to the cantilever tip, in that order; L_m is the length correlated to the inertial mass. Furthermore, the quantities L_3, L_9, L_{24} and L_{26}, that are related to the Topology 5, are shown in Fig. 3.16d and assume the following expressions:

$$L_3 = L_8 + w_1 \tag{3.85}$$

$$L_9 = L_6 + 2 \cdot w_1 \tag{3.86}$$

$$L_{24} = L_8 + 3 \cdot L_9 + 2 \cdot L_6 + L_{44} + w_2 \tag{3.87}$$

$$L_{26} = L_8 + 3 \cdot L_9 + 2 \cdot L_6 \tag{3.88}$$

Finally, the total lengths, that are mandatory in order to evaluate the elastic constants in the U-shaped beam cantilever and in Topology 5, have the following expressions:

$$L = L_{10} + w_2 \tag{3.89}$$

$$L_{TOT4} = L_8 + L_7 + 5 \cdot L_9 + 4 \cdot L_{20} + L_5 + L_{44} + w_2 \tag{3.90}$$

The equivalent section method, that is described in Appendix B (2.5 section), allowed to evaluate the mechanical stiffness and the natural frequency for both architectures, in detail, a

mechanical stiffness of 0.0190 N/m and a natural frequency of 31.5 Hz have been estimated for the simple U-shaped beam cantilever, whereas for the Topology 5 a mechanical stiffness of 0.92 mN/m and a natural frequency of 7 Hz have been appraised. Again, in Matlab & Simulink model the term correlated to the piezoelectric damping (d_{piezo}) has been neglected. In order to analyze the static and dynamic model the Simulink simulation environment has been used (as illustrated in Appendix B, 2.5 section); in particular, in static analysis the driving current (I) and the magnetic induction (B) assume constant values, that are I = 20 mA and B = 1 μT, whereas in dynamic analysis the magnetic induction is the same, but the driving current is a sinusoidal signal, having an excitation frequency equal to the natural frequency of the examined architectures; as a consequence, a Lorentz force, in amplitude, of 0.11 nN has been applied. As can be observed in Fig. 3.18 the Topology 5 shows a tip displacement (~ 0.12 μm) which is considerably greater than the displacement of the simple U-shaped beam cantilever (~ 5.79 nm).

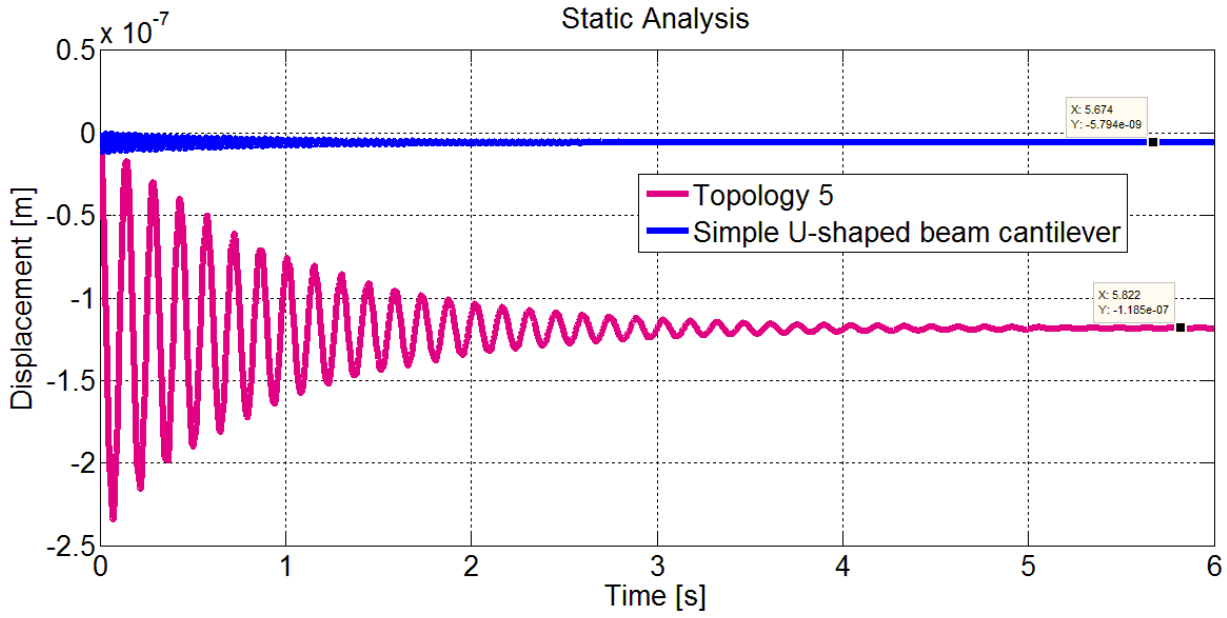

Fig. 3.18: Static analysis: Simple U-shaped beam cantilever VS Topology 5.

A similar trend has been found examining the dynamic model, in which the magnetic induction (B) is maintained constant and equal to 1 μT, the driving current is a sinusoidal signal having an

amplitude of 20 mA_{PP} and a frequency of 31.5 Hz for the simple architecture and of 7 Hz for the Topology 5. It is important to remember that both architectures have been compared at own resonance when they produce the maximum output signal.

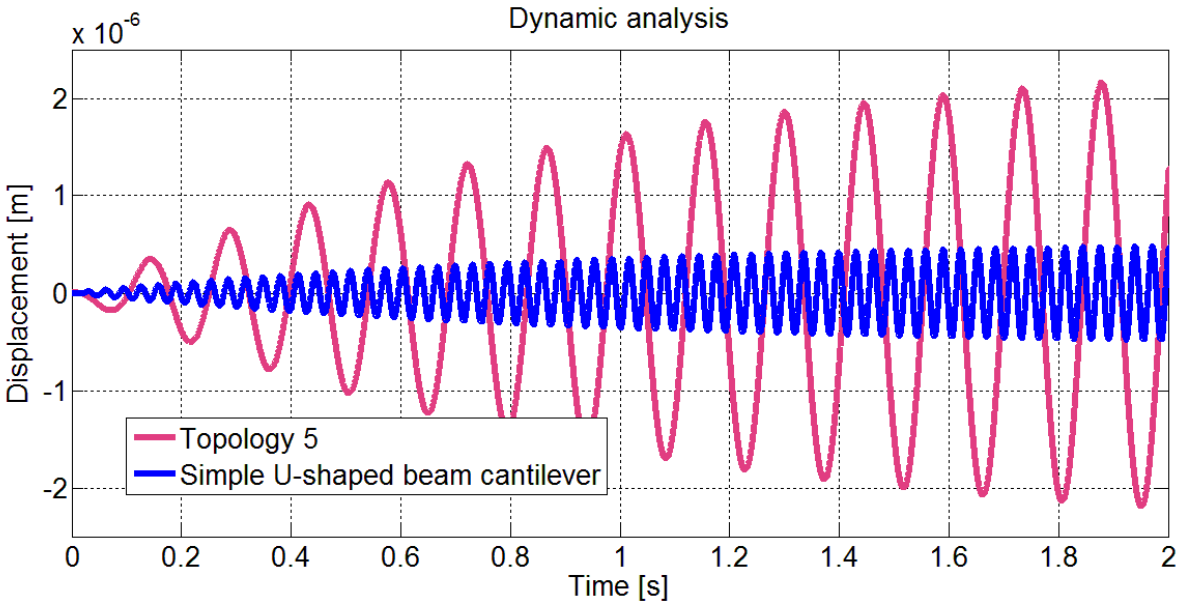

Fig. 3.19: Dynamic analysis: Simple U-shaped beam cantilever VS Topology 5.

In conclusion, considering the remarkable difference in terms of displacement between two structures, in order to reach the specifications required in this PhD project, it has been decided to deepen further the meander architecture examining a last topology, which is completely composed of meanders.

3.1.6 Simple U-shaped VS Topology 6

The Topology 6 has been designed to push the performance in terms of flexibility within the limits imposed by the PiezoMUMPs technology, that are the die dimensions 9.65 mm × 9.65 mm. Also in this case new topology, which is illustrated in Figs. 3.20c-d, has been compared to the simple U-shaped beam cantilever (see Figs. 3.20a-b) in terms of static and

dynamic analysis via Matlab & Simulink Toolbox. In relation to two designs it is essential to specify that they are not in scale and a 2D schematic is presented just to provide an idea of the design, whereas all layers have been considered for the implementation of the model. For the same reason, the inertial mass on the cantilever tip is neglected, although it has been introduced in Matlab & Simulink model.

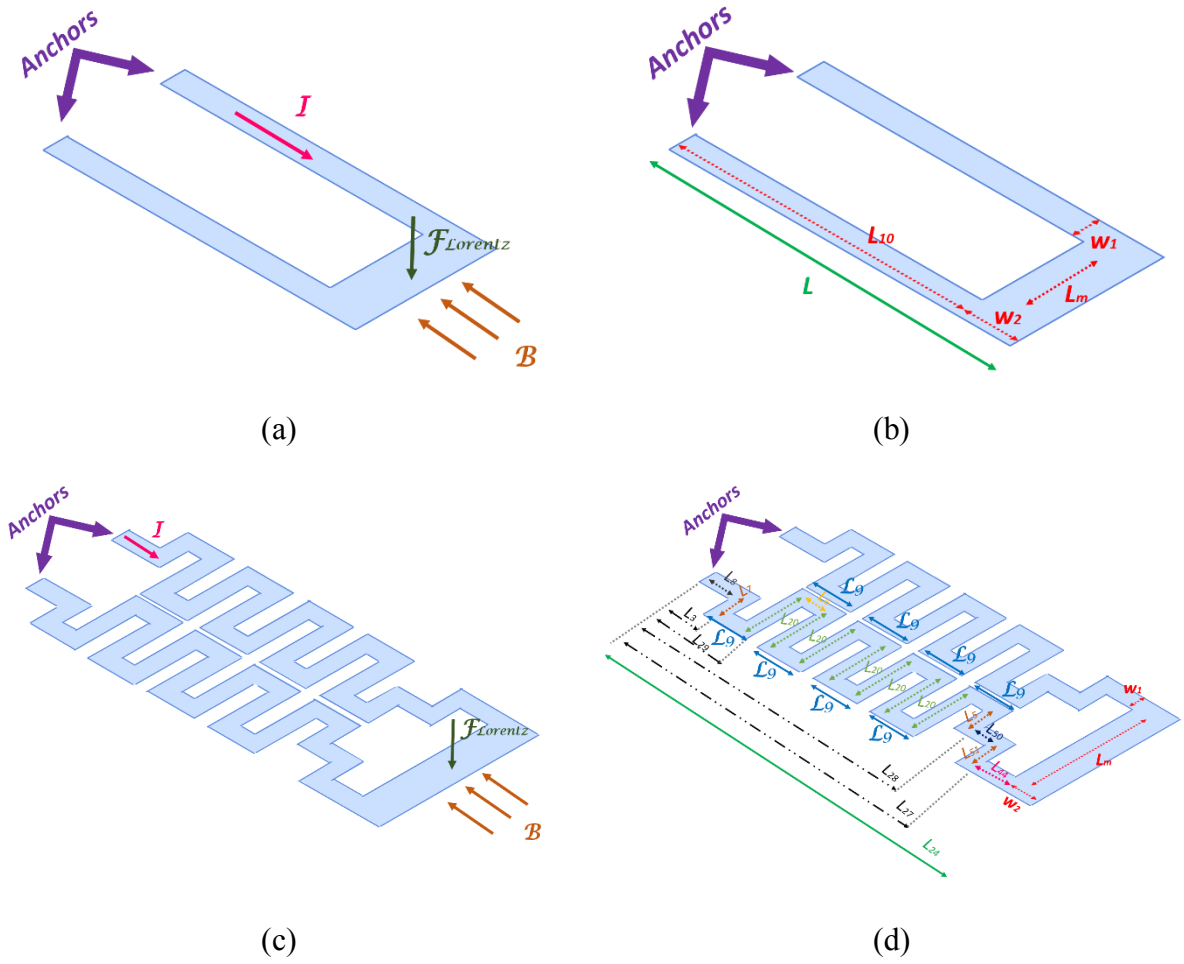

Fig. 3.20: Simple U-shaped beam cantilever: (a) Working principle; (b) Geometrical parameters; Topology 6: (c) Working principle; (d) Geometrical parameters.

The presence of a meander architecture introduces several arms in which the Lorentz force, having a different amplitude correlated to the arm length, operates. For this reason, in Fig. 3.21 all Lorentz forces which insist on the Topology 6 are inserted: in detail, $F_{Lorentz1}$ assumes the

same value with the identical direction in various arms because their length is equal; $F_{Lorentz3}$ and $F_{Lorentz4}$ are equal in module, opposite in direction and greater than previous force due to a longer arm length; finally, $F_{Lorentz}$ is the force that insists on the cantilever tip. As can be observed in Fig. 3.21 some Lorentz forces, $F_{Lorentz3,4}$, have been indicated with a different colour (pale green) because they have been neglected in the static and dynamic model for the same reasons that have been previously mentioned (their contributions neutralize). In the end only five Lorentz force contributions, indicated in green in Fig. 3.21, have been considered.

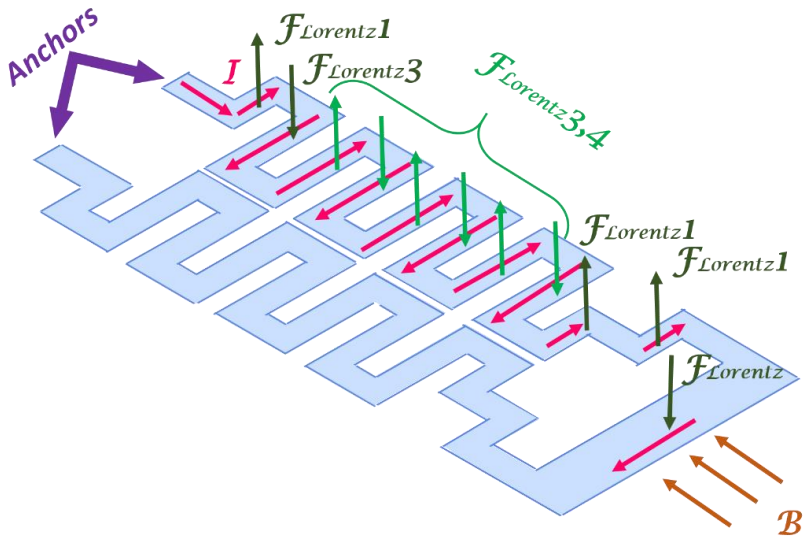

Fig. 3.21: Detail on working principle of Topology 6.

Furthermore, for the Topology 6 the principle of effects superposition is used, considering the individual contributions unrelated. Therefore, in order to analyze the static and dynamic model the following equations systems have been implemented for two architectures:

$$\begin{cases} m\ddot{x} + d\dot{x} + kx + d_{piezo}V = F_{Lorentz} & (3.91) \\ \dot{V} = K_{piezo}\dot{x} - \gamma V & (3.92) \end{cases}$$

$$m\ddot{x}_{F17} + d\dot{x}_{F17} + k_{F17}x_{F17} + d_{piezo}V = F_{Lorentz} \tag{3.93}$$

$$m\ddot{x}_{F18} + d\dot{x}_{F18} + \left(\frac{12EI}{(3L_{24}-L_3)\cdot L_3^2}\right)x_{F18} + d_{piezo}V = F_{Lorentz1} \tag{3.94}$$

$$m\ddot{x}_{F19} + d\dot{x}_{F19} + \left(\frac{12EI}{(3L_{24}-L_{28})\cdot L_{28}^2}\right)x_{F19} + d_{piezo}V = F_{Lorentz1} \tag{3.95}$$

$$m\ddot{x}_{F20} + d\dot{x}_{F20} + \left(\frac{12EI}{(3L_{24}-L_{27})\cdot L_{27}^2}\right)x_{F20} + d_{piezo}V = F_{Lorentz1} \tag{3.96}$$

$$m\ddot{x}_{F21} + d\dot{x}_{F21} + \left(\frac{12EI}{(3L_{24}-L_{29})\cdot L_{29}^2}\right)x_{F21} + d_{piezo}V = F_{Lorentz3} \tag{3.97}$$

$$\dot{V} = K_{piezo}\dot{x} - \gamma V \tag{3.98}$$

Just for completeness, eqs. (3.91) and (3.92) are related to the simple U-shaped beam cantilever whereas the behavior of the Topology 6 is described from eq. (3.93) to eq. (3.98). In relation to the technological parameters (Young's modulus and thickness) they are the same listed in Table 4, whereas the geometrical ones are tabulated in Table 9.

Simple U-shaped beam cantilever	
w_1	300 μm
w_2	500 μm
L_m	8200 μm
L_{10}	8000 μm

Topology 6	
w_1	300 μm
w_2	500 μm
L_m	8200 μm
L_5	1700 μm
L_6	300 μm
L_7	1700 μm
L_8	1500 μm
L_{44}	700 μm
L_{20}	2900 μm

L_{50}	700 μm
L_{51}	1700 μm

Table 9: List of geometrical parameters related to Simple U-shaped beam cantilever and Topology 6.

As concerns w_1 and w_2, they represent the widths related to the arm of the MEMS sensor and to the cantilever tip, in that order; L_m is the length correlated to the inertial mass. It is important to underline that the width w_1 has been increased in order to improve the robustness at the expense of the flexibility. In addition, the quantities L_3, L_9, L_{24}, L_{27}, L_{28} and L_{29}, related to the Topology 6, are shown in Fig. 3.20d and assume the following expressions:

$$L_3 = L_8 + w_1 \tag{3.99}$$

$$L_9 = L_6 + 2 \cdot w_1 \tag{3.100}$$

$$L_{24} = L_8 + 4 \cdot L_9 + 4 \cdot L_6 + w_1 + L_{50} + L_{44} + w_2 \tag{3.101}$$

$$L_{27} = L_8 + 4 \cdot L_9 + 4 \cdot L_6 + w_1 + L_{50} \tag{3.102}$$

$$L_{28} = L_8 + 4 \cdot L_9 + 4 \cdot L_6 + w_1 \tag{3.103}$$

$$L_{29} = L_8 + L_9 \tag{3.104}$$

Eventually, the total lengths, that are necessary to evaluate the elastic constants in the U-shaped beam cantilever and in Topology 6, have the following expressions:

$$L = L_{10} + w_2 \tag{3.105}$$

$$L_{TOT5} = L_8 + L_7 + 8 \cdot L_9 + 7 \cdot L_{20} + L_5 + L_{50} + L_{51} + L_{44} + w_2 \tag{3.106}$$

Using the equivalent section method for the simple U-shaped beam cantilever a mechanical stiffness of 0.00591 N/m and a natural frequency of 19.8 Hz have been estimated, whereas for Topology 6 a mechanical stiffness of 0.694 mN/m and a natural frequency of 2 Hz have been evaluated. Even once, in Matlab & Simulink model the term that represents the piezoelectric damping (d_{piezo}) has been neglected. In order to analyze the static and dynamic model the Simulink simulation environment has been used (as illustrated in Appendix B, 2.6 section); in particular, in static analysis the driving current (I) and the magnetic induction (B) are supposed as constant values, that are I = 20 mA and B = 1 μT, whereas in dynamic analysis the magnetic induction is the same, but the driving current is a sinusoidal signal, having an excitation frequency equal to the natural frequency of the examined architectures; as a consequence, a Lorentz force, in amplitude, of 2.64 μN has been applied. As can be observed in Fig. 3.22 the Topology 6 exhibits a tip displacement (~ 0.25 μm) which is considerably greater than the displacement of the simple U-shaped beam cantilever (~ 2.9 nm).

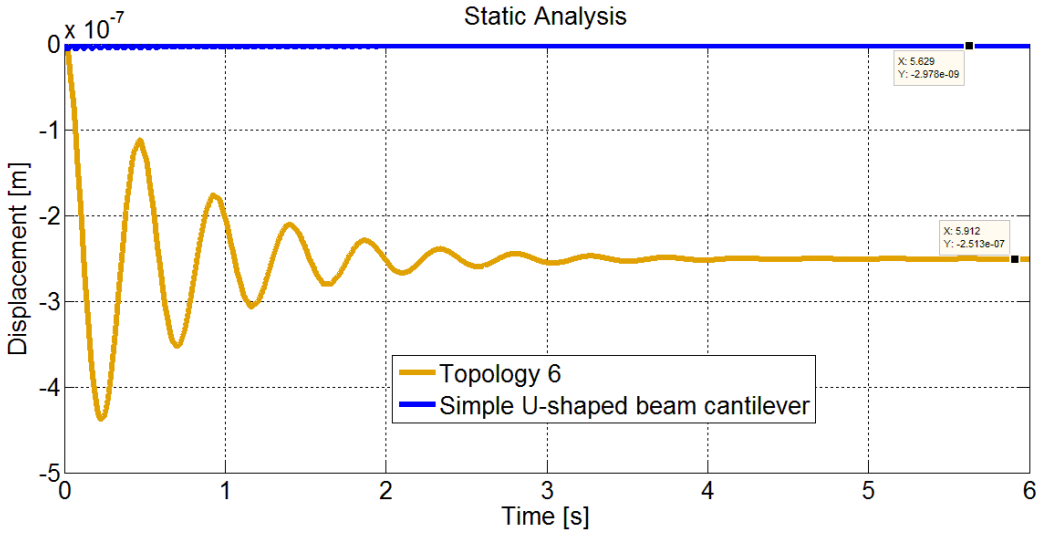

Fig. 3.22: Static analysis: Simple U-shaped beam cantilever VS Topology 6.

A similar trend has been found investigating the dynamic model (as can be seen in Fig. 3.23), in which the magnetic induction (B) is maintained constant and equal to 1 μT, the driving current is a sinusoidal signal having an amplitude of 20 mA_{PP} and a frequency of 19.8 Hz for the simple architecture and of 2 Hz for the Topology 6. It is important to remember that both architectures have been compared at own resonance when they produce the maximum output signal.

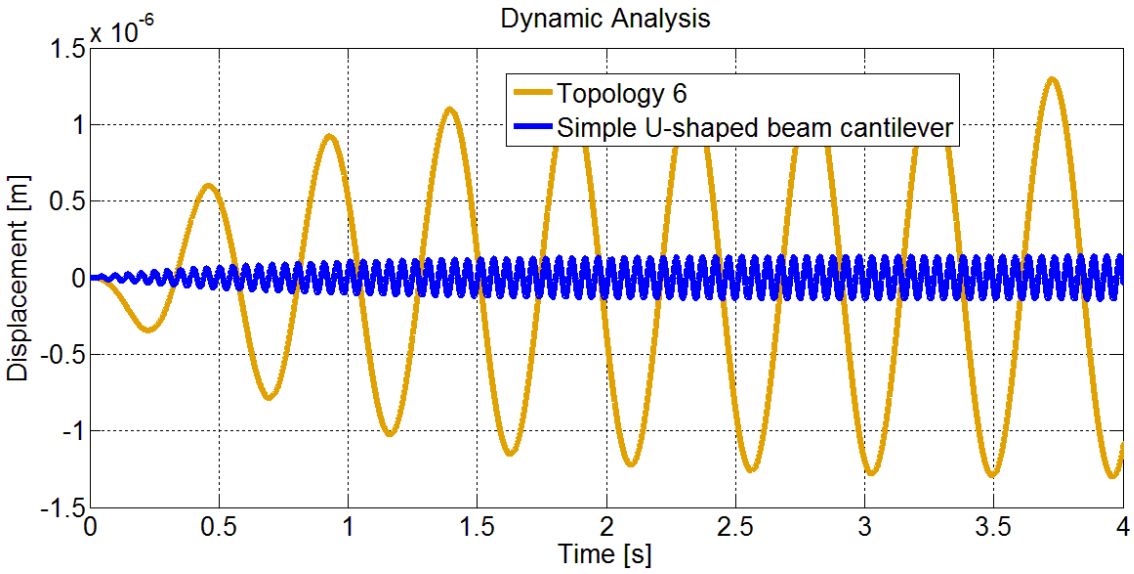

Fig. 3.23: Dynamic analysis: Simple U-shaped beam cantilever VS Topology 6.

Definitely, the inspection of the static and dynamic models allowed the evaluate the performance in terms of flexibility of several variations of U-shaped beam cantilever in order to satisfy the specifications of magnetic field sensor having a wide operative range. At the end of this exploration the Topology 6 has been selected as the most suitable to realize the MEMS sensor proposed in this manuscript.

3.2 FEM analysis in COMSOL Multiphysics environment

The analysis in Matlab & Simulink environment has been very important to validate the mechanical and transduction models, nevertheless it did not provide significant indications about the probability that the chosen design is physically capable of being suspended after its release. Indeed, the residual stress after the release could induce a structural failure in case it exceeded the maximum expected value; for this reason, after having asked to the MEMSCAP foundry some information about this aspect, a residual stress value of 77 MPa has been indicated as the maximum value experimentally estimated. Therefore, the residual stress investigation has been considered a mandatory step before the implementation of the layout; the Finite Element Model (FEM) simulations, implemented in COMSOL Multiphysics environment (5.1 Version) are presented in the present section in order to obtain a closer view of the device behaviors in terms of the displacement and the stress of the examined structures. It is interesting to underline that the FEM simulation has been carried out on both architectures, simple U-shaped beam cantilever and Topology 6, since the aim pursued in this research activity is to compare two fabricated prototypes in terms of performance in the same operative conditions. For this reason, it has been decided to develop a meander architecture and three designs of U-shaped beam cantilever, characterized by different arm lengths.

3.2.1 Meander Architecture

As previously mentioned, the Topology 6 has been chosen because it shows the best fulfillment in terms of flexibility and it has been preliminary designed in Matlab & Simulink environment taking into account the specifications on dimensions imposed by the PiezoMUMPs technology. However, since the concrete realization of the MEMS device is a very delicate process, the

FEM analysis has been implemented on a slightly smaller meander structure in order to respect the layout rules, which are described in detail in [92], with enough margin. The new geometry is displayed in Fig. 3.24, where the inertial mass, composed of thick silicon, and all three layers have been inserted (a focus about the presence of Silicon, Alumimiun Nitride and Aluminium stacks can be observed in Fig. 3.25), whereas all geometrical parameters used are listed in Table. 10.

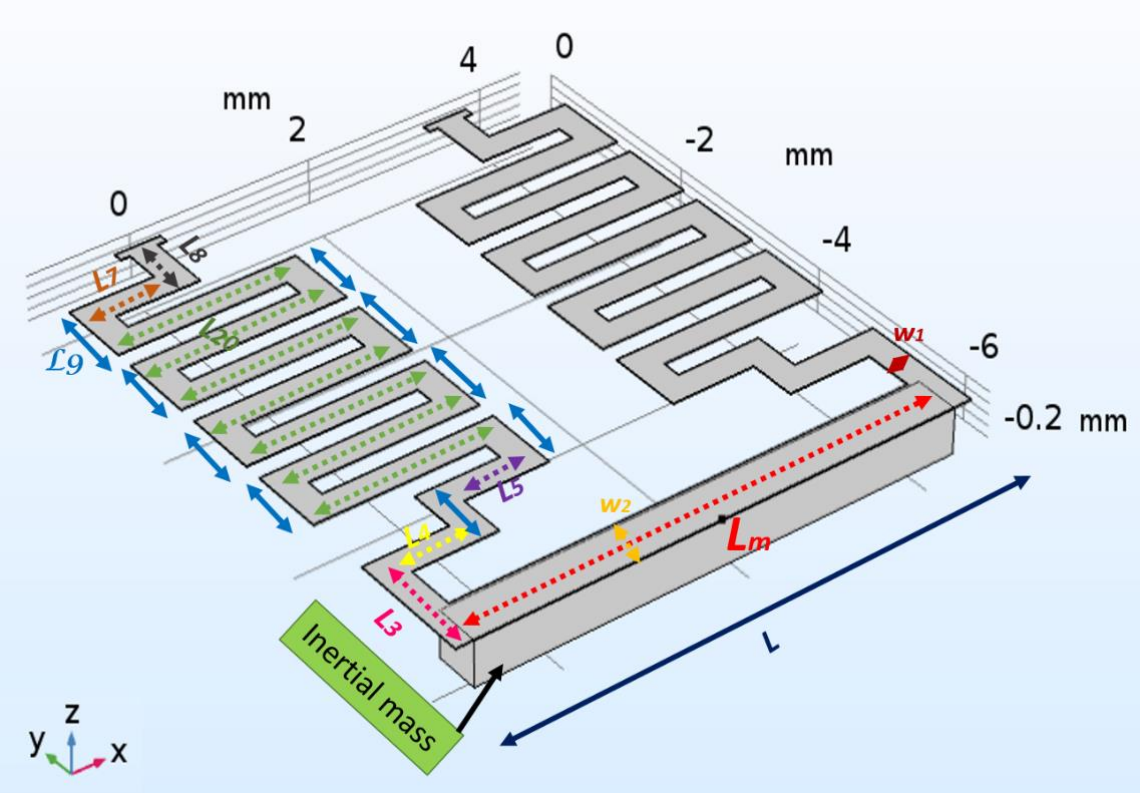

Fig. 3.24: Geometry of meander architecture in COMSOL Multiphysics.

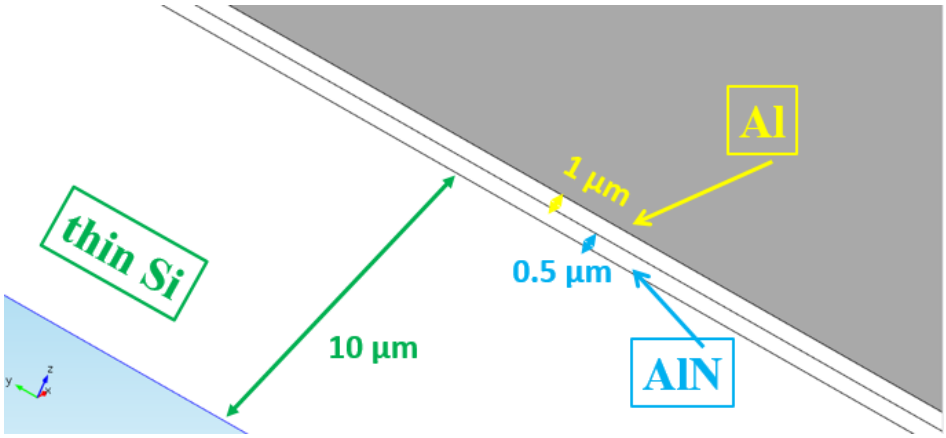

Fig. 3.25: Focus on suspended structure.

Meander Architecture	
w_1	300 µm
w_2	500 µm
L_m	5220 µm
L	5600 µm
L_3	1310 µm
L_4	1210 µm
L_5	1210 µm
L_7	1210 µm
L_8	800 µm
L_9	800 µm
L_{20}	2120 µm

Table 10: List of geometrical parameters related to the meander architecture.

In order to proceed with the FEM analysis an appropriate mesh has been realized (as shown in Fig. 3.26a) contemplating the different dimensions of the layers and of the inertial mass, and especially it has been tightened in correspondence with the critical points which are the corners, as depicted in Fig. 3.26b.

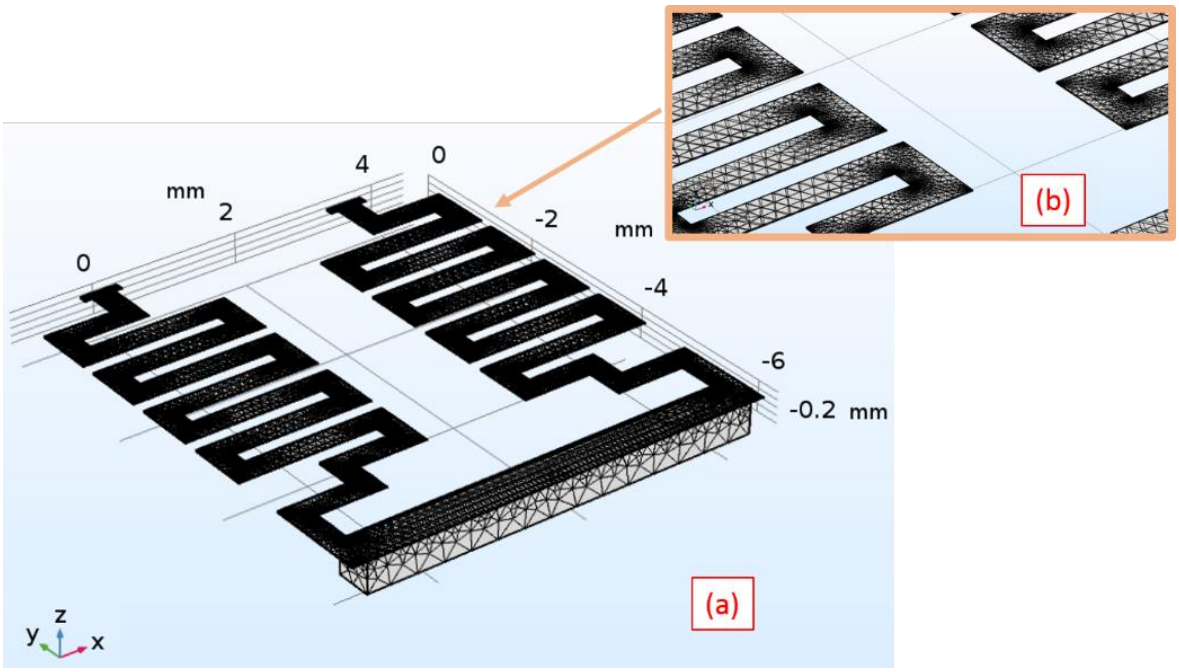

Fig. 3.26: Mesh in COMSOL Multiphysics for meander structure: (a) Designed geometry; (b) Focus on critical points.

In order to reduce the computational burden, the whole geometry has been divided in two domains: the first includes the three layers composing the meander structure and the second one is related only to the inertial mass. An optimized mesh has been obtained, indeed its implementation has been dense along the layers (in this case a fitted mesh has been considered), whereas it has been approximated in correspondence with the inertial mass (in this case a normal mesh has been imposed). In detail, a free mesh has been chosen and it consists of 351855 elements of which the tetrahedral (tets) mesh elements are 228836, the triangular mesh elements are 111056, the mesh edges are 11570 and, eventually, the mesh vertices are 393. Afterwards, an analysis in frequency domain has been selected in order to estimate the natural frequency: as can be observed in Fig. 3.27 the cantilever tip displacement as a function of the frequency allowed to estimate a natural frequency ~ 22 Hz. It is essential to specify that the analysis in frequency domain has been carried out adopting a Lorentz force, having an amplitude of 30 nN, applied to the cantilever tip in z-direction.

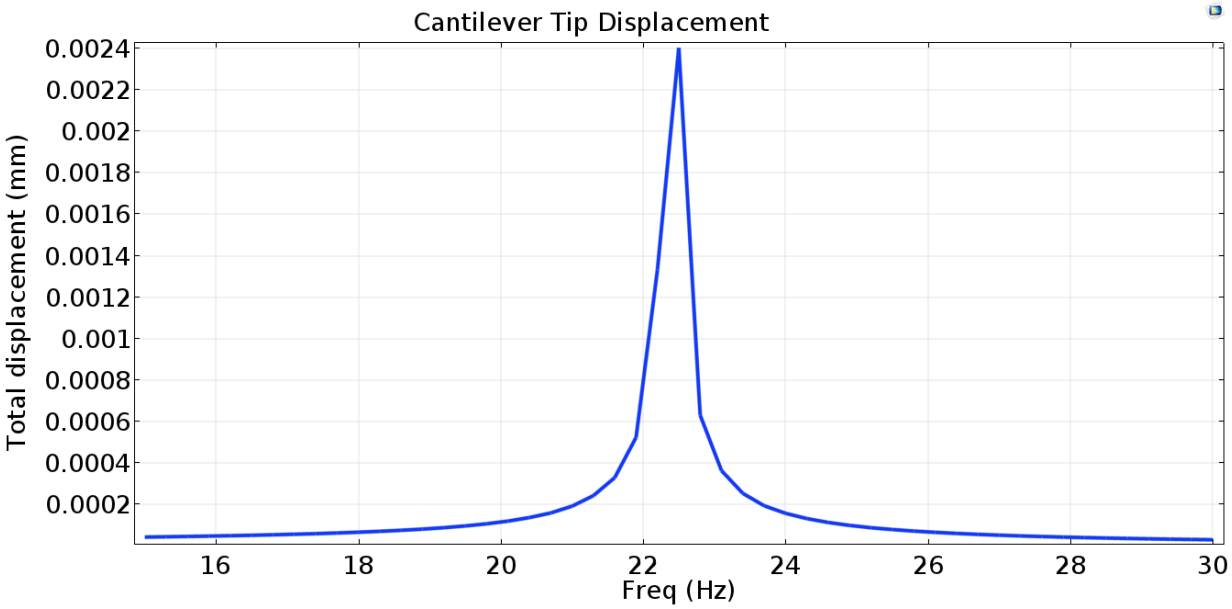

Fig. 3.27: Displacement as a function of the frequency in meander structure.

In addition, an eigen frequency analysis, considering the first six frequencies, has been realized in order to evaluate the oscillation modes; in particular, using the symmetry in the structure even order oscillation modes have been avoided. In particular, the first, third and fifth oscillation modes have been estimated and for each value of frequency the displacement and the von Mises stress, expressed in [m] and in [N/m^2] respectively, have been plotted. The eigen frequency analysis has returned the following frequencies: $f_1 = 22.5$ Hz for the first mode, $f_3 = 398$ Hz for the third mode and at last $f_5 = 910$ Hz for the fifth mode. In Fig. 3.28 the cantilever tip displacement in correspondence with f_1 is shown, whereas the von Mises stress and a focus on the most stressed points are illustrated in Figs. 3.29 a-b.

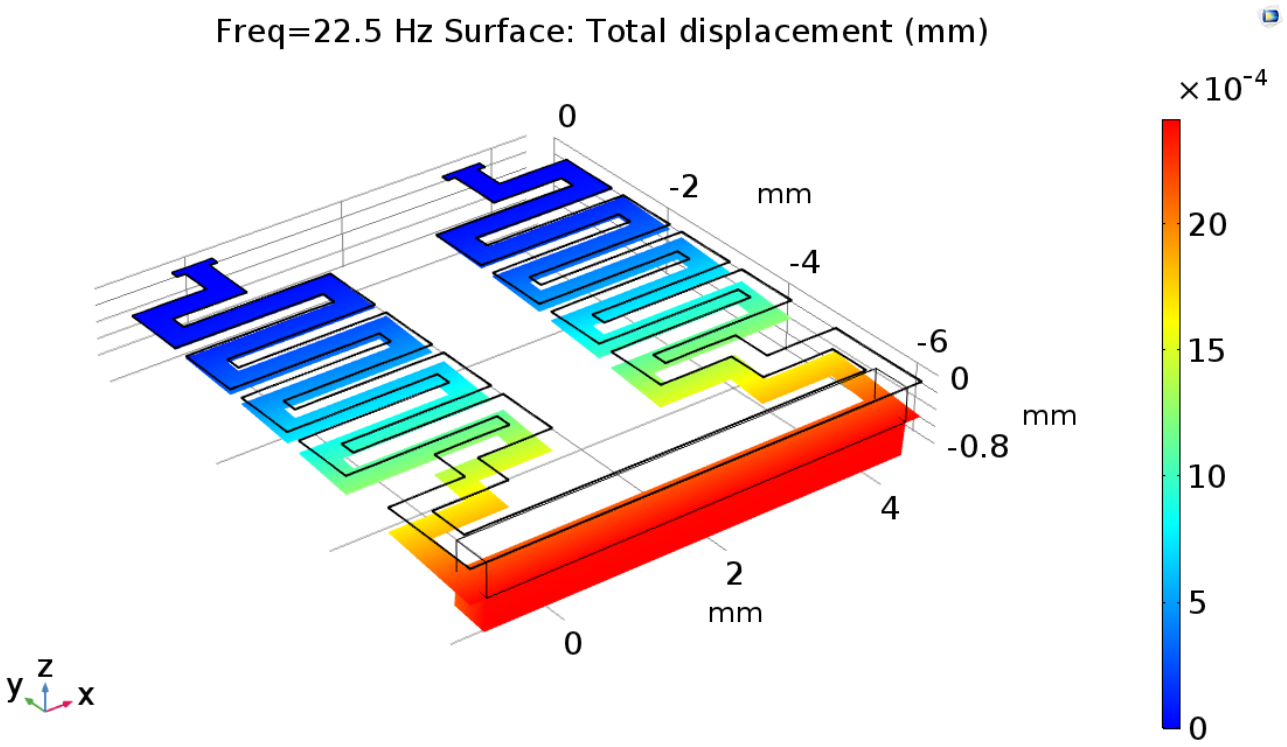

Fig. 3.28: The cantilever tip displacement as function of f_1 = 22.5 Hz.

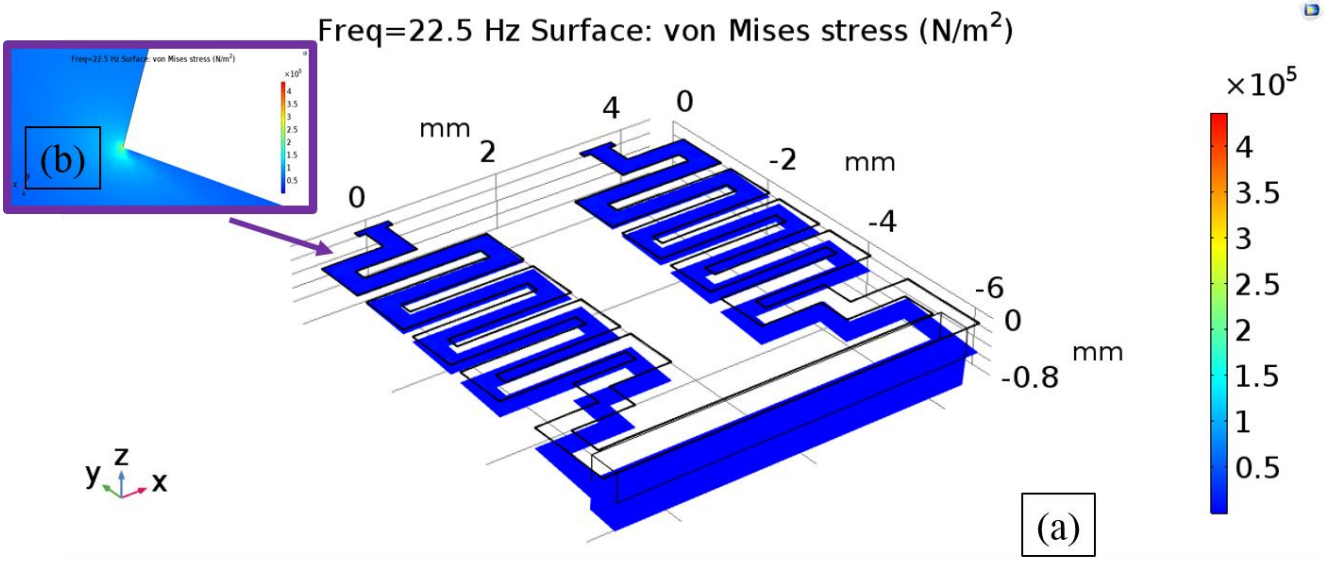

Fig. 3.29: (a) The von Mises stress as function of f_1 = 22.5 Hz; (b) Zoom on critical points.

The largest displacement is observable on the cantilever tip with an amplitude of 2.5 µm in z-direction and the maximum von Mises stress is obtained in correspondence with the anchors and it has a value of 400 kN/m^2. In relation to the third oscillation mode with f_3 = 398 Hz the highest displacement is present in the central section of the structure with a value of 0.52 µm (as displayed in Fig. 3.30), whereas in Fig. 3.31 the von Mises stress with a maximum value of 500 kN/m^2 is shown.

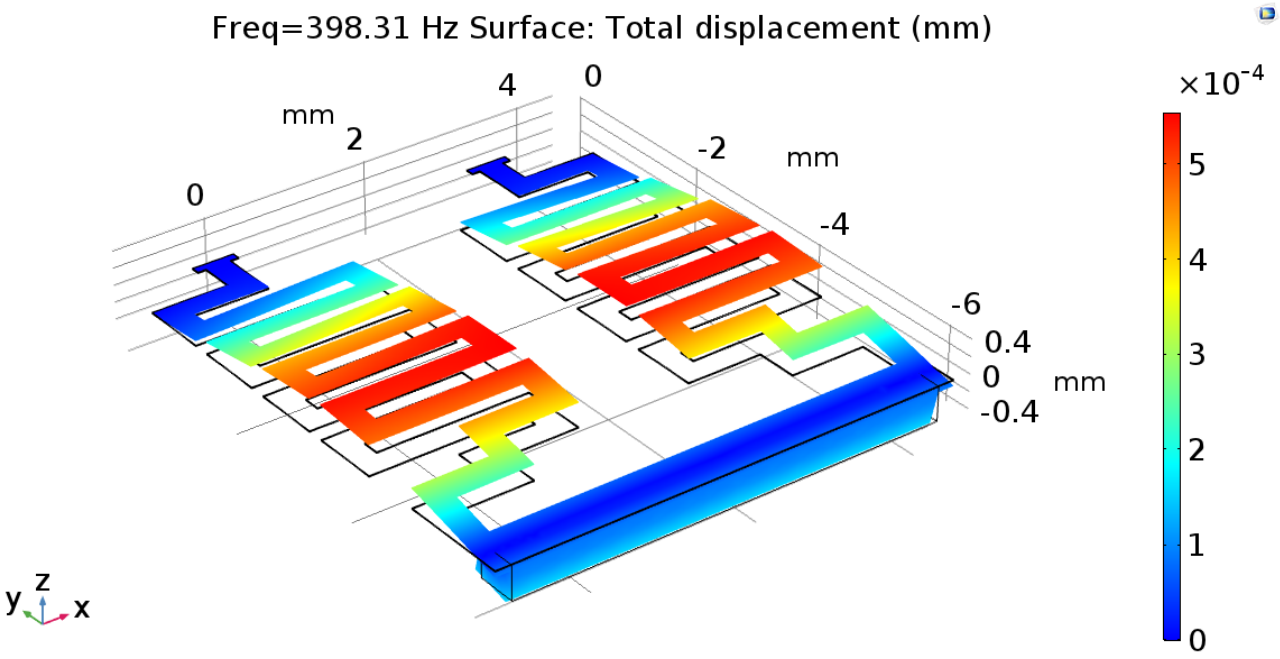

Fig. 3.30: The cantilever tip displacement as function of f_3 = 398 Hz.

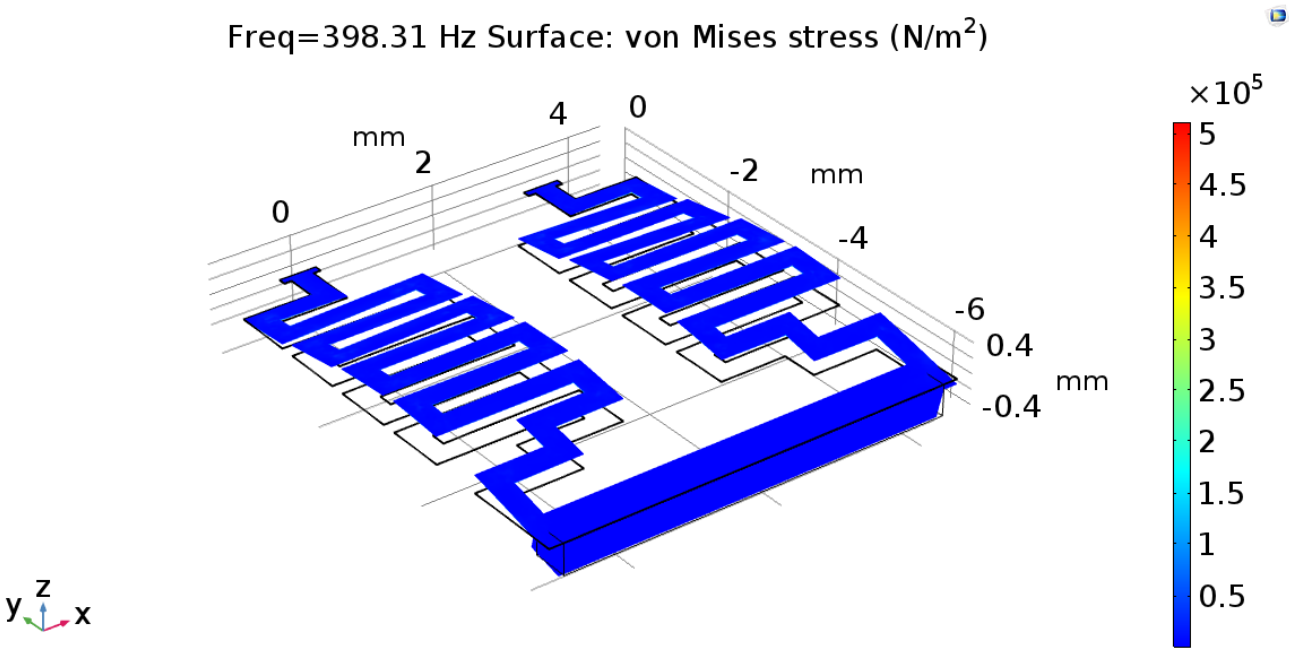

Fig. 3.31: The von Mises stress as function of f_3 = 398 Hz.

Finally, the fifth oscillation mode, having a frequency of f_5 = 910 Hz, has been considered and the following two trends (see Figs. 3.32-3.33) in terms of the displacement and the von Mises stress have been determined. In detail, in Fig. 3.32 the displacement affects essentially the central section of the meander architecture having a lateral oscillation and it presents a maximum value of 0.07 μm. As regards the von Mises stress exhibits the same critical points in comparison with the third mode, nevertheless the maximum value is lower and equal to 80 kN/m^2.

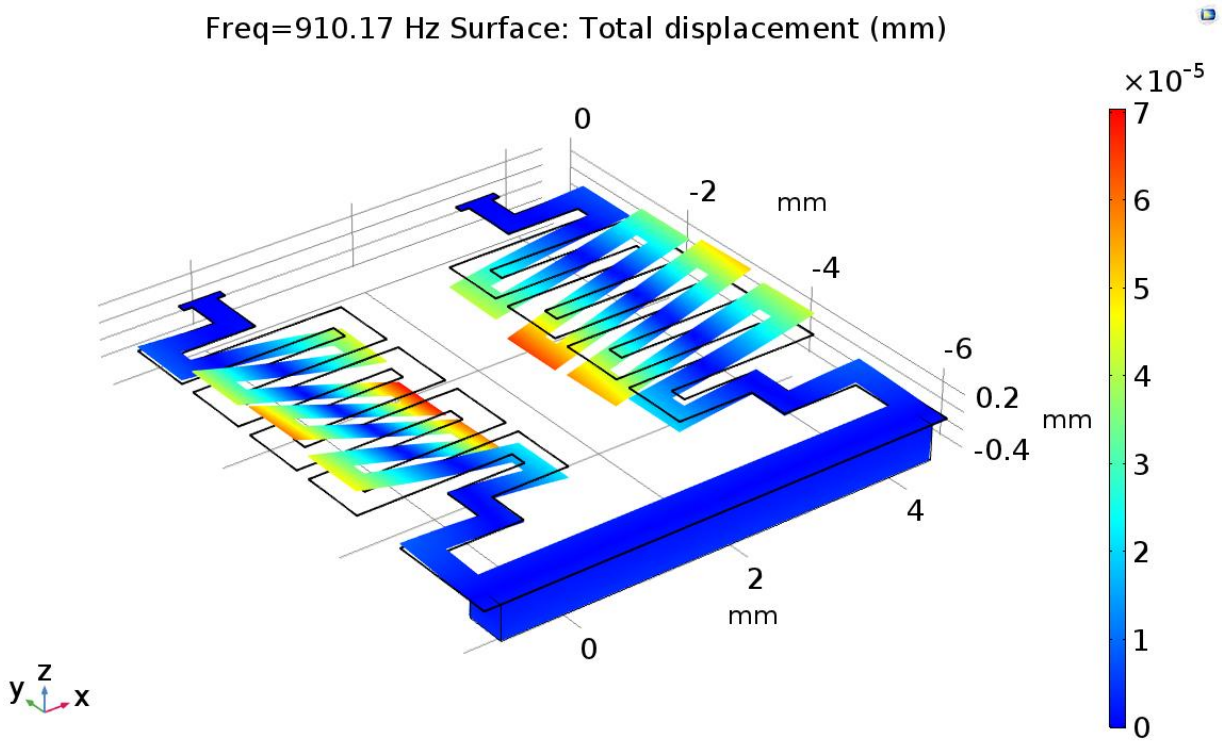

Fig. 3.32: The cantilever tip displacement as function of f_5 = 910 Hz.

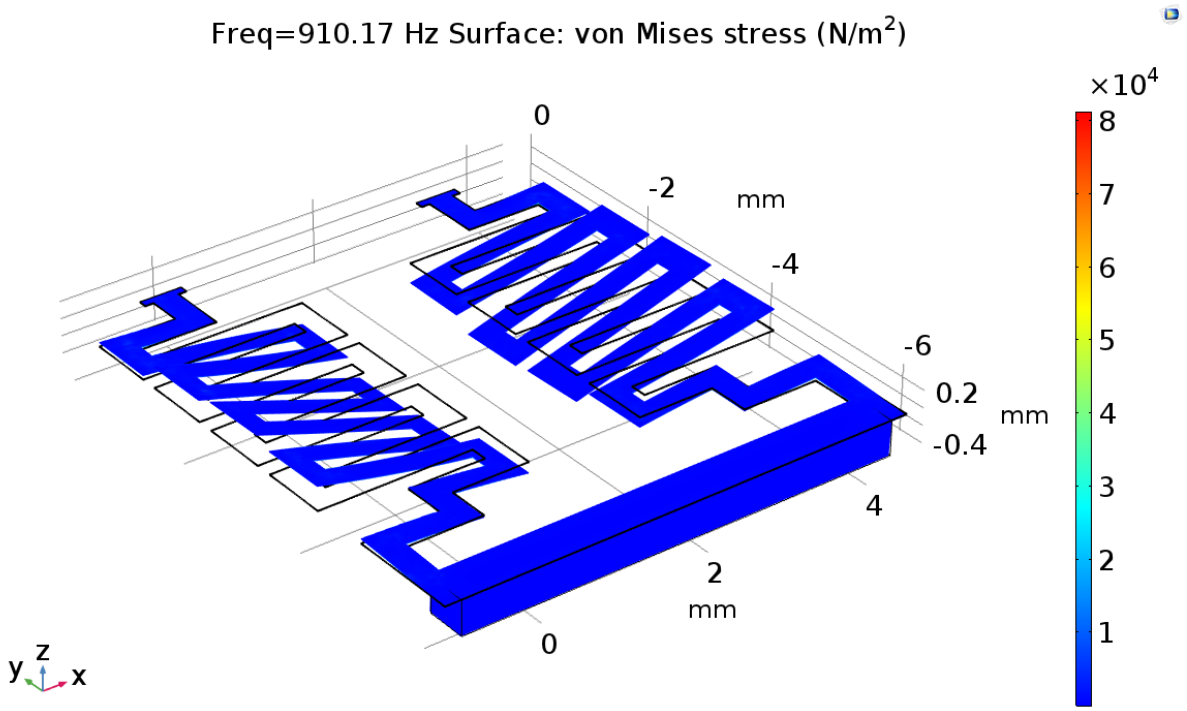

Fig. 3.33: The von Mises stress as function of f_5 = 910 Hz.

It is extremely fascinating to note that in any case the von Mises stress is lower than the maximum value that has been reported, oscillating in the range [80 – 500] kN/m^2, whereas the displacement vacillates in the range [0.07 – 2.5] μm. The FEM analysis confirmed the feasibility of realization of the meander MEMS sensor.

3.2.2 Simple U-shaped beam cantilever

In order to validate if the novelty, represented by the meander shape and introduced in new architecture, has determined an improvement in terms of performance, a comparison with the "classic" U-shaped beam cantilever, implemented in the same technology, has been believed indispensable; for this reason, although the most critical configuration with reference to the structural failure is correlated to the meander architecture, a FEM analysis has also been implemented for the simple U-shaped beam cantilever and, in particular, three different structures have been examined, where the arm length and the length in which the Lorentz force insists on are modified.

3.2.2.1 Long Structure

The first U-shaped beam cantilever architecture that has been paid attention, is defined "Long" because it exhibits the same geometrical dimensions as the structure previously examined, included the inertial mass. It is displayed in Fig. 3.34 and all geometrical parameters are listed in Table 11.

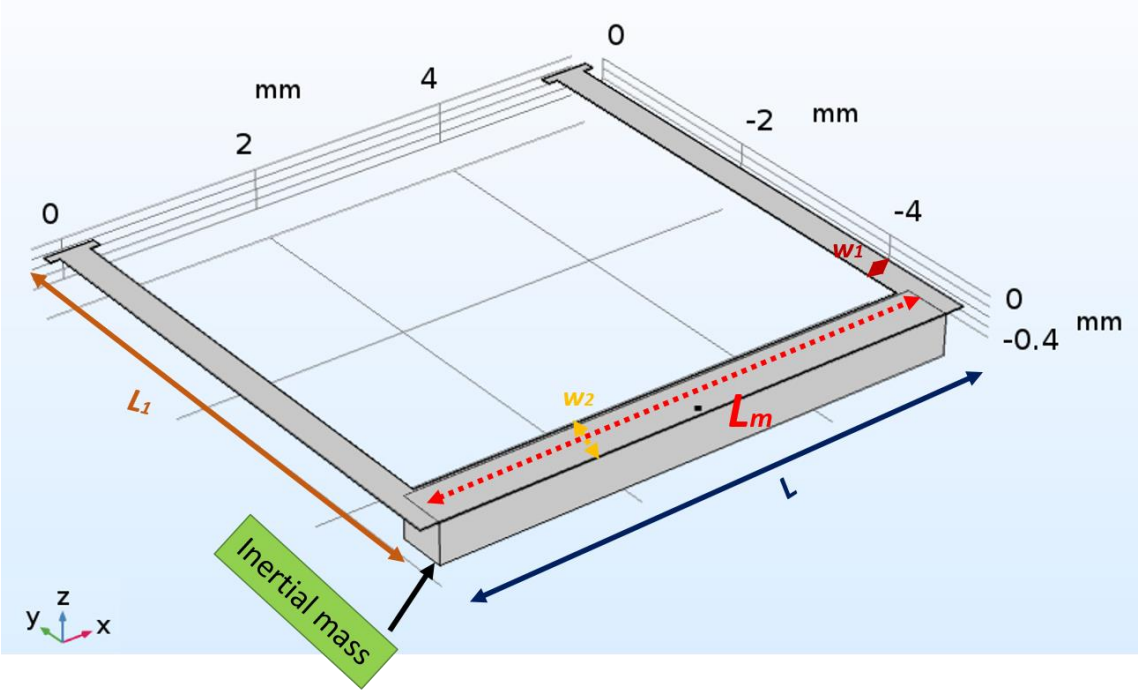

Fig. 3.34: Geometry of "Long" U-shaped beam cantilever in COMSOL Multiphysics.

"Long" U-shaped beam cantilever	
w_1	300 µm
w_2	500 µm
L_m	5220 µm
L	5600 µm
L_1	5270 µm

Table 11: List of geometrical parameters related to the "Long" U-shaped beam cantilever.

An appropriate mesh has been accomplished (see Fig. 3.35a) contemplating the different dimensions of the layers and of the inertial mass, and especially it has been tightened in correspondence with the critical points which are the corners, as depicted in Fig. 3.35b.

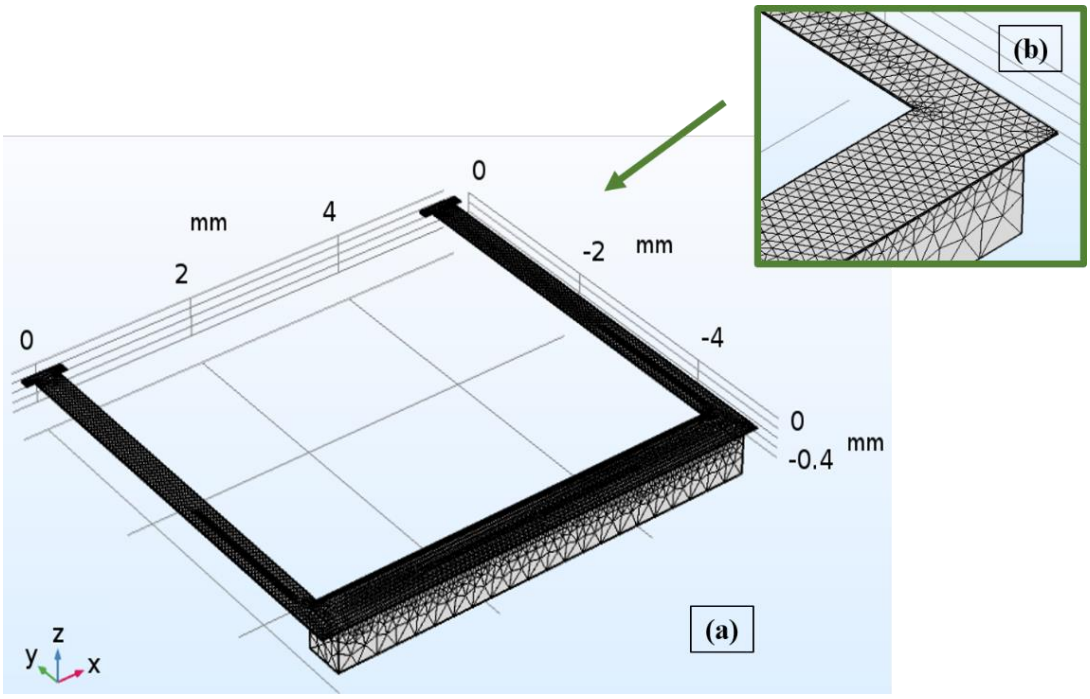

Fig. 3.35: Mesh in COMSOL Multiphysics for "Long" U-shaped: (a) Designed geometry; (b) Focus on critical points.

Also in this case, the whole geometry has been divided in two domains in order to optimize the computational calculation: the first includes the three layers composing the U-shaped structure and the second one is related only to the inertial mass. The mesh implementation has been dense along the layers (in this case a fitted mesh has been considered), whereas it has been approximated in correspondence with the inertial mass (in this case a normal mesh has been imposed). In detail, a free mesh has been chosen and it consists of 39074 elements of which the tetrahedral (tets) mesh elements are 26230, the triangular mesh elements are 11418, the mesh edges are 1385 and, eventually, the mesh vertices are 41. Afterwards, an analysis in frequency domain has been selected in order to estimate the natural frequency: as can be observed in Fig. 3.36 the cantilever tip displacement as a function of the frequency allowed to estimate a natural frequency ~ 45 Hz. It is essential to specify that the analysis in frequency domain has

been carried out adopting a Lorentz force, having an amplitude of 100 nN, applied to the cantilever tip in z-direction.

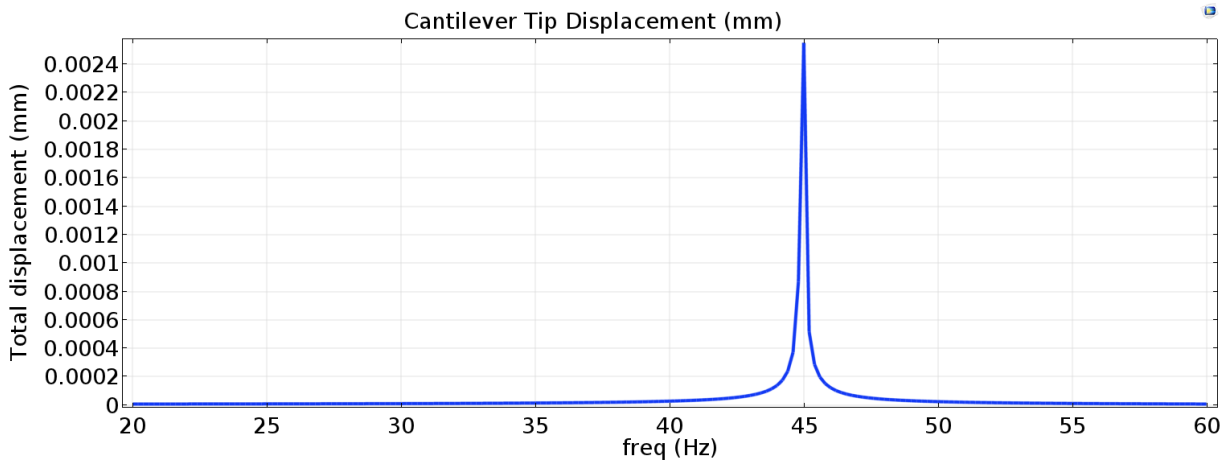

Fig. 3.36: Displacement as a function of the frequency in "Long" U-shaped beam cantilever.

Furthermore, an eigen frequency analysis has been examined in order to evaluate the oscillation modes; in particular, using the symmetry in the structure even order oscillation modes have been avoided and, therefore, the first, third and fifth oscillation modes have been estimated and for each value of frequency the displacement and the von Mises stress, expressed in [m] and in [N/m^2] respectively, have been plotted. The eigen frequency analysis has returned the following frequencies: f_1 = 45 Hz for the first mode, f_3 = 996 Hz for the third mode and at last f_5 = 3.76 kHz for the fifth mode. In detail, in Figs. 3.37a-b-c the displacements at each frequency are shown:

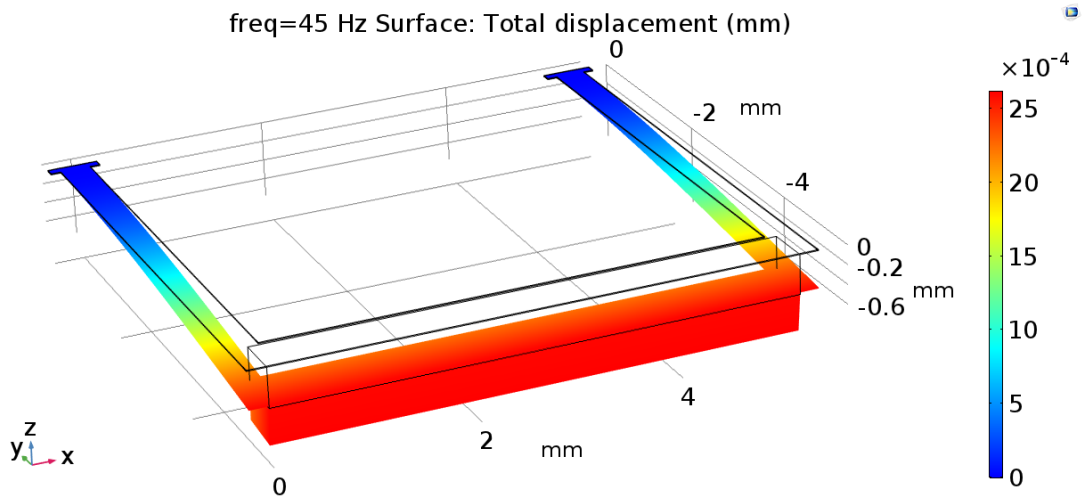
freq=45 Hz Surface: Total displacement (mm)
×10-4
25
20
15
10
5
0
0
-2
-4
mm
0
-0.2
-0.6
mm
0
2
4
mm
z
y
x

(a)

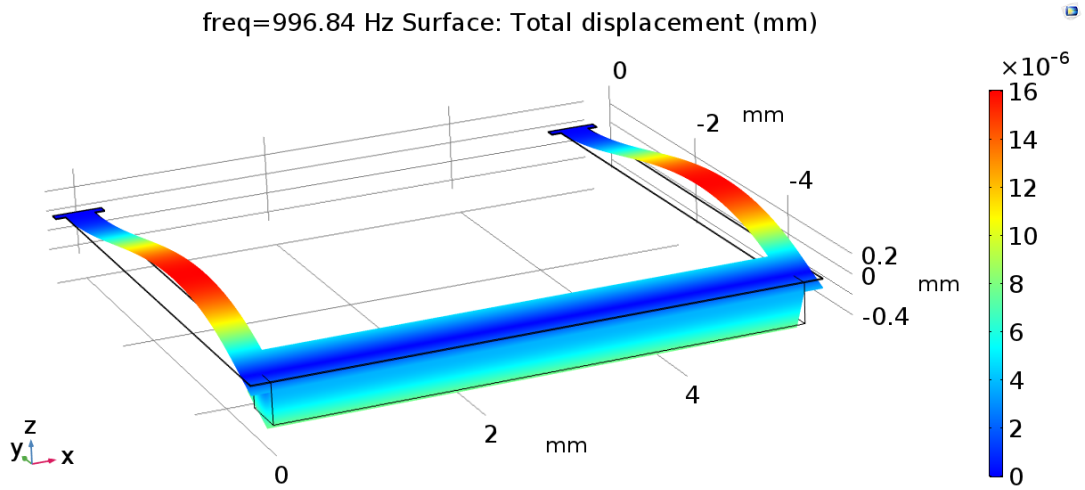
freq=996.84 Hz Surface: Total displacement (mm)
×10-6
16
14
12
10
8
6
4
2
0
0
-2
-4
mm
0.2
0
-0.4
mm
0
2
4
mm
z
y
x

(b)

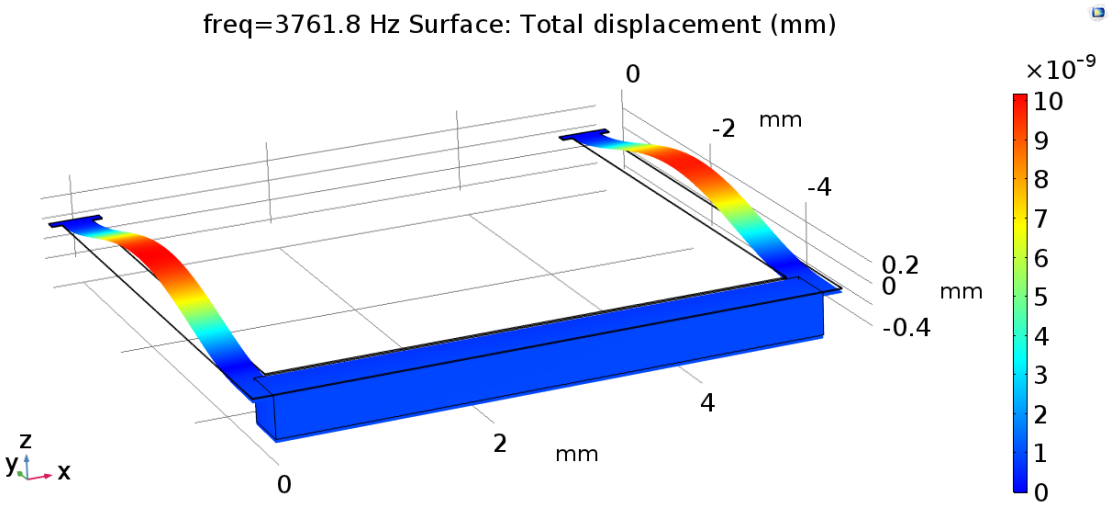
freq=3761.8 Hz Surface: Total displacement (mm)
×10-9
10
9
8
7
6
5
4
3
2
1
0
0
-2
-4
mm
0.2
0
-0.4
mm
0
2
4
mm
z
y
x

(c)

Fig. 3.37: The cantilever tip displacement in "Long" U-shaped beam cantilever: (a) At f_1 = 45 Hz; (b) At f_3 = 996 Hz; (c) At f_5 = 3.76 kHz.

As can be noted in Figs. 3.37a-b-c the displacement is maximum at frequency f_1 (~ 2.5 µm) in correspondence with the cantilever tip, whereas it is prevalent in the central section for the other frequencies; a displacement range of [10 n - 2.5 µ] m has been estimated. As regards the von Mises stress, it is proposed in Figs. 3.38a-b-c for each frequency and it has been evaluated in the range [14 – 500k] N/m^2, that is below the limit imposed by technology; as a consequence, the structure should easily resist release.

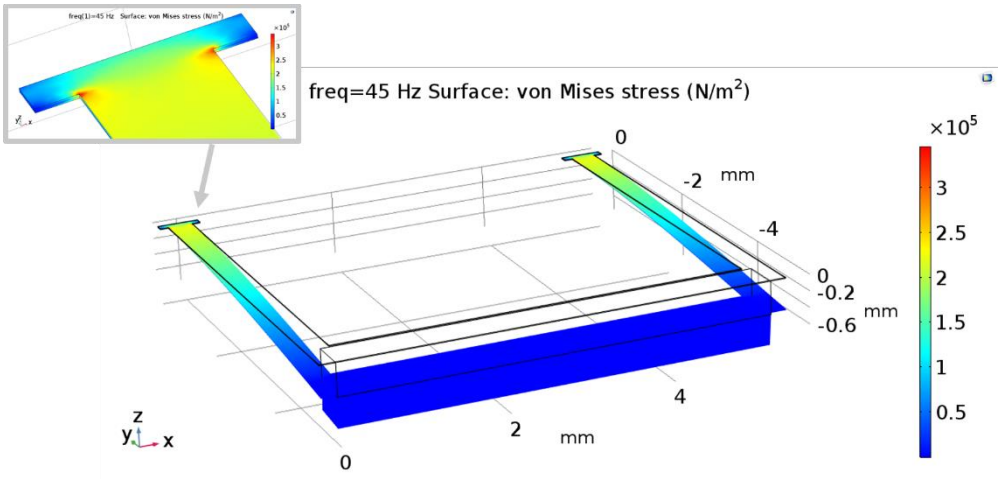

(a)

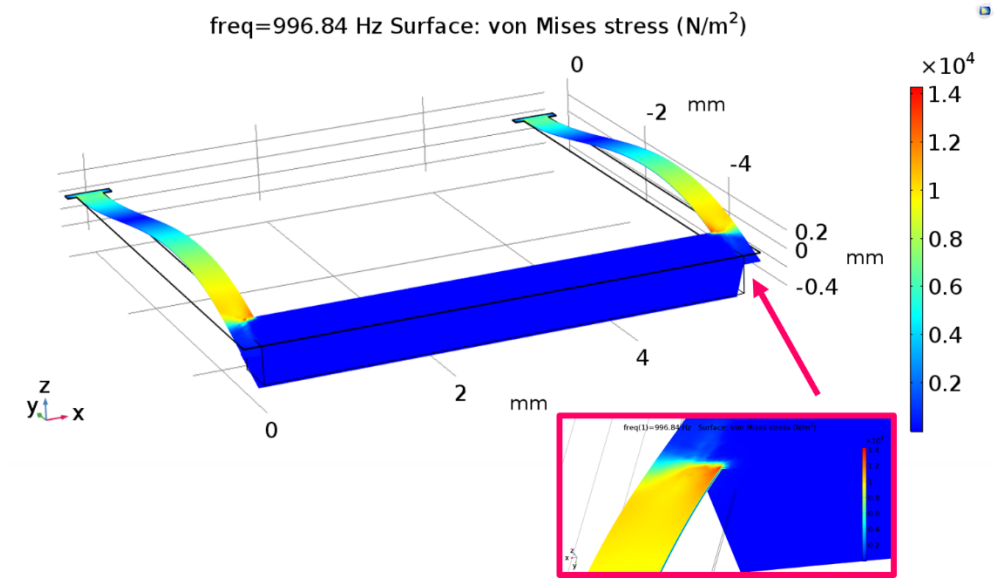

(b)

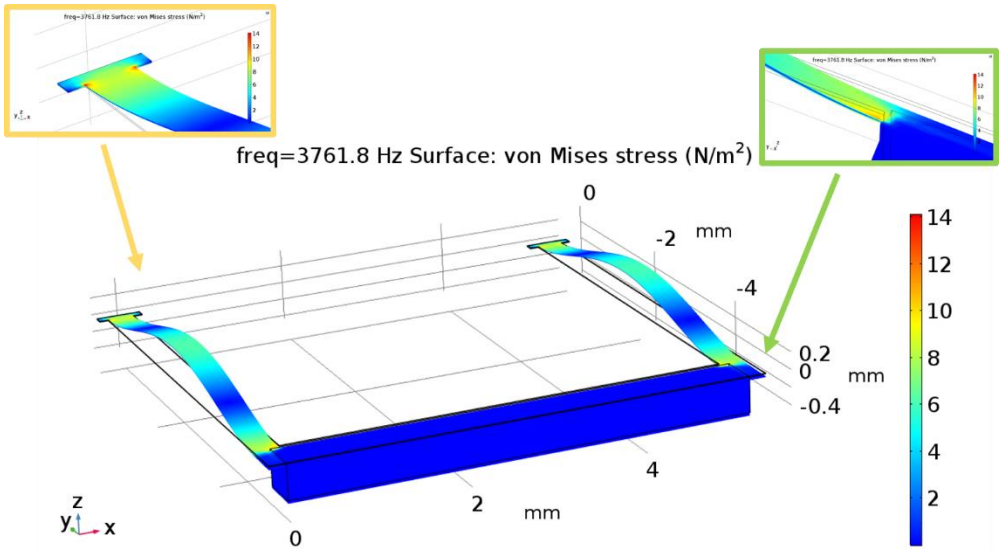

(c)

Fig. 3.38: The von Mises stress in "Long" U-shaped beam cantilever: (a) At f_1 = 45 Hz; (b) At f_3 = 996 Hz; (c) At f_5 = 3.76 kHz.

3.2.2.2 Medium Structure

An identical investigation has been carried out on a medium structure of U-shaped beam cantilever in order to predict the natural frequency and to understand the feasibility of the structure. It is presented in Fig. 3.39 and all geometrical parameters are listed in Table 12.

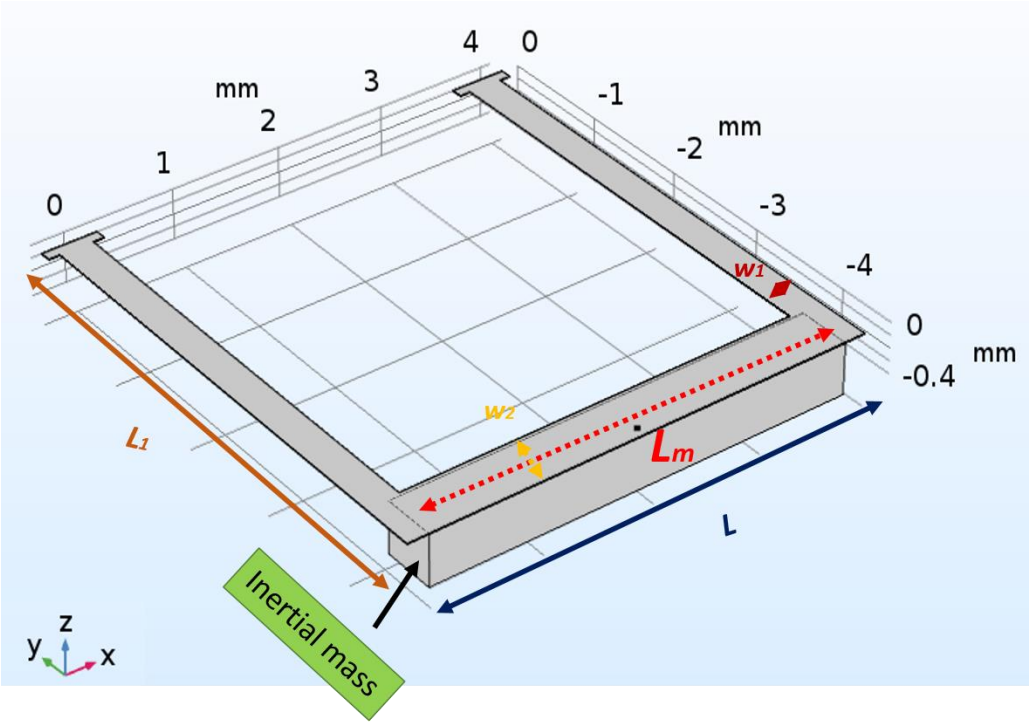

Fig. 3.39: Geometry of "Medium" U-shaped beam cantilever in COMSOL Multiphysics.

"Medium" U-shaped beam cantilever	
w_1	300 µm
w_2	500 µm
L_m	3820 µm
L	4200 µm

L_1	4540 µm

Table 12: List of geometrical parameters related to the "Medium" U-shaped beam cantilever.

A suitable mesh has been accomplished (see Fig. 3.39a) and especially it has been tightened in correspondence with the critical points which are the corners, as depicted in Fig. 3.39b.

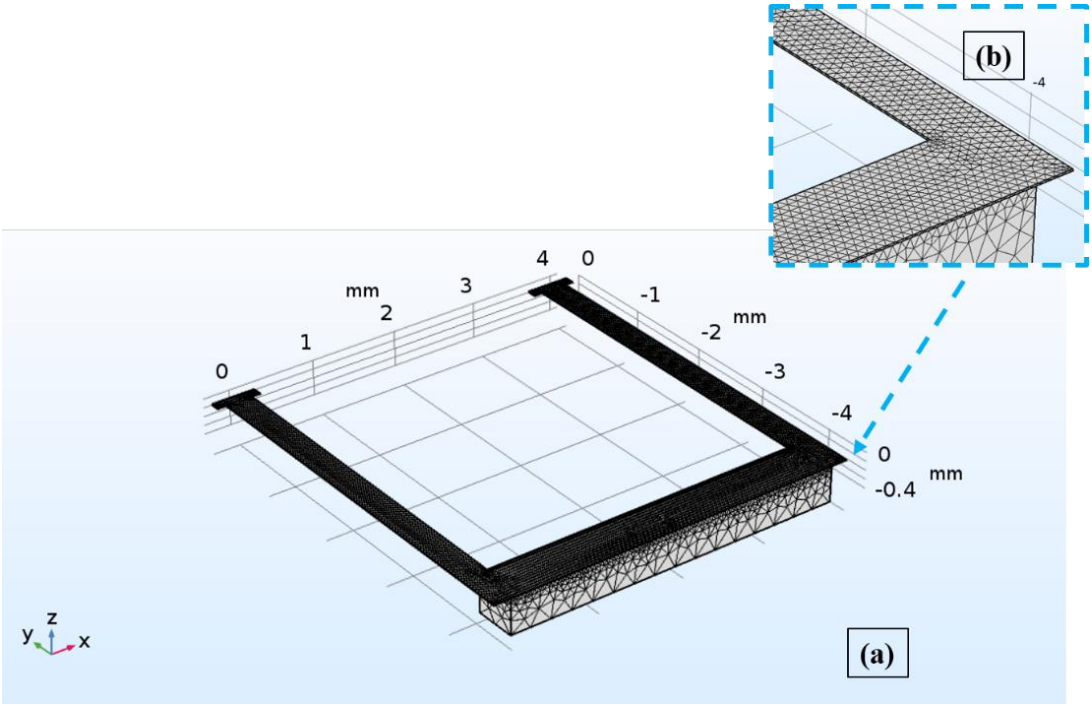

Fig. 3.40: Mesh in COMSOL Multiphysics for "Medium" U-shaped: (a) Designed geometry; (b) Focus on critical points.

The total geometry has been split into two domains in order to optimize the computational calculation: the first includes the three layers composing the U-shaped structure and the second one is related only to the inertial mass. The mesh implementation has been dense along the layers (in this case a fitted mesh has been considered), whereas it has been approximated in

correspondence with the inertial mass (in this case a normal mesh has been imposed). In detail, a free mesh has been chosen and it consists of 45100 elements of which the tetrahedral (tets) mesh elements are 30248, the triangular mesh elements are 13412, the mesh edges are 1399 and, eventually, the mesh vertices are 41. At first, an analysis in frequency domain has been implemented in order to estimate the natural frequency: as can be observed in Fig. 3.41 the cantilever tip displacement as a function of the frequency allowed to estimate a natural frequency ~ 66.4 Hz. It is essential to specify that the analysis in frequency domain has been carried out adopting a Lorentz force, having an amplitude of 100 nN, applied to the cantilever tip in z-direction.

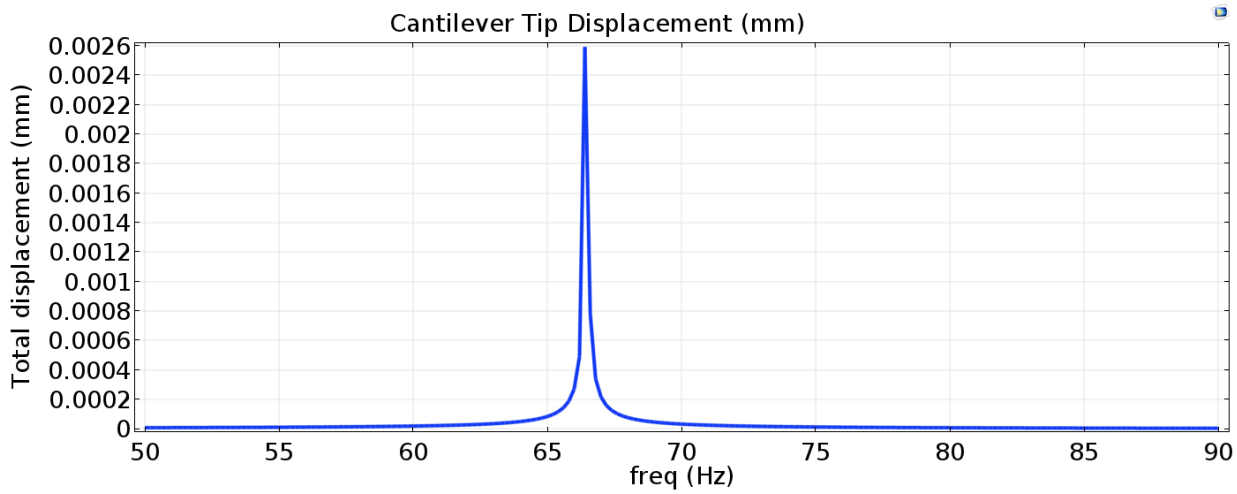

Fig. 3.41: Displacement as a function of the frequency in "Medium" U-shaped beam cantilever.

Again, an eigen frequency analysis has been examined in order to evaluate the oscillation modes with particular attention to the first, third and fifth modes; in addition, for each value of frequency the displacement and the von Mises stress, expressed in [m] and in [N/m^2] respectively, have been plotted. The eigen frequency analysis has returned the following frequencies: f_1 = 66.4 Hz

for the first mode, f_3 = 1.28 kHz for the third mode and at last f_5 = 5.24 kHz for the fifth mode. In detail, in Figs. 3.37a-b-c the displacements at each frequency are illustrated:

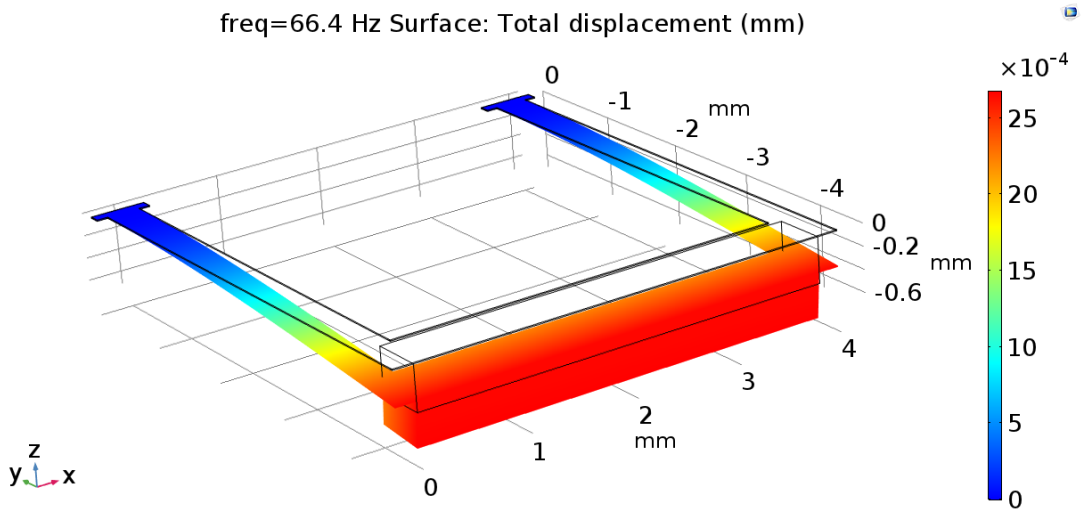

(a)

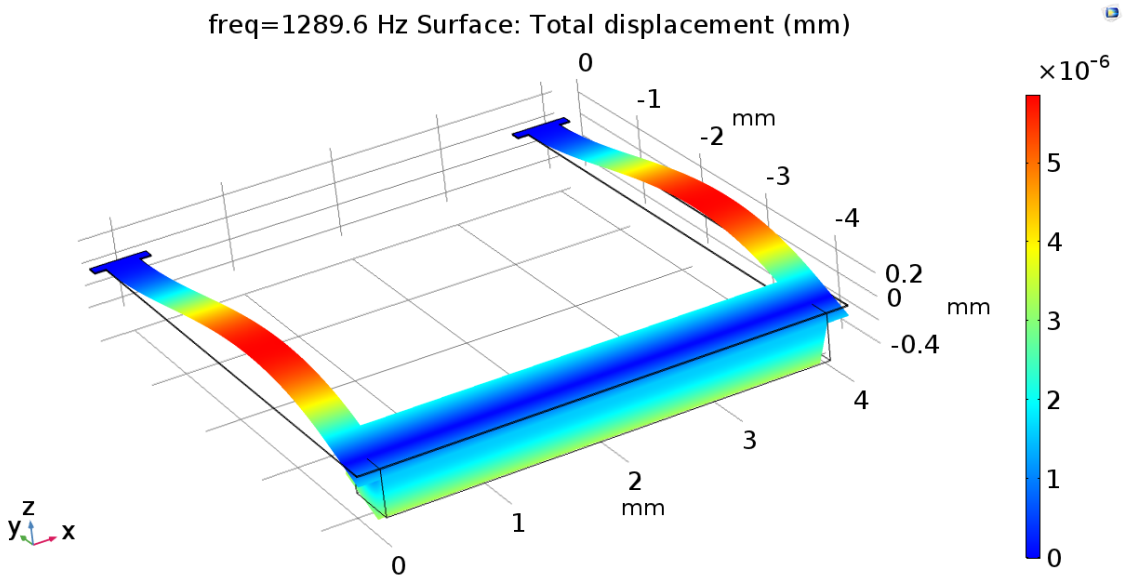

(b)

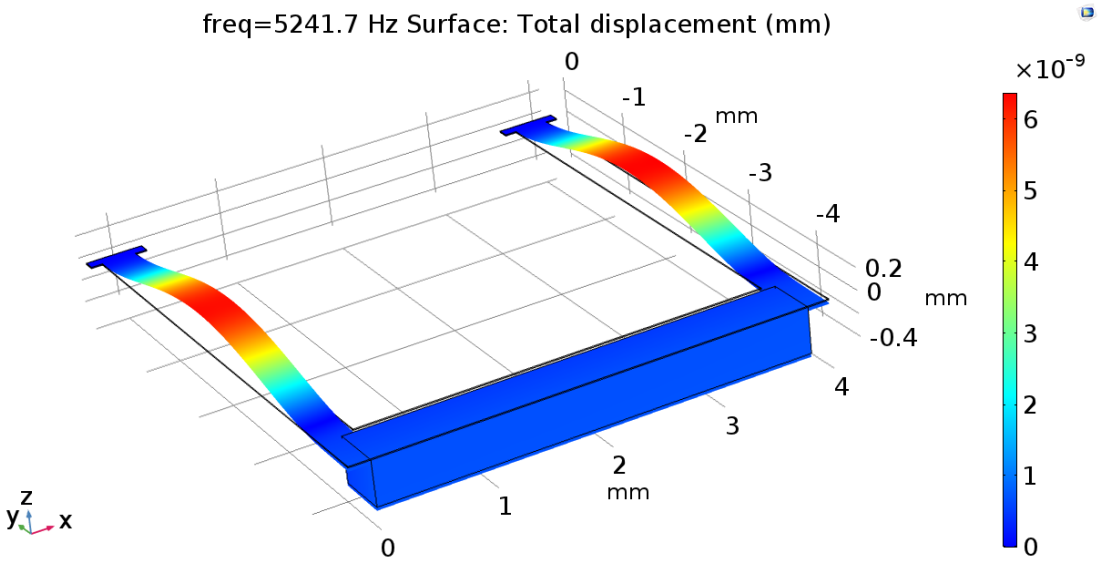

(c)

Fig. 3.42: The cantilever tip displacement in "Medium" U-shaped beam cantilever: (a) At f_1 = 66.4 Hz; (b) At f_3 = 1.28 kHz; (c) At f_5 = 5.24 kHz.

As can be observed in Figs. 3.42a-b-c the displacement is maximum at frequency f_1 (~ 2.5 μm) in correspondence with the cantilever tip, whereas it is prevalent in the central section for the other frequencies; a displacement range of [6 p - 2.5 μ] m has been estimated. As concerns the von Mises stress, it is proposed in Figs. 3.43a-b-c for each frequency and it has been evaluated in the range [12 – 450k] N/m^2, that is below the limit imposed by technology; as a consequence, the structure should easily resist release.

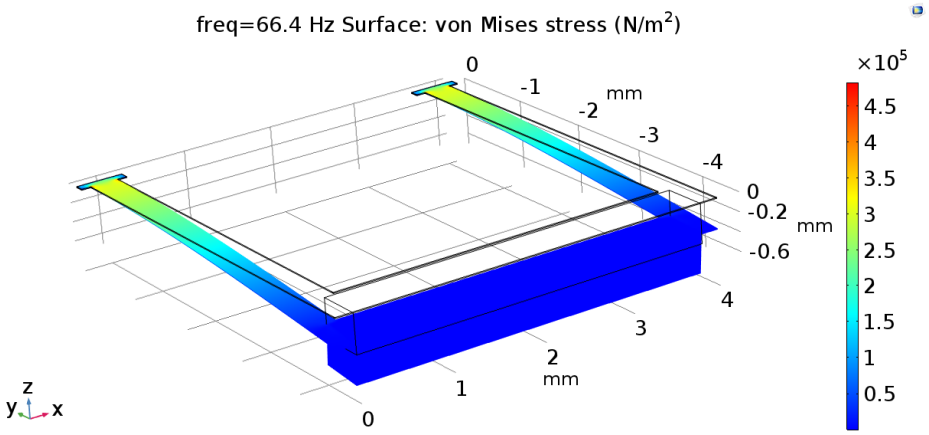
freq=66.4 Hz Surface: von Mises stress (N/m²)
×10⁵
4.5
4
3.5
3
2.5
2
1.5
1
0.5
mm
0
-1
-2
-3
-4
0
-0.2
-0.6
4
3
2
1
0
z
y
x

(a)

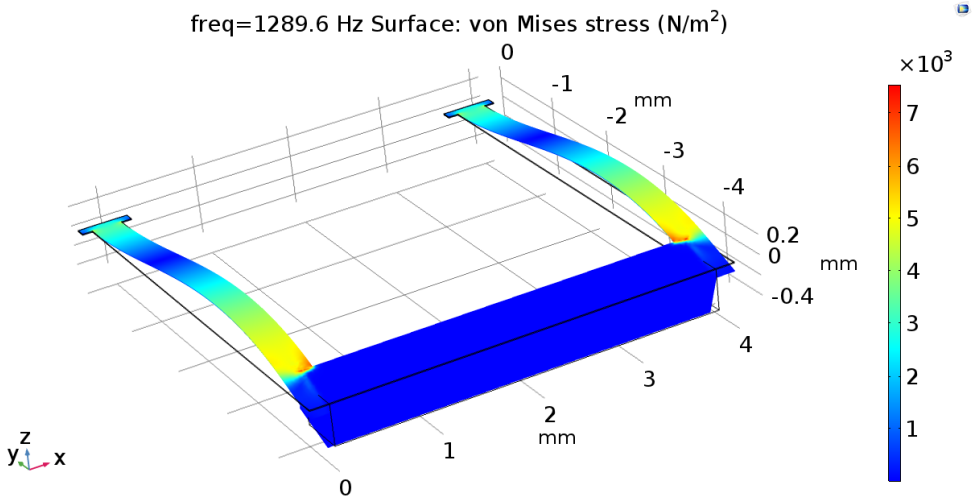
freq=1289.6 Hz Surface: von Mises stress (N/m²)
×10³
7
6
5
4
3
2
1
mm
0
-1
-2
-3
-4
0.2
0
-0.4
4
3
2
1
0
z
y
x

(b)

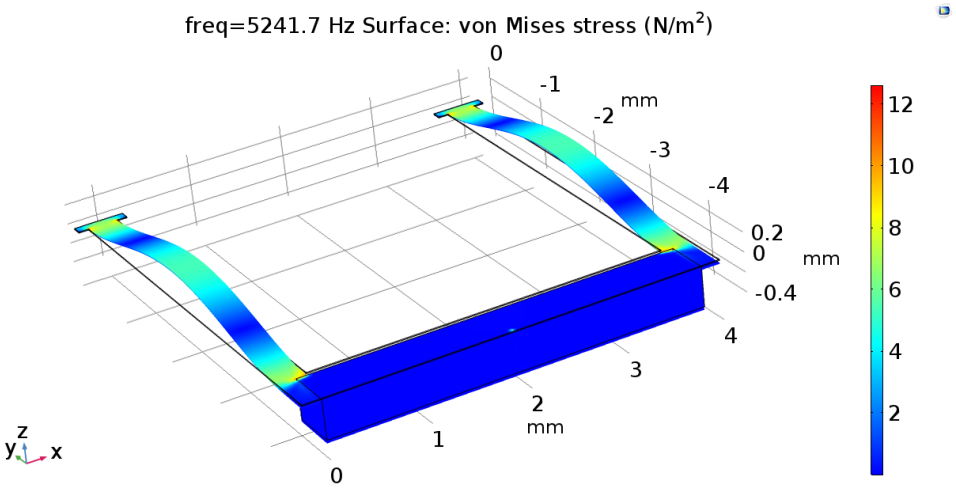
freq=5241.7 Hz Surface: von Mises stress (N/m²)
12
10
8
6
4
2
mm
0
-1
-2
-3
-4
0.2
0
-0.4
4
3
2
1
0
z
y
x

(c)

Fig. 3.43: The von Mises stress in "Medium" U-shaped beam cantilever: (a) At f_1 = 66.4 Hz; (b) At f_3 = 1.28 kHz; (c) At f_5 = 5.24 kHz.

3.2.2.3 Short Structure

As last examination, a "Short" U-shaped beam cantilever has been analyzed using the FEM model in COMSOL Multiphysics. Its structure is presented in Fig. 3.44 and all geometrical parameters are listed in Table 13.

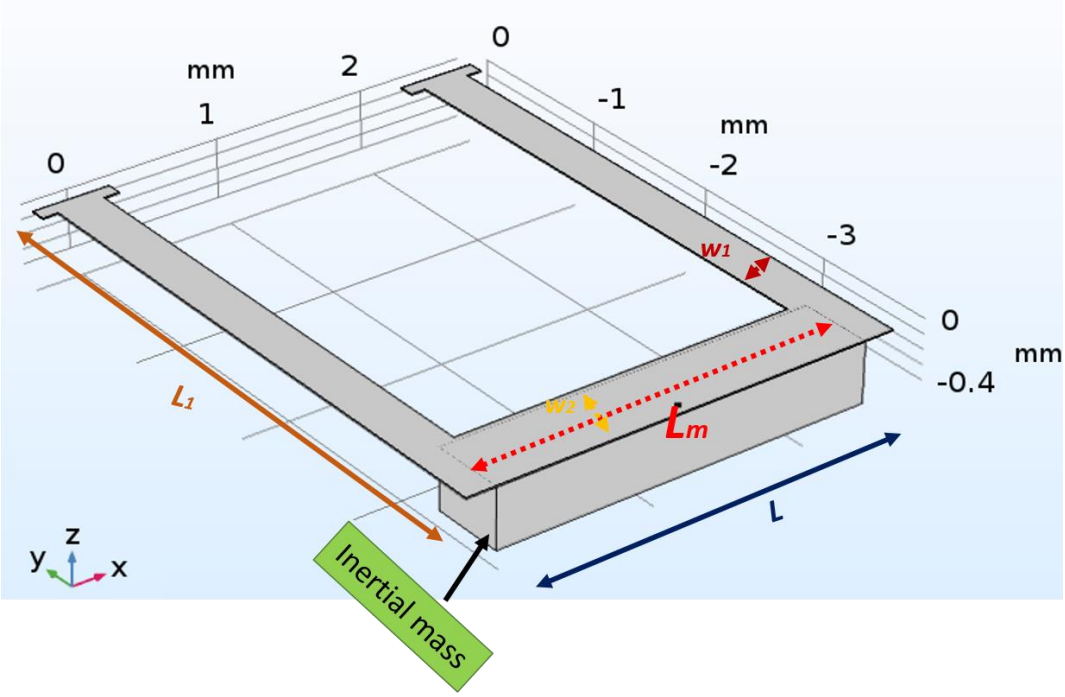

Fig. 3.44: Geometry of "Short" U-shaped beam cantilever in COMSOL Multiphysics.

"Short" U-shaped beam cantilever	
w_1	300 µm
w_2	500 µm

L_m	24200 µm
L	2800 µm
L_1	3810 µm

Table 13: List of geometrical parameters related to the "Short" U-shaped beam cantilever.

A proper mesh has been adopted (see Fig. 3.45a) and especially it has been tightened in correspondence with the critical points which are the corners, as depicted in Fig. 3.45b.

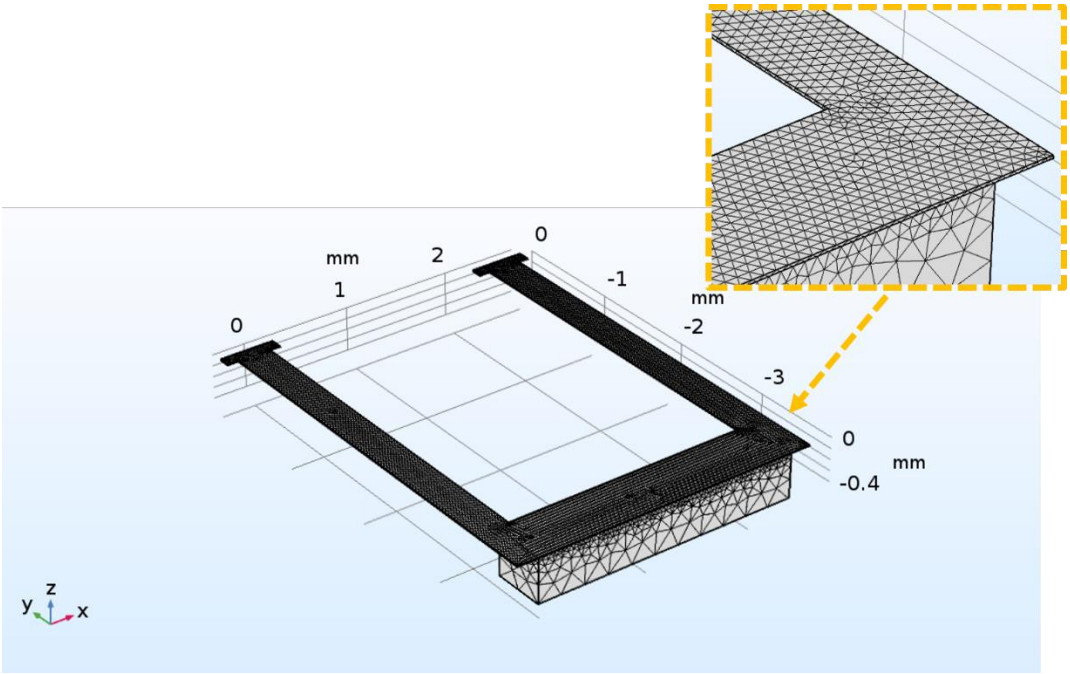

Fig. 3.45: Mesh in COMSOL Multiphysics for "Short" U-shaped: (a) Designed geometry; (b) Focus on critical points.

Also in this study case, the total geometry has been split into two domains in order to optimize the computational calculation: the first includes the three layers composing the U-shaped structure and the second one is related only to the inertial mass. The construction of the mesh

has been dense along the layers (in this case a fitted mesh has been considered), whereas it has been approximated in correspondence with the inertial mass (in this case a normal mesh has been imposed). In detail, a free mesh has been chosen and it consists of 45172 elements of which the tetrahedral (tets) mesh elements are 30388, the triangular mesh elements are 13461, the mesh edges are 1282 and, eventually, the mesh vertices are 41. At first, an analysis in frequency domain has been implemented in order to estimate the natural frequency: as can be noted in Fig. 3.46 the cantilever tip displacement as a function of the frequency allowed to estimate a natural frequency ~ 110 Hz. It is essential to clarify that the analysis in frequency domain has been carried out adopting a Lorentz force, having an amplitude of 100 nN, applied to the cantilever tip in z-direction.

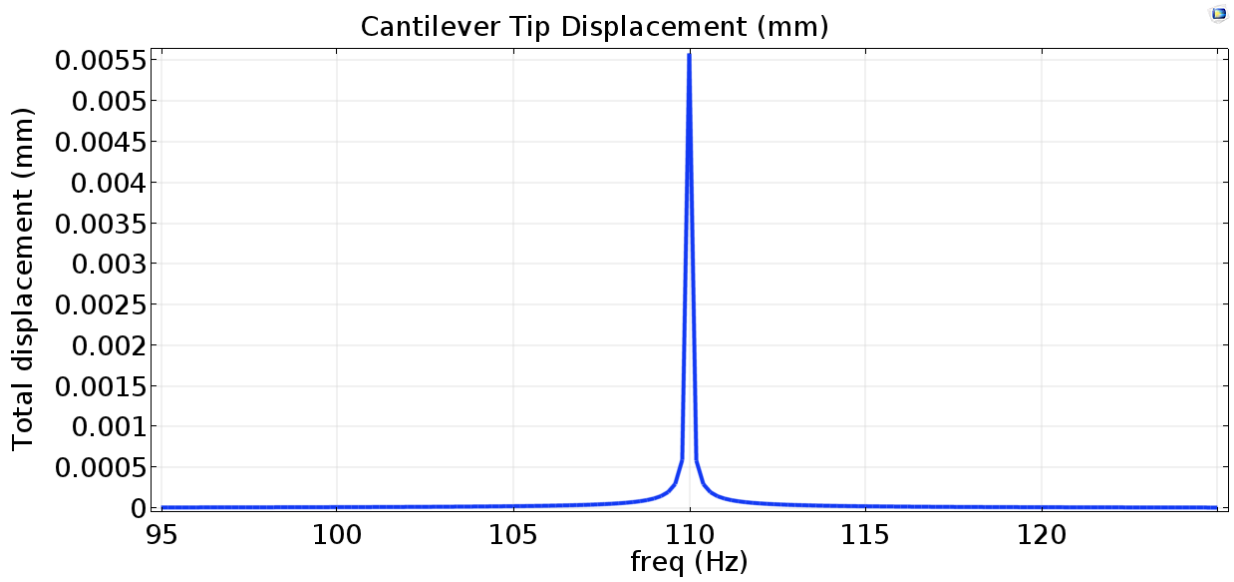

Fig. 3.46: Displacement as a function of the frequency in “Short” U-shaped beam cantilever.

Furthermore, an eigen frequency analysis has been examined in order to evaluate the oscillation modes with particular attention to the first, third and fifth modes; in addition, for each value of frequency the displacement and the von Mises stress, expressed in [m] and in [N/m^2]

respectively, have been plotted. The eigen frequency analysis has returned the following frequencies: $f_1 = 110$ Hz for the first mode, $f_3 = 1.82$ kHz for the third mode and at last $f_5 = 7.81$ kHz for the fifth mode. In detail, in Figs. 3.47a-b-c the displacements at each frequency are illustrated:

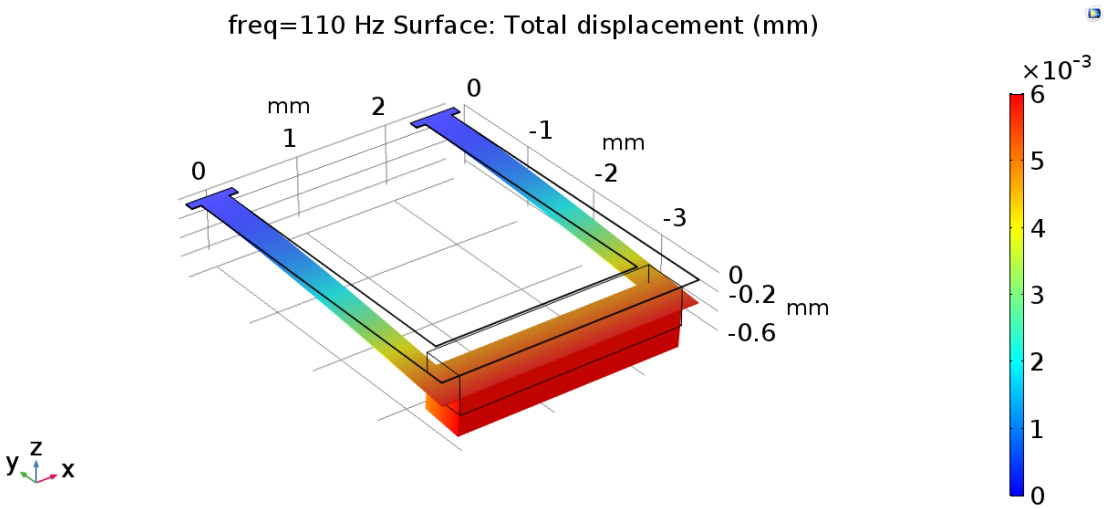

(a)

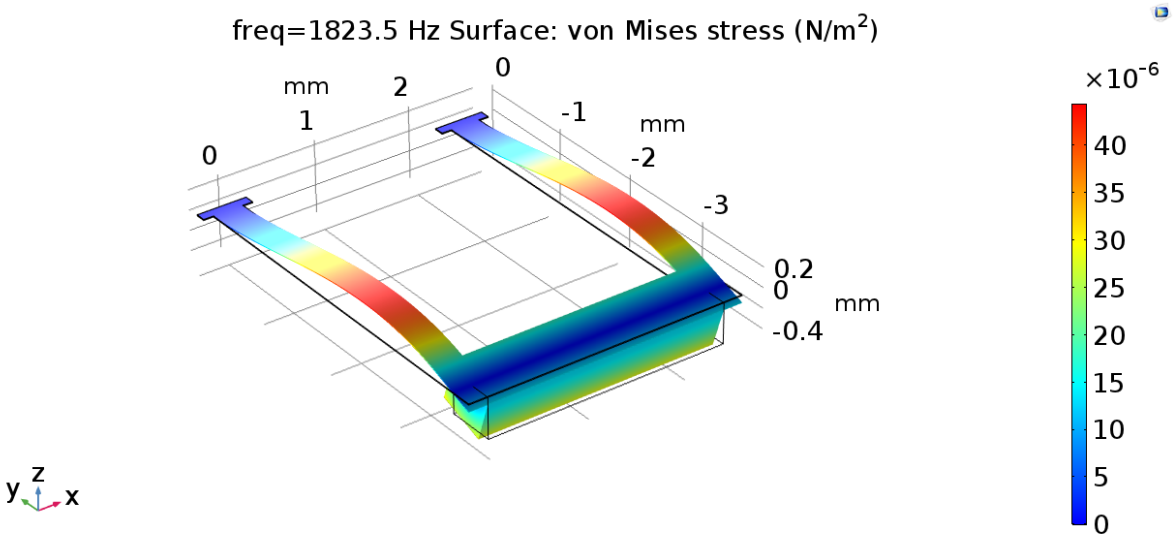

(b)

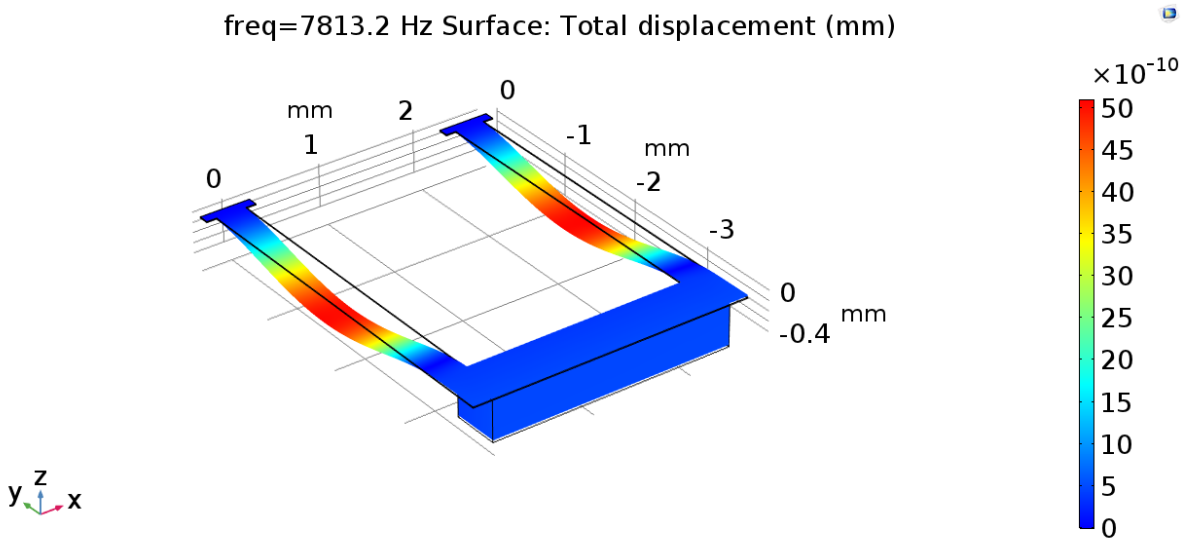

(c)

Fig.3.47: The cantilever tip displacement in "Short" U-shaped beam cantilever: (a) At f_1 = 110 Hz; (b) At f_3 = 1.82 kHz; (c) At f_5 = 7.81 kHz.

It is intriguing to note that the displacement is always maximum on the cantilever tip at the frequency f_1 (~ 6 μm), whereas it is prevalent in the central section for the other frequencies; a displacement range of [5 p - 6 μ] m has been estimated. In relation to the von Mises stress, it is proposed in Figs. 3.48a-b-c for each frequency and it has been evaluated in the range [12 – 450k] N/m^2, that is below the limit imposed by technology; thus, as a consequence, the structure should easily resist release.

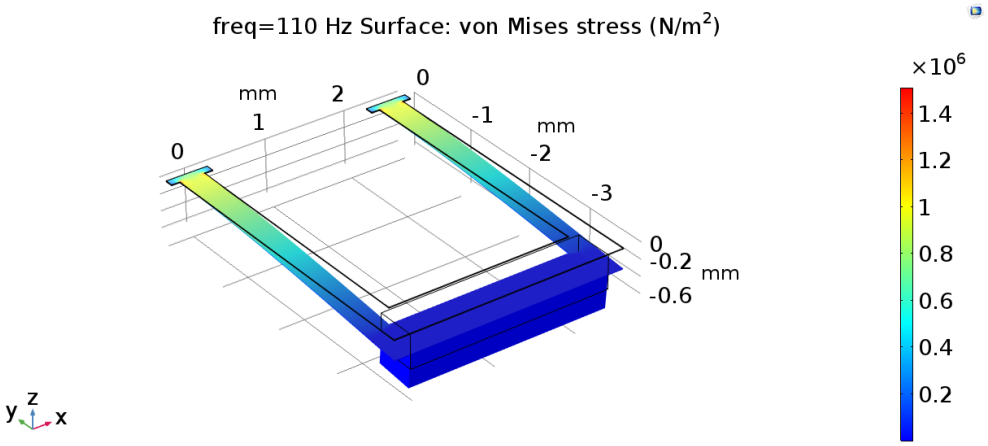
freq=110 Hz Surface: von Mises stress (N/m²)
×10⁶
1.4
1.2
1
0.8
0.6
0.4
0.2
mm
0
1
2
-1
-2
-3
-0.2
-0.6
y z x

(a)

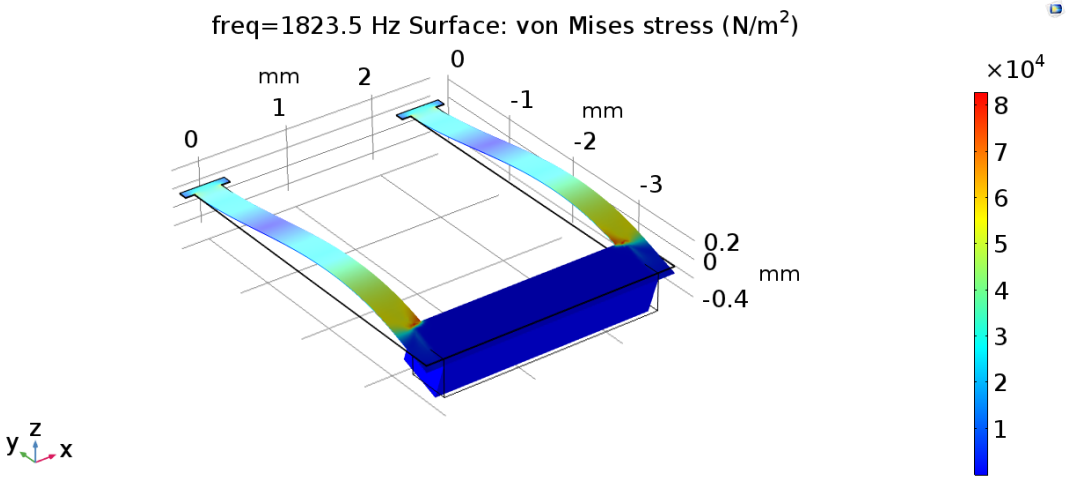
freq=1823.5 Hz Surface: von Mises stress (N/m²)
×10⁴
8
7
6
5
4
3
2
1
mm
0
1
2
-1
-2
-3
0.2
-0.4
y z x

(b)

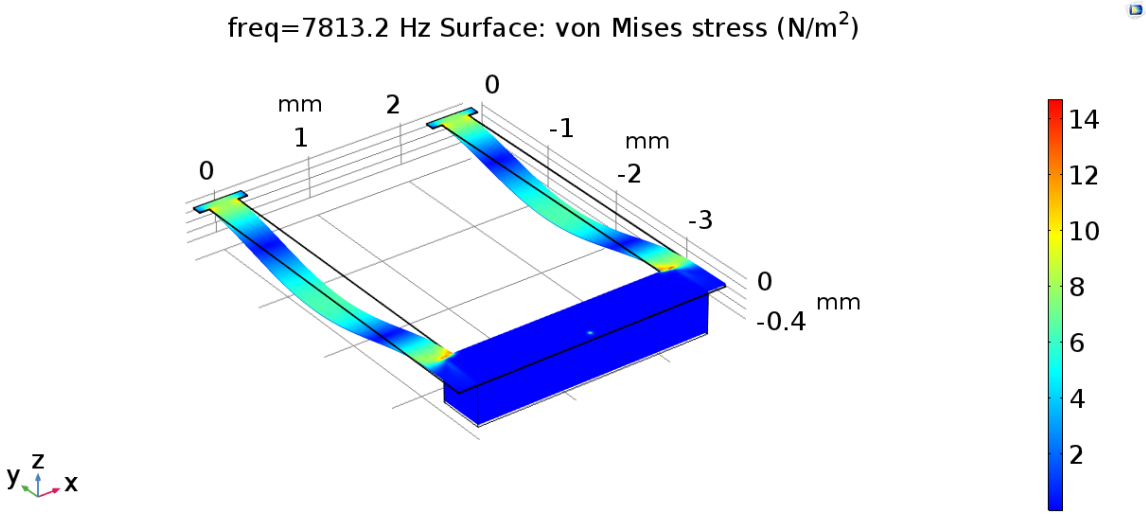
freq=7813.2 Hz Surface: von Mises stress (N/m²)
14
12
10
8
6
4
2
mm
0
1
2
-1
-2
-3
-0.4
y z x

(c)

Fig. 3.48: The von Mises stress in "Short" U-shaped beam cantilever: (a) At f_1 = 110 Hz; (b) At f_3 = 1.82 kHz; (c) At f_5 = 7.81 kHz.

3.3 Layout and design through MEMSPro CAD

Two designs have been implemented applying a suitable CAD, MEMSPro, in which the specifications inherent to the masks utilized in the PiezoMUMPs technology [92] have been inserted. Just to cite, in this process a SOI (Silicon On Insulator) wafer is used as substrate with specific characteristics in terms of thickness. After having doped the top surface of the Si layer and grown a thermal oxide with a thickness of 200 nm, a piezoelectric layer in Aluminum Nitride (AlN) of 0.5 μm is deposited. At last a metal stack composed of 20 nm chrome and 1000 nm aluminum is set down. The etching process is performed with Deep RIE (Reactive Ion Etch). In detail, five mask levels have been used:

- SOI
- PZFILM
- PADMETAL
- PADOXIDE
- TRENCH

The SOI mask defines the Silicon On Insulator pattern, where both the suspended structure and the bulk are designed. It is important to underline that the "white" sections indicate the removal of the thin Silicon, leaving the oxide layer SiO_2 uncovered. The PZFILM mask depicts the piezoelectric layer, AlN, that is deposed on whole microelectromechanical structure. Next step is represented by PADMETAL mask which delineates the metallic contact in aluminum (Al), essential to drive the current into the MEMS device; in addition, the aluminum pads are needed to carry inside and outside the device electric signals, or even to fix the potential on a specific

layer, such as the voltage on Silicon bulk. The PADOXIDE mask is used to isolate the AlN piezoelectric stack in order to measure an electric signal; for this reason, it is placed on the constraints. Finally, the TRENCH mask is utilized to define the areas that must be released, digging the thick Silicon from bottom; in other terms all "blue" section, as shown below, identify the suspended structure. As previously mentioned, two designs, represented by a new meander architecture and a "classic" U-shaped beam cantilever, have been implemented in the same fabrication technology in order to compare the performance of both. In addition, the SOI frame has been provided by the MEMSCAP foundry due to the specific and strict die dimensions, that are 11.15 mm × 11.15 mm, although the active area is only 9.65 mm × 9.65 mm (see Fig. 3.49).

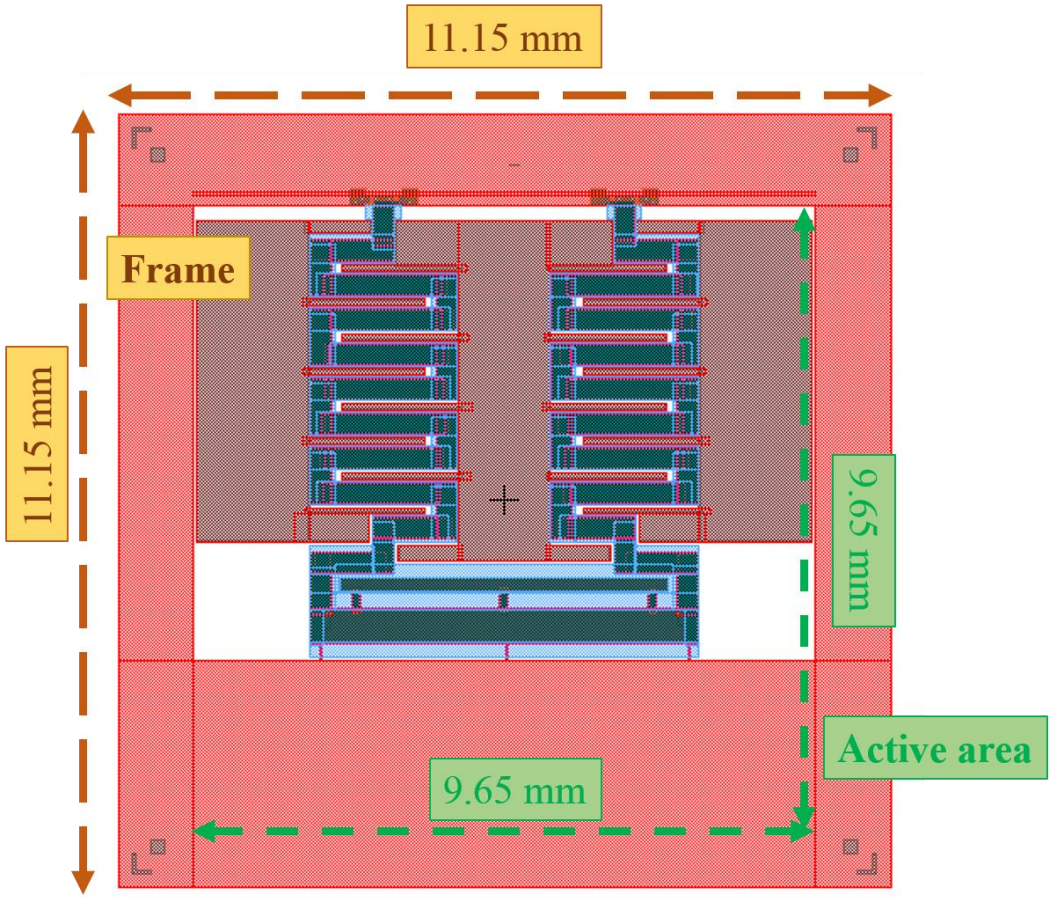

Fig. 3.49: Frame of the PiezoMUMPs process.

As concerns the meander architecture, it has been fulfilled respecting the same geometrical parameters listed in Table 10 in order to esteem that the residual stress is below the maximum limit; for this reason, refer to the previous paragraph to know its dimensions. The whole layout of the meander structure is shown in Fig. 3.50, where in violet four aluminum pads, that are necessary to set the Silicon bulk potential, are placed in the corners of the frame.

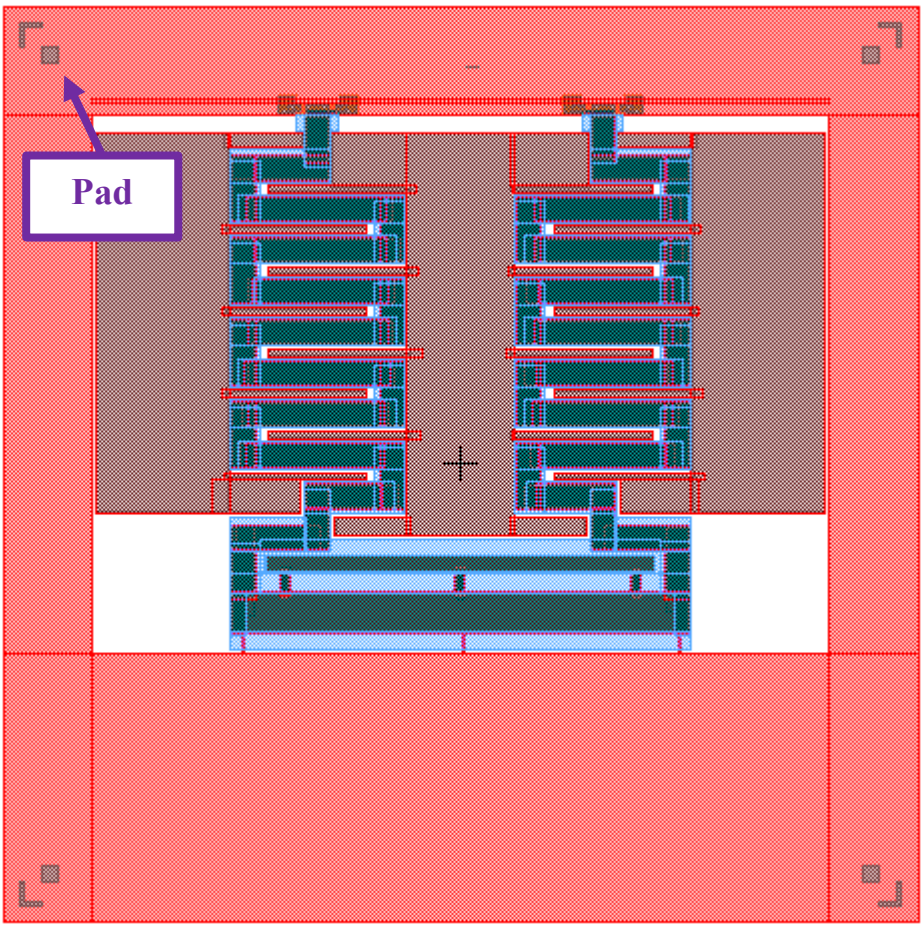

Fig. 3.50: Layout of meander architecture.

It is believed crucial to discuss the architecture without the TRENCH (the “blue” mask); for this reason, the same layout without the TRENCH is proposed in Fig. 3.51, where it is possible to notice a second inertial mass, that has been introduced in order to improve the sensitivity of the device and the presence of three electrodes having the interdigit shape.

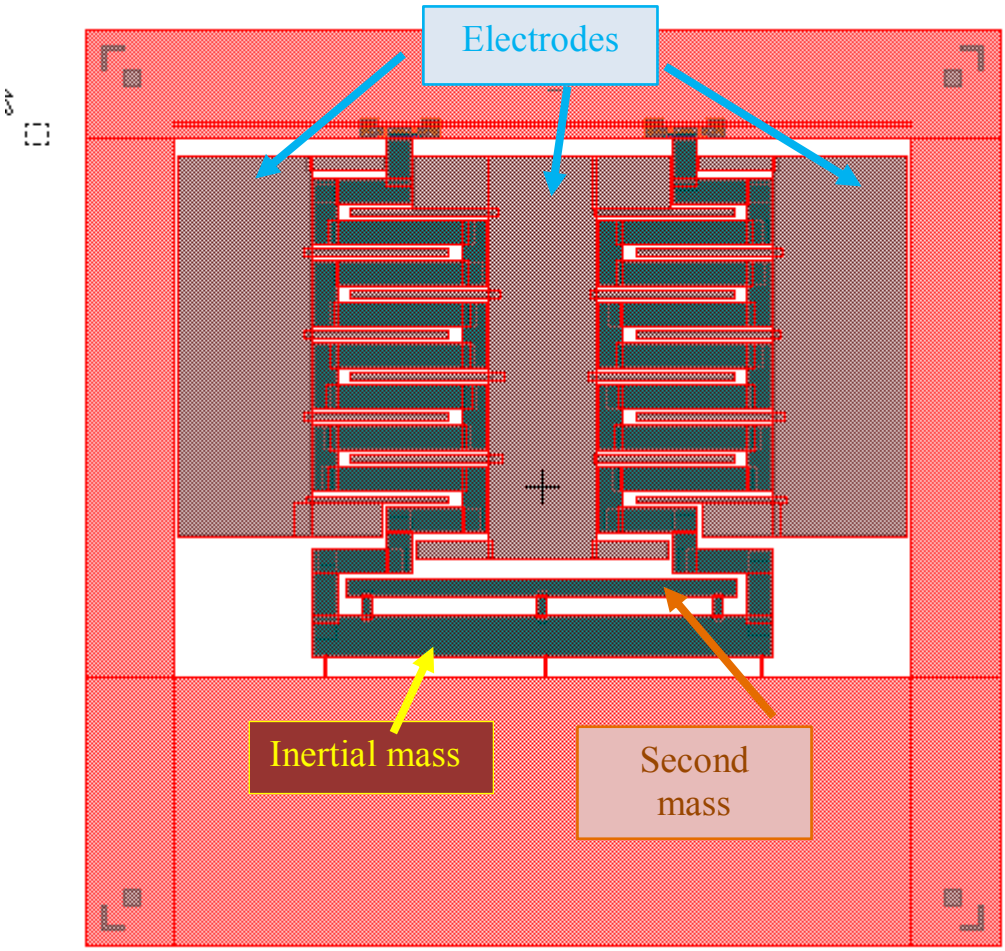

Fig. 3.51: Focus on meander architecture layout.

It is intriguing to highlight that the insertion of electrodes has been a pondered choice that led to a dual purpose: capacitive damping and capacitive readout. As regards the first aspect, the

existence of electrodes determines a capacitive coupling, in other terms a capacitance, between the interdigit and the meander: in the zero condition, when no Lorentz force is applied, a capacitance can be measured since the combination meander – interdigit is similar to a flat and parallel face capacitor; on the contrary, when the micromechanical structure is actuated by Lorentz force these distributed capacitances throughout the structure oppose the deflection of MEMS device, thus performing a damping function. As concerns the second point, the capacitive variation due to the deflection of the meander architecture during the actuation can be used to implement a capacitive readout strategy, capable of correlating the magnetic field to be measured with a capacitive variation. In this manner, two possible readout strategies have been developed in a unique die. As previously mentioned, the PADOXIDE mask is essential to avoid the short circuit of the piezoelectric layer, as shown in Fig. 3.52: two pads have been inserted just for convenience, in order to use one for the driving current and the other for the output voltage.

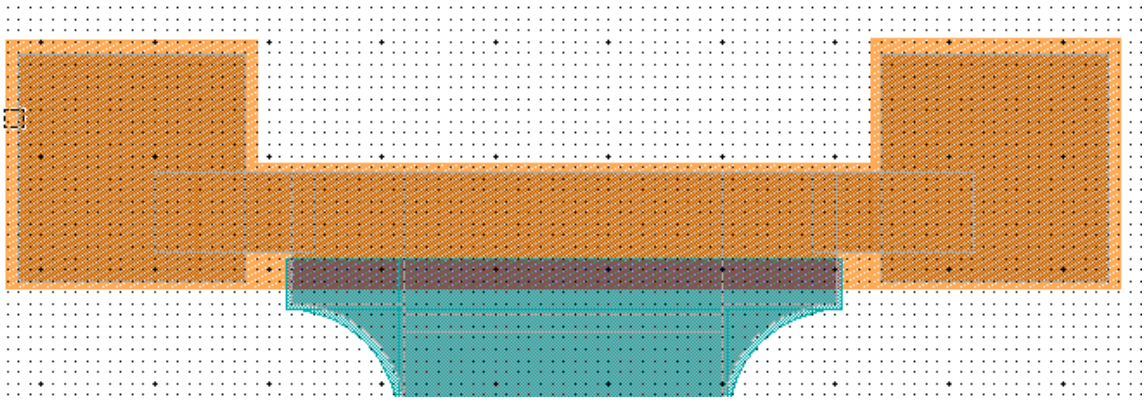

Fig. 3.52: Focus on PADOXIDE mask.

In addition, it is believed very important to pay attention to the TRENCH mask, which allows to dig the structure from bottom and to release it; for simplicity, in Figs. 3.52a-b only SOI (in pink)

and TRENCH (in blue) masks are presented: where the SOI mask is covered by the TRENCH mask the structure has been released and is composed of a layer of thin Silicon (10 μm), a layer of aluminum nitride (0.5 μm) an a layer of aluminum (1 μm). In Fig. 3.52b a detail about the inertial masses is displayed: they contain all layers, included the bulk, and for this reason the masses are removed by the TRENCH.

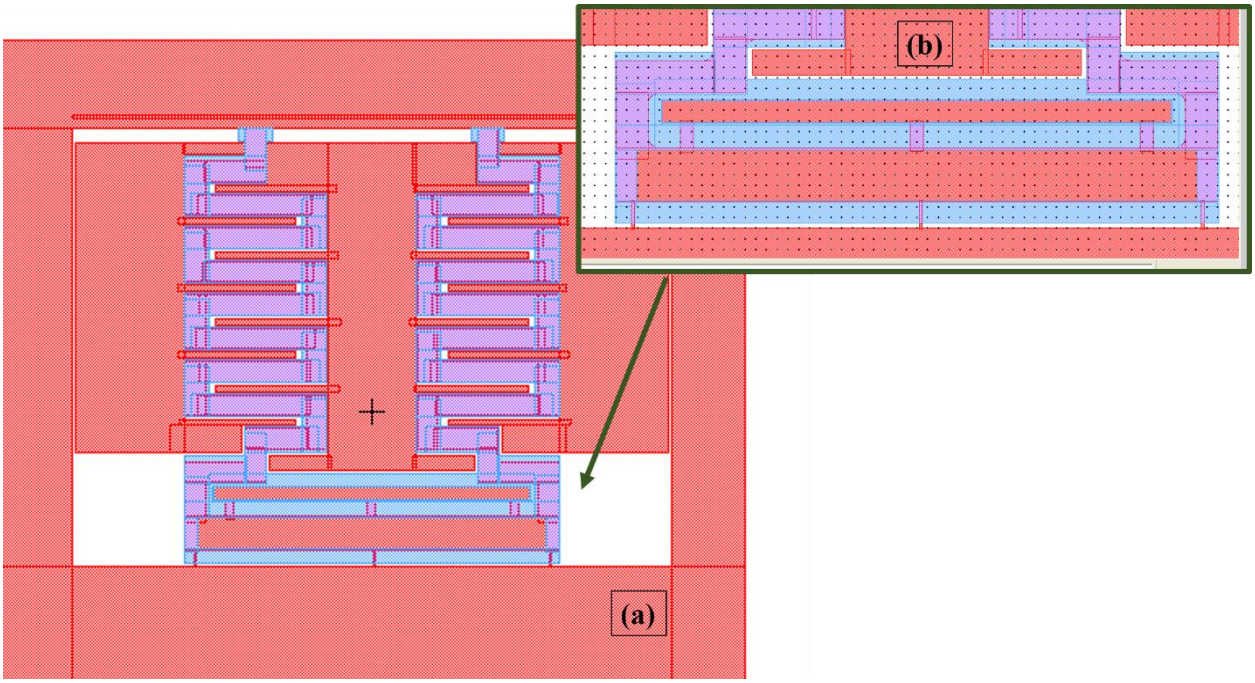

Fig. 3.53: Detail on TRENCH mask and inertial masses.

The second layout regarded the realization of a “classic” cantilever beam device: in particular, taking into the die dimensions and the active area it has been decided to implement three structures in a “matryoshka” configuration, as depicted in Fig. 3.54. Also in this design, the presence of external pads is mandatory to impose the potential to the Silicon bulk and the task performed by capacitive electrodes is again dual, in other words the capacitive damping and the capacitive readout have been inserted.

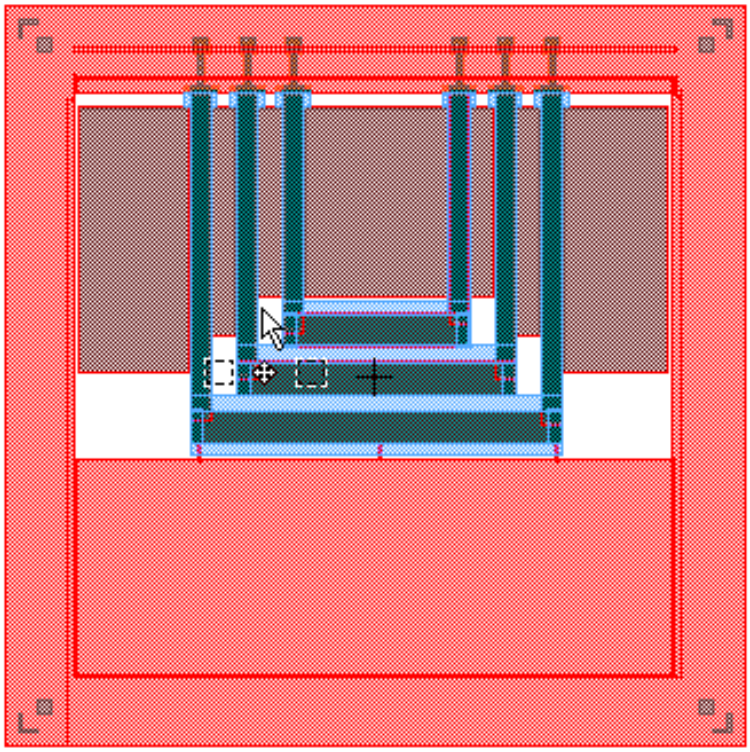

Fig. 3.54: Layout of "classic" U-shaped beam cantilever architecture.

As concerns the dimensions of single MEMS devices, they are exactly the same as described previously during the COMSOL Multiphysics analysis in order to esteem a residual stress that is below the maximum stress responsible of the structural failure; for this reason, refer to the previous paragraph to know their dimensions (Tables 11, 12 and 13). It is important to examine the architecture without the TRENCH (the "blue" mask); for this reason, the same layout without the TRENCH is proposed in Fig. 3.55, where it is possible to notice the presence of three inertial masses, which are 220 μm apart from each other, and the presence of numerous electrodes having the interdigit shape and exhibiting the identical double function.

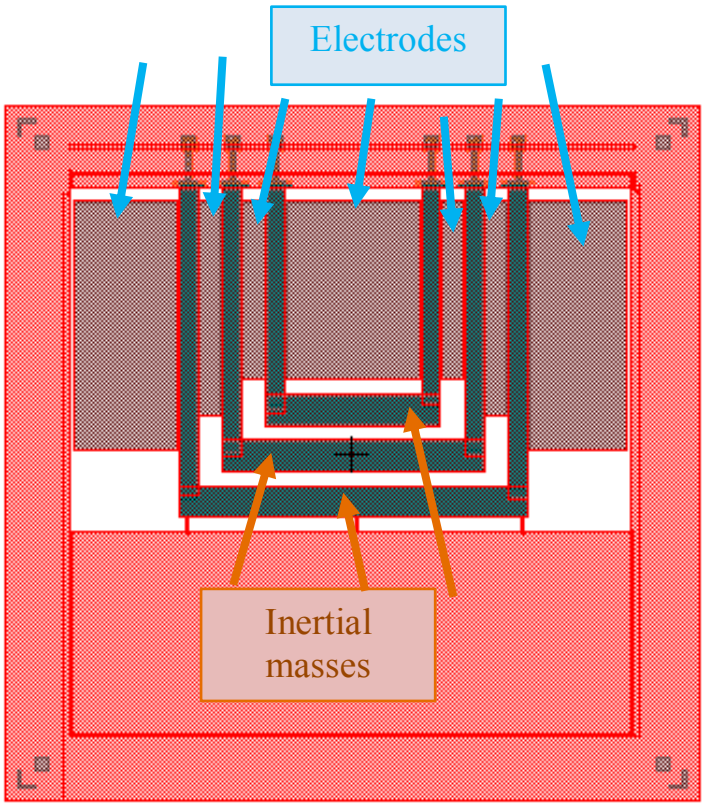

Fig. 3.55: Focus on “classic” U-shape beam cantilever layout.

As previously mentioned, the PADOXIDE mask is essential to avoid the short circuit of the piezoelectric layer, as shown in Fig. 3.56. In addition, it is believed very important to pay attention to the TRENCH mask, which allows to dig the structure from the bottom and to release it; just for completeness, in Fig. 3.57 a detail about the inertial masses is displayed: they contain all layers, included the bulk, and for this reason the masses are removed by the TRENCH.

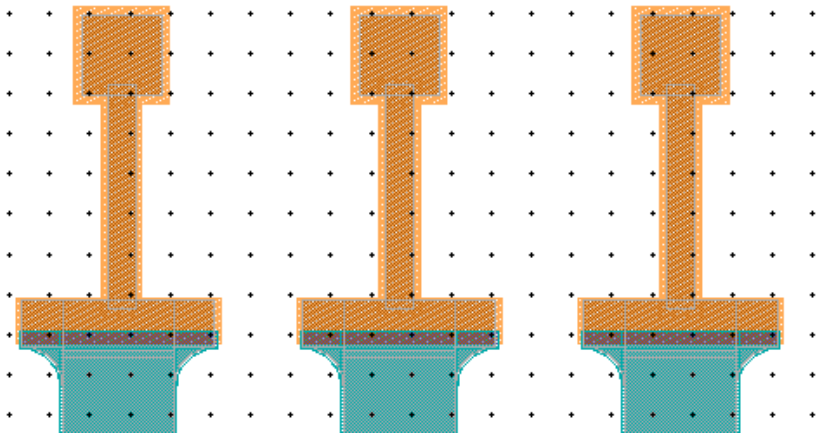

Fig. 3.56: Focus on PADOXIDE mask.

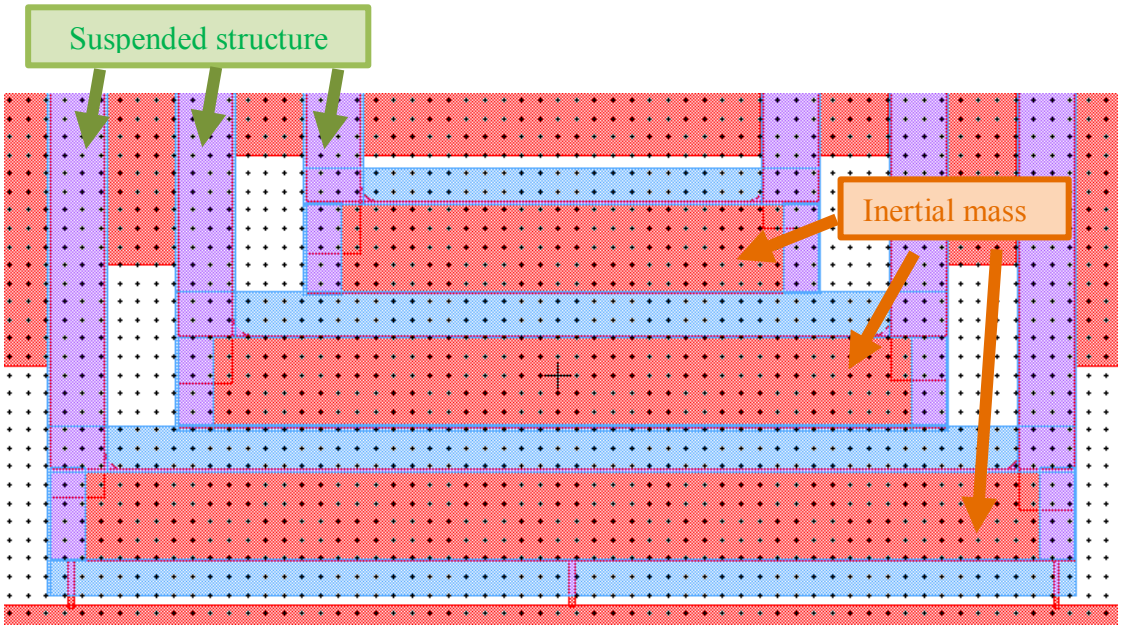

Fig. 3.57: Detail on TRENCH mask and inertial masses in “classic” U-shaped beam cantilever.

In conclusion, two layouts have been implemented in order to fabricate several prototypes of MEMS device. It is essential to specify that the realization of two designs required the respect of numerous layout rules that are not listed in this manuscript, nevertheless it is possible to appreciate them in reference [92].

3.4 Optimization of sensor design through a differential configuration

Afterwards, an optimization of the design in both architectures has been realized implementing a reduced version of the previous prototypes and a differential configuration. As regards the resized MEMS devices, their accomplishment has been dictated to the necessity to satisfy a warning suggested by the MEMSCAP foundry: it is not advisable to create structures whose length is greater than 5 mm in order to ensure a uniform deposition of the piezoelectric material. Since the second device run has been provided for using the PiezoMUMPs technology the identical frame and masks have been utilized and, as a consequence, in Fig. 3.58 the new reduced designs are shown.

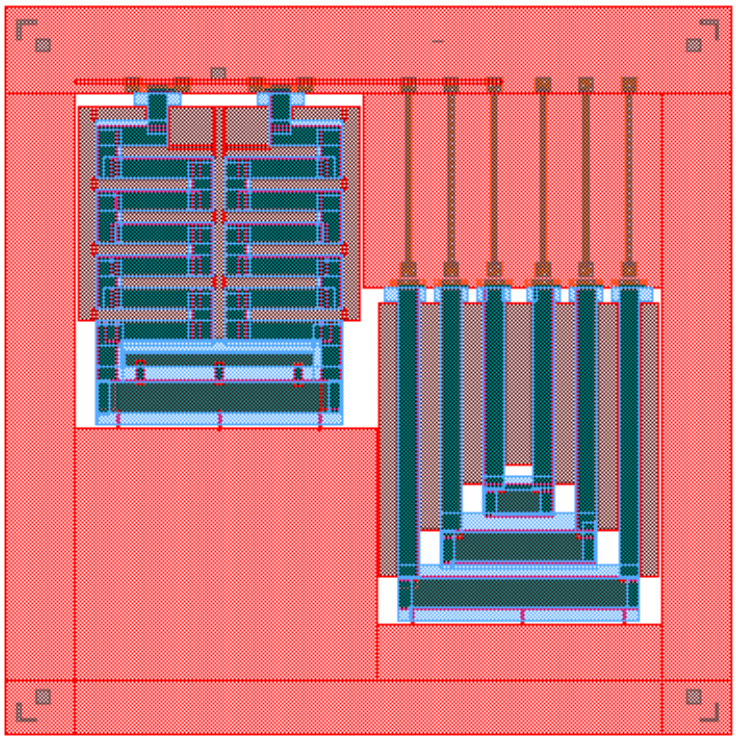

Fig. 3.58: Layout optimization: resized devices.

It is interesting to mention that two designs did not assemble on the same plane in order to save the robustness of the die due to the wide TRENCH area, that, anyway, does not violate the specification imposed by the technology [92], that is:

$$\text{Etched Area} < 35\ \text{mm}^2$$

In relation to the resized meander architecture, a focus is illustrated in Fig. 3.59, whereas all geometrical parameters are classified in Table 14.

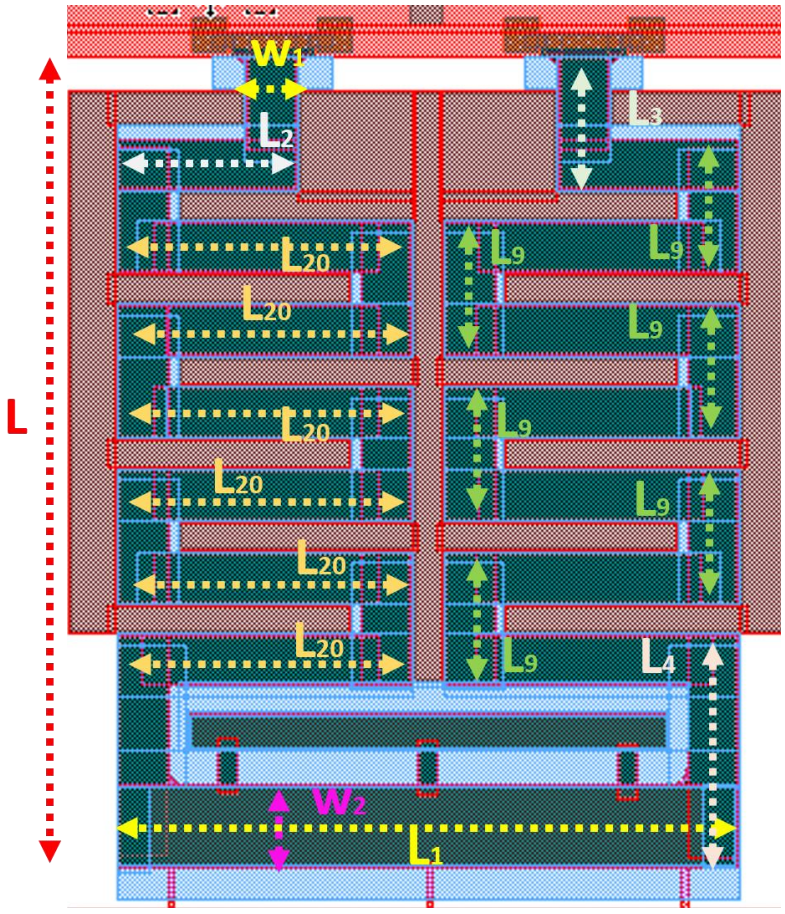

Fig. 3.59: Meander optimization: focus and geometrical parameters.

Optimized meander architecture	
w_1	300 μm
w_2	500 μm
L	5310 μm
L_1	3740 μm
L_2	1076 μm
L_3	800 μm
L_4	1810 μm
L_9	800 μm
L_{20}	1766 μm

Table 14: List of geometrical parameters related to the resized meander architecture.

Also in this case, the double readout strategy has been adopted, a second inertial mass has been introduced to improve the sensitivity and, finally, a double pad for each constraint has been used as in the "original" version. Related to the "classic" U-shaped beam cantilever other three layouts have been designed, as shown in Fig. 3.59 and in detail in Fig. 3.60; in particular, in this last picture a reference is presented about all geometrical quantities that, then, are listed in Table 15.

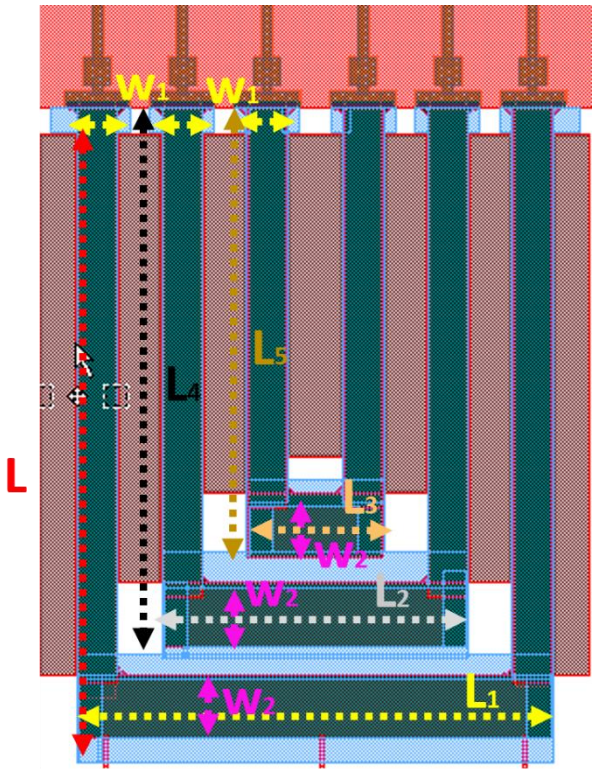

Fig. 3.60: Simple U-shaped beam cantilever optimization: focus and geometrical parameters.

Optimized simple U-shaped beam cantilever architecture	
w_1	300 µm
w_2	500 µm
L	4900 µm
L_1	3690 µm
L_2	2370 µm
L_3	1050 µm
L_4	4200 µm
L_5	3500 µm

Table 15. List of geometrical parameters related to the resized simple U-shaped architecture.

As regards the second layout, it is composed of two meander structures and two simple U-shaped beam cantilever structures in differential configuration. This configuration has been selected considering that anywhere the MEMS sensor is located it will be always influenced by the environmental noise, that is a white noise having a bandwidth around 400 Hz; as a consequence, regardless of the presence of an external magnetic field to be detected, the integrated device, that works at the resonance, will tend to deform due to the effect of an external force correlated to the environmental noise (F_{Noise}). For this reason, adopting a differential configuration allows to estimate the output voltage correlated to the noise as a common mode signal and thus deleting it (in Fig. 3.61 the differential strategy is illustrated).

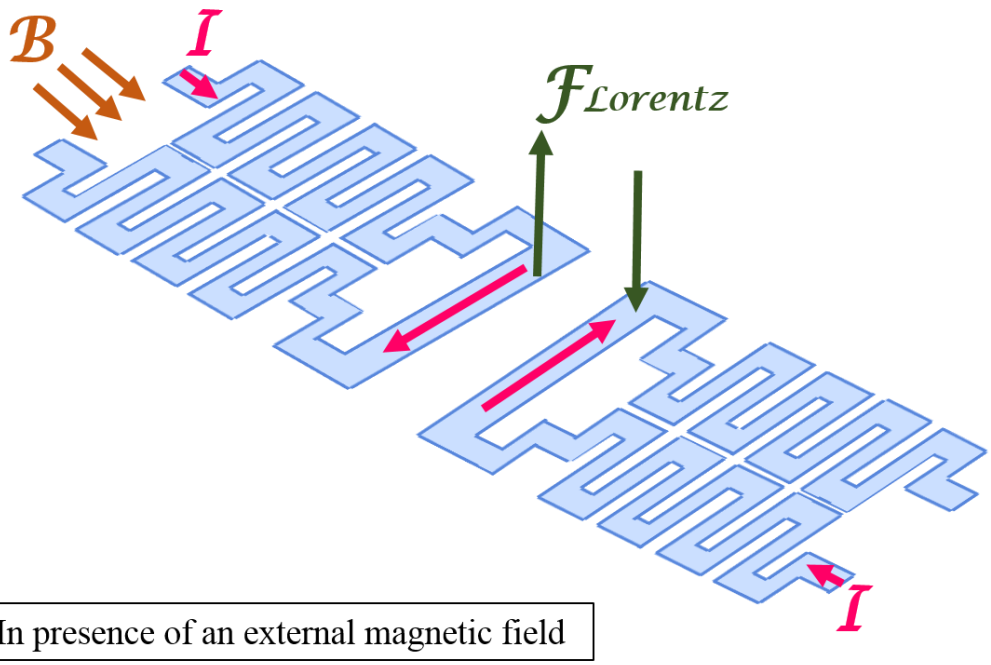

In presence of an external magnetic field

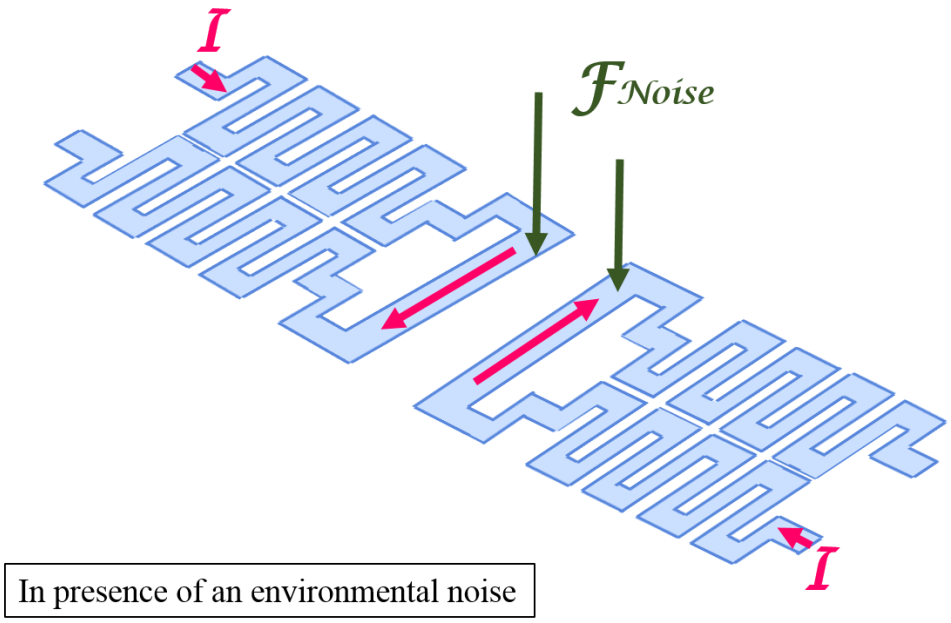

Fig. 3.61: The working principle of the differential configuration.

The discussed strategy is very ordinary where the working field is unshielded or other noise sources can affect the measurements; therefore, while for the high magnetic field amplitudes the problem is somewhat contained, for low magnetic field amplitudes the suppression of the noise becomes an essential prerogative to ensure correct operation of the MEMS sensor. The layout showing the double differential configuration is displayed in Fig. 3.62, in which it is important to note that the asymmetry between two pair of structures is finalized to preserve the robustness of the die, as in the previous optimized layout. Also in this case, the double readout strategy has been adopted (capacitive and piezoelectric), and, a pair of pads for each constraint has been used; nevertheless, compared to the previous versions the second inertial mass has been deleted due to a reduction of the active area, and, for the equal reason, a meander has been removed, thus decreasing the flexibility.

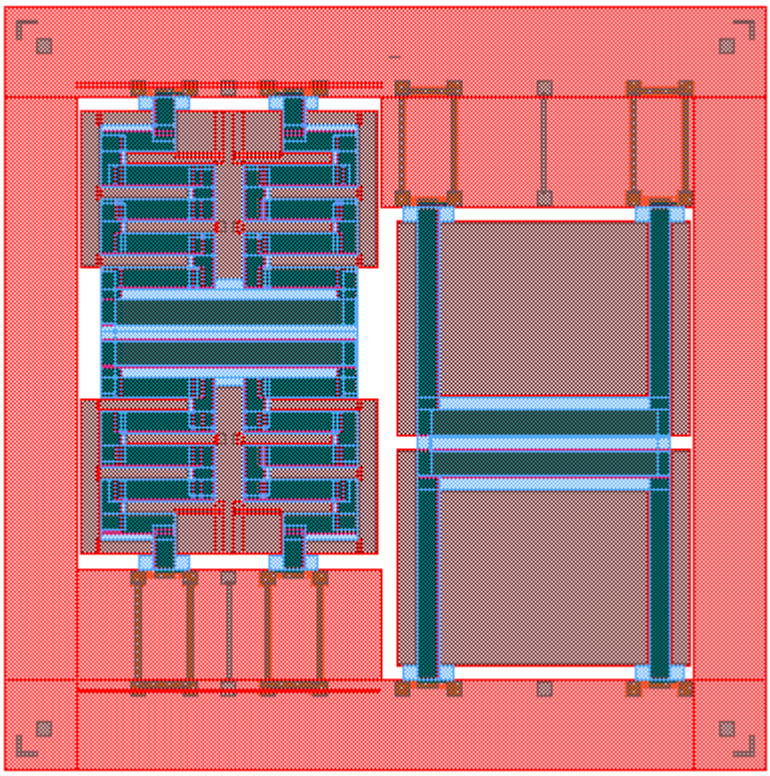

Fig. 3.62: Meander structure and Simple U-shaped beam cantilever optimization: Differential configuration.

Examining the layout without the TRENCH mask (see Fig. 3.63) it is possible easily to distinguish the structure that will be suspended, in which the stacks of thin Silicon, Aluminum Nitride and Aluminum are overlapped, always respecting the layout rules, and the electrodes for the capacitive damping and capacitive readout, that are composed of the whole SOI stack and the Aluminum layer. In addition, all geometrical parameters that are indicated in Fig. 3.63, are listed in Table 16.

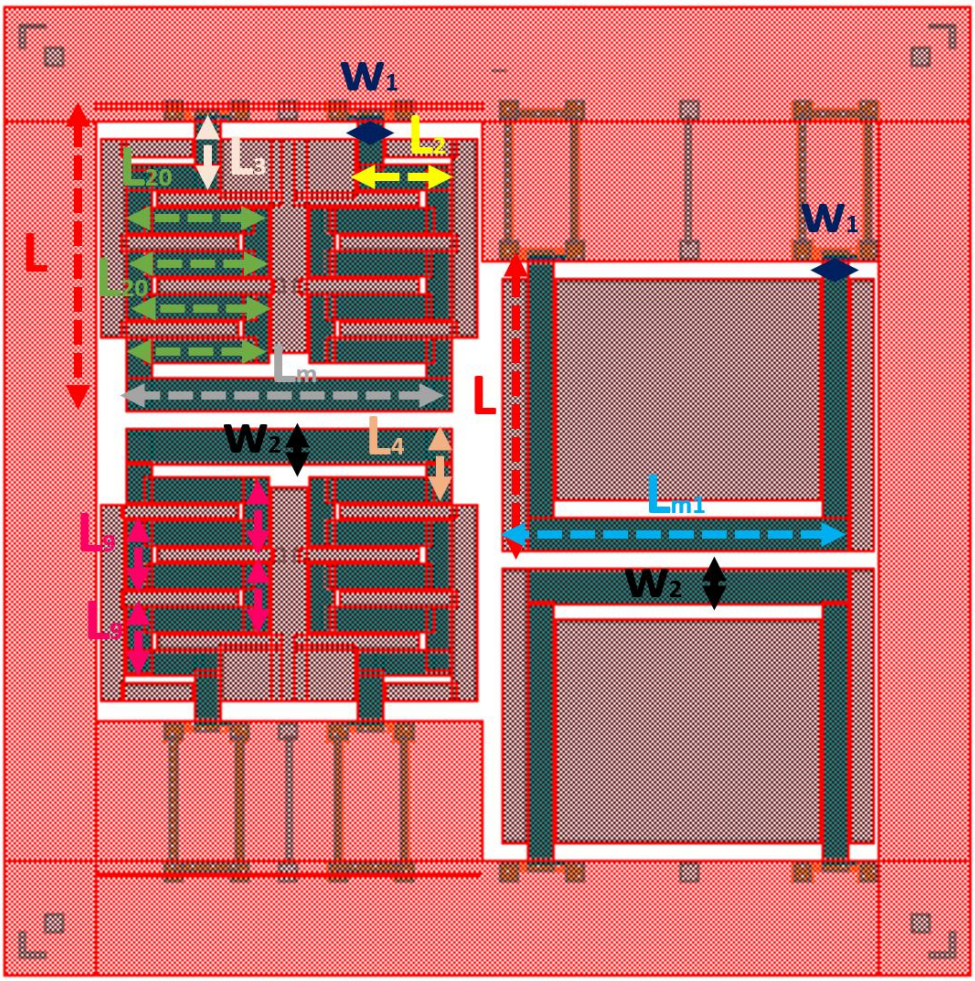

Fig. 3.63: Meander structure and Simple U-shaped beam cantilever optimization: Detail on geometrical parameters.

Optimized differential U-shaped beam cantilever	
w_1	300 µm
w_2	500 µm
L	3350 µm
L_{m1}	3070 µm

Optimized differential meander architecture	
w_1	300 µm
w_2	500 µm
L	3350 µm
L_m	3470 µm
L_2	1076 µm
L_3	800 µm
L_4	850 µm

L_9	800 μm
L_{20}	1645 μm

Table 16: List of geometrical parameters related to the differential structures.

Finally, the detail on the TRENCH mask, that allows to release the structures, is illustrated in Figs. 3.64a-b, and it is related to the differential configuration of both architectures. Also in this case, the suspended structures are composed of a thin Silicon layer, having a thickness of 10 μm, an aluminum nitride (AlN) layer with a thickness of 0.5 μm and, lastly, an aluminum (Al) layer having a thickness of 1 μm. As regards the inertial mass, they are not covered by the TRENCH mask, therefore another layer constituted by thick Silicon, having a thickness of 400 μm, is contemplated in the evaluation of the inertial mass.

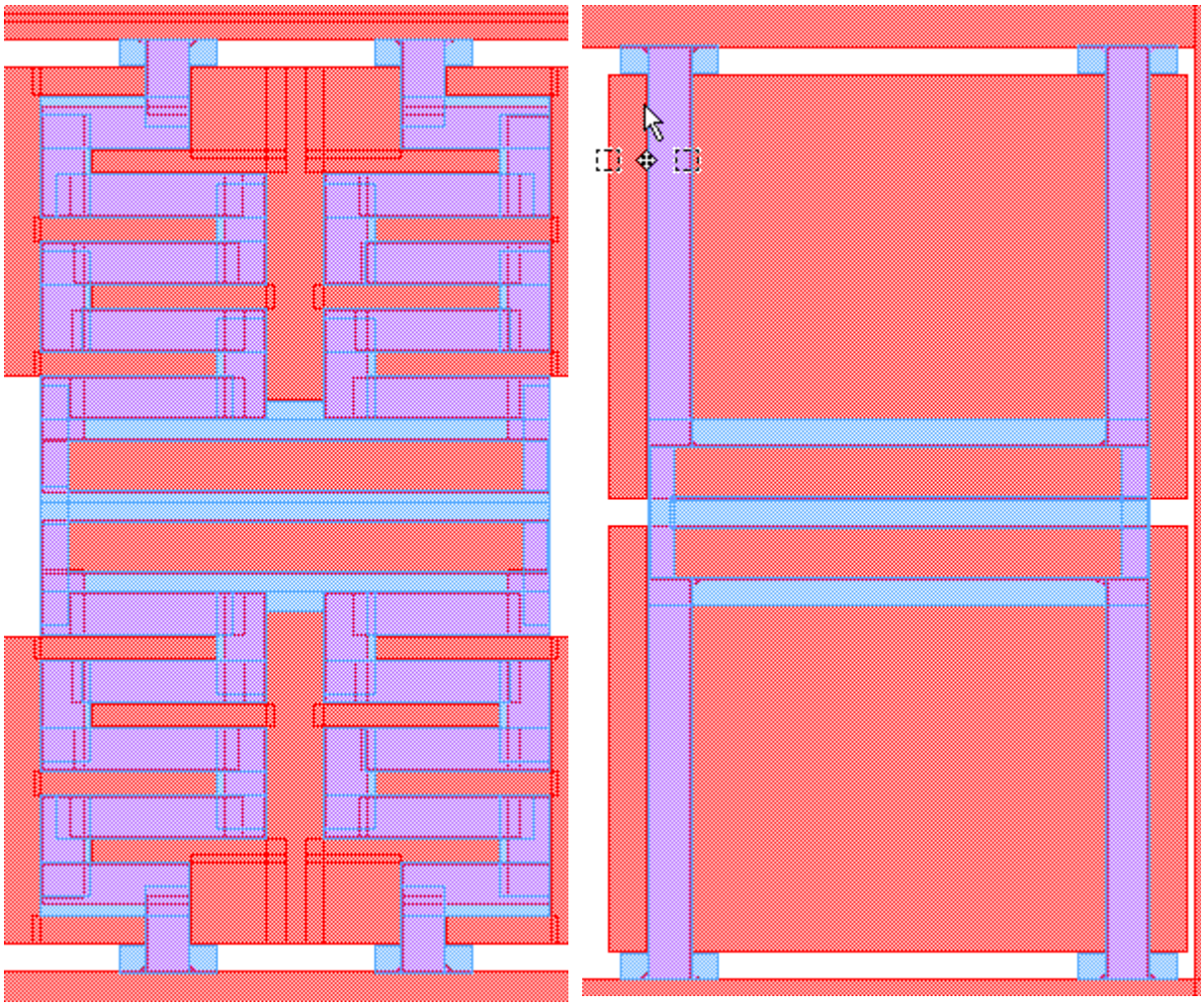

(a) (b)

Fig. 3.64: Meander structure and Simple U-shaped beam cantilever optimization: TRENCH mask.

All designs just designed have been sent to the MEMSCAP foundry that have fabricated them and thus shipped.

With this presentation the Chapter 3 is concluded, and the following chapter is dedicated to the preliminary tests and to the characterization of the discussed prototypes.

Chapter 4

Testing and Characterization

This last chapter is focused on the preliminary tests and the characterization of prototypes realized. Since four prototypes, two of which are the optimized version of the previous ones, have been realized in two different completely time phases, it has been believed mandatory to split the following dissertation considering at the beginning the first run, that has been indicated by the MEMSCAP foundry with the foundry run number PiezoMUMPs-15, and afterwards the second run, including the optimized devices, to which the foundry assigned the foundry run number PiezoMUMPs-19. As previously mentioned, the first run contemplates the two single designs in two different dies, in which a meander architecture (see Fig. 3.50) and three "classic" U-shaped beam cantilevers in "matryoshka" configuration (see Fig. 3.54) are implemented. On the contrary, the second run involves the optimized versions, characterized by a differential configuration of both architectures in one die and resized structures in the other die.

4.1 Foundry run number PiezoMUMPs-15

Just for completeness, two designs have been submitted and commissioned in May 2018 and they have been spent and arrived in September 2018.

4.1.1 SEM images of fabricated MEMS devices

As first step, a collection of SEM images related to two integrated MEMS prototypes has been carried out in order to highlight the potential presence of defects and to verify the correct release of the structure. In Fig. 4.1 a weak beam at 5 kV has been used to visualize sharply the sensor: in pale grey the Silicon Oxide (SiO_2) of SOI substrate is shown and it plays the role of insulation, whereas in black the dig is visible.

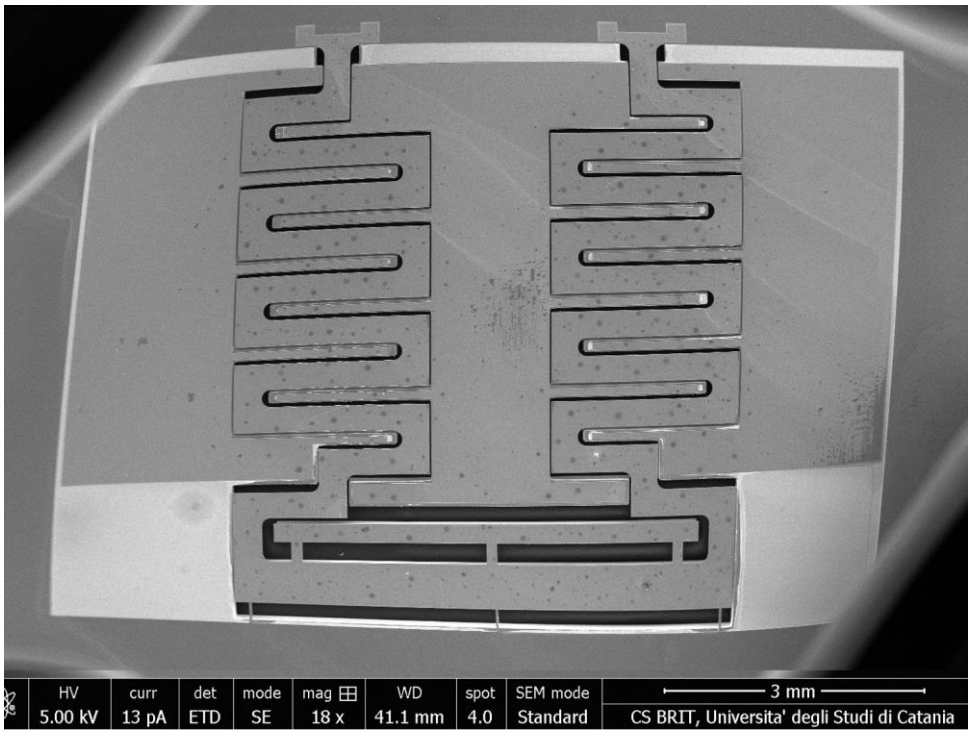

Fig. 4.1: SEM image of meander MEMS device.

It is worthy to specify that during the layout realization, in order to protect the architecture from a possible breakage three thin slices connected the proof mass to the bulk (as displayed in Figs. 4.2a-b): their presence does not constitute an obstacle because dies are attached to a plastic support that can be removed using a hotplate at the temperature of 95 C°; as result, three thin slices are also removed (see Fig. 4.2c).

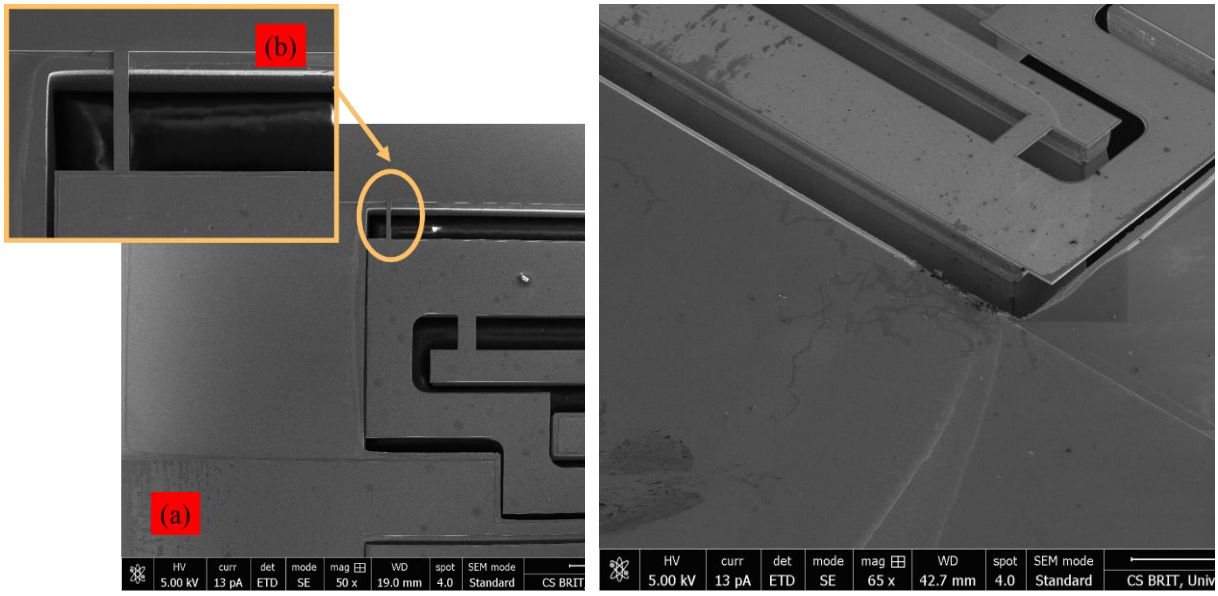

(a-b) (c)

Fig. 4.2: Proof mass: (a) Focus on final part of the MEMS sensor; (b) Detail on thin Si support; (c) Removal of thin Si support.

Another relevant point, that deserves a particular attention, is the constraint in order to understand if the suspended structure is properly anchored and the dig took place in the right way; for this reason, a focus on the anchor is shown in Figs. 4.3a-b.

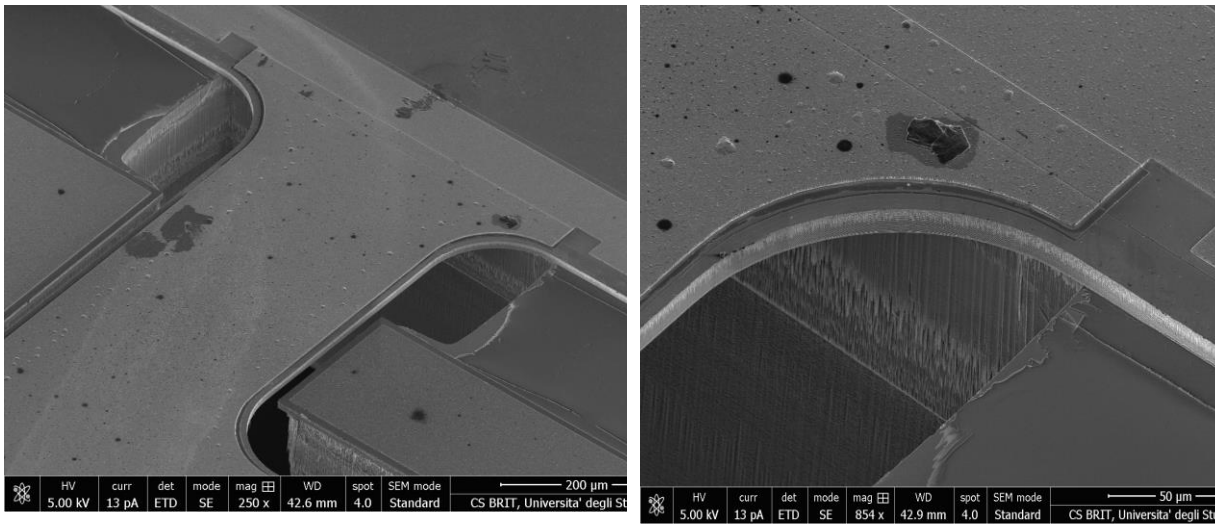

(a) (b)

Fig. 4.3: Meander structure: (a) The anchor of the suspended structure; (b) Focus on constraint.

As predicted, after the release the residual stress imposed an initial deformation to the meander architecture (note Fig. 4.4), modifying the interface surface between the electrode and the spring and thus the capacitance.

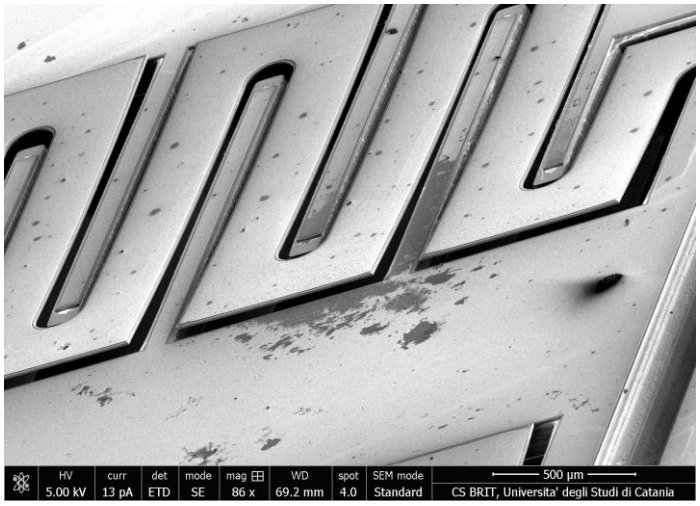

Fig. 4.4: Focus on the spring of the Meander structure.

As concerns three U-shaped beam cantilevers in "matryoshka" configuration, they are illustrated in Fig. 4.5, in which it is possible also to read the aluminum writing "D.I.E.E.I.-UNICT"; again, in pale grey the Silicon Oxide (SiO_2) is exposed, whereas in grey the metal (Al) layer is deposed.

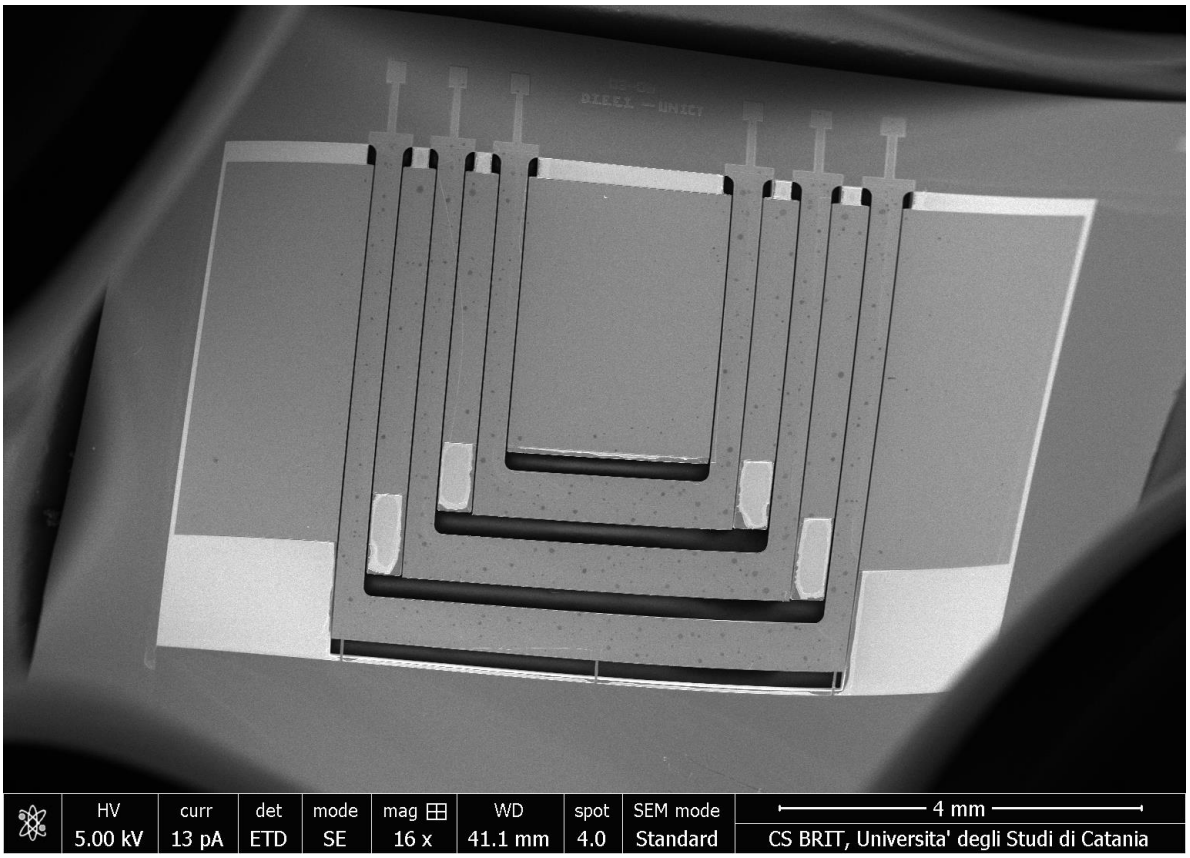

Fig. 4.5: SEM image of "classic" U-shaped beam cantilever.

Also in this case, three thin Silicon slices have been introduced in the most external architecture in order to avoid its break, as focused in Fig. 4.6a, whereas an additional focus allows to accentuate the presence of the Silicon bulk on the composition of the inertial mass (as depicted in Fig. 4.6b).

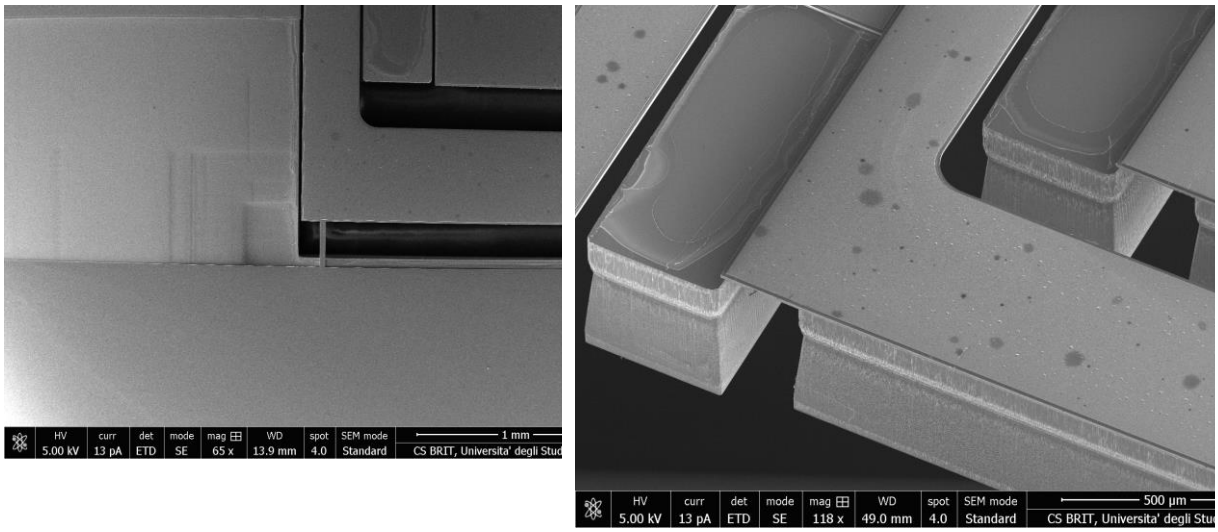

(a) (b)

Fig. 4.6: "classic" U-shaped beam cantilever: (a) Focus on Silicon support; (b) Detail on the inertial mass.

Finally, a last very interesting aspect is represented by the cross-section of the suspended structure (indicated as Fig. 4.7), where it is easy to distinguish the thin Silicon stack of 10 µm (in yellow), the piezoelectric stack, AlN (in pink), having a thickness of 0.5 µm, and the metal stack, composed of aluminum (Al) and chrome (Cr), having thickness of 1 µm and 20 nm, respectively, underlined in green.

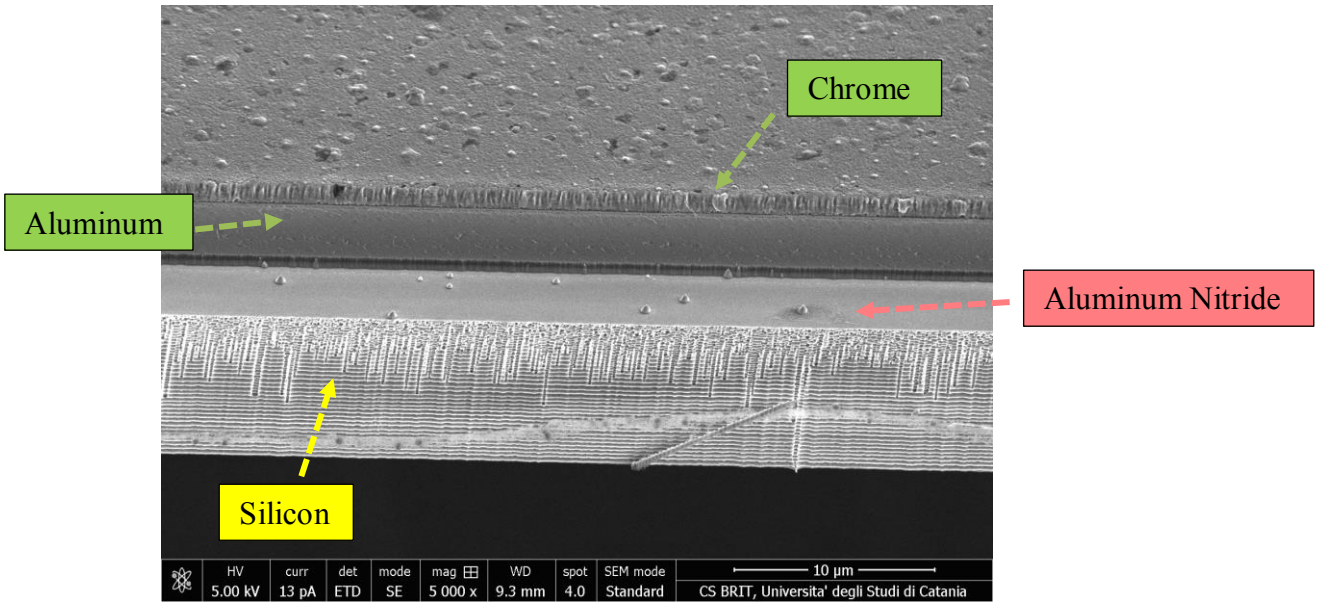

Fig. 4.7: Cross-section of MEMS device in PiezoMUMPs technology.

4.1.2 Preliminary Tests

It is interesting to note that for each layout fifteen dies have been fabricated, nevertheless during the transport some dies broke, and this drawback has been exploited to analyze individually the springs represented by the meander arms. The dies are shown in Figs. 4.8a-b: it is intriguing to note that the electrodes are symmetric obviously and they do not reach the inertial mass because a residual stress after the release has been predicted, and therefore an almost total absence of interface surface between the electrode and the electromechanical system determines a very small if not absent capacitive contribution.

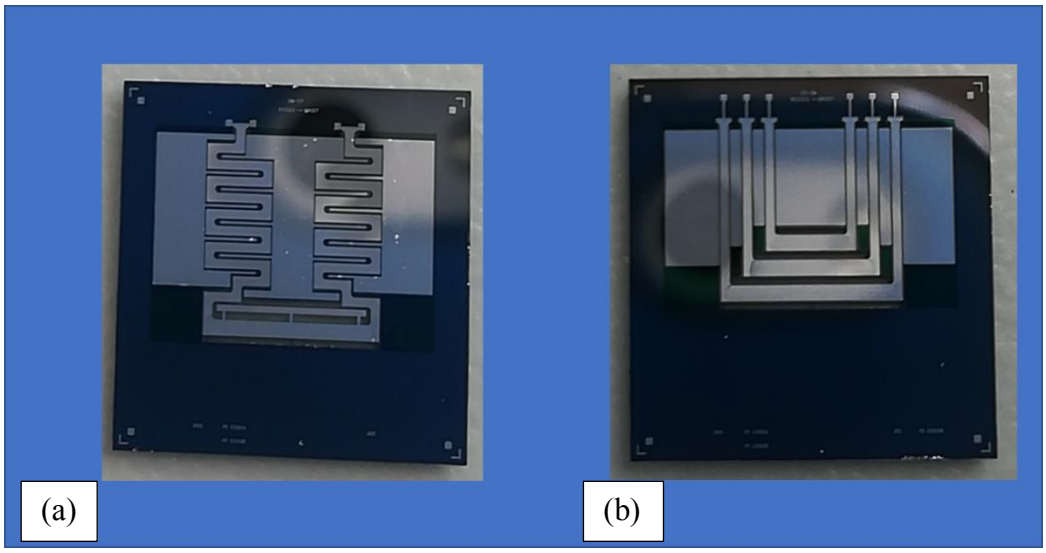

Fig. 4.8: Die: (a) Meander structure; (b) Simple U-shaped beam cantilever.

As earlier introduced, the broken meander MEMS devices have been used to test the spring reactivity and the capability of the piezoelectric (AlN) layer to provide a voltage as output signal if an impulsive mechanical stress is applied; for this reason, a microscope Alessi REL 3200 probe station has been used to contact the output pads (as illustrated in Fig. 4.9) and to acquire the output signal through the oscilloscope Agilent Technologies DSO-X 3024A. Furthermore, the static resistance has been measured using a digital multimeter GBC, KDM-400USB model, obtaining an input resistance of 8.4 Ω, that is comparable to a short circuit, and an output resistance of 18 kΩ; this last experimental value implies the existence of a resistive as well as capacitive coupling, that could represent an obstacle to right operation.

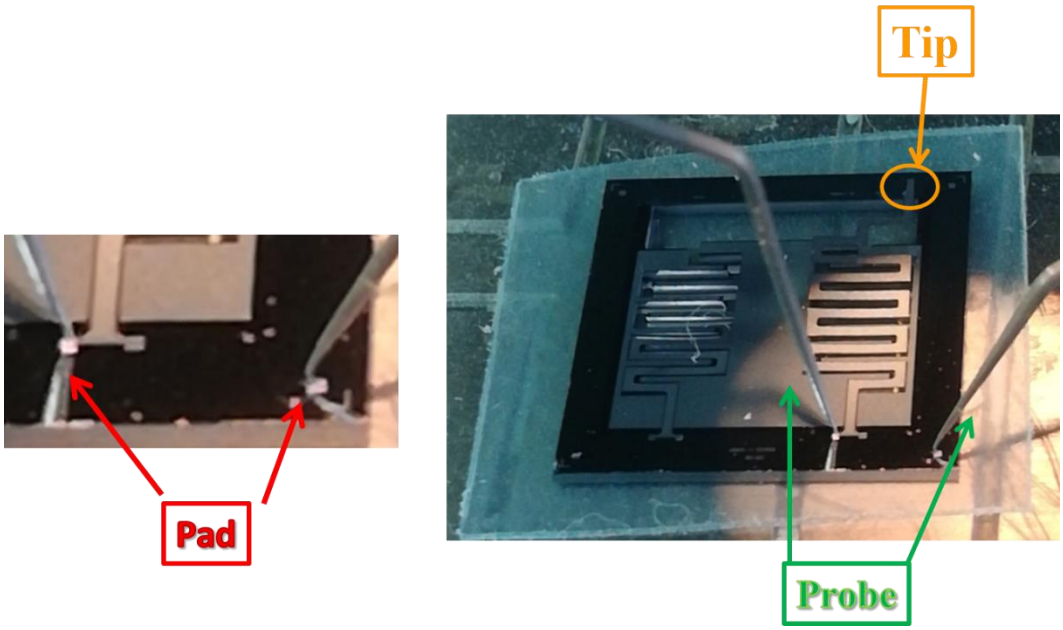

Fig. 4.9: Preliminary test on spring reactivity.

After the application of the mechanical stress and the acquisition of the output signal by means of the oscilloscope, the post-processing analysis has been implemented in Matlab & Simulink environment and plotted in Figs. 4.10a-b, where it is possible to observe in blue, due to the application of the impulsive stress, the generation of a voltage, having an amplitude of 30 mV, that tends to soften (see the zoom in Fig. 4.10b). In addition, a filter with a moving window has been used in order to filter the signal having the frequency of 50 Hz, and the new behavior is shown in red.

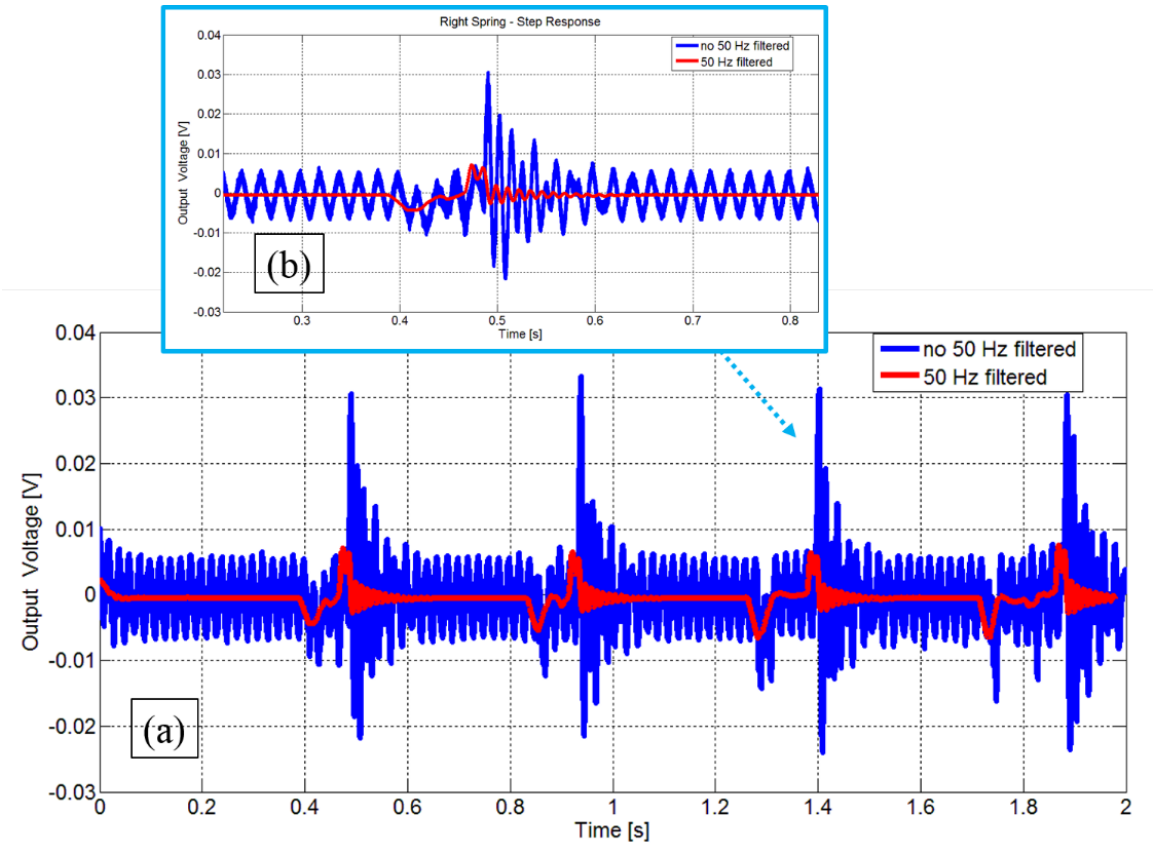

Fig. 4.10: The piezoelectric output as a function of an impulsive mechanical stress.

It is intriguing to underline that this preliminary study provided interesting information about the piezoelectric output, in other terms the piezoelectric readout strategy, however no information on the capacitive readout. For this reason, an Agilent E5061B Network Analyzer has been utilized to estimate the variation of the capacitance due to the spring movement (pay attention to Fig. 4.11a). In detail, two lines of copper tape have been used to connect the central electrode and the pad inherent to the suspended structure, in order to evaluate the capacitance (as described in Fig. 4.11b). Furthermore, the estimation of the capacitance occurred comparing the rest condition and the maximum pressing condition, that has been imposed in order to maximize the interface surface, as clarified in Fig. 4.12.

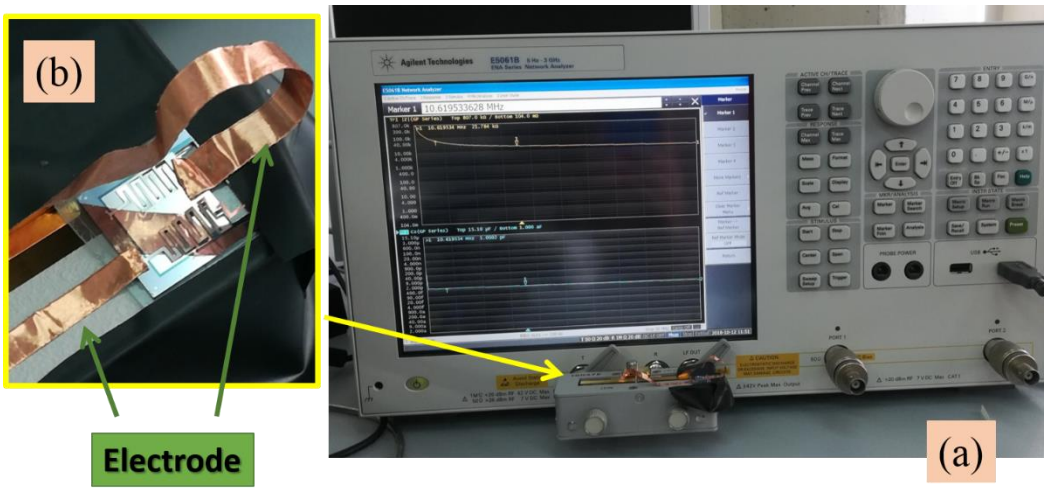

Fig. 4.11: The capacitive readout through the Agilent E5061B network analyzer.

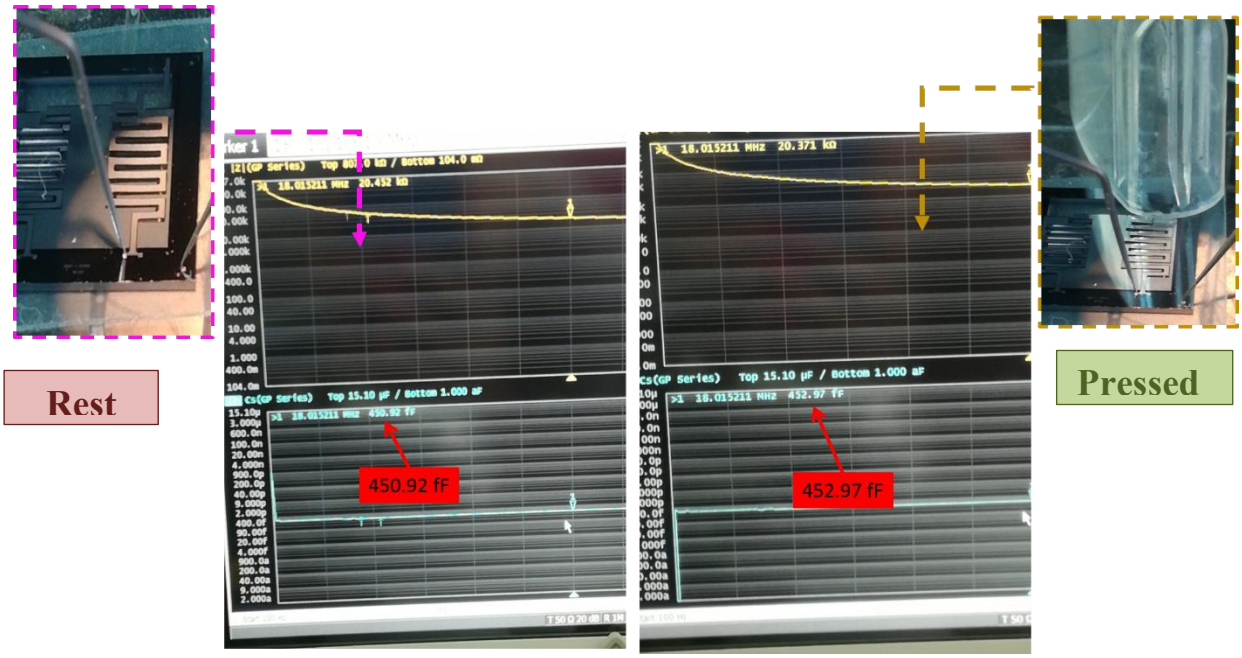

Fig. 4.12: Evaluation of capacitive output variation through the Network analyzer.

In detail, a rest capacitance of 450 fF and a maximum pressing capacitance of 452 fF have been measured, and, as a consequence, a modification of 2 fF has been appreciated. As predicted, the

capacitive contribution is very small and, therefore, a suitable conditioning circuit should be integrated into to die to detect these capacitive ranges.

After this preparatory test it is essential to specify that the packaging and bonding phases have been required in order to characterize the MEMS devices as sensor.

4.1.3 Meander MEMS device as Inertial sensor

As earlier denoted, in order to proceed with the characterization of the meander MEMS device the packaging and bonding processes on a PCB board have been required as mandatory, and the result is exhibited in Fig. 4.13; just for completeness, the PCB board has dimensions 45 mm x 45 mm. The procedure occurred thanks to the technical support of the STMicroelectronics, in Catania's site.

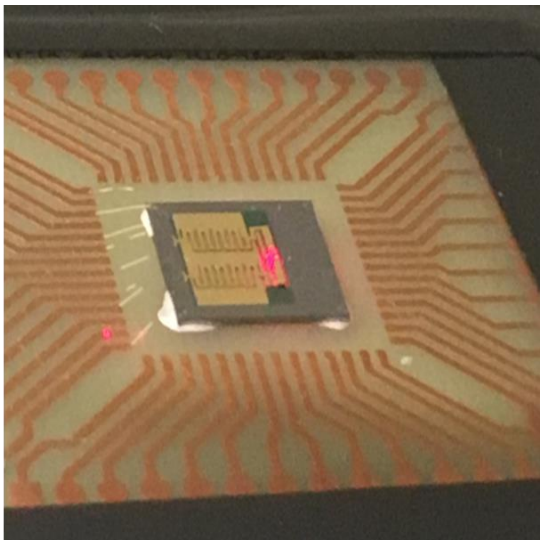

Fig. 4.13: Packaging and bonding of Meander MEMS device [99].

It is believed intriguing to underline that the aim pursued in this research activity is the implementation and fabrication of a micromechanical system in PiezoMUMPs technology to be utilized as magnetic field sensor having features of a wide operative range. However, its applicative context is not univocal, indeed another possible method of use is as inertial sensor, in other terms as accelerometer. In detail, in [99] (IEEE copyright line © 2011 IEEE) we have tested and characterized the integrated meander sensor for inertial measurements; the meander architecture used as spring in order to decrease the elastic constant and, as consequence, to reduce its resonant frequency and, eventually, to increase the useful area to be occupied by the AlN material which is utilized as self-generating layer. A suitable designed proof mass has been adopted to operate at low frequency, increasing the sensitivity of the entire device, whose design and the geometrical parameters are reproduced in Fig. 4.14.

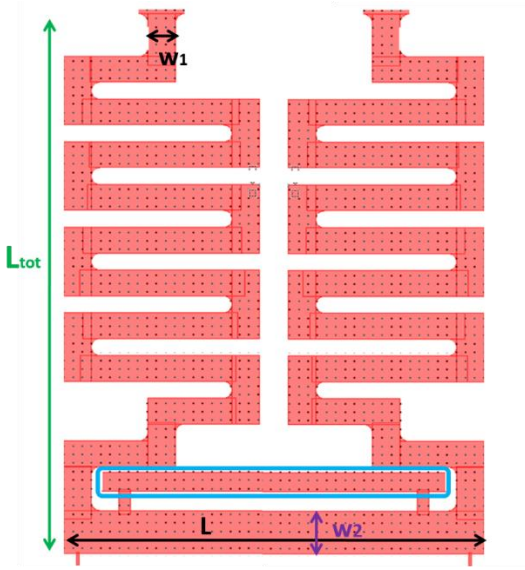

Fig. 4.14: Schematic and geometrical parameters of inertial sensor [99] (IEEE copyright line © 2019 IEEE).

As concerns the quantities indicated in the previous figure, w_1 = 300 μm is the arm width, w_2 = 500 μm is the tip width, whereas the inertial mass width has been reduced of 25 μm to

preserve the layout rules (w_m =475 μm); finally, L = 5600 μm is the length in which the "main" Lorentz force insists and L_{tot} = 6314 μm is the linear length of the meander. Just to specify that all other parameters are listed in Table 10 and they have been used to estimate the elastic constant of the whole structure. Also as accelerometer, the principal advantage in this device is represented by the presence of the integrated AlN stack, used to generate an electrical signal directly available as sensor output, without the necessity to be correlated to the variation of resistance (resistive output) or capacitance (capacitive output). It is intriguing to remark that the MEMS device has been realized to develop a considerable flexibility, therefore, the instantaneous consequence is the possibility to obtain a large output signal in correspondence with a small mechanical excitation. The whole system can be described, as known, by the second-order differential equation, that has been previously discussed in eq. (3.4) and reproduced in this section together with the piezoelectric transduction mechanism in eqs. (4.1), (4.2):

$$m\ddot{x} + d\dot{x} + kx = f(t) \tag{4.1}$$

$$V(t) = \int \left(\Pi \dot{x} - \gamma V(t)\right) \tag{4.2}$$

where d is the mechanical damping, that has been estimated by literature [98], k is the mechanical stiffness, evaluated by the equivalent section method, Π = -2.5 V/m is the coupling constant, $\gamma = {}^{1}/_{RC}$ = 100 kHz, because RC, that is the load of the piezoelectric layer, is the product between R = 1 MΩ and C = 10^{-11} F and m is the proof mass, that has been determined using eq. (4.3):

$$m = \rho_{Si} \cdot V = \rho_{Si} \cdot t_{Si_{bulk}} \cdot L \cdot w_m = 2.36 * 10^{-6} \text{ kg} \tag{4.3}$$

in which ρ_{Si} = 2329 kg/m^3 is the silicon density and $t_{Si_{bulk}}$ is the bulk thickness, having a size of 400 µm. Furthermore, it is important to highlight that in this study case the microelectromechanical structure is not actuated by Lorentz force, but rather a sinusoidal force with angular pulsation ω and having the following expression:

$$f(t) = k \cdot x \cdot \cos \omega t \tag{4.4}$$

In order to characterize the MEMS accelerometer a suitable experimental setup has been implemented and illustrated in Fig. 4.15, where it is possible to recognize a function generator, two lasers, an electrodynamics shaker and an oscilloscope.

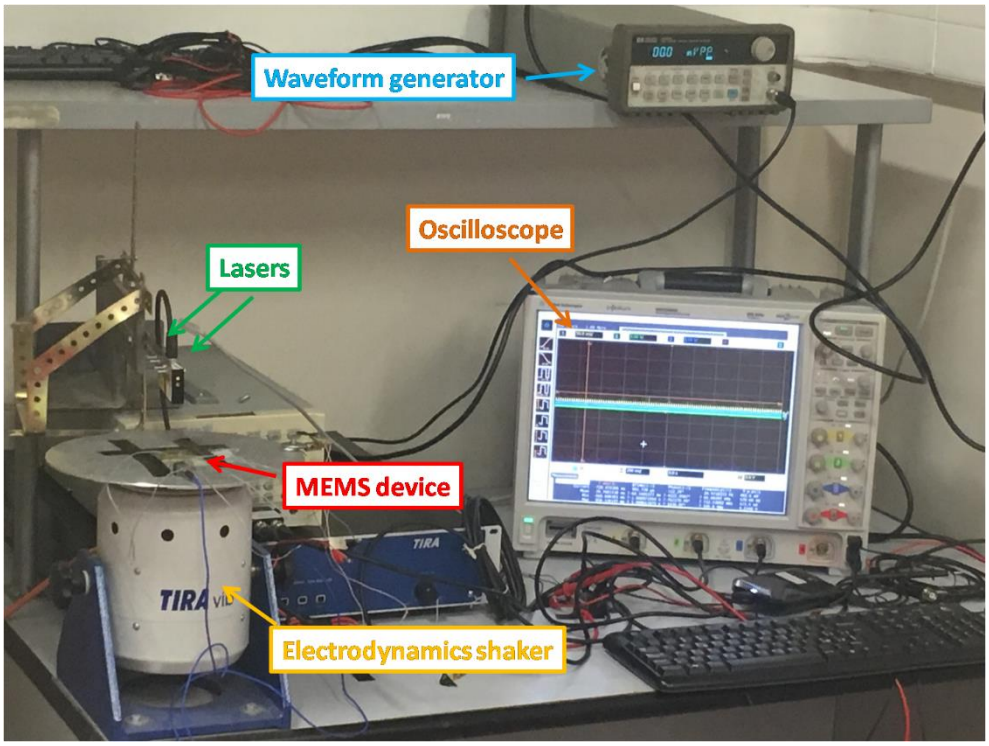

Fig. 4.15: Inertial sensor: Experimental setup [99] (IEEE copyright line © 2019 IEEE).

In detail, the waveform generator has been utilized to impress an accurate acceleration to the MEMS device through an electrodynamics shaker TIRAvib, which can be examined in Fig. 4.16a. Furthermore, the MEMS sensor has been fixed on the plate of the electrodynamics shaker (as illustrated in Fig. 4.16b) and two lasers have been used to measure displacements of the anchor and the tip of the sensor (as underlined in Fig. 4.16b). Lastly an Infiniium MSO9064A oscilloscope has been adopted in order to acquire the signals.

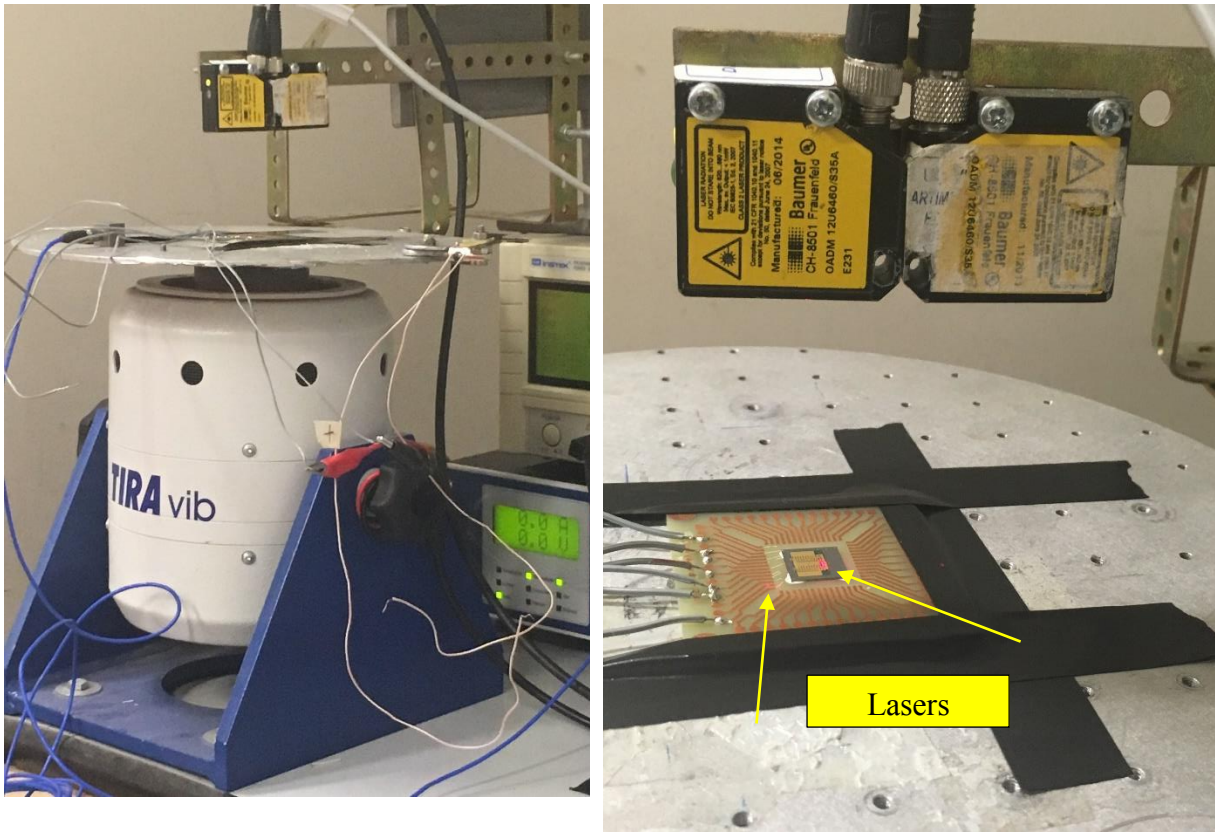

(a) (b)

Fig. 4.16: Focus on: (a) Electrodynamic shaker; (b) Lasers [99] (IEEE copyright line © 2019 IEEE).

The first step has concerned the estimation of the resonance frequency through the application of an external acceleration of ~ 0.6 m/s^2. In particular, a resonance frequency of ~ 20 Hz has been experimentally estimated through the analysis of the output voltage as a consequence of the application of several mechanical frequencies, as illustrated in Fig. 4.17, where it is evident that the greatest amplitude of the output voltage has been achieved in correspondence with a frequency of 20 Hz. In particular, a sinusoidal signal having an amplitude of 300 mVpp and a frequency in the range [0 - 35] Hz has been applied.

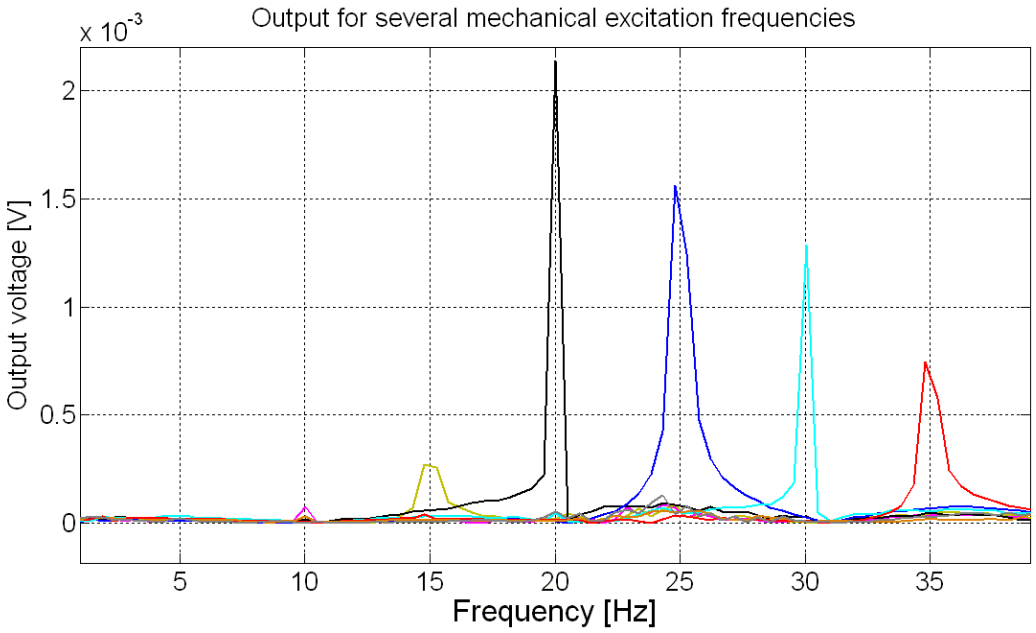

Fig. 4.17: Analysis around the resonance frequency (20 Hz) [99] (IEEE copyright line © 2019 IEEE).

Afterwards, the piezoelectric output has been evaluated as a function of the mechanical acceleration at the resonance frequency as shown in Fig. 4.18, where ten measurements have been collected for each acceleration value.

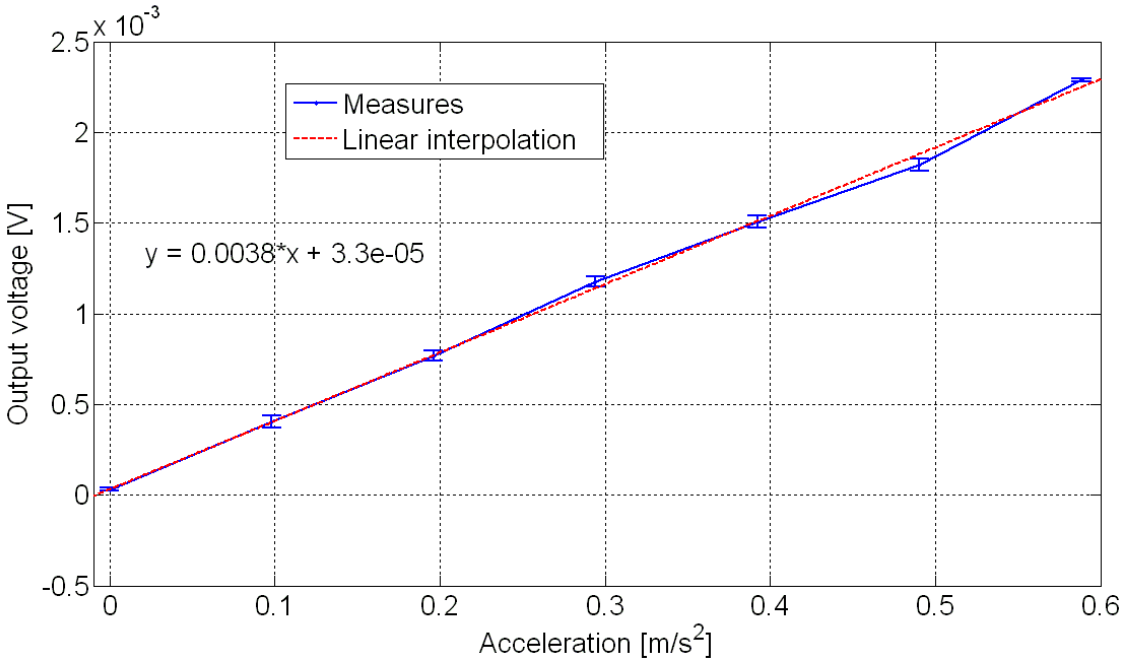

Fig. 4.18: Piezoelectric output as a function of the external acceleration [99] (IEEE copyright line © 2019 IEEE).

It is interesting to note that the mean value and the corrisponding uncertainty have been included in the diagram. Furthermore, a sensitivity of ~ 0.0038 V/(m/s^2), a noise level of ~ 3.37×10-5 V and a resolution of ~ 0.0089 m/s^2 have been estimated. These features arouse interest considering that they have been obtained with a MEMS able to work at low frequency, with a voltage transduction and compact device. In addition, it is worth noting that very significant sensitivity has been obtained taking into account that very low external accelerations have been applied. The tip displacement and the relative piezoelectric output as a function of the external acceleration, have been also analyzed and both are presented in Fig. 4.19. As it can be noted a maximum output of about 2.3 mV has been obtained for an acceleration level of about 0.6 m/s^2.

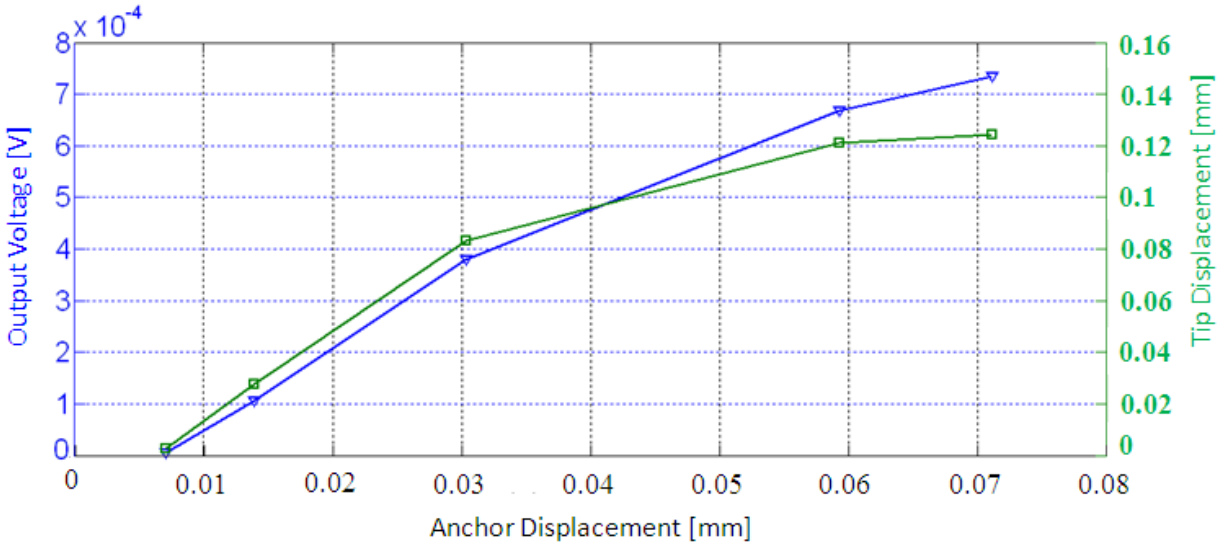

Fig. 4.19: The tip displacement and the output across the AlN layer as a function of the anchor displacement [99] (IEEE copyright line © 2019 IEEE).

In conclusion, as inertial sensor the proposed architecture of measurement improves the state of the art considering that in the device an Aluminum Nitride (AlN) layer is used to generate an output voltage as function of the acceleration without the adoption of supplementary active conditioning circuits. Furthermore, through the adoption of a meander structure, higher performance, low frequency response and a low-stiffness device has been conceived with, at the same time, high useful active area for the self-generating AlN layer. It is important to underline that very low accelerations have been impressed to the MEMS device and nevertheless a significant sensitivity has been estimated.

4.1.4 Meander MEMS device as Magnetic field sensor

In order to characterize the meander MEMS device as magnetic field sensor a period of five months has been spent at CERN (European Organization of Nuclear Research), placed in Espl. des Particules 1, 1211 Meyrin, Geneva, Switzerland (shown in Fig. 4.20).

Fig. 4.20: The main entrance of CERN.

The research and testing activity involved the MM (Magnetic Measurements) group, located in Building 30, and having available the whole Building 311, shown in Fig. 4.21, as measurements laboratory. It is interesting to note that the Building 311 is used to test and calibrate magnets which will subsequently be located along the LHC tunnel, where LHC is an acronym for Large Hadron Collider.

Fig. 4.21: Building 311: Magnetic measurements laboratory.

Several types of magnets are used to compose the LCH tunnel, such as dipoles, quadrupoles and sextuples; for this reason, a brief dissertation about the composition and the structure of LHC is believed necessary to frame the context in which the magnetic field measurements have been carried out. The LHC tunnel is long 27 km and it is the final part of the particle accelerator (as depicted in Fig. 4.22). Just for completeness, in the past the particles beam was composed of electrons, that are much lighter than protons, and the most external ring used to increase the beam velocity was called LEP. Afterwards the beam composition has been modified accelerating and deflecting protons bunches (around $1.15*10^{11}$ particles for bunch), that have a higher mass, and

thus a greater energy is developed during the impact. The working principle of the accelerator is based on the application of high electric fields and high magnetic fields with different function; in detail, the electric field is applied through the RF cavity in a unique place that is LINAC (acronym for LINear ACcelerator), whereas the magnetic field is exercised along the whole tunnel to deflect the protons beam. In relation to this point it is significant a classification of the used magnets which are split essentially in dipoles and quadrupoles: the first ones perform the function of deflecting the particles bunches, while the second ones compress and focalize the particles bunches.

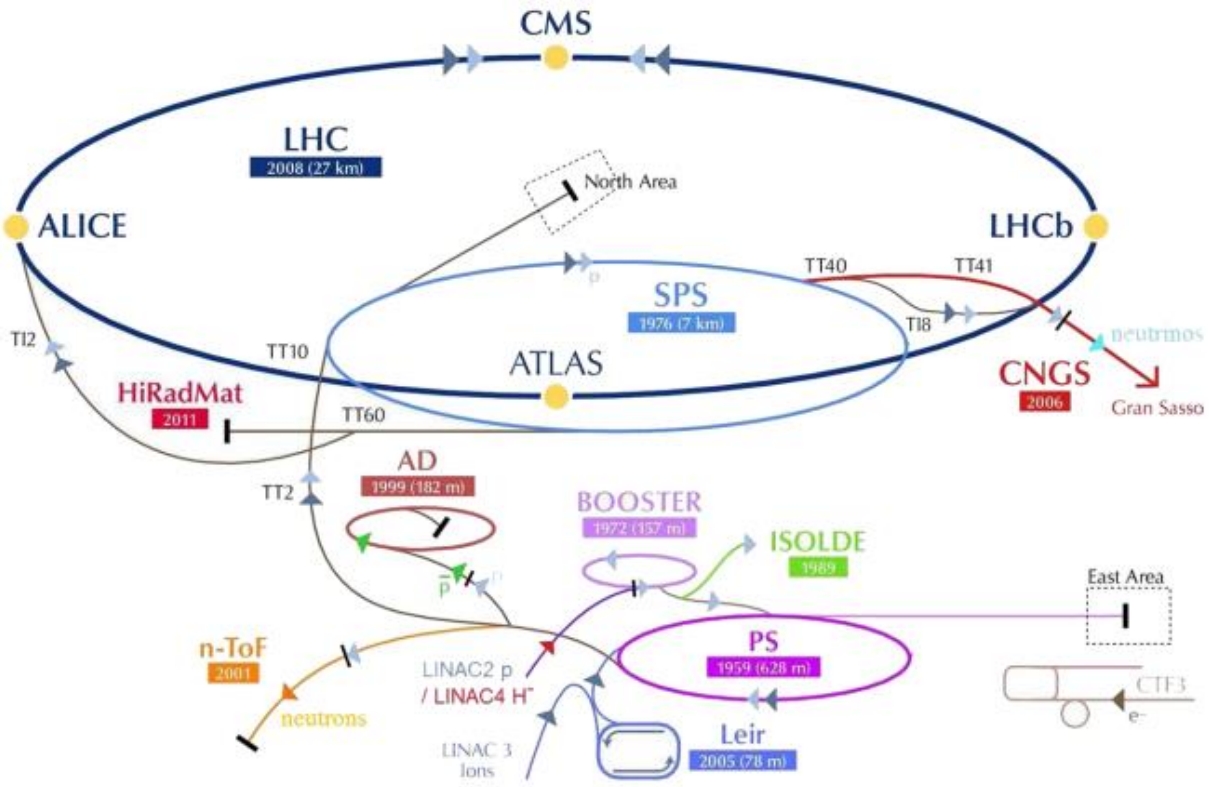

Fig. 4.22: Schematic of CERN accelerator [100].

The path carried out by the particles bunches is the following: LINAC, PS (Proton Synchrotron), SPS (Super Proton Synchrotron) and LHC. It is noteworthy to mention that from LINAC two protons beam will collide in LCH tunnel in four detectors, indicated with ATLAS, CMS, ALICE and LHCb, that are located at the depth of 100 m. Just for curiosity, ATLAS and CMS detectors exhibit different processing techniques and work in pairs in a complementary way, in order to confirm or to deny what has been discovered.

In addition, it is indispensable to emphasize that the magnets used in the LHC tunnel are superconductive magnets having helium-cooling system, whereas dipoles and quadrupoles utilized in Building 311 exhibit a water-cooling system and they are displayed in Figs. 4.23a-b.

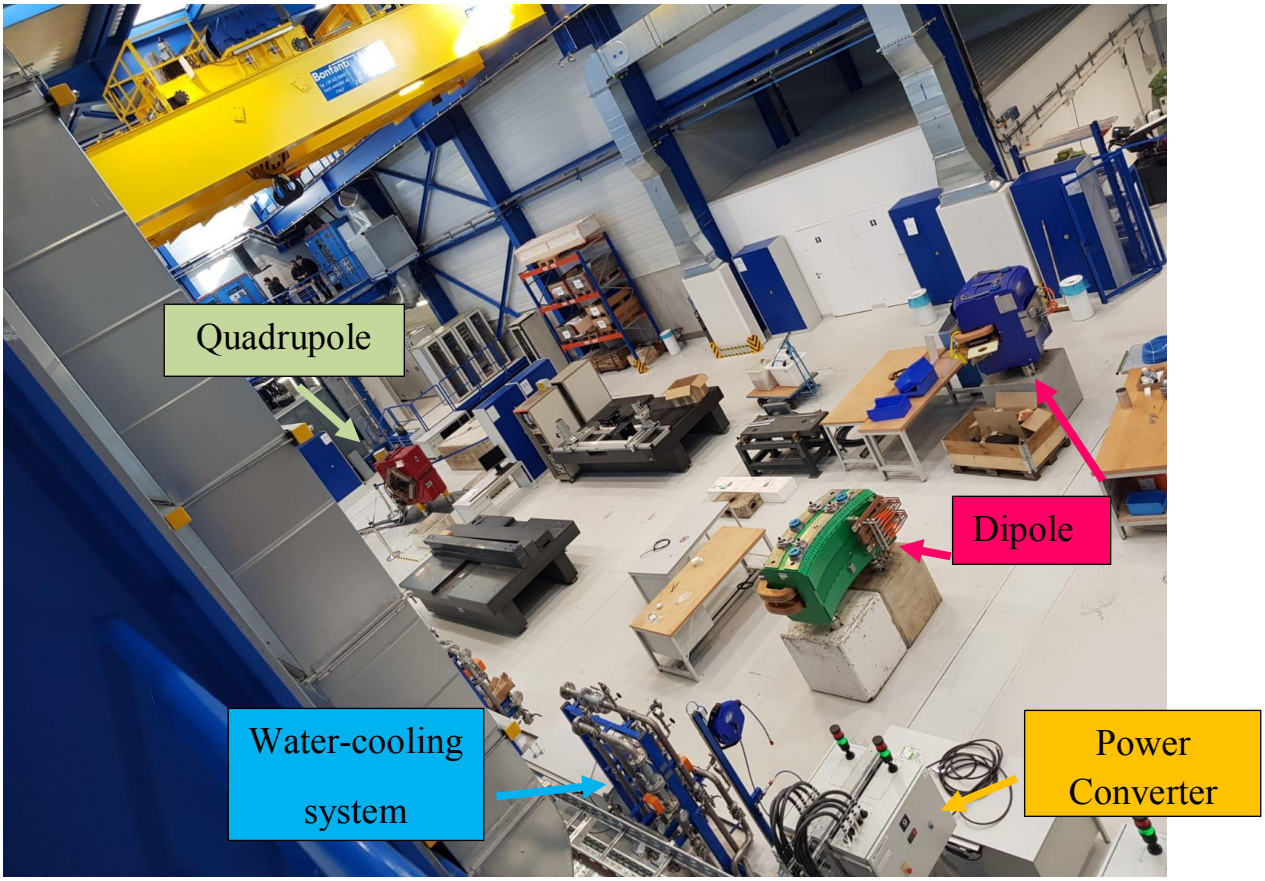

(a)

(b)

Fig. 4.23: The interior of Building 311: (a) Detail on several magnets; (b) Reference dipole.

In order to test and to characterize the MEMS devices the yellow dipole, which is shown in Figs. 4.24a-b, has been utilized, in which the direction of the induced magnetic field is correlated to the verse of the DC current provided by the power converter to the dipole spirals. Typically, for the measurements carried out with the yellow dipole the magnetic field direction has been fixed, as described in Fig. 4.24a, whereas a rotation has been imposed to the device in order to analyze the behavior of the MEMS sensor due to the application of the Lorentz Force in a different direction. The dipole characteristics are illustrated in Fig. 4.24b, where the maximum nominal DC current that can be supplied is 810 A, the static resistance at 20 °C is 10.73 mΩ, the magnetic induction at I_{max} is 0.73 T and, eventually, the magnet weight is 1100 kg.

(a) (b)

Fig. 4.24: The yellow dipole at Building 311: (a) Design; (b) Characteristics.

As can be easily understood, the characterization of the microelectromechanical system required the implementation of a suitable experimental setup, that is displayed in Fig. 4.25, composed of an AC current source, a teslameter, the MEMS sensor, a dipole and a DAQ board. In detail, the KEITHLEY 6221 DC and AC CURRENT SOURCE is used to drive a sinusoidal current into the MEMS device, which is placed inside the yellow dipole with different orientations. A teslameter, PROJEKT ELEKTRONIC Gmbh BERLIN, is introduced into the dipole, proximally in the middle in order to verify the amplitude of the static magnetic field produced by the

DC current, that is generated by the power converter. The output voltage of the MEMS device is sent to a DAQ board, NI usb-6366, connected to a LabVIEW routine, that acquires the input current, the output of the piezoelectric layer and the output signal of the teslameter.

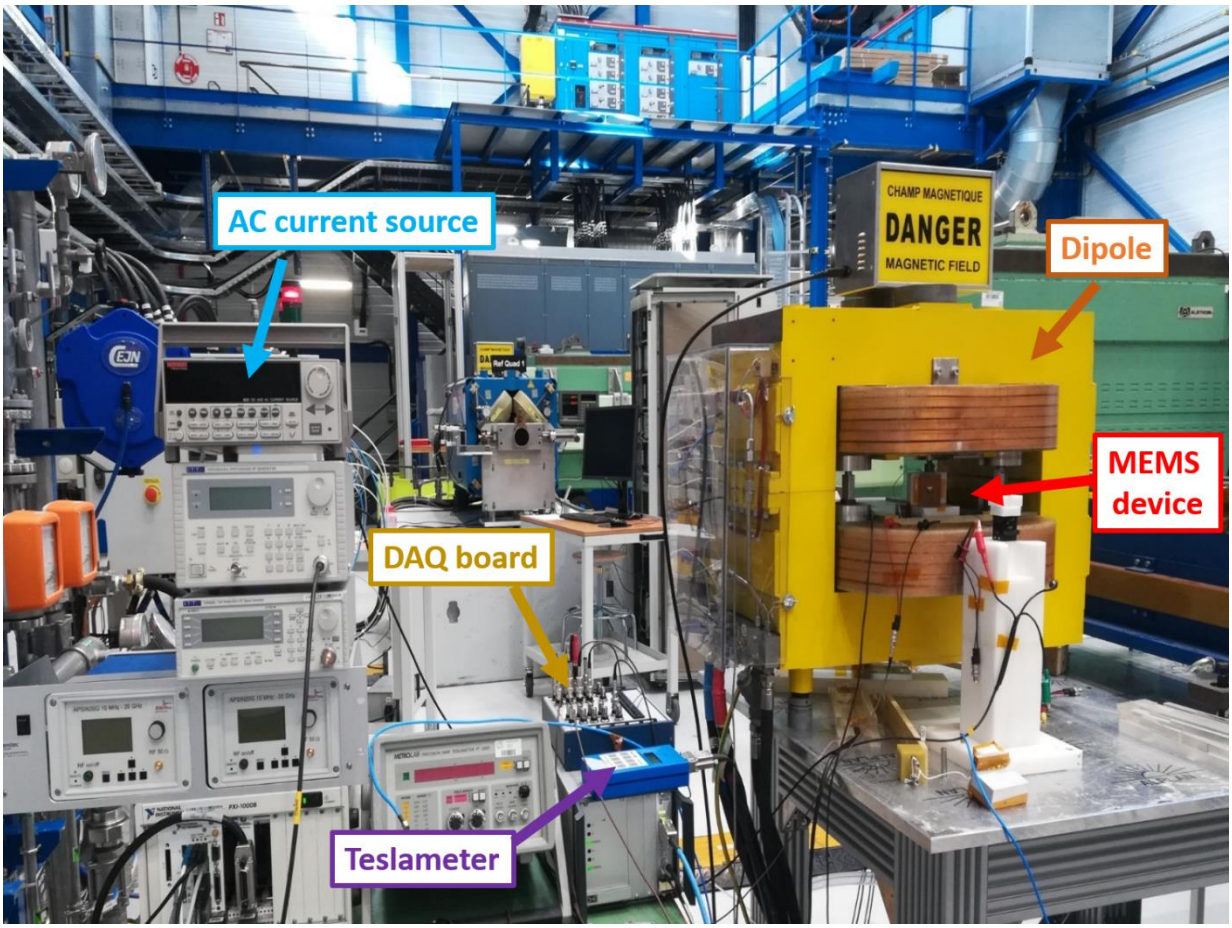

Fig. 4.25: The experimental setup.

It is essential to underline that an important element of the experimental setup is missing in Fig. 4.25, and it is the power converter; the motivation must be sought in the existence of a special station used exclusively to pilot the power converter, as shown in Fig. 4.26, where a special code string enables a specific power converter, that is the TRANSTECKNIC1 for the

yellow dipole, in order to supply the current ramp. In relation to this point it is worthy to notice that not only the current amplitude but also the speed with which the DC current reaches full capacity (defined "ramp") can be established. Furthermore, the relationship between the DC current generated by the power converter and the intensity of the magnetic field generated inside the dipole is expressed by the ratio 0.877165 mT/A, which means that for each DC current supplied by the power converter and having the amplitude of 1 A, a static magnetic field with intensity of 0.877165 mT is generated.

Fig. 4.26: The power converter station.

In order to proceed with the characterization two different orientations of the integrated magnetic field sensor inside the dipole have been analyzed since, as long discussed, the direction and the amplitude of the Lorentz force is strictly correlated to the relationship between the directions of

input current driven into the device and the external magnetic field to be measured. A polystyrene structure has been implemented in order to provide a rigid support to the PCB board with the MEMS sensor in both directions without introducing electromagnetic interference; in Figs. 4.27a-b two examined orientations are illustrated, in which, in detail, the perpendicular direction is shown in Fig 4.27a and the planar direction is displayed in Fig. 4.27b.

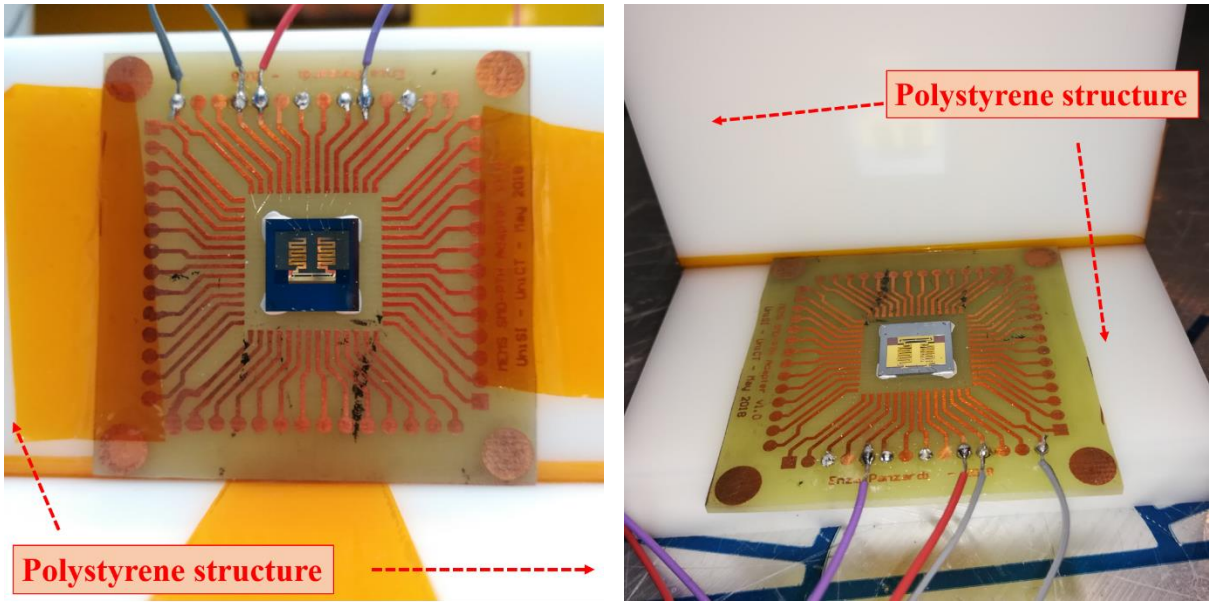

(a) (b)

Fig. 4.27: Meander MEMS device: (a) Perpendicular direction; (b) Planar direction.

It is intriguing to specify that the magnetic induction *B* could have two directions of propagation that are correlated to the direction of the DC current in the turns of the dipole, however, as previously specified, it has been decided to keep the magnetic induction in the same direction, as shown in Fig. 4.24a. As a consequence, the orientation of the integrated sensor implicates a different Lorentz force application, as explained in Figs. 4.28a-b: in any case the AC current driven into the device (*I*), the magnetic induction (*B*) and the Lorentz force ($F_{Lorentz}$) are perpendicular to each other, nevertheless in the perpendicular condition the Lorentz force is

applied in the direction of preferential tip deformation, guaranteeing the maximum displacement and thus the greatest output voltage, whereas in planar condition the Lorentz force is imposed along a direction that does not introduce a tip deformation, and thus no output signal.

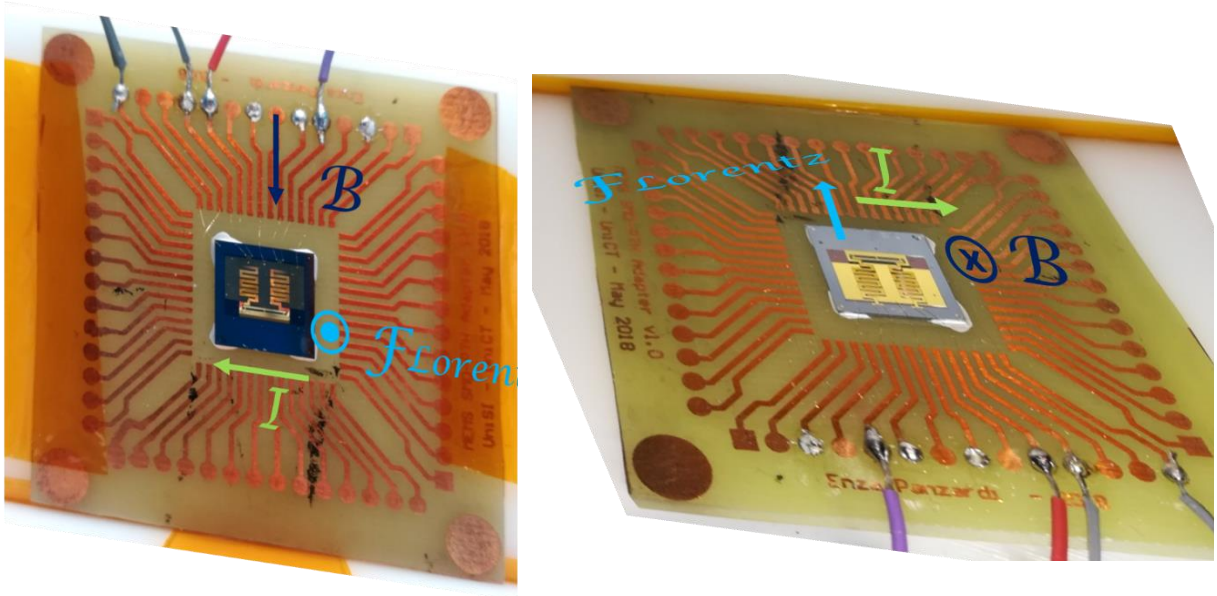

(a) (b)

Fig. 4.28: Relationship among I, B and $F_{Lorentz}$ in Meander device: (a) Perpendicular direction; (b) Planar direction.

Since a relevant characteristic of the meander MEMS sensor is to detect the magnetic field in directional way, two configurations have been analyzed in order to validate the working principle.

Therefore, as regards the perpendicular direction case, the same experimental setup illustrated previously in Fig. 4.25 has been used with the MEMS device oriented as shown in Fig. 4.29: a sinusoidal current having a frequency of 20 Hz and an amplitude in the range [0 - 100] mA_P, provided by the AC current source, is driven into the MEMS sensor; a teslameter is placed inside the dipole in order to monitor the DC magnetic field generated, whereas the MEMS device is

connected through the LEMO connectors to the AC current source as input and to the DAQ board as output.

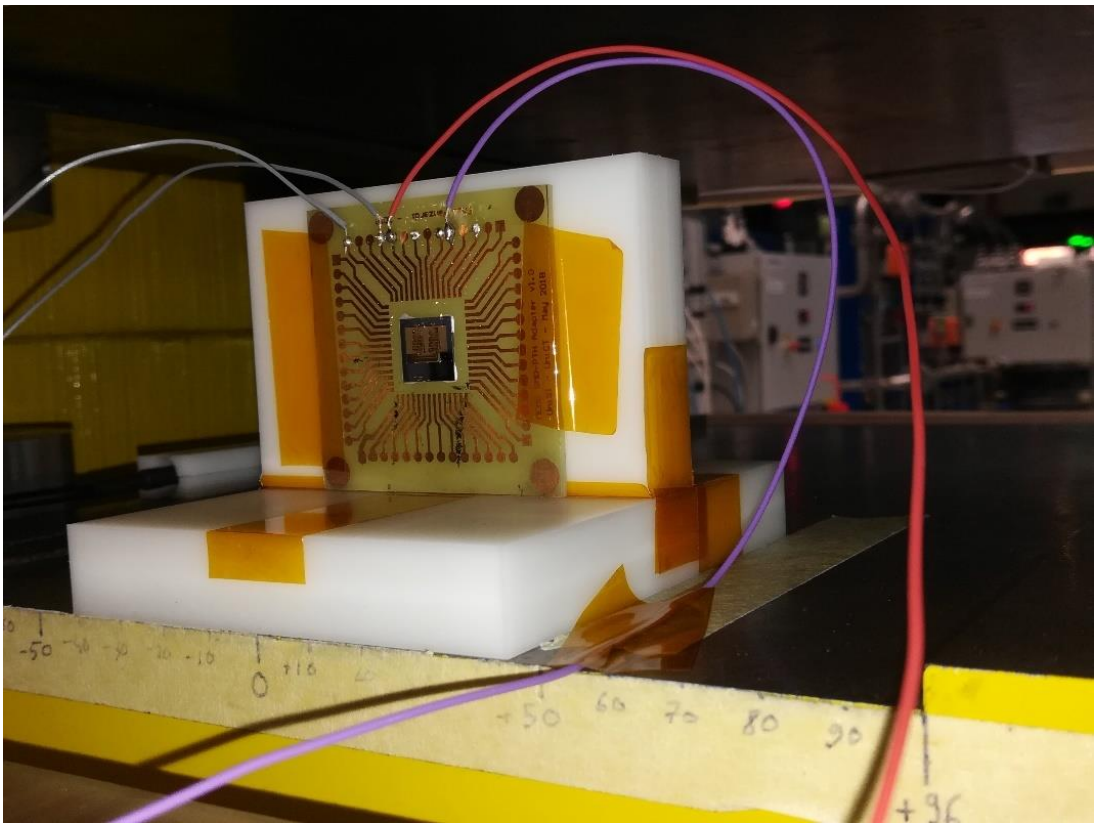

Fig. 4.29: MEMS sensor into the dipole: Perpendicular direction.

It is interesting to underline that the frequency of the sinusoidal current has been selected because it has been earlier demonstrated that the MEMS sensor exhibit a resonant frequency exactly at 20 Hz. In addition, the power converter station is utilized to supply a DC current to the dipole with a specific ramp (that has been decided on 5 A/s), however a minimum DC current value around 1 A must be imposed to guarantee a continuous and constant magnetic field; in other terms, the yellow dipole is not capable of keeping with precision a magnetic induction below

1 mT. For this reason, in order to implement a magnetic induction in the range [0 - 25] mT, the following table (see Table 17) has been created, respecting the ratio 0.877165 mT/A:

DC current by power converter	***Ramp***	***Magnetic induction into the dipole***
1 A	5 A/s	0.877 mT
5.7 A	5 A/s	5 mT
11.4 A	5 A/s	10 mT
17.1 A	5 A/s	15 mT
22.8 A	5 A/s	20 mT
28.5 A	5 A/s	25 mT

Table 17: Correlation between the DC current supplied by the power converter and the magnetic induction generated into the dipole: List of DC current values imposed.

As is now known the relationship between the AC current into the integrated sensor and the Lorentz force is linear due to the following equation:

$$F_L = \left(\vec{I}_{cant} \times \vec{B}\right) \cdot L = I_{cant} \cdot B \cdot L \cdot \sin\theta \tag{4.5}$$

Therefore, as first step the eq. (4.5) has been verified examining the piezoelectric output as a function of the AC driving current, in which a frequency of 20 Hz and an amplitude in range [0 - 100] mA_P with steps of 5 mA_P have been applied, considering four different magnetic

induction values, that are 5 mT, 10 mT. 15 mT and 20 mT. As can be observed in Fig. 4.30 the output voltage, expressed in term of rms (root mean square) value, presents a linear trend with the increase of the driving current and therefore of the applied Lorentz force.

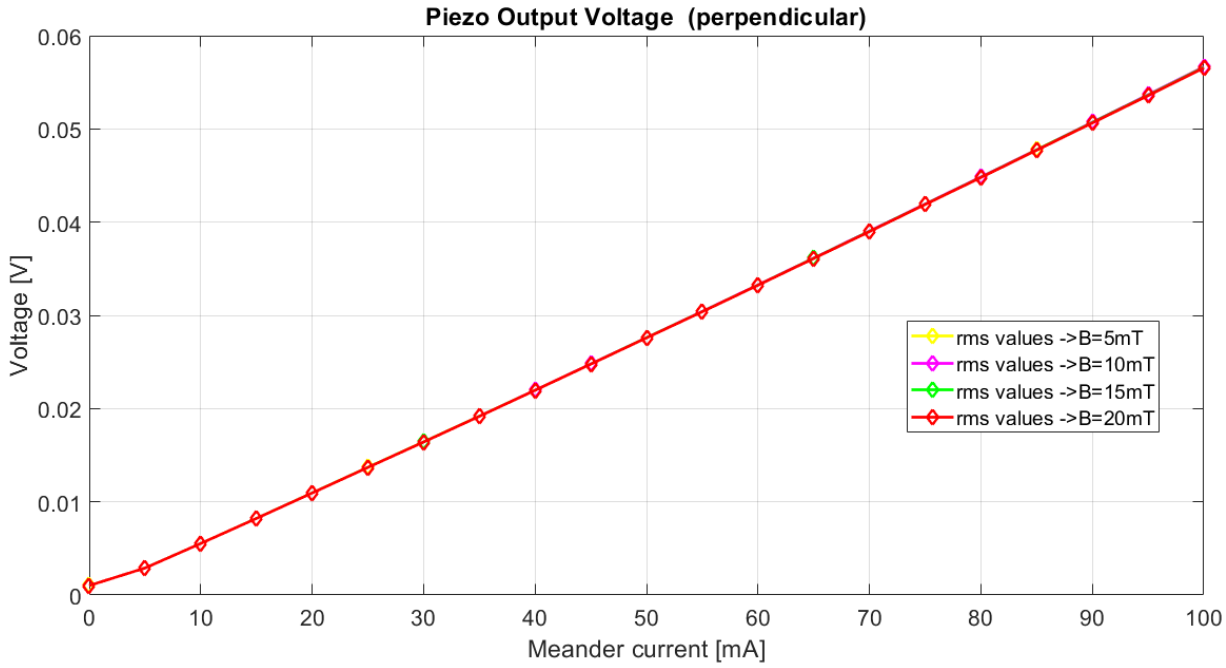

Fig. 4.30: Piezoelectric voltage as a function of the driving current in perpendicular direction.

It is important to note that zooming in on the previous picture it is possible to appreciate that the MEMS device is capable to distinguish several amplitudes of the magnetic induction for each value of the sinusoidal current with a coherent behavior (see Fig. 4.31).

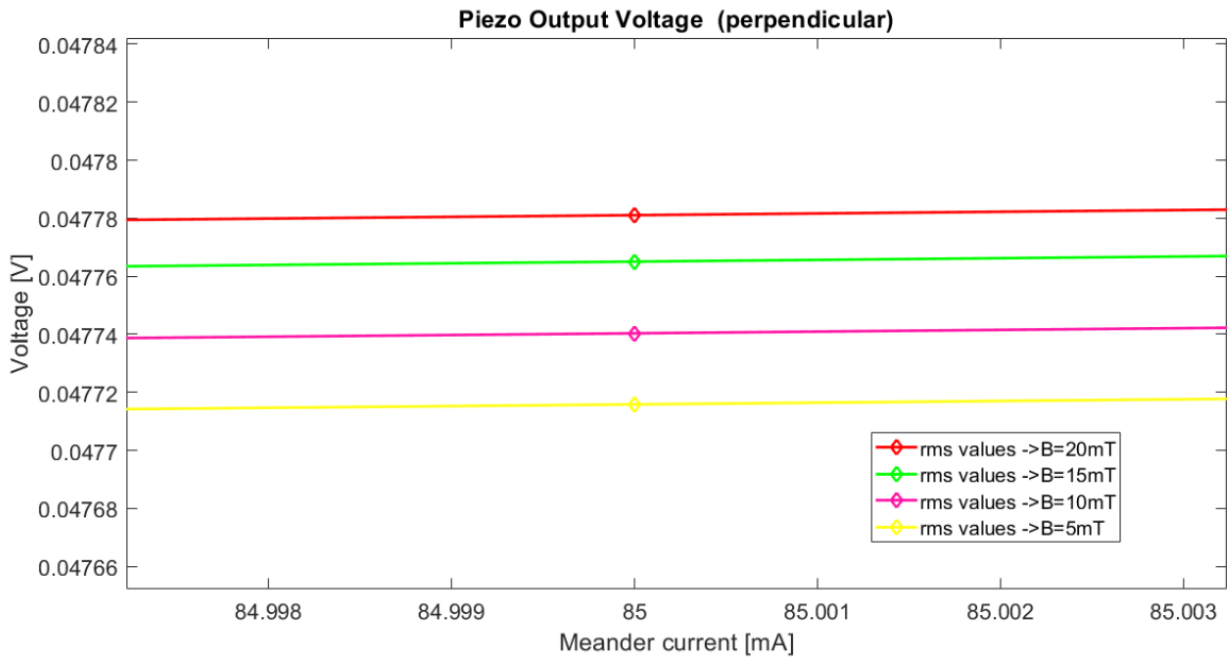

Fig. 4.31: Zoom of the piezoelectric voltage as a function of the driving current in perpendicular direction.

Afterwards, the AC driving current into the MEMS sensor has been kept constant and the piezoelectric output voltage, expressed in rms value, as a function of the external magnetic induction applied has been investigated. In detail, in a first study case, described in Fig. 4.32, a sinusoidal current with a frequency of 20 Hz and an amplitude of 10 mA value has been driven into the sensor and an external magnetic induction has been applied in the range [0 - 25] mT.

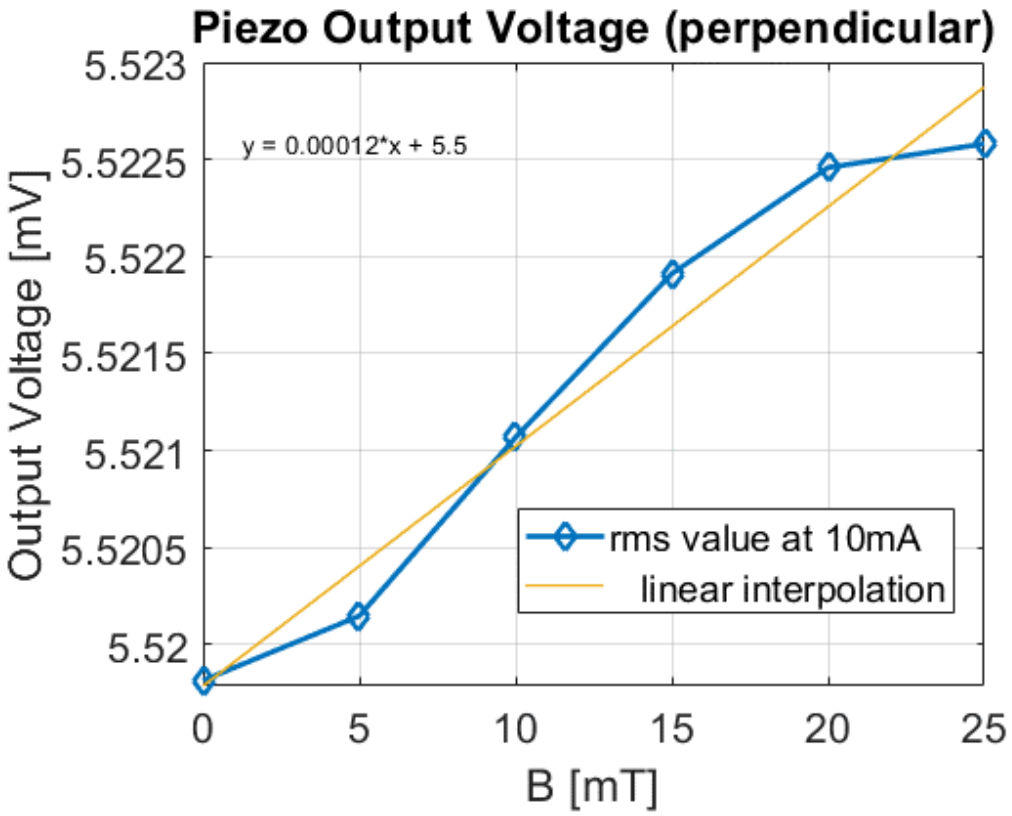

Fig. 4.32: The piezoelectric voltage as a function of the magnetic induction in the range [0 - 25] mT for a driving current of 10 mA and frequency of 20 Hz in perpendicular direction.

As can be noted the magnetic field sensor is capable of discerning several magnetic induction values in the range [0 - 25] mT, setting the sinusoidal driving current; in addition, in orange the linear interpolation is displayed. Eventually, it is essential to notice that a sensitivity of 12×10-5 V/T has been experimentally estimated.

In order to confirm the validity of the working principle and the correlation between the increase of the driving current and the increase of the performance in term of sensitivity another similar result has been acquired increasing the driving current to 40 mA and considering the same range [0 - 25] mT for the magnetic induction. In Fig. 4.33 the rms values of the output voltage as a function the magnetic induction applied are presented; it is interesting to note that an increase of

the piezoelectric voltage is measured in correspondence with the increase of *B* and an improvement of the performance has been certified, as expected, since a sensitivity value of 28×10-5 V/T has been estimated.

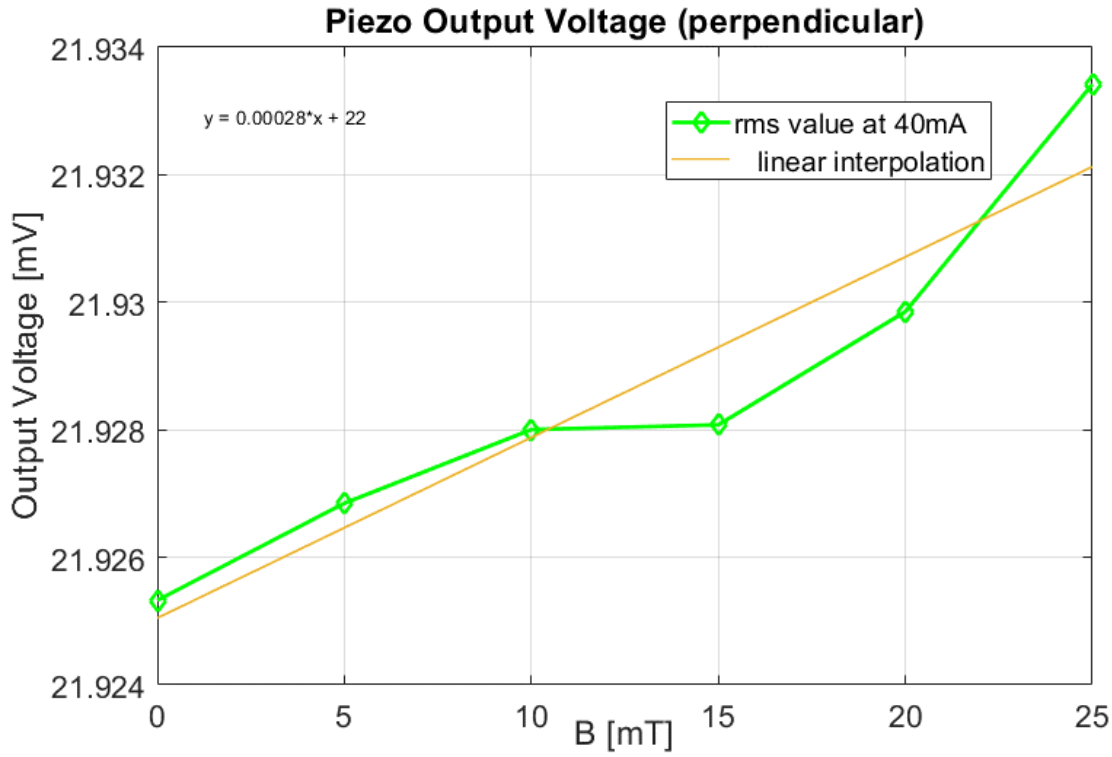

Fig. 4.33: The piezoelectric voltage as a function of the magnetic induction in the range [0 – 25] mT for a driving current of 40 mA and frequency of 20 Hz in perpendicular direction.

In order to demonstrate that the MEMS device operates as directional sensor the same measurements have been carried out rotating of 90° the magnetic field sensor (called "planar" direction) inside the yellow dipole. In this configuration the Lorentz force does not act along the preferential direction of deformation, therefore a reduced performance is expected. At first the piezoelectric output as a function of the AC driving current, having a frequency of 20 Hz and an

amplitude in range [0 - 100] mA_P with steps of 5 mA_P, has been analyzed, considering four different magnetic induction values, that are 5 mT, 10 mT. 15 mT and 20 mT. As can be observed in Fig. 4.34 the output voltage, expressed in term of rms (root mean quare) value, exhibits a linear trend with the increase of the driving current and therefore of the applied Lorentz force.

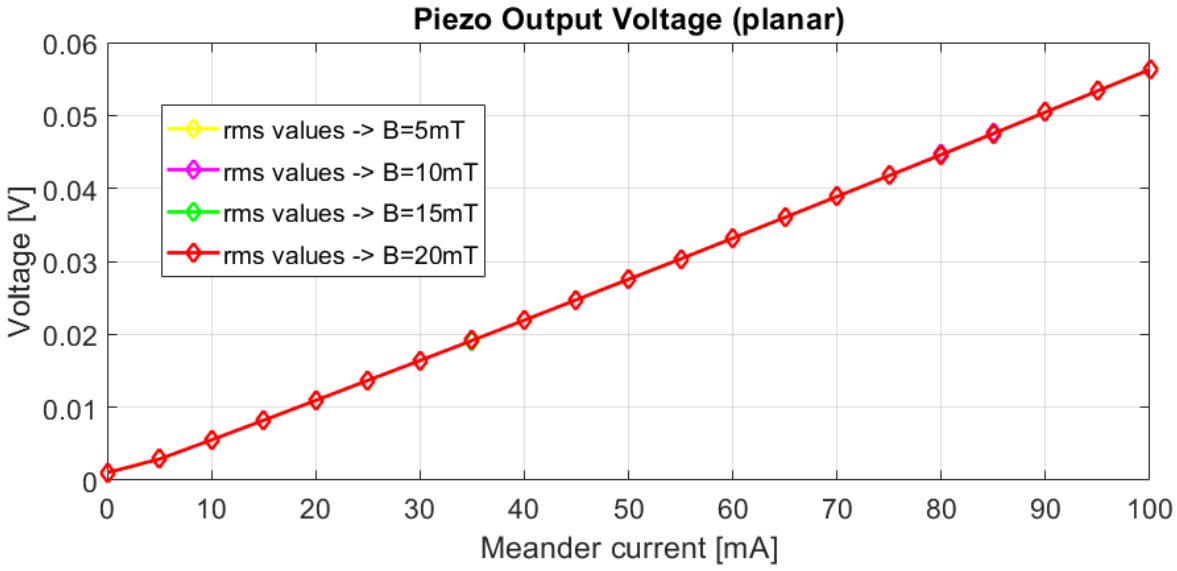

Fig. 4.34: Piezoelectric voltage as a function of the driving current in planar direction.

However, zooming in on the previous picture the MEMS device is not capable to discern several amplitudes of the magnetic induction for each value of the sinusoidal current with a coherent trend (as shown Fig. 4.35).

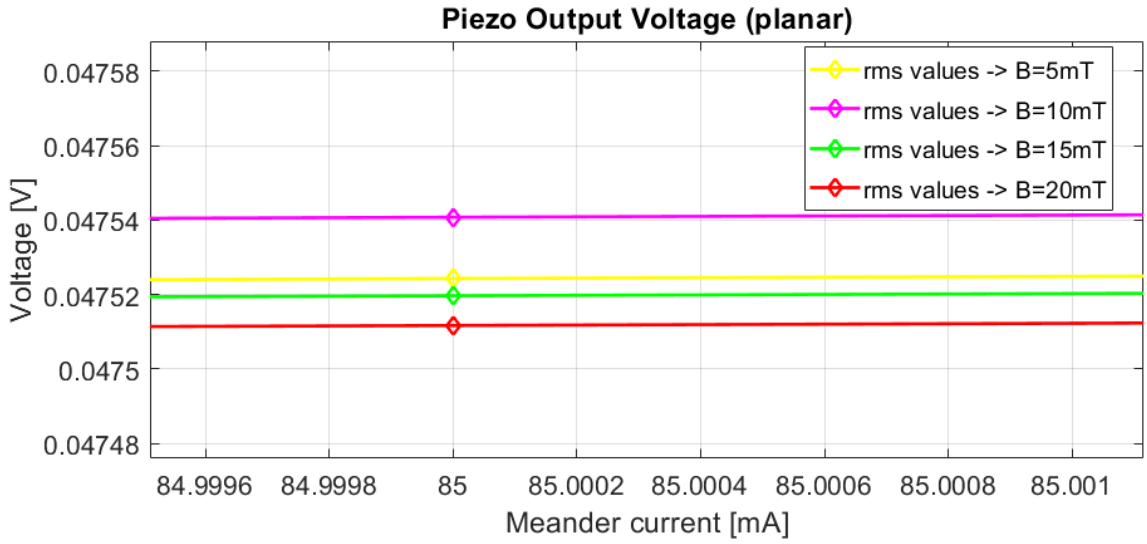

Fig. 4.35: Zoom of the piezoelectric voltage as a function of the driving current in planar direction.

In the next step the AC driving current into the MEMS sensor has been maintained constant and the piezoelectric output voltage as a function of the external magnetic induction has been explored. In particular, in order to compare planar and perpendicular directions the same operative conditions have been reproduced; hence, a sinusoidal current with a frequency of 20 Hz and an amplitude of 10 mA has been driven into the sensor and an external magnetic induction has been applied in the range [0 - 30] mT (as displayed in Fig. 4.36).

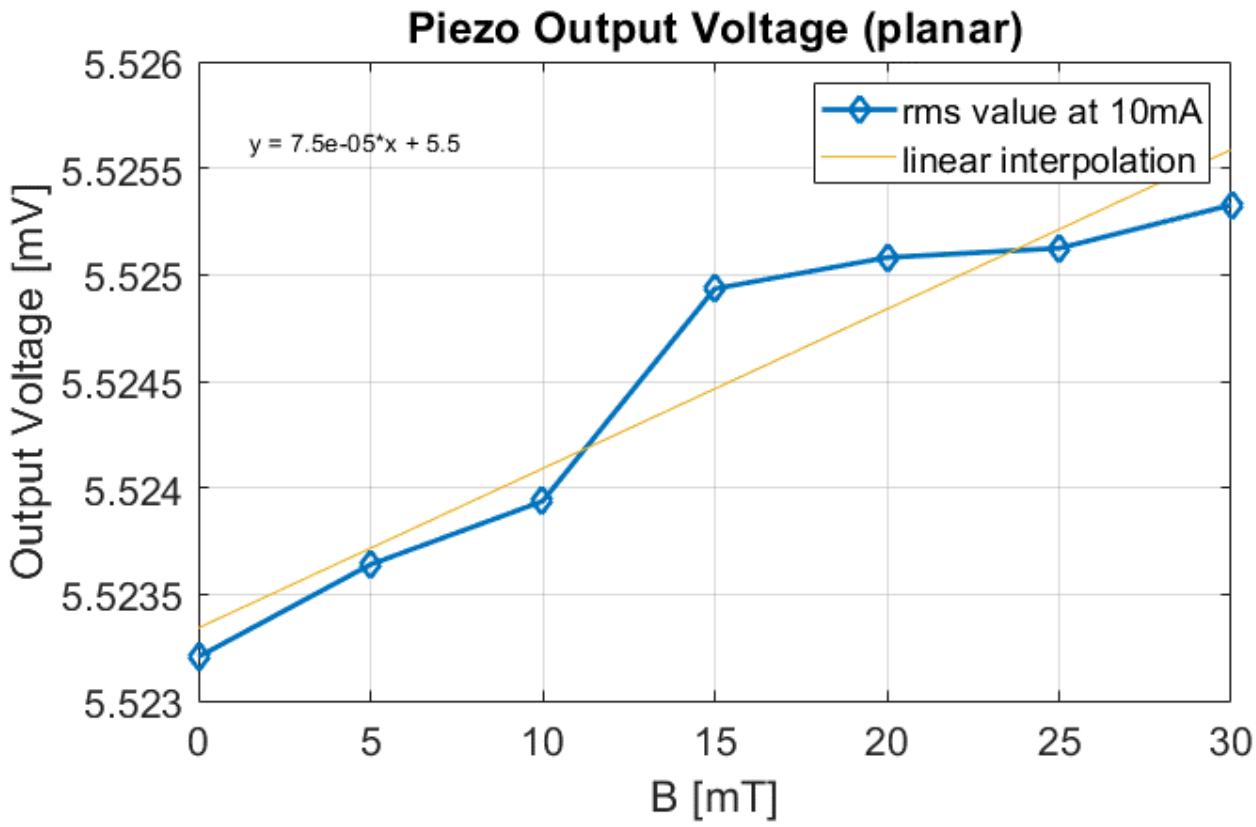

Fig. 4.36: The piezoelectric voltage as a function of the magnetic induction in the range [0 - 30] mT for a driving current of 10 mA and frequency of 20 Hz in planar direction.

It is evident that the MEMS sensor is capable of discerning several magnetic induction values in the range [0 - 30] mT, setting the sinusoidal driving current with a coherent trend; however it is essential to highlight that a lower sensitivity of 7.5×10-5 V/T has been experimentally evaluated than the perpendicular direction.

Finally, another similar result has been acquired increasing the driving current to 40 mA and considering the same range [0 - 30] mT for the magnetic induction. In Fig. 4.37 the output voltage, expressed in terms of rms values, as a function the magnetic induction applied is illustrated; it is noteworthy to note that an increase of the piezoelectric voltage is measured in

correspondence with the increase of *B* and an improvement of the performance has been confirmed, as expected, since a sensitivity value of 25×10-5 V/T has been estimated.

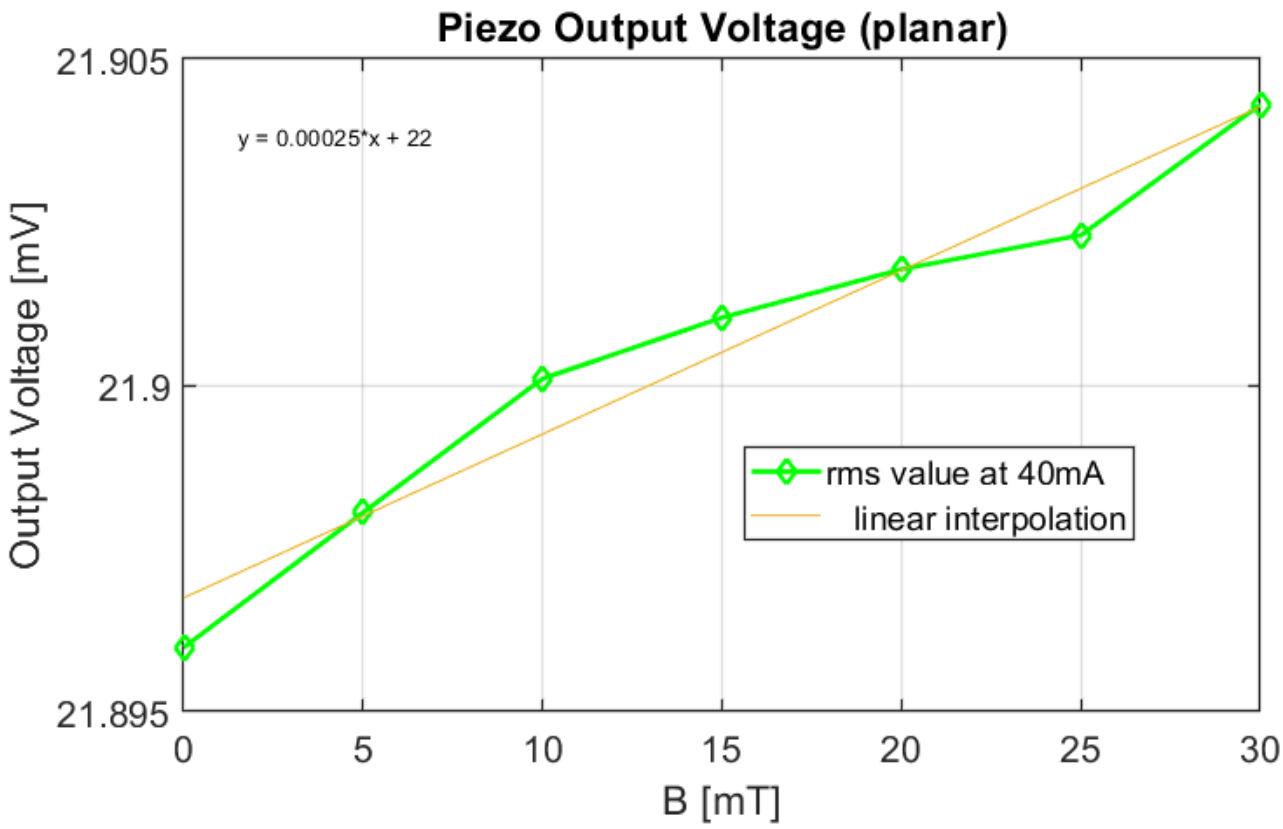

Fig. 4.37: The piezoelectric voltage as a function of the magnetic induction in the range [0 – 30] mT for a driving current of 40 mA and frequency of 20 Hz in planar direction.

In conclusion, the following table (see Table 18) allows to compare the performance of the meander MEMS sensor in two operative directions and to affirm that the sensitivity is directly correlated with the sinusoidal current driven into the device and, furthermore, the planar direction is less sensitive than the perpendicular direction.

Meander MEMS sensor	*Perpendicular direction*	*Planar direction*
AC driving current: 10 mA	**S=12×10-5 V/T**	**S=7.5×10-5 V/T**
AC driving current: 40 mA	**S=28×10-5 V/T**	**S=25×10-5 V/T**

Table 18: Comparison in terms of sensitivity of two working directions for MEMS device.

4.1.5 "Medium" simple U-shaped beam cantilever as Magnetic field sensor

In order to compare the new meander architecture with the "classic" U-shaped beam cantilever the "medium" structure of simple U-shaped beam cantilever has been considered, utilizing the same experimental setup and almost the same procedure. In detail, the experimental setup is always illustrated in Fig. 4.25, the acquisition procedure is the same, whereas in post-processing analysis the maximum value of the FFT (Fast Fourier Transform) in the piezoelectric output voltage has been evaluated, and, finally, two directions, perpendicular and planar, have been investigated; however, taking account into that the architecture to be examined is less flexible, a wide magnetic induction range has been analyzed. In order to carry out the characterization two different orientations of the medium U-shaped beam device inside the dipole have been analyzed, for the identical motivations discussed previously. A polystyrene structure has been implemented in order to provide a rigid support to the PCB board with the MEMS sensor in both directions without introducing electromagnetic interference; in Figs. 4.38a-b two investigated orientations

are illustrated: in particular, the perpendicular direction is shown in Fig 4.38a and the planar direction is displayed in Fig. 4.38b.

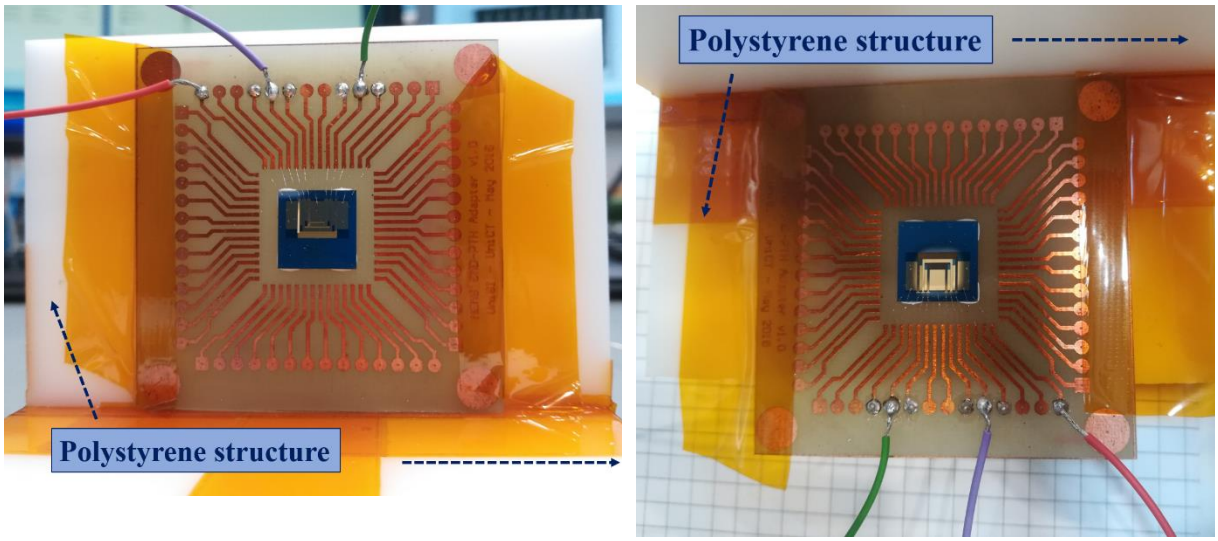

(a) (b)

Fig. 4.38: Medium U-shaped beam cantilever device: (a) Perpendicular direction; (b) Planar direction.

Also in this study case, the orientation of the integrated sensor implicates a different Lorentz force application: in detail, in the perpendicular condition the Lorentz force is applied in the direction of preferential tip deformation, guaranteeing the maximum displacement and thus the greatest output voltage, whereas in planar condition the Lorentz force is imposed along a direction that does not introduce a tip deformation, and thus no output signal.

Since the U-shaped beam cantilever sensor "feels" the magnetic field in directional way, two configurations have been analyzed in order to validate the working principle.

Consequently, as regards the perpendicular direction case, the experimental setup illustrated previously in Fig. 4.25 has been used with the MEMS device oriented as shown in Fig. 4.39. As

first step, the resonance frequency has been investigated applying a sinusoidal current into the MEMS device, having a fixed amplitude of 50 mA_P and a frequency range of [0 - 100] Hz, and thus acquiring through a LabVIEW routine the piezoelectric voltage and evaluating, in post-processing, the maximum amplitude of the FFT of the output voltage. It is important to specify that the frequency range has been selected taking account into the FEM results reached in COMSOL Multiphysics; indeed, in accordance with the Fig. 3.41 a resonance frequency of 70 Hz has been experimentally estimated.

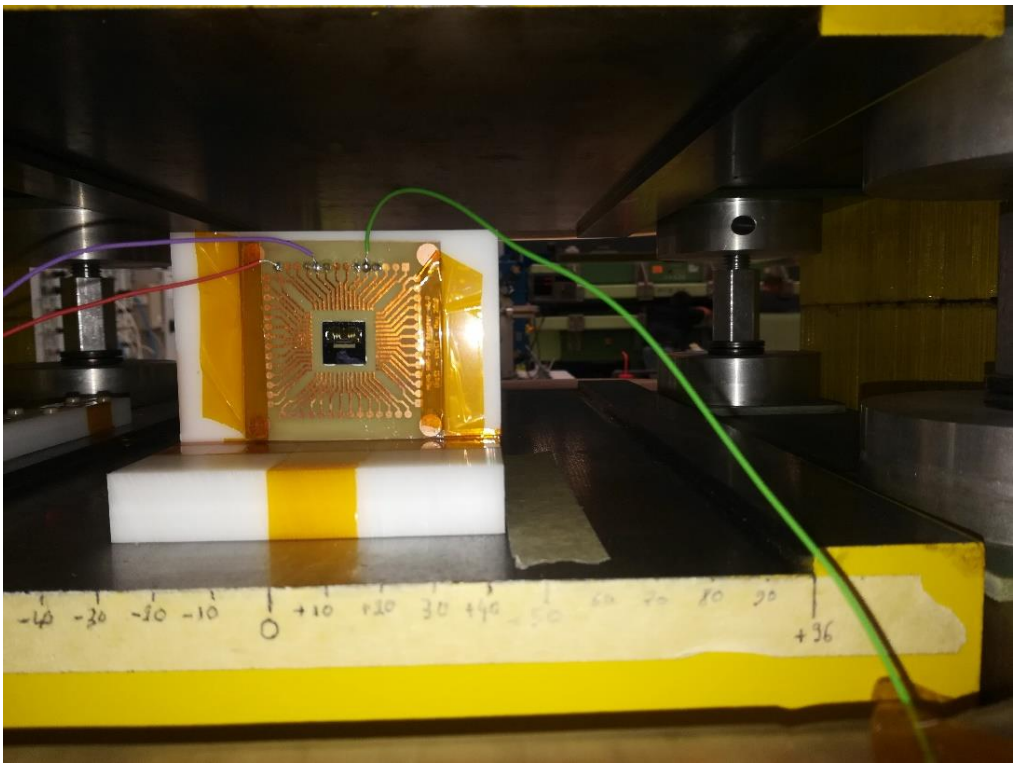

Fig. 4.39: "Medium" U-shaped beam cantilever sensor into the dipole: perpendicular direction.

Therefore, in order to proceed with the characterization, a sinusoidal current having a frequency of 70 Hz and an amplitude in the range [0 - 100] mA_P, provided by the AC current source, is

driven into the MEMS sensor; a teslameter is placed inside the dipole in order to monitor the DC magnetic field generated, whereas the MEMS device is connected through the LEMO connectors to the AC current source as input and to the DAQ board as output. It is believed worthy to highlight that another magnetic induction range has been adopted and, as a consequence, other specifications have been imposed to the power converter; in particular, in order to implement a magnetic induction in the range [0 - 500] mT, a ramp of 50 A/s has been established to the power converter and a suitable DC current has been supplied (see Table 19) respecting the ratio 0.877165 mT/A:

DC current by power converter	***Ramp***	***Magnetic induction into the dipole***
57 A	50 A/s	50 mT
114 A	50 A/s	100 mT
228 A	50 A/s	200 mT
342 A	50 A/s	300 mT
456 A	50 A/s	400 mT
570 A	50 A/s	500 mT
684 A	50 A/s	600 mT

Table 19: Correlation between the DC current supplied by the power converter and the magnetic induction generated into the dipole in the "Medium" U-shaped device: List of DC current values imposed.

Also in this case, the piezoelectric output as a function of the AC driving current has been analyzed, where the sinusoidal current has a frequency of 70 Hz and an amplitude in range [0 - 100] mA_P with steps of 5 mA_P, and six different magnetic induction values, that are 50 mT, 100 mT. 200 mT, 300 mT, 400 mT and 500 mT, have been applied. In Fig. 4.40 the output

voltage, expressed in term of maximum value of the FFT of the piezoelectric voltage, is presented and it is interesting to observe a linear trend with the increase of the driving current and therefore of the applied Lorentz force.

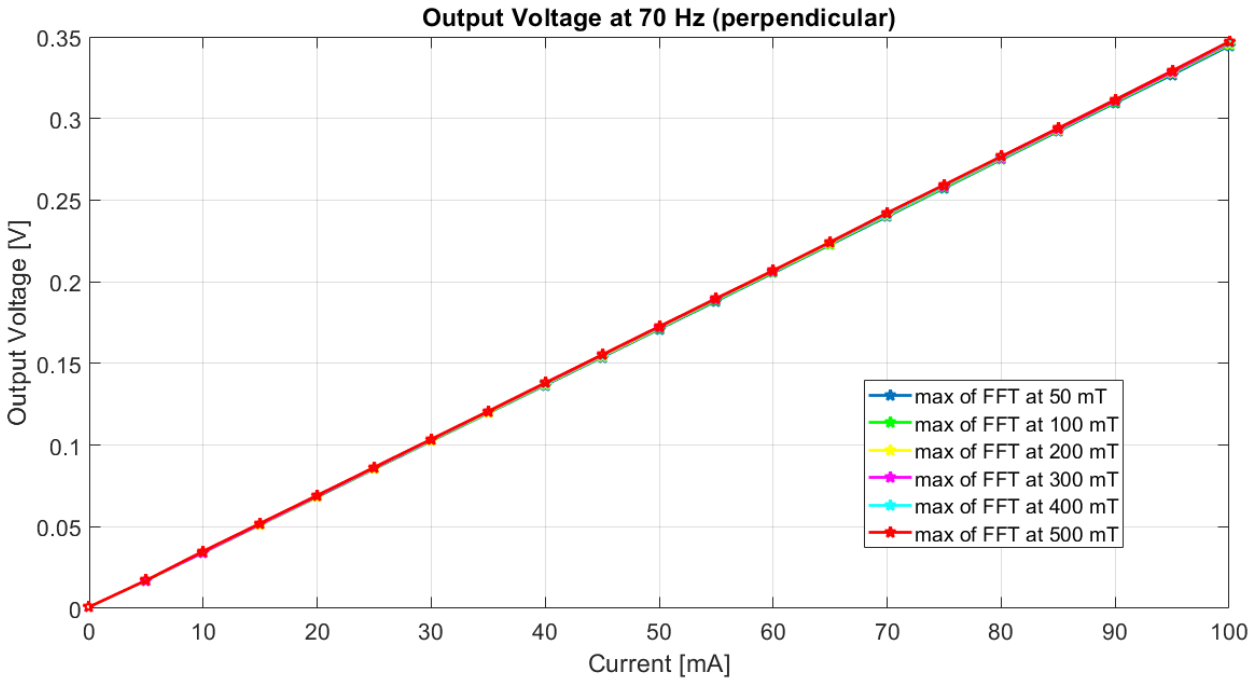

Fig. 4.40: "Medium" U-shaped cantilever sensor: Piezoelectric voltage as a function of the driving current in perpendicular direction.

Zooming in on the Fig. 4.40 it is intriguing to notice that the MEMS device "feels" and detects several amplitudes of the magnetic induction for each value of the sinusoidal current with a coherent behavior (see Fig. 4.41).

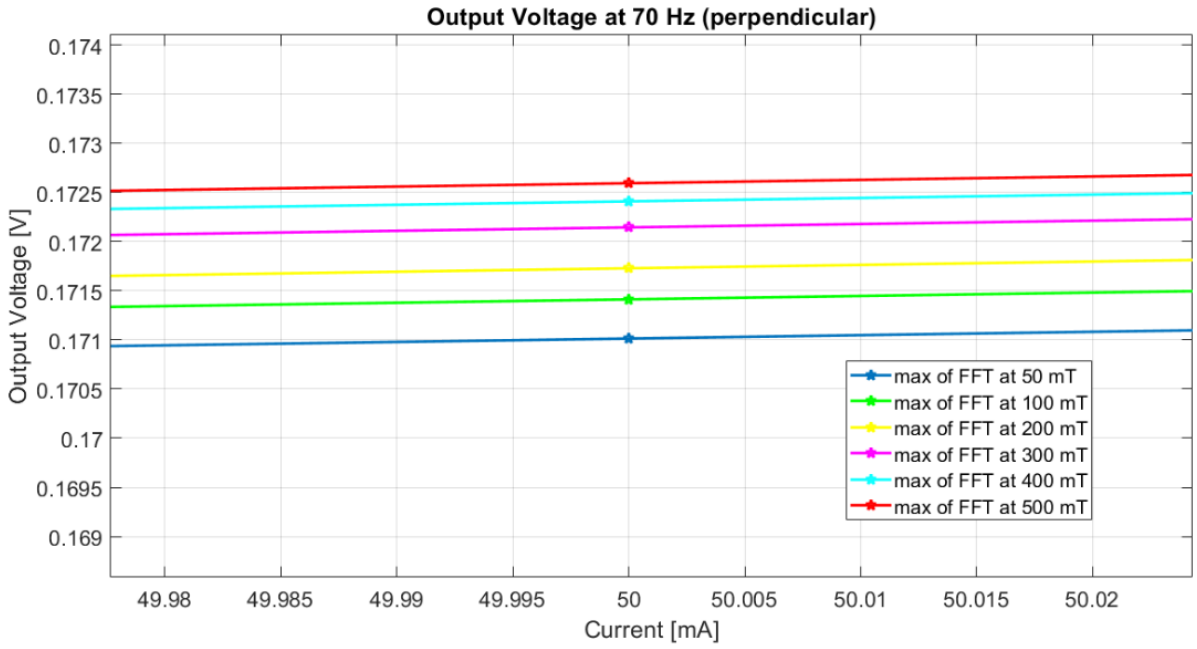

Fig. 4.41: "Medium" U-shape beam sensor: Zoom of the piezoelectric voltage as a function of the driving current in perpendicular direction.

Thereafter, the AC driving current into the MEMS sensor has been kept constant and the piezoelectric output voltage as a function of the external magnetic induction applied has been examined. In detail, in Fig. 4.42 the output voltage, expressed in terms maximum amplitude of the FFT, as a function of an external magnetic induction is proposed, in which a sinusoidal current with a frequency of 70 Hz and an amplitude of 20 mA has been driven into the sensor and an external magnetic induction has been applied in the range [0 - 600] mT.

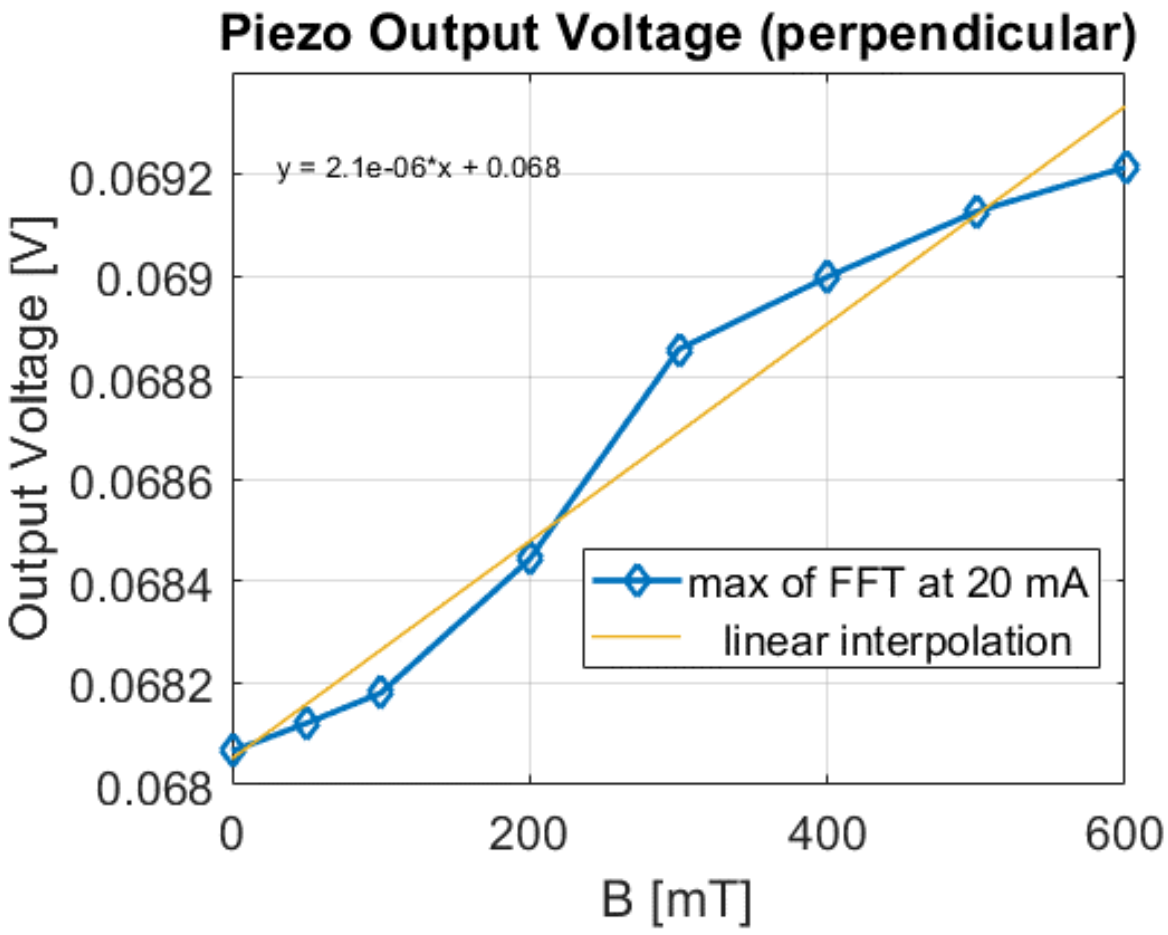

Fig. 4.42: "Medium" U-shaped beam sensor: The piezoelectric voltage as a function of the magnetic induction in the range [0 - 600] mT for a driving current of 20 mA and frequency of 70 Hz in perpendicular direction.

It is interesting to observe that the magnetic field sensor is capable of distinguish several magnetic induction values in the range [0 - 600] mT, setting the sinusoidal driving current at 20 mA; in addition, in orange the linear interpolation is displayed. Eventually, it is essential to notice that a sensitivity of 2.1×10-6 V/T has been experimentally estimated.

In order to validate the working principle and the correlation between the increase of the driving current and the increase of the performance in term of sensitivity another similar result has been acquired increasing the driving current to 60 mA and considering the same range [0 - 600] mT for the magnetic induction. In Fig. 4.43 the maximum values of FFT of the output voltage as a

function the magnetic induction applied are presented; it is interesting to note that an increase of the piezoelectric voltage is measured in correspondence with the increase of *B* and an improvement of the performance has been certified, as expected, since a sensitivity value of 2.6×10-6 V/T has been estimated.

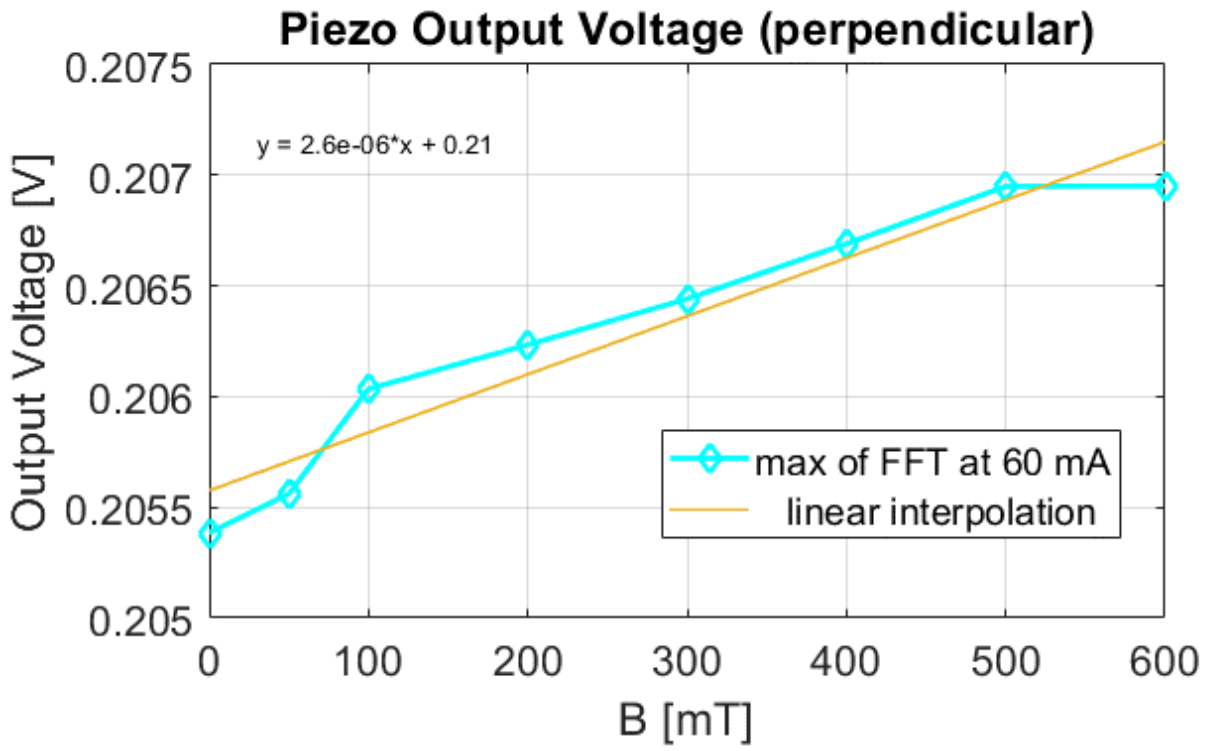

Fig. 4.43: "Medium" U-shaped beam device: The piezoelectric voltage as a function of the magnetic induction in the range [0 – 600] mT for a driving current of 60 mA and frequency of 70 Hz in perpendicular direction.

In order to demonstrate that the MEMS device operates as directional sensor the same measurements have been carried out rotating of 90° the magnetic field sensor ("planar" direction) inside the yellow dipole. In this configuration the Lorentz force does not act along the preferential direction of deformation, therefore a reduced performance is expected. Firstly, the piezoelectric output as a function of the AC driving current, having a frequency of 70 Hz and an

amplitude in range [0 - 100] mA_P with steps of 5 mA_P, has been analyzed, considering six different magnetic induction values, that are 50 mT, 100 mT. 200 mT, 300 mT, 400 T and 500 mT. As can be observed in Fig. 4.44 the output voltage, expressed in terms of maximum amplitude of FFT, exhibits a linear trend with the increase of the driving current and therefore of the applied Lorentz force.

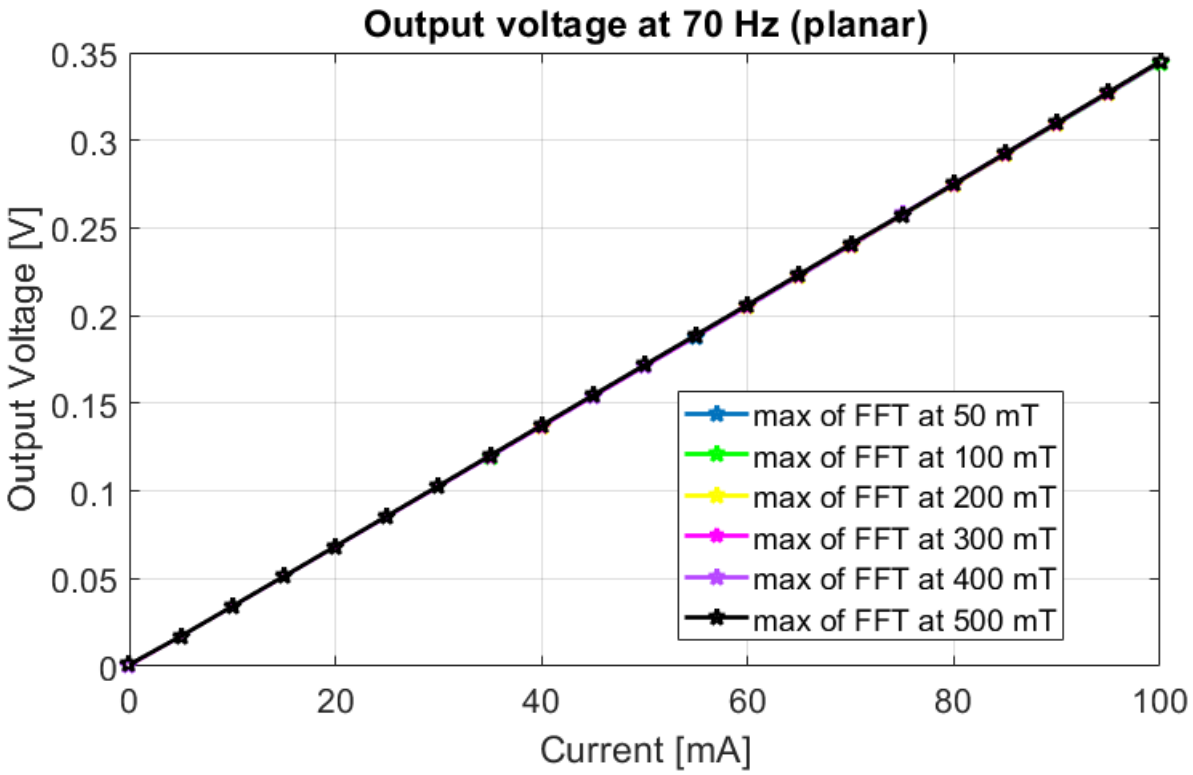

Fig. 4.44: "Medium" U-shaped beam device: Piezoelectric voltage as a function of the driving current in planar direction.

Nevertheless, a careful observation allowed to discover that the MEMS device is not capable to discern several amplitudes of the magnetic induction for each value of the sinusoidal current with a coherent trend (as shown Fig. 4.45).

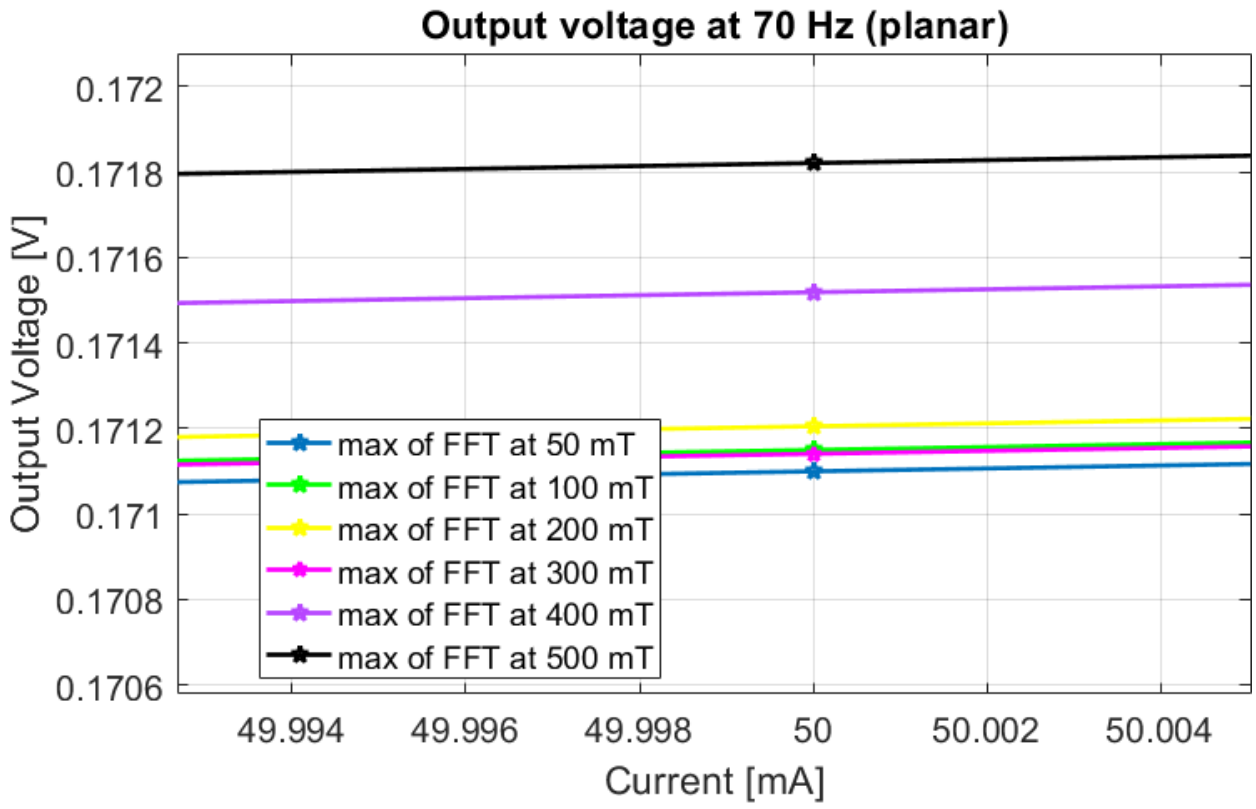

Fig. 4.45: "Medium" U-shaped beam device: Zoom of the piezoelectric voltage as a function of the driving current in planar direction.

Afterwards, the AC driving current into the MEMS sensor has been maintained constant and the piezoelectric output voltage as a function of the external magnetic induction has been investigated. In particular, in order to compare planar and perpendicular directions the same operative conditions have been reproduced; hence, a sinusoidal current with a frequency of 70 Hz and an amplitude of 20 mA has been driven into the sensor and an external magnetic induction has been applied in the range [0 - 600] mT (as displayed in Fig. 4.46).

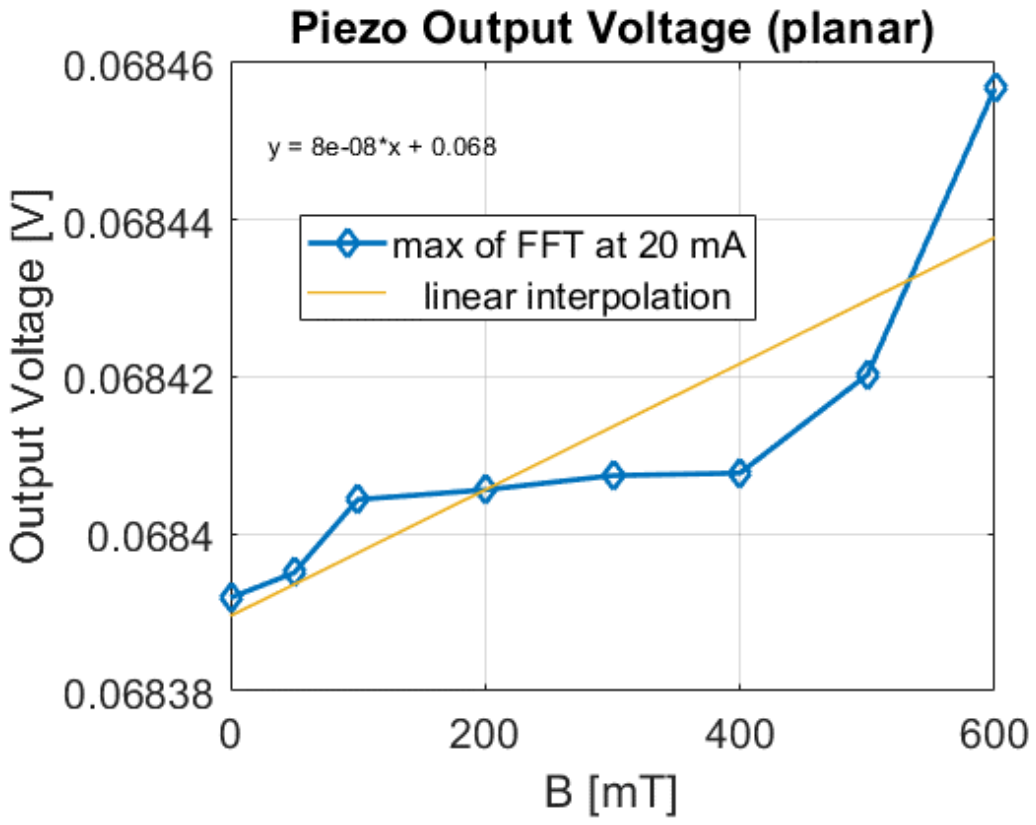

Fig. 4.46: "Medium" U-shaped beam device: The piezoelectric voltage as a function of the magnetic induction in the range [0 - 600] mT for a driving current of 20 mA and frequency of 70 Hz in planar direction.

Also in this case, the MEMS sensor is capable of measure several magnetic induction values in the range [0 - 600] mT, fixing the sinusoidal driving current with a coherent trend; however it is essential to highlight that a lower sensitivity of 8×10-8 V/T has been experimentally measured than the perpendicular direction.

Eventually, another similar result has been detected increasing the driving current to 60 mA and considering the same range [0 - 600] mT for the magnetic induction. In Fig. 4.47 the output voltage, expressed in terms of maximum value of the FFT, as a function the magnetic induction applied is illustrated; it is fascinating to note that an increase of the piezoelectric voltage is

measured in correspondence with the increase of *B* and an improvement of the performance has been confirmed, as expected, since a sensitivity value of 9.9×10-7 V/T has been estimated.

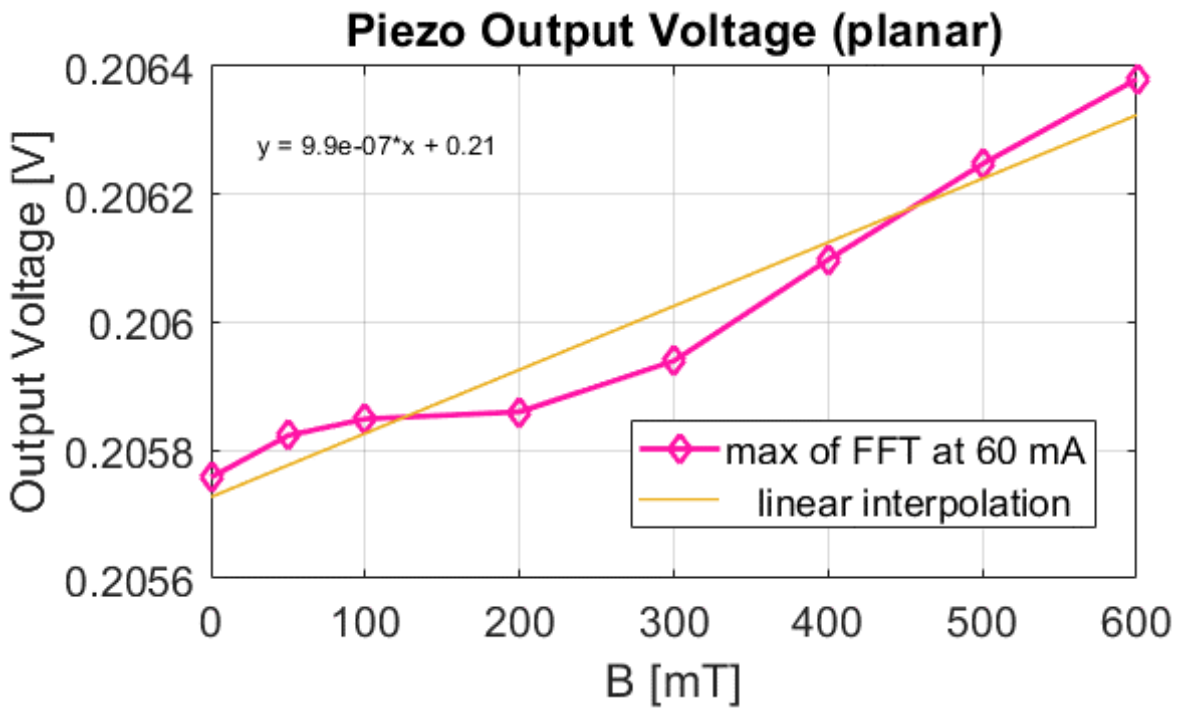

Fig. 4.47: "Medium" U-shaped beam device: The piezoelectric voltage as a function of the magnetic induction in the range [0 – 600] mT for a driving current of 60 mA and frequency of 70 Hz in planar direction.

In conclusion, the performance in terms of sensitivity of the "Medium" U-shaped beam sensor in two operative directions are listed in Table 20 and it is possible to affirm that the sensitivity is directly correlated with the sinusoidal current driven into the device and, furthermore, the planar direction is less sensitive than the perpendicular direction.

"Medium" U-shaped beam sensor	*Perpendicular direction*	*Planar direction*
AC driving current: 20 mA	**S=2.1×10-6 V/T**	**S=8×10-8 V/T**
AC driving current: 60 mA	**S=2.6×10-6 V/T**	**S=9.9×10-7 V/T**

Table 20: "Medium" U-shaped beam device: Comparison in terms of sensitivity of two working directions.

4.2 Foundry run number PiezoMUMPs-19

This section is dedicated to the second run PiezoMUMPs in which a differential configuration and a reduced version of the Meander MEMS prototype and the "classic" U-shaped beam cantilever have been implemented in order to perform magnetic field measurements in Paradox Engineering company, in Novazzano, for the "smart city parking" application. Just for completeness, two designs have been submitted and commissioned in September 2019 and they have been spent and arrived in January 2020.

The dies are shown in Figs. 4.48a-b: in accordance with the previous layout, electrodes have been introduced to perform a double role, represented by the capacitive damping and the capacitive readout strategy. Furthermore, in the differential configuration the second inertial mass has been deleted due to a reduction of the active area, and, for the equal reason, a meander has been removed, thus decreasing the flexibility.

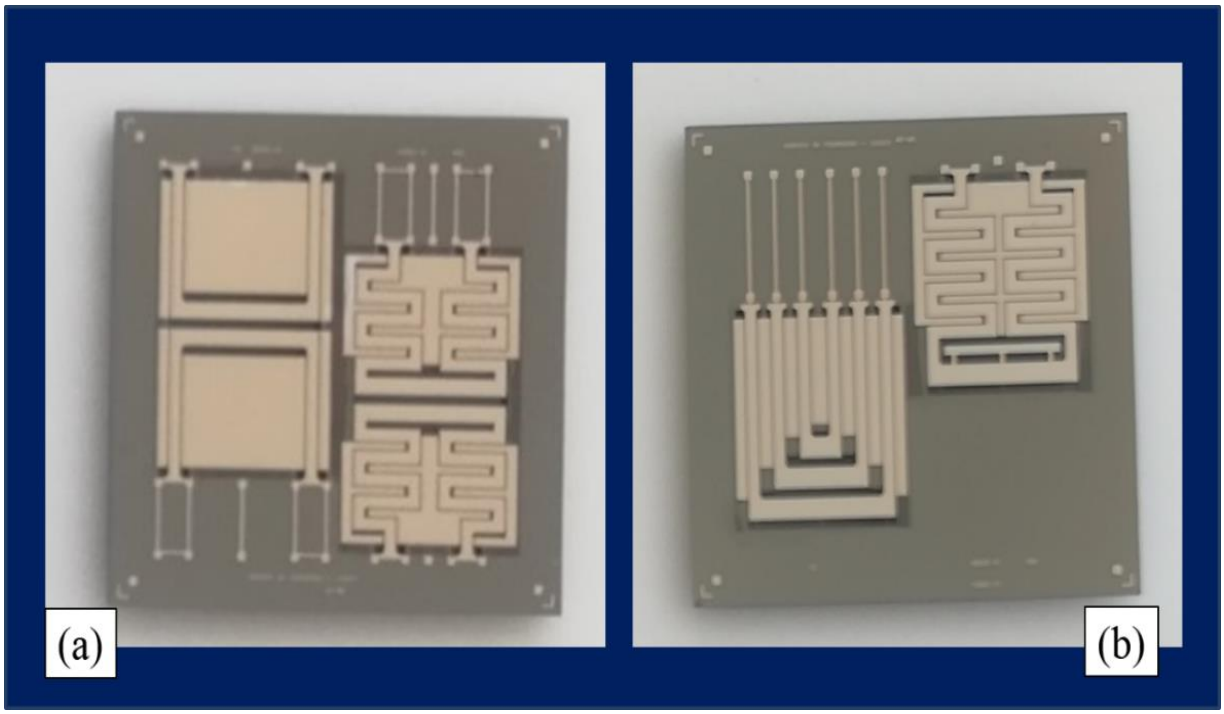

Fig. 4.48: Second run die of both prototypes: (a) Differential configuration; (b) Reduced version.

Although the following aspect has been previously discussed it is considered necessary to remark that two designs did not assemble on the same plane in order to save the robustness of the die due to the wide TRENCH area. In order to proceed with the characterization both dies have been packaged and bonded (see Figs 4.49 a-b) with the support of STMicroelectronics company, located in Catania's site.

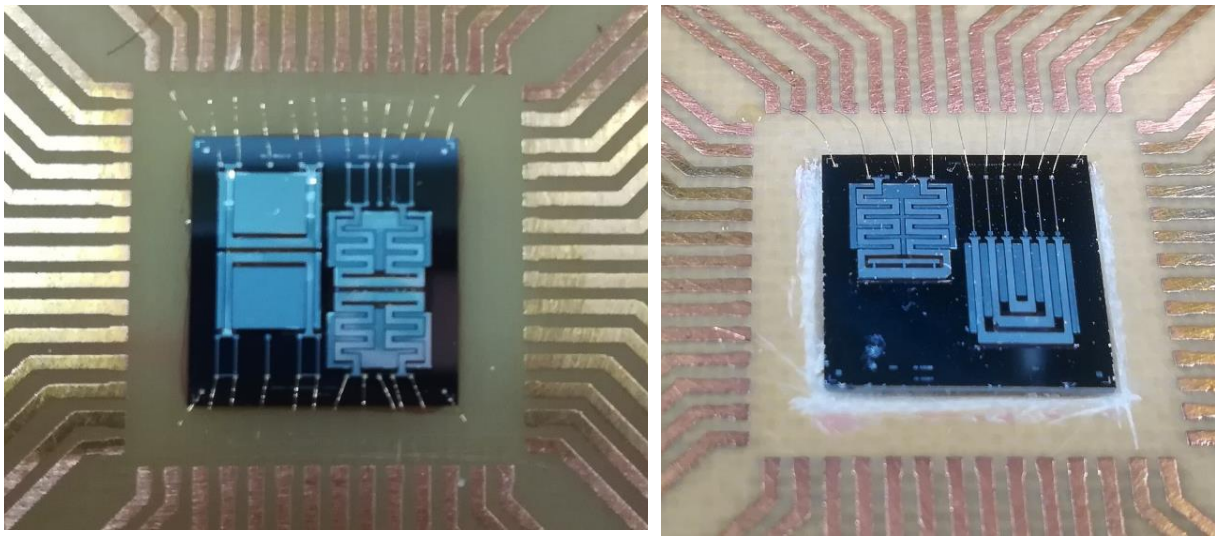

(a) (b)

Fig. 4.49: Packaging and bonding in: (a) Differential configuration; (b) Reduced version.

4.2.1 Driving and Conditioning circuits

For the purpose of characterizing new prototypes a suitable experimental setup has been studied and analyzed. It is important to specify that in both cases a V-I converter has been used to provide a known AC current into the MEMS devices, whereas a different acquisition system has been adopted to process the output voltage coming from the deformation of the piezoelectric layer (AlN).

In detail, as concerns the resized MEMS sensors in Fig. 4.50 the working principle is described: as it can be observed a V-I converter is used to drive an AC current into the MEMS device and the output voltage, correlated to the mechanical deformation of the AlN stack which is actuated by Lorentz force in presence of an external magnetic field, is acquired by a DAQ board (NI-

USB 6255) through a suitable LabVIEW routine. The post-processing analysis is implemented in Matlab & Simulimk.

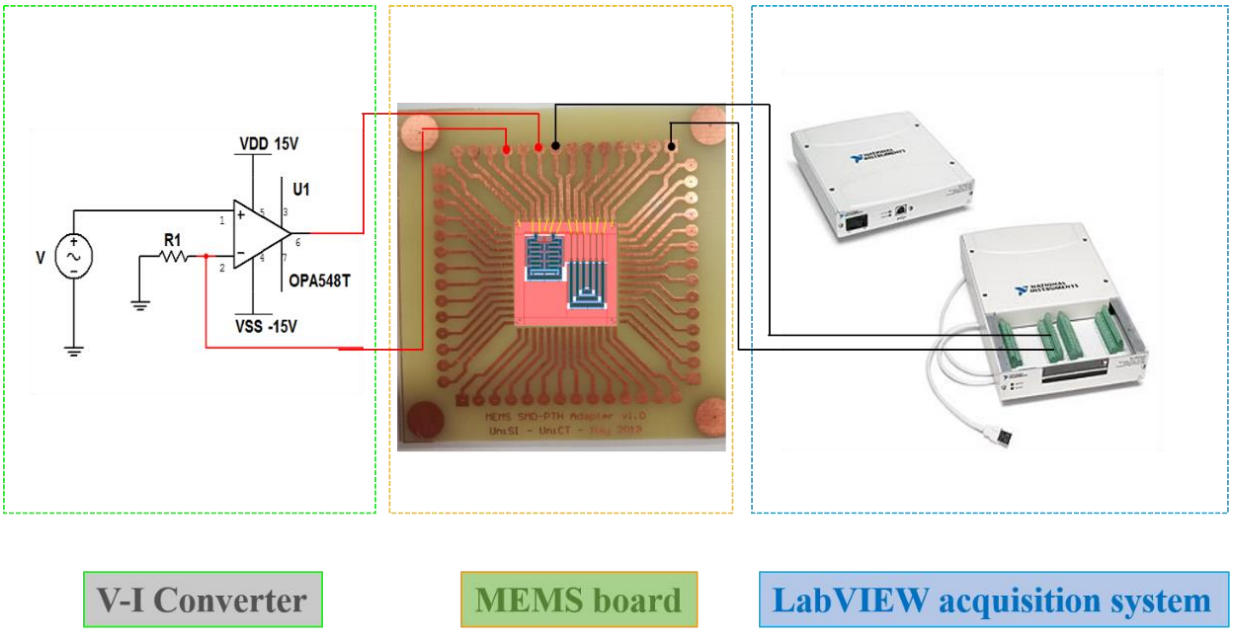

Fig. 4.50: The working principle in reduced MEMS prototypes.

As regards the second configuration, a dissimilar approach has been borrowed to process the differential signal related to the two microelectromechanical systems that operate in phase opposition. It is noteworthy to underline that the driving circuit did not change, and it is represented by a V-I converter, without any consideration, in this context, about the opportunity of using a low power circuit to generate the required current. In relation to the conditioning circuit a detailed investigation has been carried out taking into account the need to manipulate a differential signal that could require suitable techniques in order to reduce the noise and, probably, to amplify the voltage descending from the difference between two output voltages of two meander MEMS devices. For this reason, an operational amplifier having very high accuracy

has been inspected selecting, at the end, the STZ121 component (produced by STMicroelectronics), which exhibits an input offset voltage of 5 μV at 25 °C. In particular, the STZ121 operational amplifier has been used in a precision instrumentation amplifier schematic, as illustrated in Fig. 4.51, where the resistor R_g is utilized to modify the amplification gain.

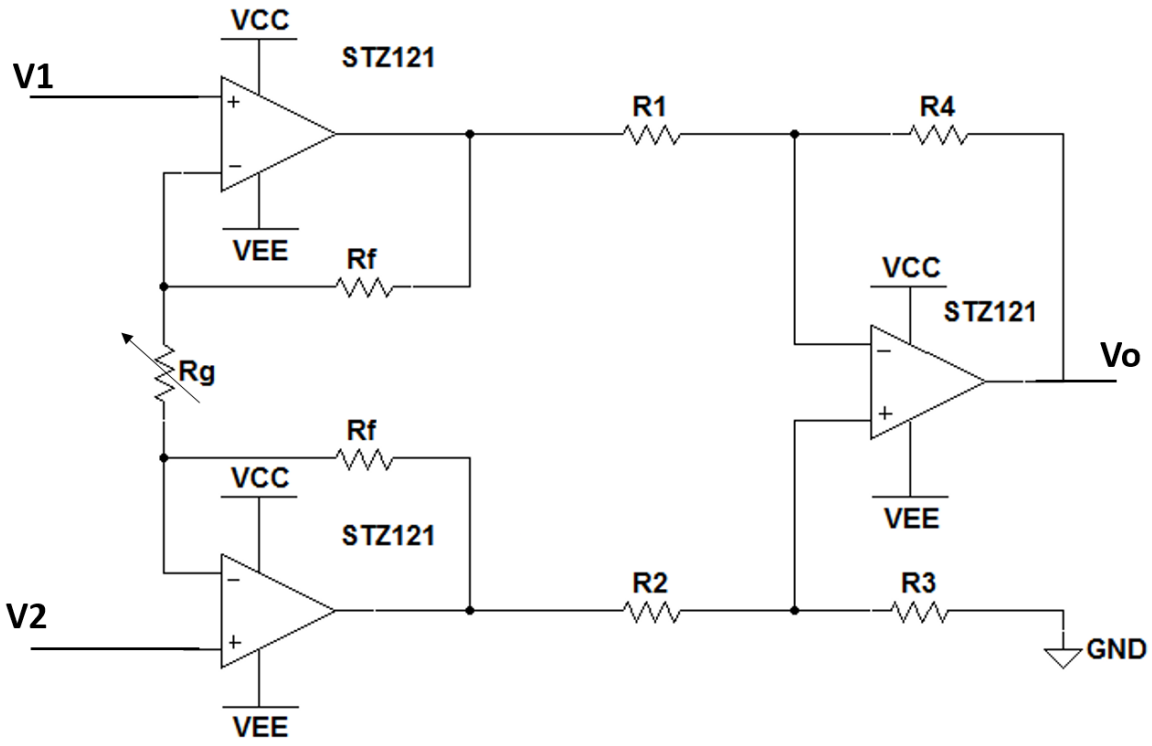

Fig. 4.51: Instrumentation amplifier schematic.

It is interesting to mention that if $R_1 = R_2$ and $R_3 = R_4$ the transfer function assumes the following expression:

$$V_o = (V_2 - V_1) \cdot \left[\frac{R_4}{R_2} \cdot \frac{2 \cdot R_f}{R_g} + 1\right] \tag{4.6}$$

Therefore, the working principle of MEMS prototypes in differential configuration is presented in Fig. 4.52, in which a sinusoidal current, generated by the V-I converter, is driven into the MEMS devices connected in series, whereas the output voltages are sent to the instrumentation amplifier.

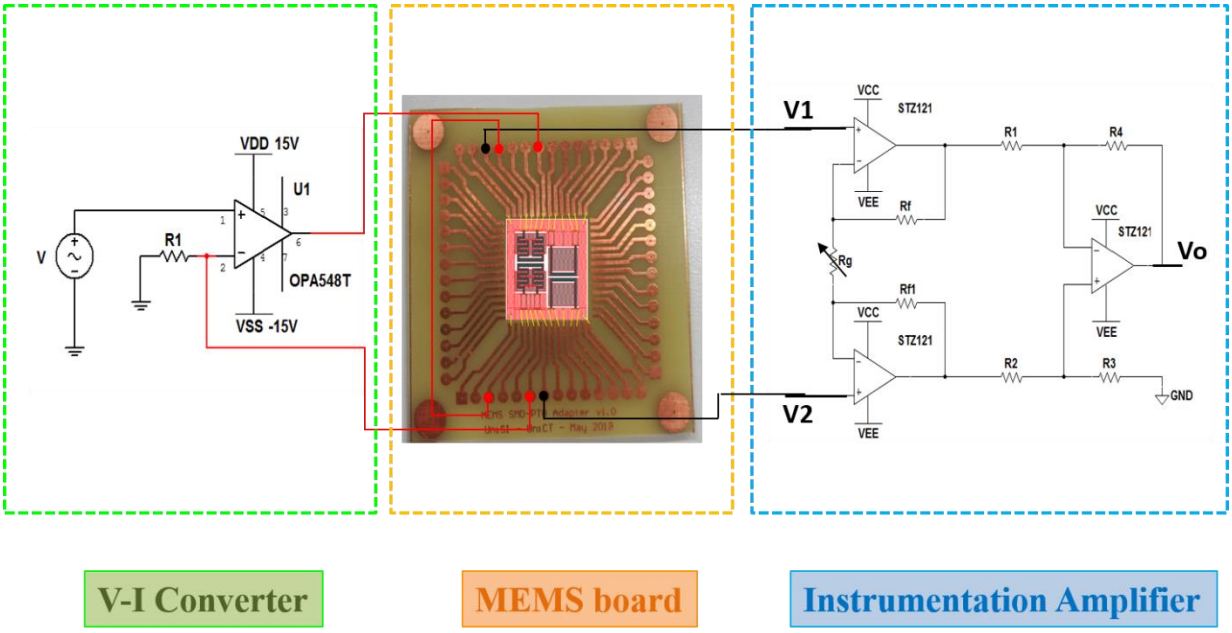

Fig. 4.52: The working principle of MEMS prototypes in differential configuration.

Just to clarify, it is believed important to specify that two MEMS devices have been connected in a specific way in order to satisfy the condition described in Fig. 3.61; hence, a focus on the input current path is shown in Figs. 4.53a-b, where it is possible to observe how the suitable connection between the MEMS sensors (see Fig. 4.53a) allows the current to flow on the tips in the opposite directions guaranteeing the differential principle (as illustrated in Fig. 4.53b).

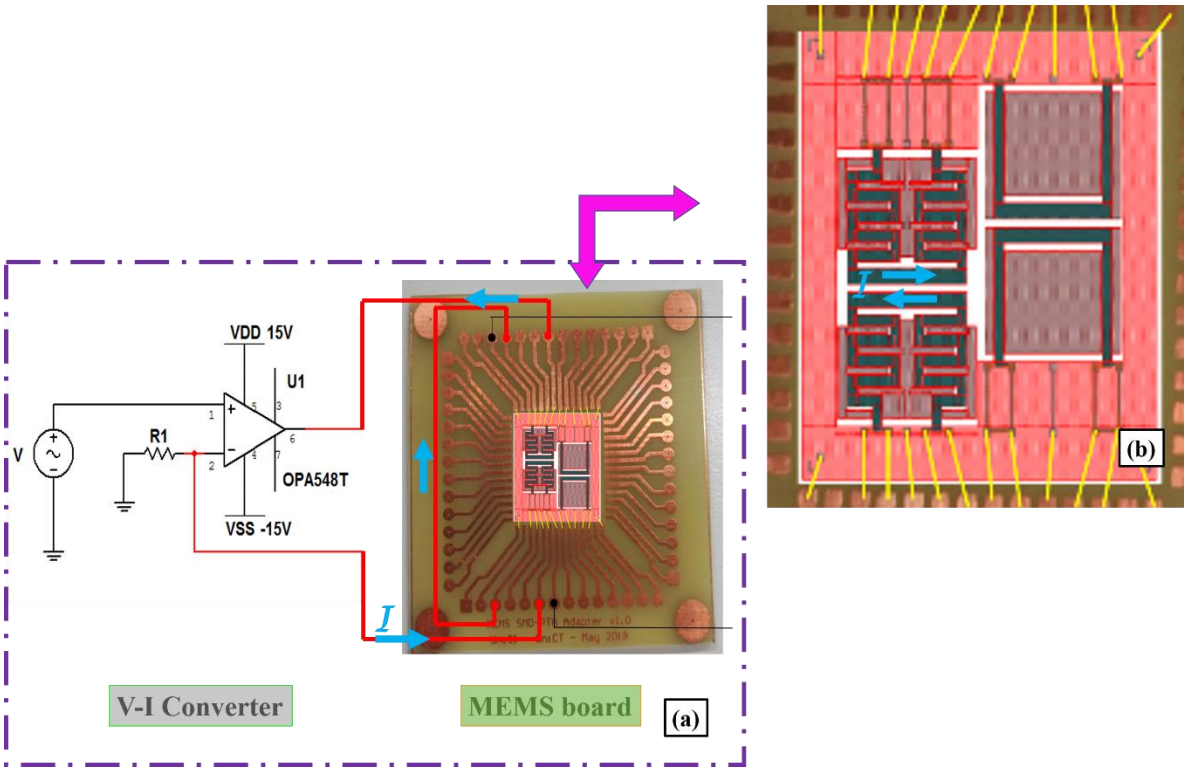

Fig. 4.53: Focus on differential configuration: (a) Series connection between MEMS devices; (b) Current path on the tips of MEMS sensors.

Moreover, in order to reduce the noise sources two PCB boards, acronym for Printed Circuit Board, have been implemented using an appropriate CAD, KiCad, that is user friendly enough. Two different layouts, related to the driving and conditioning circuits, have been realized, as shown in Figs 4.54a-b, where the yellow frame indicates the edge cuts, whereas the copper tracks are displayed in red and they have a width of 250 μm. Just to specify, in Fig. 4.54a the layout of the V-I converter is presented, on the contrary the instrumentation amplifier layout is exhibited in Fig. 4.54b.

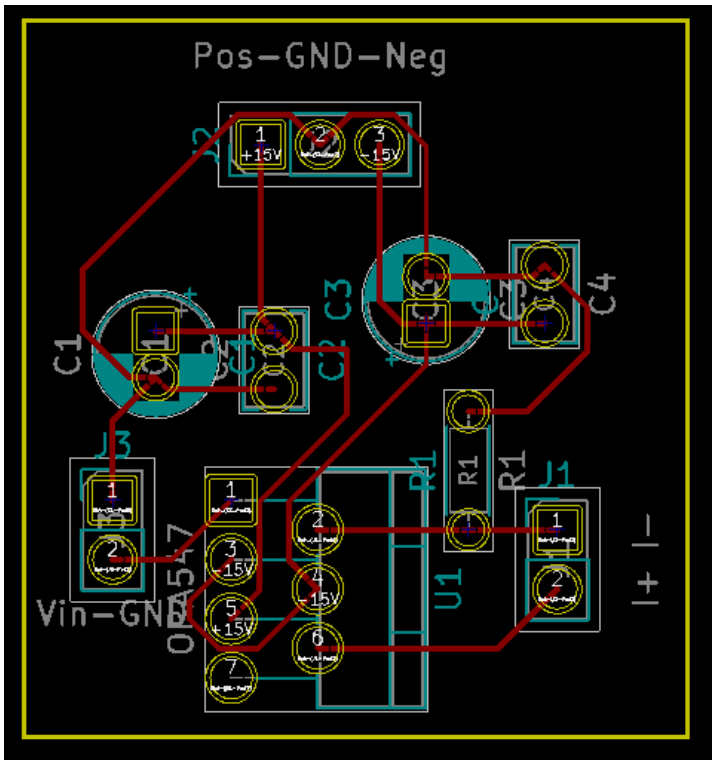

(a)

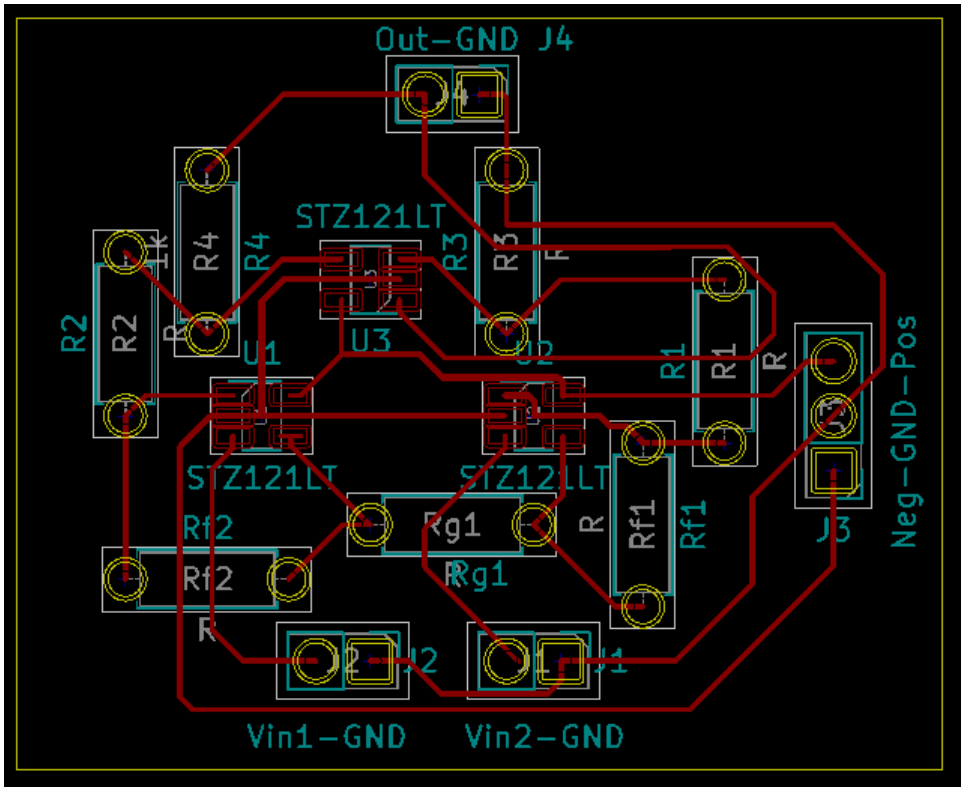

(b)

Fig. 4.54: PCB layouts: (a) The V-I converter; (b) The instrumentation amplifier.

Therefore, at the end, replacing the PCB boards to the schematics illustrated in Fig. 4.52 the following flow chart with the MEMS device and real circuits is proposed in Fig. 4.55.

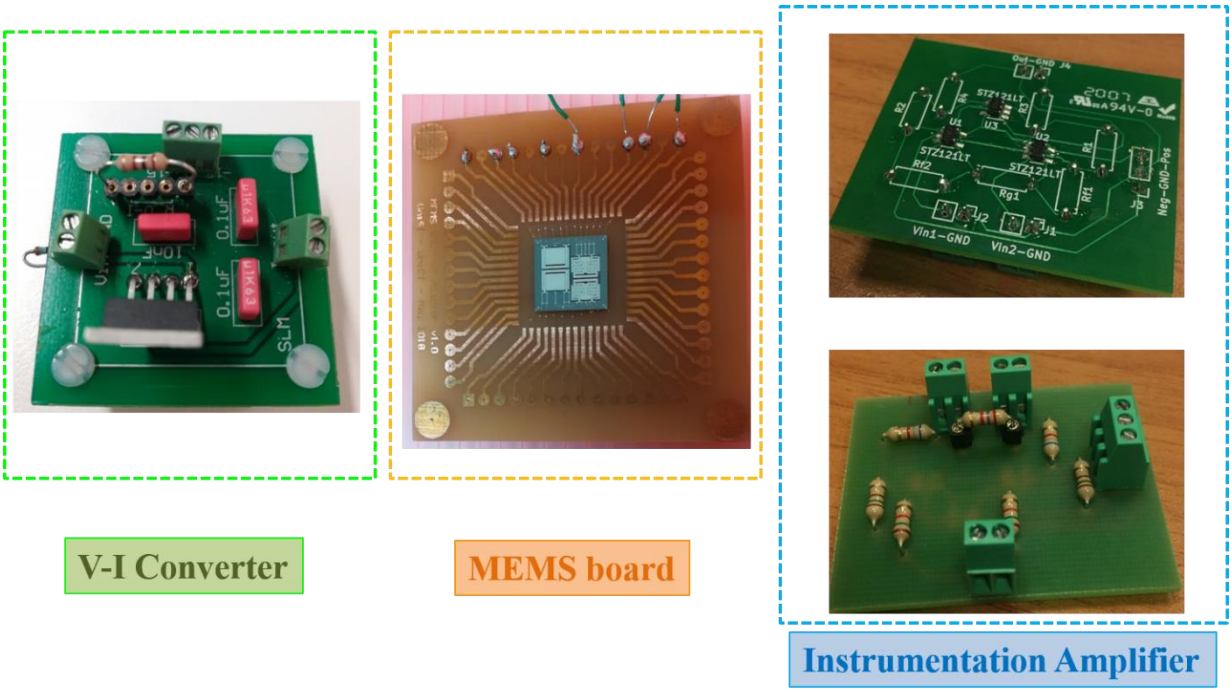

Fig. 4.55: PCB boards of driving and conditioning circuits.

As first step the validation of both PCB board has been performed in order to confirm the right working principle.

Unfortunately, the pandemic correlated to the COVID-19 virus imposed to lock the research activity and no characterization and test, planned in accordance with the Paradox Engineering company, with the MEMS devices in differential configuration have been carried out.

Conclusion

In this thesis, the investigation performed on a new architecture of integrated magnetic field sensor in order to realize a microelectromechanical (MEMS) device with a wide operative range has been presented. The research activity has been focused on a "tunable" magnetic sensor that exploits Lorentz force, that is in fact correlated to the product between the AC current driven into the sensor and the external magnetic field to be measured. After a detailed examination related to the state of art (SOA) on Lorentz force magnetometers, it has been decided to focus on the U-shaped beam cantilever that has been realized in different fabrication technologies, such as CMOS, SOIMUMPs and PiezoMUMPs.; in particular, the PiezoMUMPs has been estimated as the most promising technique, due to the presence of an integrated piezoelectric stack, Aluminum Nitride (AlN), that is utilized to generate an electric output. This latter aspect represents one of the most important advantages in this process; in fact an electric signal is directly available in the output of the sensor and, in this manner, the sensor output is a voltage not correlated to variation of resistance (resistive output) or capacitance (capacitive output).

In order to inspect the opportunity of realizing a MEMS magnetometer having an operative range [1 μT – 2 T] an extensive analysis of the static and dynamic model related to numerous architectures has been implemented in Matlab & Simulink environment; this investigation allowed to compare the "standard" structure of a U-shaped beam cantilever with several variations in order to evaluate the best performance in terms of displacement in the same operative condition.

Afterwards, a meander architecture has been selected as the most promising, and FEM analysis in COMSOL Multiphysics has been carried out for determining the residual stress, since if it exceeds the value indicated by MEMS foundry a structural failure could occur after the release.

The FEM analysis confirmed the feasibility of the new architecture and, therefore, the design has been fulfilled using a suitable CAD, MEMSPro. In particular way, two designs have been implemented in order to compare the performance of both the new architecture and a "classic" U-shaped beam cantilever.

A first preliminary analysis demonstrated the flexibility of the single spring and the piezoelectric answer when an impulsive signal is applied.

In DIEEI laboratory in University of Catania (Italy), a full characterization of the meander MEMS device as inertial sensor has been performed, obtaining a sensitivity of ~ 0.0038 V/(m/s^2), a noise level of ~ 3.37×10-5 V and a resolution of ~ 0.0089 m/s^2. These features arouse interest considering that they have been obtained with a MEMS able to work at low frequency due to the fact the resonance frequency has been estimated at 20 Hz, with a voltage transduction and compact device. In addition, it is worth noting that very significant sensitivity has been obtained taking into account that very low external accelerations have been applied.

In order to characterize the meander MEMS magnetometer a period of five months has been spent at CERN (European Organization for Nuclear Research) in Geneva, collaborating with the MM (Magnetic Measurement) group and testing the magnetic field sensor in their laboratory. The yellow dipole, capable of producing a constant magnetic induction nominally until 800 mT, has been used to perform the measurements, whereas a sinusoidal current has been driven into the MEMS device; the combined action of the AC current into the device and the magnetic induction to be measured generates the actuation of the MEMS sensor through the application of Lorentz force. Taking into account the MEMS prototype exhibits a preferential direction of deformation, the direction of Lorentz force application is a relevant aspect; for this reason, two different orientations of the magnetometer inside the dipole have been considered, demonstrating that the perpendicular direction manifests better performance than the planar direction. In detail, a sensitivity of 12×10-5 V/T has been determined in the perpendicular direction in

correspondence of a sinusoidal driving current, having a frequency of 20 Hz and an amplitude of 10 mA, and a magnetic induction in the range [0 - 25] mT, whereas a lower sensitivity, S = 7.5×10-5 V/T, has been evaluated in the same operative conditions in the planar direction. A similar trend has been appreciated considering the same range of the magnetic induction but increasing the amplitude of the driving current (at 40 mA), keeping constant the frequency at 20 Hz: in detail, a sensitivity of 28×10-5 V/T in perpendicular direction and a sensitivity of 25×10-5 V/T in planar direction have been estimated.

In the last part of this research activity a "classic" U-shaped beam cantilever, realized in the identical technology, has been tested as magnetometer in order to validate the working principle and to have an idea in terms of performance. At first the resonance frequency has been experimentally determined driving a sinusoidal current into the simple U-shaped beam device, having an amplitude of 50 mA and a frequency in the range [0 - 100] Hz: in accordance with found in FEM analysis the resonance frequency has been evaluated 70 Hz. Also in this case, two different directions, perpendicular and planar, of the MEMS sensor inside the dipole have been investigated, confirming that the perpendicular direction presents greater sensitivity than the planar direction. In detail, a sensitivity of 2.1×10-6 V/T has been determined in the perpendicular direction in correspondence of a sinusoidal driving current, having a frequency of 70 Hz and an amplitude of 20 mA, and a magnetic induction in the range [0 - 600] mT, whereas a lower sensitivity, S = 8×10-8 V/T, has been evaluated in the same operative conditions in the planar direction. The same tendency has been found considering the same range of the magnetic induction but increasing the amplitude of the driving current (at 60 mA), keeping constant the frequency at 70 Hz: in detail, a sensitivity of 2.6×10-6 V/T in perpendicular direction and a sensitivity of 9.9×10-7 V/T in planar direction have been estimated.

In addition, as last step, an optimization design, having a differential structure, has been implemented in order to reduce the environmental noise.

In conclusion, a new prototype of MEMS magnetometer has been investigated, adopting a piezoelectric readout strategy thanks to the presence of an AlN layer integrated in the PiezoMUMPs technology. During three years of research activity, the new architecture has been implemented, deepening the static and dynamic model through Matlab & Simulink environment, the structural failure, connected to the residual stress, through the FEM analysis in COMSOL Multiphysics, the realization of the layout using the MEMSPro CAD. Finally, a characterization has been carried out as accelerometer and as magnetometer.

Furthermore, considering the applicative duality of this research activity, that is the dispersion of the magnetic field in an accelerator particle and the "smart cities parking" application, a collaboration with the company Paradox Engineering is expected as concerns the detection of "weak" magnetic fields, in order to test new PiezoMUMPs prototypes. In relation to this point it is important to remark that a standard vehicle induces a geomagnetic field alteration of around 1 μT, and at the moment, optical systems are typically adopted to monitor the presence of free or occupied lots in a parking garage. Therefore, the aim pursued in this PhD activity is to provide a new alternative method, that exploits characteristics of a self-generating, low-cost and low-power device, in order to supervise the lots occupancy. Just to specify, the realized MEMS sensor can be considered a low cost device because it is composed primarily of Silicon, whose fabrication technology is long established; in addition, since the MEMS device does not operate in shielded conditions the environmental noise induces a vibration in the structure, regardless to the presence of a magnetic field to be detected, and, as a consequence, the electrical signal developed by the piezoelectric material could be stored and used to supply the conditioning circuit. For the "smart city parking" application a differential configuration of MEMS magnetic field sensors has been realized and suitable driving and conditioning circuits have been implemented as PCB circuits using an appropriate CAD, KiCad. A preliminary test about the conditioning circuit has been carried out in order to validate the working principle of the instrumentation amplifier.

Unfortunately, the pandemic correlated to the COVID-19 virus imposed to lock the research activity and no characterization and test, planned in accordance with the Paradox Engineering company, with the MEMS devices in differential configuration have been accomplished.

Bibliography

[1] S. Butzmann and R. Buchhold, *"A new differential magnetoresistive gear wheel sensor with high suppression of external magnetic fields [automotive applications]"*, IEEE Conf. SENSORS, Vienna, Austria, 24-27 Oct 200.

[2] J. Nam, W. Lee, E. Jung and G. Jang, *"Magnetic Navigation System Utilizing a Closed Magnetic Circuit to Maximize Magnetic Field and a Mapping Method to Precisely Control Magnetic Field in Real Time"*, IEEE Transactions on Industrial Electronics, vol. 65, n. 7, pp. 5673 – 5681, July 2018.

[3] R. Berešík, J. Puttera, J. Kurty and J.Jurčo, *"Magnetic sensor system concept for ground vehicles detection"*, International Conference on Military Technologies (ICMT), Brno, Czech Republic, 31 May-2 June 2017.

[4] A. Beninato, V. Sinatra, G. Tosto, M. Castagna, S. Petralia, S. Conoci, and S.Baglio, *"Inductive integrated biosensor with extended operative range for detection of magnetic beads for magnetic immunoassay"*, IEEE Transactions on Instrumentation and Measurement, 66, Issue 2, pp. 348 – 359, 2017.

[5] C.P.O. Treutler, *'Magnetic sensors for automotive applications'*, Sensors Actuators A 109 (2001), pp. 2-6.

[6] M. Youssef; M. A. Yosef; M. El-Derini, *'GAC: Energy-Efficient Hybrid GPS-Accelerometer-Compass GSM Localization',* Global Telecommunication Conference (GLOBECOM 2010), 2010 IEEE.

[7] H. Witschnig, A. Morici, B. Schaffer and J. Zimmer, *"A fully monolithic integrated anisotropic magnetoresistance based on angle sensor for automotive"*, 17th International Conference on Solid-State Sensors, Actuators and Microsystems (TRANSDUCERS & EUROSENSORS XXVII), Barcelona, Spain, 16-20 June 2013.

[8] C. Trigona, B. Andò, V. Sinatra, C. Vacirca, E. Rossino, L. Palermo, S. Kurukunda and S. Baglio, *"Implementation and Characterization of a Smart Parking System based on 3-axis Magnetic Sensors"*, IEEE I2MTC, Taipe, Taiwan, 23-26 May 2016.

[9] P. Josephs-Franks, L. Hao, A. Tzalenchuck, J. Davies, O. Kazakova, J. C. Gallop, L. Brown and J. C. Macfarlane, *'Measurement of the spatial sensitivity of miniature SQUIDs using magnetic tipped STM'*. J. Supercond. Sci. Technol. 2003, *16*, pp. 1570 - 1574.

[10] H. Weinstock, "SQUID Sensors: Fundamentals, Fabrication and Applications", Springer Science & Business Media, Dec 6, 2012.

[11] P. Marcon and K. Ostanina, *"Overview of Methods for Magnetic Susceptibility Measurement"*, PIERS Proceedings, Kuala Lumpur, Malaysia, 27-30 March, pp. 420 - 424, 2012.

[12] D. Drunga, C. Amanna, J. Beyera, A. Kirstea, M. Petersa, F. Ruedea, Th. Schuriga, C. Hinnrichsb and H.-J. Barthelmessb, *"High-Performance dc SQUID Sensors and Electronics"* IEEE/CSC & ESAS European Superconductivity News Forum, no. 1, July 2007.

[13] S. Tanaka, T. Matsuo, K. Kobayashi, M. Kabasawa, Takeyoshi Ohtani and S. Ariyoishi, *"Measurement of Magnetic Nanoparticles by Small HTS SQUID Array"*, IEEE Transaction on Applied Superconductivity vol. 28, no. 4, Art. Seq. Num.: 1600304, June 2018.

[14] P. Madhusudan and J. Bhargav, *"Subsystem simplification of SQUID magnetometer based magnetoencephalogram using application specific integrated circuits"*, IEEE Inter. Conf. on Inventive Computing and Informatics (ICICI), 23-24 Nov. 2017, Coimbatore, India.

[15] K. Kobayashi, M. Yoshizawa and D. Oyama, *"Development of SQUID magnetometer with direct-feedback noise cancellation for magnetocardiogram without magnetically shielded room"*, IEEE Transactions on applied superconductivity, vol. 27, no. 4, 1601504, June 2017.

[16] A. Tsukamoto, S. Adachi, Y. Oshikubo and K. Tanabe, *"Design and fabrication of directly-coupled HTS-SQUID magnetometer with a multi-turn input coil"*, IEEE Transactions on applied superconductivity, vol. 23, no. 3, p. 1600304, June 2013.

[17] M. Aldouman, T. Meydan and P. Williams, *"A planar coil fluxgate magnetometer using multi-core configuration"*, IEEE SENSORS, 1 - 4 Nov. 2015, Busan, South Korea.

[18] B. Andò, S. Baglio, V. Caruso, V. Sacco and A. Bulsara, *"Multilayer based technology to build RTD Fluxgate Magnetometer"*, Sensors & Transducers Magazine, vol.65, issue 3, pp. 509 – 514, March 2006.

[19] Y. Wang, J. Li, X. Zhang, S. Chen and C. Ji, *"Resolution improved innovation of coupled core fluxgate magnetometer for low frequency magnetic field detection"*, IEEE SENSORS, 29 Oct.-1 Nov. 2017, Glasgow, UK.

[20] I. Sasada, *"Low-noise fundamental-mode orthogonal fluxgate magnetometer built with an amorphous ribbon core"*, IEEE Transactions on Magnetics, vol. 54, no. 11, November 2018.

[21] C. Trigona, V. Sinatra, B. Andò, S. Baglio and A. R. Bulsara, *"Flexible Microwire Residence Times Difference Fluxgate Magnetometer"*, IEEE TIM vol. 66, no. 3, pp. 559 – 568, March 2017.

[22] B. Andò, S. Baglio, A.R. Bulsara and C. Trigona, *"Design and characterization of a microwire fluxgate magnetometer"*, Sensors and Actuators A 151, pp. 145 – 153, 2009.

[23] B. Gavazzi, P. Le Maire, J. Mercier de Lépinay, P. Calou and M. Muschy, *"Fluxgate three-component magnetometers for cost-effective ground, UAV and airborne magnetic surveys for industrial and academic geoscience applications and comparison with current industrial standards through case studies"*, Geomechanics for Energy and the Environment, vol. 20 Art. Seq. Num.: 100117, December 2019.

[24] B. Andò, S. Baglio, R. Crispino, S. Graziani, V. Marletta, A. Mazzaglia, V. Sinatra, D. Mascali and Giuseppe Torrisi, *"A Fluxgate based approach for ion beam current measurement in electron cyclotron resonance ion sources beamline"*, IEEE I2MTC, 14-17 May 2018, Houston, TX, USA.

[25] B. Andò, S. Baglio, R. Crispino, S. Graziani, V. Marletta, A. Mazzaglia, V. Sinatra, D. Mascali and Giuseppe Torrisi, *"A Fluxgate-based approach for ion beam current measurement in ecris beamline: design and preliminary investigations"*, IEEE TIM, vol. 68, no. 5, pp. 1477 – 1484, May 2019.

[26] C. Trigona, V. Sinatra, B. Andò, S. Baglio, A.R. Bulsara, G. Mostile, M. Zappia and A. Nicoletti, *"Measurements of Iron Compound Contentin the Brain, using a Flexible Core Fluxgate Magnetometer at Room Temperature"*, IEEE Transactions on Instrumentation and Measurement, vol. 67, no 4, pp. 971 – 980, April 2018.

[27] C. Trigona, V. Sinatra, B. Andò, S. Baglio, A.R. Bulsara, G. Mostile, M. Zappia and A. Nicoletti, *"RTD-Fluxgate sensor for measurements of metal compounds in neurodegenerative diseases"*, IEEE I2MTC, 22-25 May 2017, Turin, Italy.

[28] G. T. Nikolov, S. V. Vutev and B. M. Nikolova, *"Magnetic Fields Measurement with AMR Sensors"*, Annual Journal of Electronics pp. 148 – 151, 2009.

[29] A. Zambrano and H. G. Kerkhoff, *"Improving the dependability of AMR sensors used in automotive applications"*, 22nd IEEE European Test Symposium (ETS), Limassol, Cyprus, 22-26 May 2017.

[30] L. Jogschies, D. Klaas, R. Kruppe, J. Rittinger, P. Taptimthong, A. Wienecke, L. Rissing and M. C. Wurz, *"Recent Developments of Magnetoresistive Sensors for Industrial Applications"*, Sensors, vol. 15, pp. 28665 – 28689, 2015.

[31] Z. Ning, W. Sansheng and L. Hua, *"The application of AMR sensor in the magnetic object detection and localization"*, IEEE 13th ICEMI, pp. 159 – 162, Yangzhou, China, 20-22 October 2017.

[32] G. Binasch, P. Grünberg, F. Saurenbach and W. Zinn, *"Enhanced magnetoresistance in layered magnetic structures with antiferromagnetic interlayer exchange"*, Phys. Rev. B., vol. 39, pp. 4828 – 4830, 1989.

[33] R. Ranchal, M. Torija, E. L´opez, M.C. S´anchez, M.C. Aroca and C. S´anchez, *"P. The influence of anisotropy on the magnetoresistance of permalloy–copper–permalloy thin films"*, Nanotechnology, vol. 13, pp. 392 - 397, 2002.

[34] C. Reig, S. Cardoso, S. Mukhopadhyay and S. Chandra, "Giant magneto resistance (GMR) Sensors: From Basis to State-of-the-Art applications" Springer; Berlin, Germany, pp. 133 – 156, 2013.

[35] G. Reiss, H. Brueckl, A. Huetten, J. Schotter, M. Brzeska, M. Panhorst, D. Sudfeld, A. Becker, P. B. Kamp, A. Puehler et al., *"Magnetoresistive sensors and magnetic nanoparticles for biotechnology",* J. Mater. Res., vol 20, pp. 3294 – 3302, 2005.

[36] A. Auge, A. Weddemann, F. Wittbracht and A. Hütten, *"Magnetic ratchet for biotechnological applications*", Appl. Phys. Lett. 2009;94.

[37] T. Bever, K. Pruegl, W. Raberg, A. Strasser and J. Zimmer, Sensors and Measuring Systems 2014. In Proceedings of the Sensoren und Messysteme 2014, Nuremberg, Germany, 3–4 June, pp. 1 4, 2014.

[38] Z. Q. Lei, G. J. Li, W. F. Egelhoff, Jr., P. T. Lai, and P. W. T. Pong, *"Review of Noise Sources in Magnetic Tunnel Junction Sensors"*, IEEE Transactions on Magnetics, vol. 47, no. 3, pp. 602 – 612, March 2011.

[39] J. M. Almeida and P. P. Freitas, *"Field detection in MgO magnetic tunnel junctions with superparamagnetic free layer and magnetic flux concentrators,"* J. Appl. Phys. vol. 105, pp. 07E722, 2009.

[40] V. S. Luong, J.-T. Jeng, J.-H. Hsu, C.-R. Chang and C.-C. Lu *"Tunneling-magnetoresistance vector magnetometer with deflection flux-chopper"*, IEEE Transactions on Magnetics, vol. 52, no. 7, pp. 4001204, July 2016.

[41] R. Guerrero, M. Pannetier-Lecoeur, C. Fermon, S. Cardoso, R. Ferreira and P. P. Freitas, *"Low frequency noise in arrays of magnetic tunnel junctions connected in series and parallel"*, J. Appl. Phys. vol. 105, pp. 113922, 2009.

[42] V.-S. Luong, C.-H. Chang, J.-T. Jeng, C.-C. Lu, J.-H. Hsu and C.-R. Chang, *"Reduction of Low-Frequency Noise in Tunneling-Magnetoresistance Sensors with a Modulated Magnetic Shielding,"* IEEE Trans. Magn., vol. 50, no. 11, pp. 4005904, Nov, 2014.

[43] X. Li, J. Hu, W. Chen, L. Yin and X. Liu, *"A novel high-precision digital tunneling magnetic resistance-type sensor for the nanosatellites' space application"*, Micromachines 2018, 9, 121.

[44] D. Robbes, *"Highly sensitive magnetometers—A review"*, Sens. Actuators, A, vol. 129, pp. 86 - 93, 2006.

[45] F. Mahboubian, H. Sardari, S. Sadeghi and F. Sarreshtedari, *"Design and Implementation of a Low Noise Earth Field Proton Precession Magnetometer"*, IEEE 27th Iranian Conference on Electrical Engineering (ICEE), Yazd, Iran, 30 April-2 May 2019.

[46] Y. Huang, J. Ge, H. Dong and H. Liu, *"An automatic wideband 90◦ phase shifter for optically pumped cesium magnetometers,"* IEEE Sensors Journal, vol. 17, no. 23, pp. 7928 – 7934, 2017.

[47] H. Liu, W. Luo, H. Dong, J. Ge, Z. Liu, Z. Yuan, J. Zhu and H. Zhang, *"Design and implementation of a tuning-matching framework for a high-sensitivity broad band proton precession magnetometer sensing coil"*, IEEE Sensor Journal, 2019 (Early Access).

[48] H. Liu, H. Dong, J. Ge, Z. Liu, Z. Yuan, J. Zhu and H. Zhang, *"High-precision sensor tuning of proton precession magnetometer by combining principal component analysis and singular value decomposition"*, IEEE Sensors Journal, vol. 19, no. 21, 1st November, 2019.

[49] H. Liu, H. Dong, J. Ge, Z. Liu, Z. Yuan, J. Zhu and H. Zhang, *"Efficient performance optimization for the magnetic data readout from a proton precession magnetometer with low-rank constraint"*, IEEE Transactions on Magnetics, vol. 55, no. 8, p. 9300104, August 2019.

[50] J. Kitching, S. Knappe and E. A. Donley, *"Atomic Sensors-A Review"*, IEEE Sensor Journal, vol. 11, n. 9, pp. 1749 – 1758, September 2011.

[51] T. Scholtes, V. Schultze, R. IJsselsteijn, S. Woetzel and H.-G. Meyer, *"Light-narrowed optically pumped Mx magnetometer with a miniaturized Cs cell"*, Physical Review A 84, 043416, 2011.

[52] T. M. Tierney, N. Holmesb, S. Mellora, J. D. Lopez, G. Roberts, R. M. Hill, E. Boto, J. Leggett, V. Shah, M. J. Brookes, Richard Bowtell and G. R. Barnes, *"Optically pumped magnetometers: From quantum origins to multi-channel magnetoencephalography"*, NeuroImage 199, pp. 598 – 608, 2019.

[53] S. Knappe, T. Sander and L. Trahms, Optically-Pumped Magnetometers for MEG, Springer-Verlag Berlin Heidelberg 2014, pp. 993 – 999.

[54] S. Knappe, TH. Sander, O. Kosch, F. Wiekhorst, J. Kitching and L. Trahms, Appl Phys Lett 97, p. 133703, 2010.

[55] O. Alem, TH. Sander, R. Mhaskar, J. LeBlanc, H. Eswaran, U. Steinhoff et al., Phys Med Biol 60 4797-811, 2015.

[56] G.-M. Sung, W.-S. Lin and C.-P. Yu, *"Two-dimensional folded hall sensor fabricated in standard CMOS technology"*, IEEE Sensors, Taipei, Taiwan, 28-31 Oct. 2012.

[57] S. Leroy, S. Rigert, A. Laville, A. Ajbl and G. F. Close, *"Integrated Hall-based magnetic platform for position sensing"*, IEEE ESSCIRC, Leuven, Belgium, 11-14 Sept. 2017.

[58] M. Crescentini, M. Marchesi, A. Romani, M. Tartagni and P. A. Traverso, *"A broadband, on-chip sensor based on Hall effect for current measurements in smart power circuits"*, IEEE TIM, vol. 67, no. 6, June 2018.

[59] J. García-Martín, J. Gómez-Gil and E. Vázquez-Sánchez, *"Non-destructive techniques based on eddy current testing"*, Sensors 11 (3), pp. 2525 – 2565, 2011.

[60] B. Liu, Y. Sun, Y. Ding, P. Cao, A. Liu, S. Yang Ong, M. Tiong, G. Cheng, M. N. Islam, R. Jain, T. L. Tan, E. Quek and E.-H. Toh, *"Low-power and high-sensitivity system-on-chip Hall effect sensor"*, IEEE Sensors, Glasgow, UK, 29 Oct.-1 Nov. 2017.

[61] Z. Zhang, F. Lyu, S. He, L. Li, J. Sha, H. Pan, Z. Zhang and Yifan Pan, *"High sensitivity horizontal hall sensors in 0.35 μm BCD technology"*, IEEE IMCCC, Qinhuangdao, China, 18-20 Sept. 2015.

[62] H. Pfleiderer, *"Magnetodiode model"*, Solid-State Electronics, vol. 15, issue 3, pp. 335 - 353, 1972.

[63] T. Phetchakul, W. Luanatikomku, W. Yamwong and A. Poyai, *"The mechanism of dual Schottky magnetodiode"*, IEEE ECTICon., Phetchaburi, Thailand, 16-18 May 2012.

[64] W. Liang-gong, *"A new type of tachometer circuit based on series magneto-diode"*, Proceedings of SPIE - The International Society for Optical Engineering 5774, pp. 571 - 574, January 2005.

[65] T. Phetchakul, P. Sottip, C. Leepattarapongpan, N. Penpondee, P. Pengpad, A. Srihapat, C. Hruanun and A. Poyai, *The deflection length and emitter width on sensitivity of magnetotransistor"*, IEEE NEMS, Kaohsiung, Taiwan, 20-23 Feb. 2011.

[66] C. Leepattarapongpan, T. Phetchakul, P. Pengpad, A. Srihapat, W. Jeamsaksiri, E. Chaowicharat, *"The magnetotransistor for 2-axis magnetic field measurement in CMOS technology"*, IEEE ECTI-CON, Hua Hin, Thailand, 24-27 June 2015.

[67] V. Zieren, O. Wunnicke, K. Reimann, A. Duinmaijer and R. Rijal, *"MOS-gated bipolar magnetotransistors for 360° angular sensing"*, IEEE Sensor, Valencia, Spain, 2-5 Nov. 2014.

[68] T. Otto, S. Kurth, S. Voigt, A. Morschhauser, M. Meinig, K. Hiller, M. Moebius and M. Vogel, *"Integrated Microsystems for Smart Applications"*, Sensors and Materials, vol. 30, no. 4, pp. 767 – 778, 2018.

[69] M. Pandit, C. Zhao, G. Sobreviela, X. Zou and A. Seshia, *"A high resolution differential mode-localized MEMS accelerometer"*, IEEE Journal of Microelectromechanical systems, vol. 28, no. 5, October 2019.

[70] H. Cao, Y. Liu, Y. Zhang, X. Shao, J. Gao, K. Huang, Y. Shi, J. Tang, C. Shen and J. Liu, *"Design and experiment of dual-mass MEMS gyroscope sense closed system based on bipole compensation method"*, IEEE Access, vol. 7, pp. 49111 – 49124, 11 April 2019.

[71] D. Han, J. Wang, S. Yuan, T. Yang, B. Chen, G. Teng, W. Luo, Y. Chen, Y. Li, M. Wang, Y. Yin, X. Jin, S. Zhang and J. Feng, *"A MEMS pressure sensor based on double- ended tuning fork resonator with on-chip thermal compensation"*, IEEE Transducers & Eurosensors XXXIII, Berlin, Germany, 23-27 June 2019.

[72] Y. Okamoto, H. Takehara, K. Fujimoto, T. Ichiki, T. Ohba and Y. Mita, *"On-chip high-voltage charge pump with MEMS post-processed standard 5-V CMOS on SOI for electroosmotic flow micropumps"*, IEEE Electron Device Letters, vol. 39, no. 6, pp. 851 – 854, June 2018.

[73] M. Bao, Analysis and Design Principles of MEMS Devices, Chapter 2 - Mechanics of Beam and Diaphragm Structures, Elsevier, pp. 32 – 114, 2005.

[74] J. Pérez Sanjurjo, E. Prefasi, C. Buffa and R. Gaggl, *"A capacitance-to-digital converter for MEMS sensors for smart applications"*, Sensors 17(6): 1312, June 2017.

[75] A. Ota, W. Petchmaneelumka, T. Cheypoca, A. Rerkratn and V. Riewruja, *"Front-End interfacing circuit for capacitive sensor"*, IEEE ICITEE, Chiang Mai, Thailand, 29-30 Oct. 2015.

[76] F. Keplinger, S. Kvasnica, A. Jachimowicz, F. Kohl, J. Steurer, H. Hauser, *"Lorentz force based magnetic field sensor with optical readout"*, Sensors and Actuators A 110, pp. 112 – 118, 2004.

[77] D.K. Wickenden, J.L. Champion, R. Osiander, R.B. Givens, J.L. Lamb, J.A. Miragliotta, D.A. Oursler and T.J. Kistenmacher, *"Micromachined polysilicon resonating xylophone bar magnetometer"*. Acta Astronaut. 52, pp. 421 – 425, 2003.

[78] J. O. Dennis, F. Ahmad, M. H. Bin Md Khir and N. H. Bin Hamid, *"Optical characterization of Lorentz force based CMOS-MEMS magnetic field sensor"*, Sensors, vol. 15, pp. 18256 - 18269, 2005.

[79] C. Trigona, V. Sinatra, A. R. Fallico, S. Puglisi, B. Andò and S. Baglio, *"Dynamic spatial measurements based on a bimorph artificial whisker and RTD-fluxgate magnetometer"*, IEEE I2MTC, Auckland, New Zealand, 20-23 May 2019.

[80] Piezo Film Sensors Technical Manual Images SI Inc. https://www.imagesco.com/sensors/piezofilm.pdf

[81] S. Ghosh and J. E.-Y. Lee, *"An ultra-sensitive piezoelectric-on-silicon flapping mode MEMS lateral field magnetometer"*, IEEE, EFTF/IFCS, Besancon, France, 9-13 July 2017.

[82] D.H. Ren, M.Y. Cui, L.Q. Wu, T.W. Guo, C.T. Xu and Z. You, *"MEMS torsional resonant magnetometer for the attitude determination in space"*, IEEE, Transducers and Eurosensors XXVII, Barcelona, Spain, 16-20 June 2013.

[83] G. Laghi, S. Dellea, A. Longoni, P. Minotti, A. Tocchio, S. Zerbini and G. Langfeldera, *"Torsional MEMS magnetometer operated off-resonance for in-plane magnetic field detection"*, Sensors and Actuators A, vol. 229, pp. 218 – 226, 2015.

[84] M. Al-Shaibah, W. Syed, B. An, Z. Mohammad, S. AlDahmani, D. Choi and I. Elfadel, *"Modeling and analysis of a navigational, Lorentz-Force, z-axis MEMS magnetometer in a standard process"*, IEEE DTIP, Paris, France, 12-15 May 2019.

[85] C. Trigona, V. Sinatra, G. Crea, B. Andò and S. Baglio, *"Characterization of a PiezoMUMPs microsensor for contactless measurements of DC-electrical current"*, IEEE, TIM (Early Access), 2019.

[86] J. S. Wu, D. W. Chen, *"Dynamic analysis of a uniform cantilever beam carrying a number of elastically mounted point masses with dampers"*, Journal of Sound and Vibration, vol. 229(3), pp. 549 - 578, 2000.

[87] V. Beroulle, Y. Bertrand, L. Latorre and P. Nouet, *"Monolithic piezoresistive CMOS magnetic field sensors"*, Sensors and Actuators A 103, pp. 23 – 32, 2003.

[88] S. Baglio, L. Latorre and P. Nouet, *"Resonant magnetic field microsensors in standard CMOS technology"*, IEEE, IMTC, Venice, Italy, 24-26 May 1999.

[89] F. Keplinger, S. Kvasnica, H. Hauser and R. Grössinger, *"Optical readouts of cantilever bending designed for high magnetic field application"*, IEEE Transactions on magnetics, vol. 39, no. 5, pp. 3304 - 3306, September 2003.

[90] M. Li, S. Nitzan and D. A. Horsley, *"Frequency-Modulated Lorentz Force Magnetometer With Enhanced Sensitivity via Mechanical Amplification"*, IEEE Electron device letters, vol. 36, no. 1, pp. 62 – 65, January 2015.

[91] R. Sunieg, Y. Li, K.-U. Kirstein, T. Vancura, H. Baltes and 0. Brand, *"Resonant magnetic field sensor with frequency output"*, IEEE, Journal of Microelectromechanical Systems, vol. 15, no 5, October 2006.

[92] http://www.memscap.com/products/mumps/piezomumps, accessed on July 20, 2018. [Online].

[93] X. He, S. Chen, J. Sun, *"Applying the equivalent section method to solve beam subjected lateral force and bending-compression column with different moduli"*, Inter. Journal of Mechanical Sciences, ELSEVIER, vol. 49, Issue 7, pp. 919 – 924, 2007.

[94] B. Andò, S. Baglio, G. L'Episcopo, V. Marletta, N. Savalli, C. Trigona, *"A BE-SOI MEMS for inertial measurement geophysical applications"*, IEEE Transactions on Instrumentation and Measurement vol. 60, no. 5, Article Number 5723005, pp. 1901 - 1908, 2011.

[95] G. K. Fedder, *"Simulation of microelectromechanical systems"*, PhD Thesis, 1994.

[96] J.M. Gere, S.P. Timoshenko, Mechanics of Materials, PWS Publishing Company, Boston, 1997.

[97] http://www.advancepipeliner.com/Resources/Others/Beams/Beam_Deflection_Formulae.pdf

[98] B Andò, S Baglio, C Trigona, N Dumas, L Latorre and P Nouet, *"Nonlinear mechanism in MEMS devices for energy harvesting applications"*, J. Micromech. Microeng. 20 (2010) 125020.

[99] V. Sinatra, C. Trigona, B. Andò and S. Baglio, *"Self-generating microsensor with meander architecture for performance enhancement in inertial systems"*, IEEE M&N, Catania, Italy, 8-10 July 2019.

[100] Y. Nie, R. Schmidt, V. Chetvertkova, G. Rosell-Tarragó, F. Burkart and D. Wollmann, *"Numerical simulations of energy deposition caused by 50 MeV—50 TeV proton beams in copper and graphite targets"*, Physical review accelerators and beams 20, 081001 (2017).

Appendix

1. Appendix A: PiezoMUMPs Technology

In this Appendix the PiezoMUMPs fabrication process is described [92]. Just to offer an exhaustive overview it is important to mention that the PiezoMUMPs technology has been introduced by MEMSCAP which works within the commercial program MUMPs® (Multi-User MEMS Processes) in order to provide proof of concept MEMS fabrication to companies, research entities and so on. Furthermore, it is essential to highlight that all fabrication steps in PiezoMUMPs technology have been explained using drawings not in scale collected directly by the user guide of this process which is based on a simple 5-masks level SOI pattern and etch. In a SOI (Silicon-On-Insulator) wafer, that represents the substrate, the following layers with their dimensions are utilized:

- Silicon thin layer (thickness): 10 μm ± 1 μm;
- Silicon oxide, SiO_2, (thickness): 1 μm ± 0.05 μm;
- Silicon wafer, that is the substrate, (thickness): 400 μm ±5 μm;

However, the process originates from 150mm n-type double-side polished Silicon On Insulator wafers which are then diced using a laser at a thickness of 400 μm.

The first step is presented in Fig. A.1 where the top surface of the Silicon layer (t = 10 μm) of a SOI wafer is doped through the deposition of a phosphosilicate glass (PSG) layer and annealing at 1050 °C for 1 hour in Argon in order to introduce the Phosphorous (F) dopant into the top surface of the Silicon layer; in addition a Bottom Side Oxide layer is initially present to save the substrate.

Fig. A.1: Silicon Doping.

Afterwards, a 2000 Å thermal oxide is grown, coated with positive photoresist and lithographically patterned using the first level mask (PADOXIDE) and the patterned area is removed with a reactive ion etch (RIE), as shown in Fig. A.2.

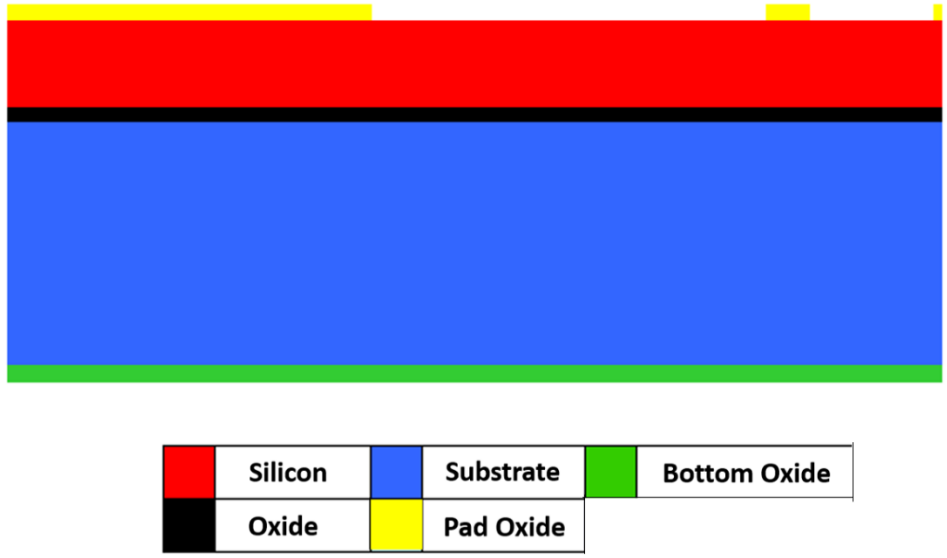

Fig. A.2: Thermal Oxide.

The first deposited layer is the piezoelectric material, Aluminum Nitride (AlN), which has a piezoelectric strain coefficient, d_{33}, on the order of [3.4 - 6.5] pC/N and a thickness of 0.5 µm. It is deposited by reactive sputtering, afterwards the wafers are coated with positive photoresist, lithographically patterned using the second level mask (PZMETAL) and then developed. Finally, it is wet etched (see Fig. A.3).

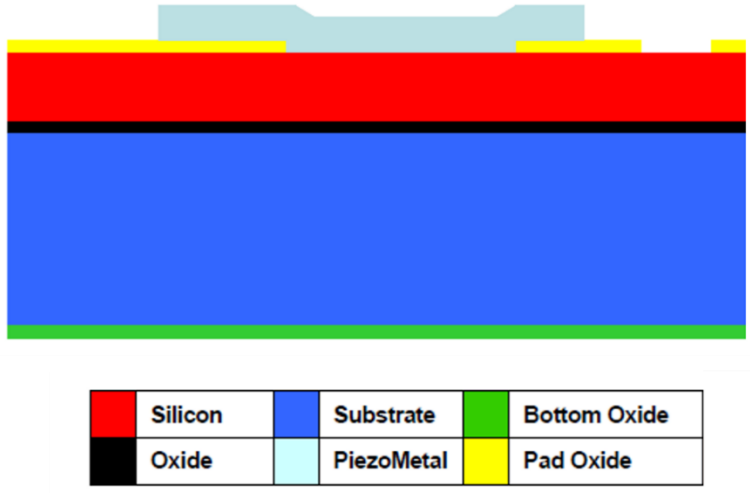

Fig. A.3: Piezoelectric Metal Liftoff - Mask Level: PZMETAL.

The second deposited layer in the process is the Pad Metal, composed of a metal stack of 20 nm of chrome and 1 µm of aluminum and patterned through a liftoff process. For this reason, the wafers are coated with negative photoresist and lithographically patterned using the third level mask (PADMETAL), and then developed. photoresist is then dissolved to leave behind metal in the opened areas (as illustrated in Fig. A.4).

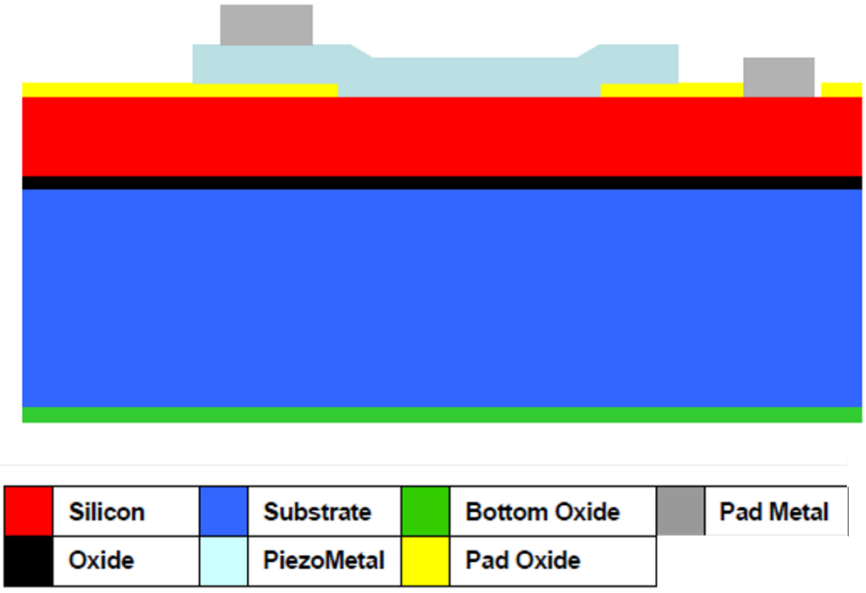

Fig. A.4: Pad Metal Liftoff - Mask Level: PADMETAL.

In the next step the wafers are coated with UV-sensitive photoresist and lithographically patterned using the fourth level mask (SOI), and then developed. The oxide layer is etched via RIE, whereas the deep reactive ion etching (DRIE) is used to etch the Silicon down to the Oxide layer. After etching, the photoresist is chemically stripped (see Fig. A.5).

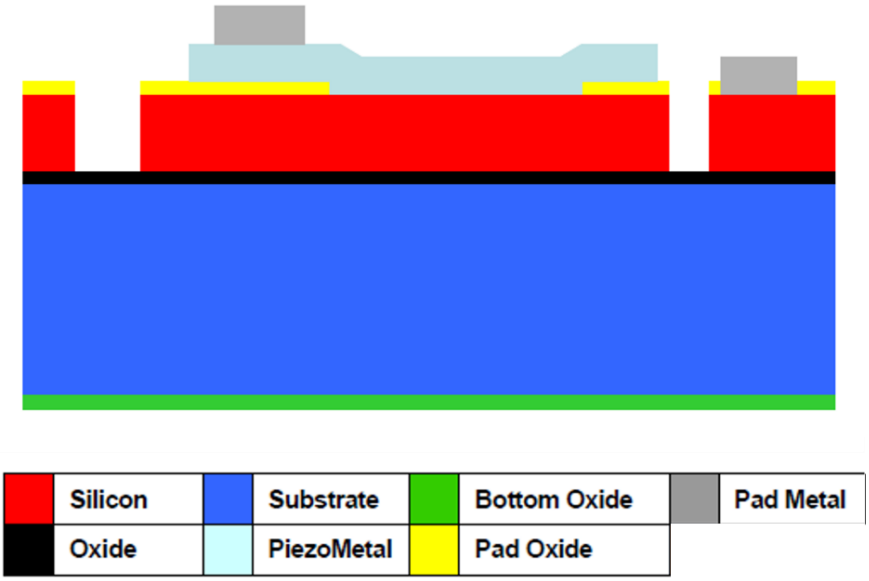

Fig. A.5: Silicon Patterning - Mask Level: SOI.

A frontside protection material is deposited to the top surface of the Silicon layer. The wafers are then reversed in order to lithographically pattern the bottom side using the fifth mask level TRENCH. The Bottom Side Oxide layer (the green layer in Fig. A.5) is removed using Reactive Ion Etching (RIE), whereas DRIE is subsequently used to etch the Substrate layer. Afterwards, a wet oxide etch process is then used to remove the Buried Oxide layer in the regions defined by the TRENCH mask (as shown in Fig A.6).

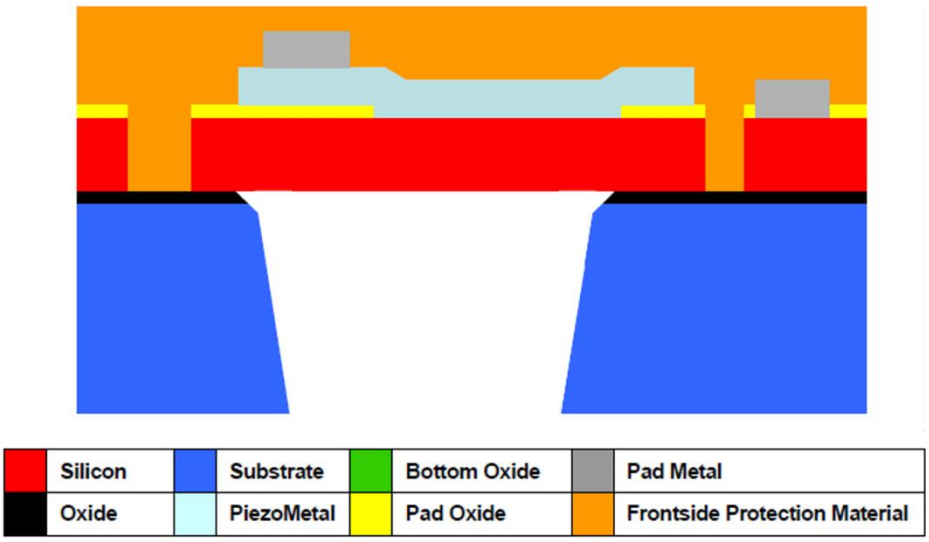

Fig. A.6: Substrate Patterning - Mask Level: TRENCH.

Eventually, the front side protection material is removed through a dry etch process and the structure is released, concluding the fabrication process (note in Fig. A.7 the final result).

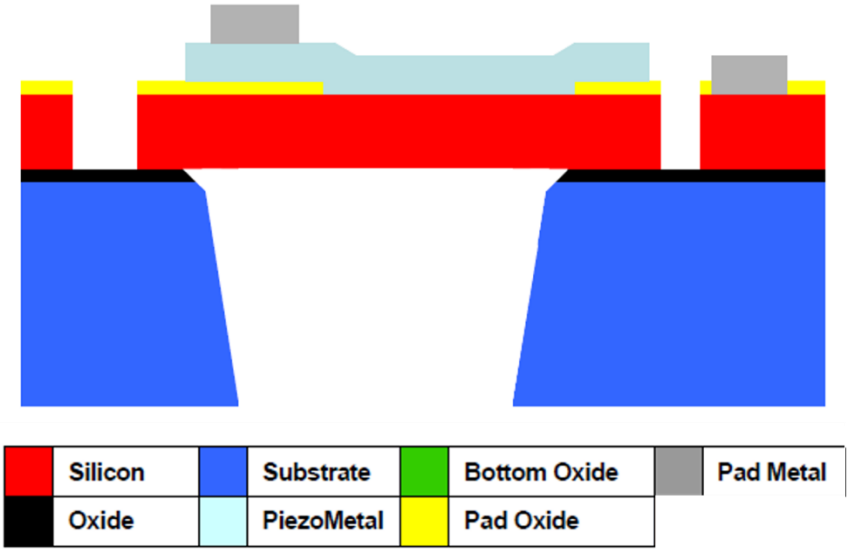

Fig. A.7: “Release” – Protection layer and Oxide layer removal.

2. Appendix B: Simulations in Matlab & Simulink environment

2.1. U-shaped beam cantilever VS Topology 1

A Matlab code has been implemented in order to obtain a parametric system and to determine all variables expressed in all equations which describe the static and dynamic model.

MATLAB CODE

```
%% U-shaped beam cantilever parameters
%% LENGTHS
 L10=6400e-6; % arm length [m]
 lm=4500e-6; % length pertinent to the inertial mass [m]
 w2=100e-6; % width pertinent to the inertial mass [m]
 w1=100e-6; % arm width[m]
 l_perp=lm+2*w1; % length where the Lorentz force operates [m]

%% Topology 1 parameters
%% LENGTHS
 L5=1500e-6;
 L6=100e-6;
 L7=1500e-6;

%% TICKNESS
 t_Si=10e-6; % Silicon [m]
 t_Al=1e-6; % Aluminum [m]
 t_AlN=0.5e-6; % Aluminum Nitride [m]
 t_tot=t_Si+t_Al+t_AlN;

%% LAYERS DENSITIES
 dens_Si=2.3e3; % expressed in [kg/m^3]
 dens_Al=2.7e3; % expressed in [kg/m^3]
 dens_AlN=3.3e3; % expressed in [kg/m^3]
```

```
 massa=lm*w2*(dens_Si*t_Si+dens_Al*t_Al+dens_AlN*t_AlN);   %   evaluation   of
inertial mass in kgr!!!

%% Parameters of Aluminum Nitride stack
 epsilon_33 = 7.9659*10^(-11); % product between epsi_0* epsi_rel (9) [F/m]
 e_31 = -0.58; % coming from the expression d_31/(s_11+s_12) [C/m^2]

%% Other parameters
 Rl =330*10^3; % load on AlN [Ohm]
 d =0.000001; % mechanical damping
 d_piezo =0.0069; % piezoelectric transduction damping
 miu_0 = 4*pi*10^(-7);

%% Parameters used to estimate the elastic constant
%% Simple U-shaped beam cantilever (total length)
 L=L10+w2;
%% Topology 1
 L4=900e-6;
 L8=5200e-6;
 L1=L4+2*w1+L6+L8+w2;
 L2=2*w1+L6+L8;
 L3=L8+w1;
 L_tot=L4+L5+L6+L7+L8+2*w1+w2; %% total length

%% Other parameters
 gamma = t_AlN/(Rl*epsilon_33*w1*l_perp);
 K_piezo  =  e_31*t_AlN/(epsilon_33*w1*l_perp);  % coupling  constant  of  the
piezoelectric stack

%% Parameters used to create a magnetic field
 h_dist =1e-3; % radius of conductor [m]
```

%%%%%%% EQUIVALENT SECTION METHOD

```
%% Young's Moduli
 E_Si=170*10^9; % Silicon
 E_AlN=310*10^9; % Aluminum Nitride
 E_Al=70*10^9; % Aluminum

 E=[E_Si E_AlN E_Al]; % Young's moduli vector
 T=[t_Si t_AlN t_Al]; % Thickness vector
 larghezza=[w1 w1 w1];
 E_max=max(E);

 for i=1:1:length(E)
  w_norm(i)=larghezza(i)*(E(i)/E_max);
 end

 for i=1:1:length(T)
  s_norm(i)=w_norm(i)*T(i);
 end

 tk=0;
 for i=1:1:length(T)
  h(i)=tk+(T(i)/2);
  tk=tk+T(i);
 end

 somma_sh=0;
 somma_s=0;
```

```
 for i=1:1:length(s_norm)
  somma_sh=somma_sh+(s_norm(i)*h(i));
  somma_s=somma_s+s_norm(i);
 end

 hn=somma_sh/somma_s;

 for i=1:1:length(T)
  Ix(i)=((T(i)^3)*w1*E(i)/E_max)/12;
 end

 for i=1:1:length(T)
  I_norm(i)=Ix(i)+(s_norm(i)*(hn-h(i))^2);
 end

 In=0;
 for i=1:1:length(I_norm)
  In=In+I_norm(i);
 end
 tot=0;
 for i=1:1:length(I_norm)
  c(i)=E(i)*I_norm(i);
  tot=c(i)+tot; % [N*m2]
 end

 K_strain = 3*((L)^2)/(E_max*w1*((t_tot)^2)); % parameter related to the axial
strain
%%%%%%

% Mechanical stiffness
 k=6*tot/(L^3); % Simple U-shaped beam cantilever [N/m]
% Topology 1
 k1=6*tot/((L_tot)^3);
 kF1=(12*tot)/((3*L1-L3)*L3^2);
 kF2=(12*tot)/((3*L1-L2)*L2^2);

% Current into the conductor
 I_cond=5e-3;

 omega=sqrt(k/massa); % Related to the Simple U-shaped beam cantilever
 freq=omega/(2*pi);
 omega1=sqrt(k1/massa); % Related to the Topology 1
 freq1=omega1/(2*pi);

% Driving current into the Simple U-shaped beam cantilever
 I_cant=20e-3; % [App]

% Evaluation of magnetic induction
 B=miu_0*I_cond/(2*pi*h_dist); % ([H]*[A])/([m2])=[Wb]/[m2]=[T]

% Lorentz Force
 Fl=I_cant*B*l_perp;
```

SIMULINK SCHEMATIC

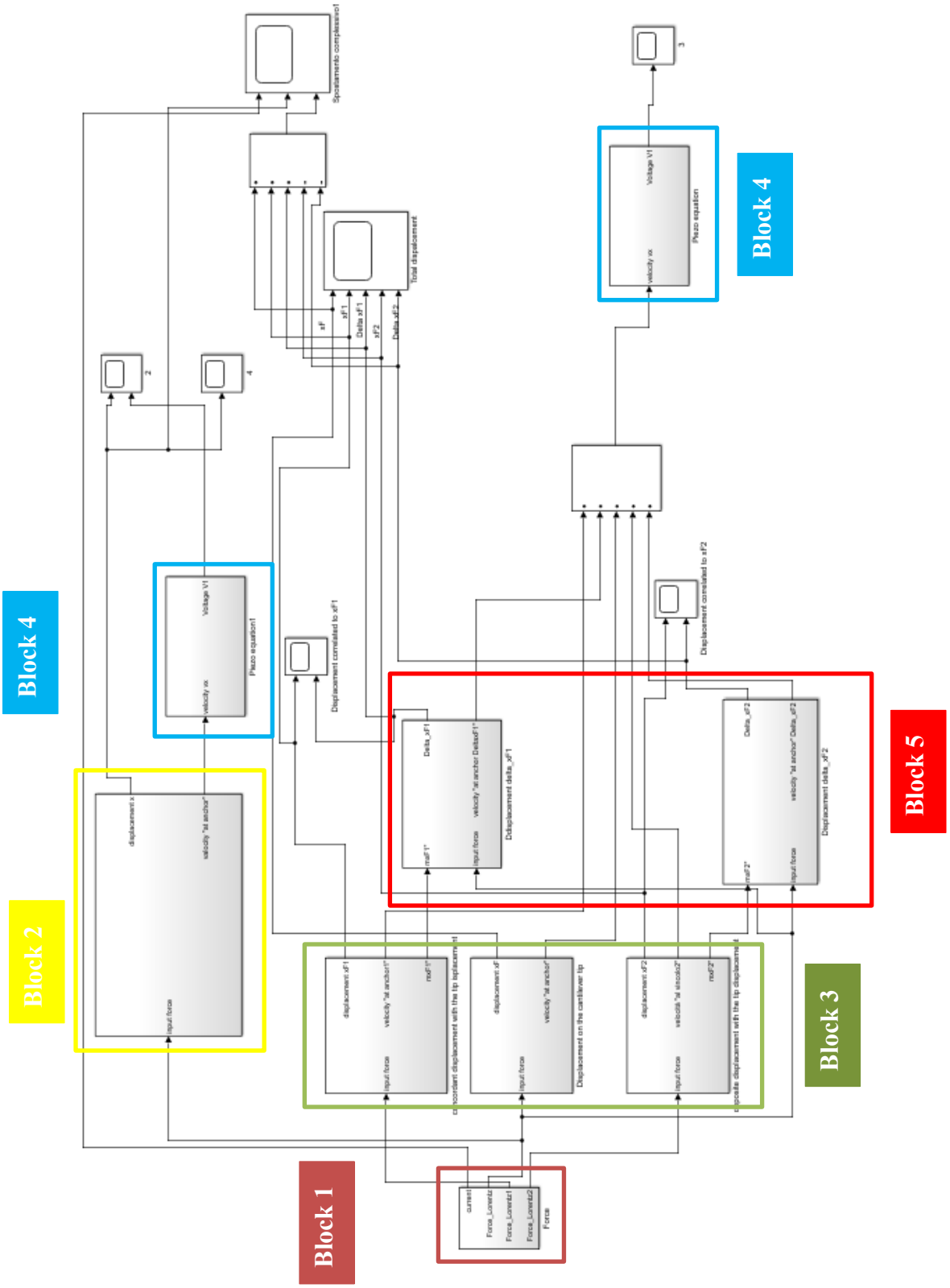

Fig. B.1: Simulink schematic: Simple VS Topology 1.

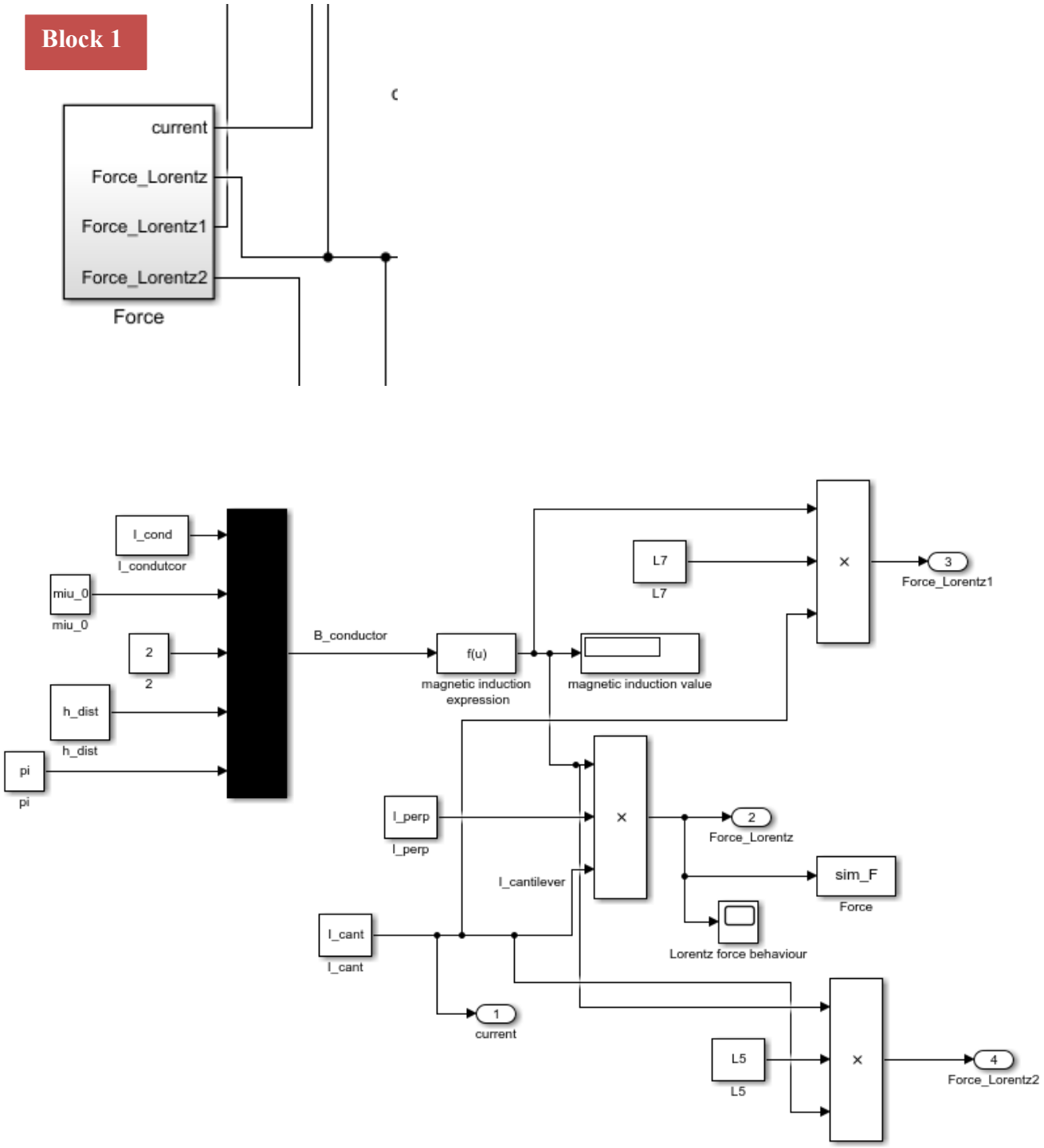

Fig. B.2: Zoom on Lorentz force in static analysis.

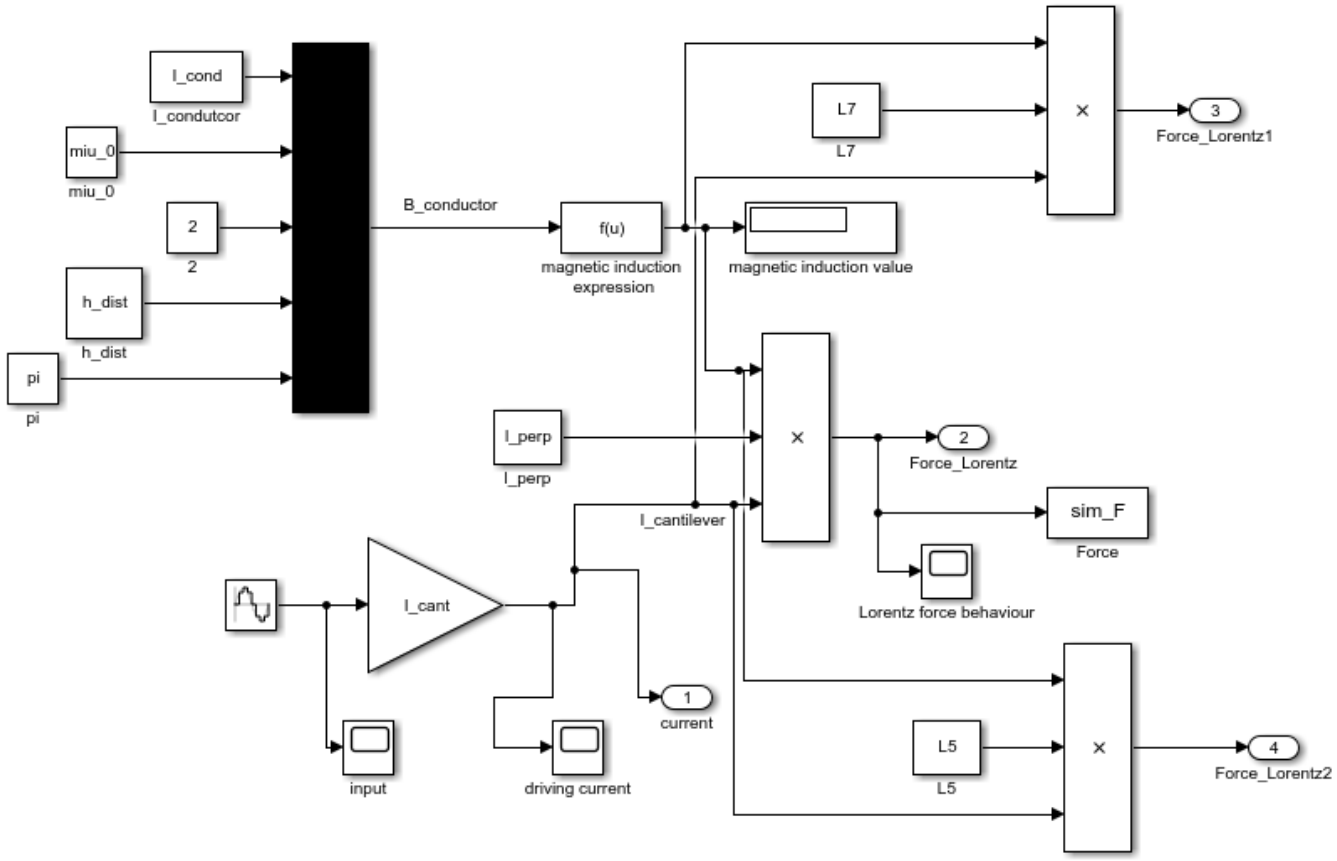

Fig. B.3: Zoom on Lorentz force in dynamic analysis.

Block 2

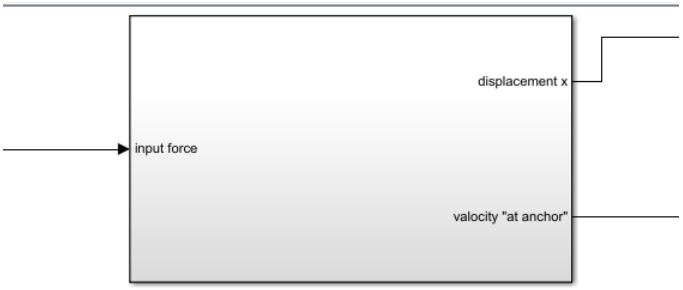

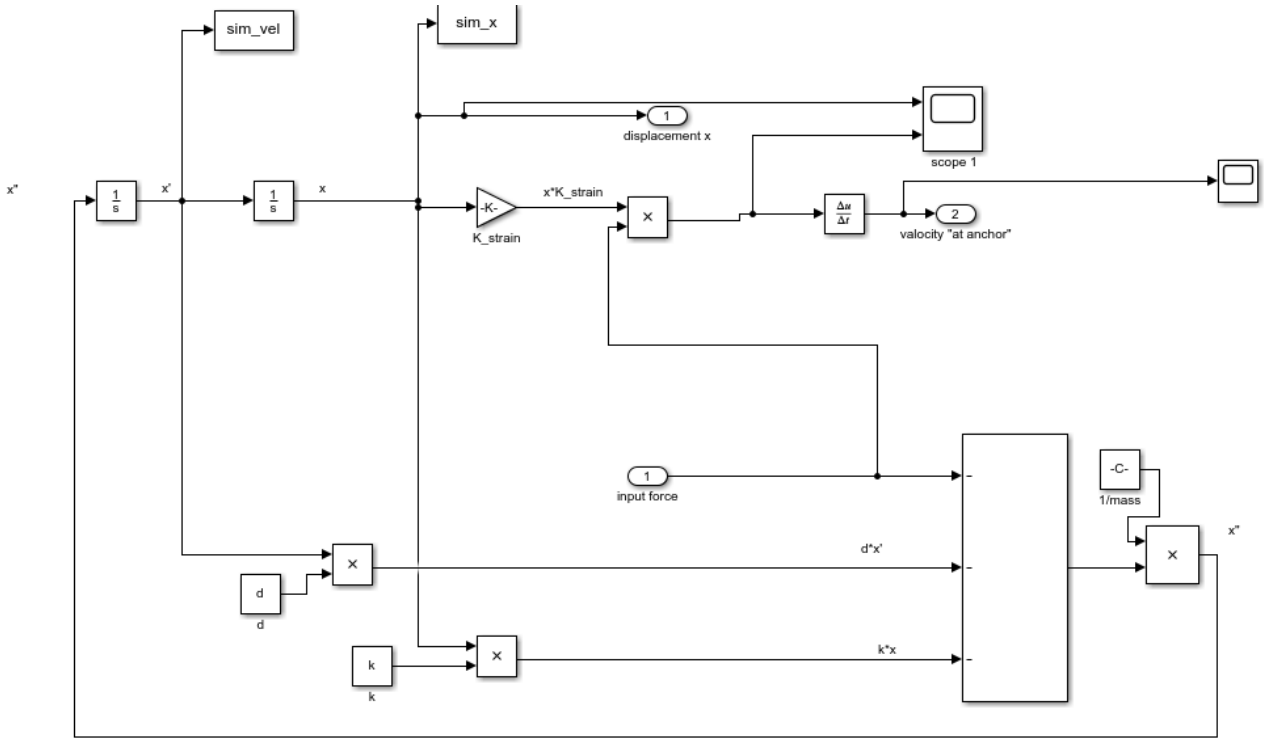

Fig. B.4: Simple U-shaped beam cantilever: Mass-spring-damper system.

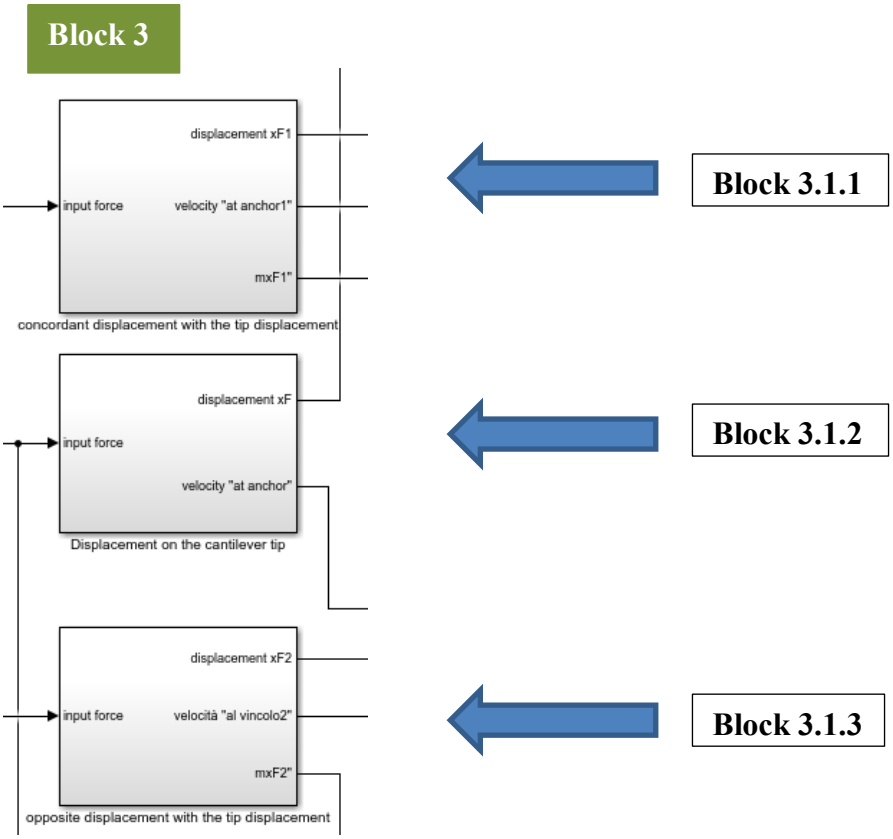

Block 3.1.1

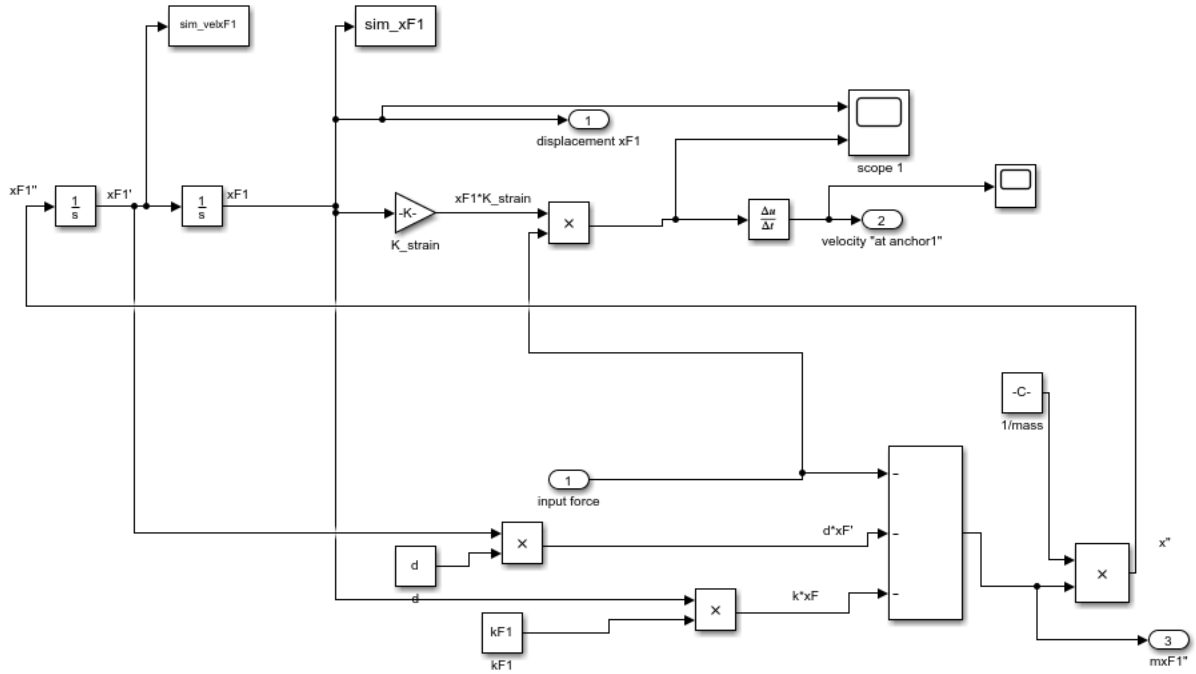

Fig. B.5: Topology 1: Mass-spring-damper system, concordant with the tip displacement.

Block 3.1.2

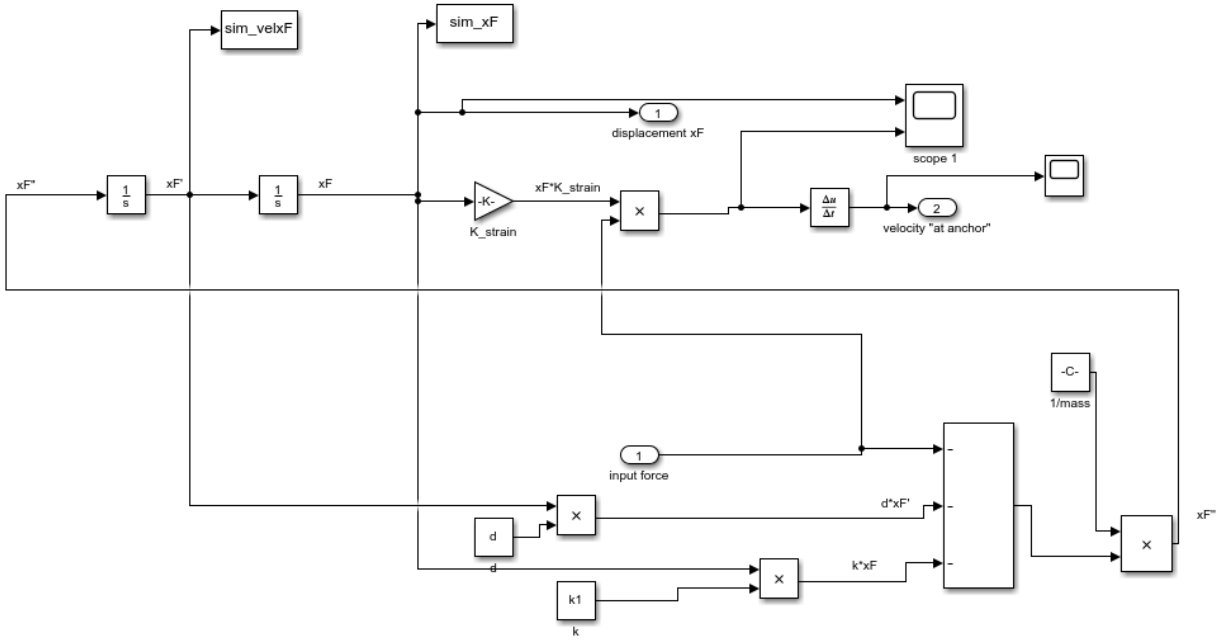

Fig. B.6: Topology 1: Mass-spring-damper system.

Block 3.1.3

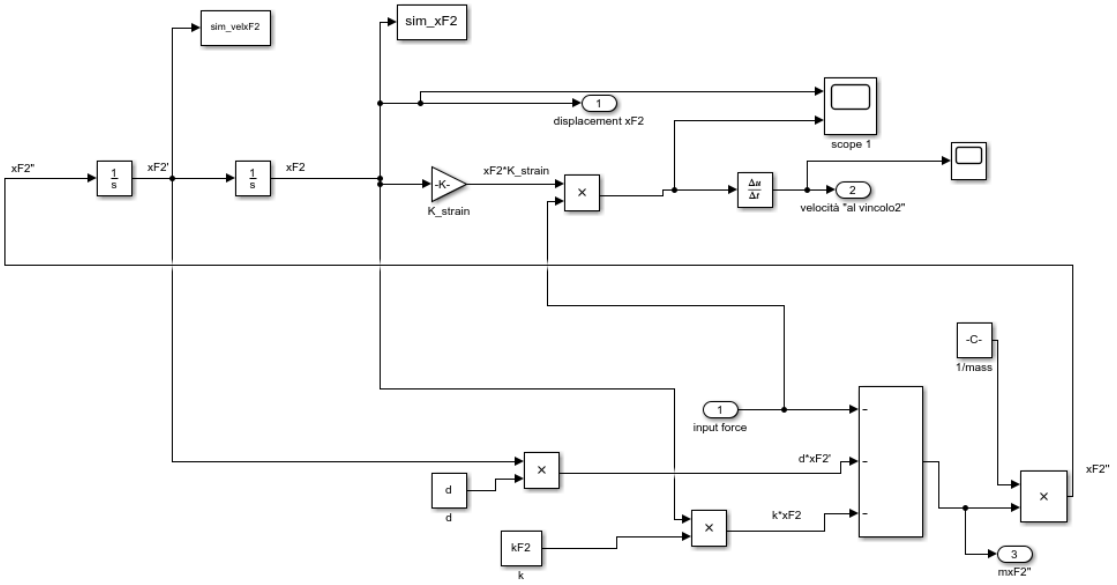

Fig. B.7: Topology 1: Mass-spring-damper system, opposite displacement with the cantilever tip displacement.

Block 4

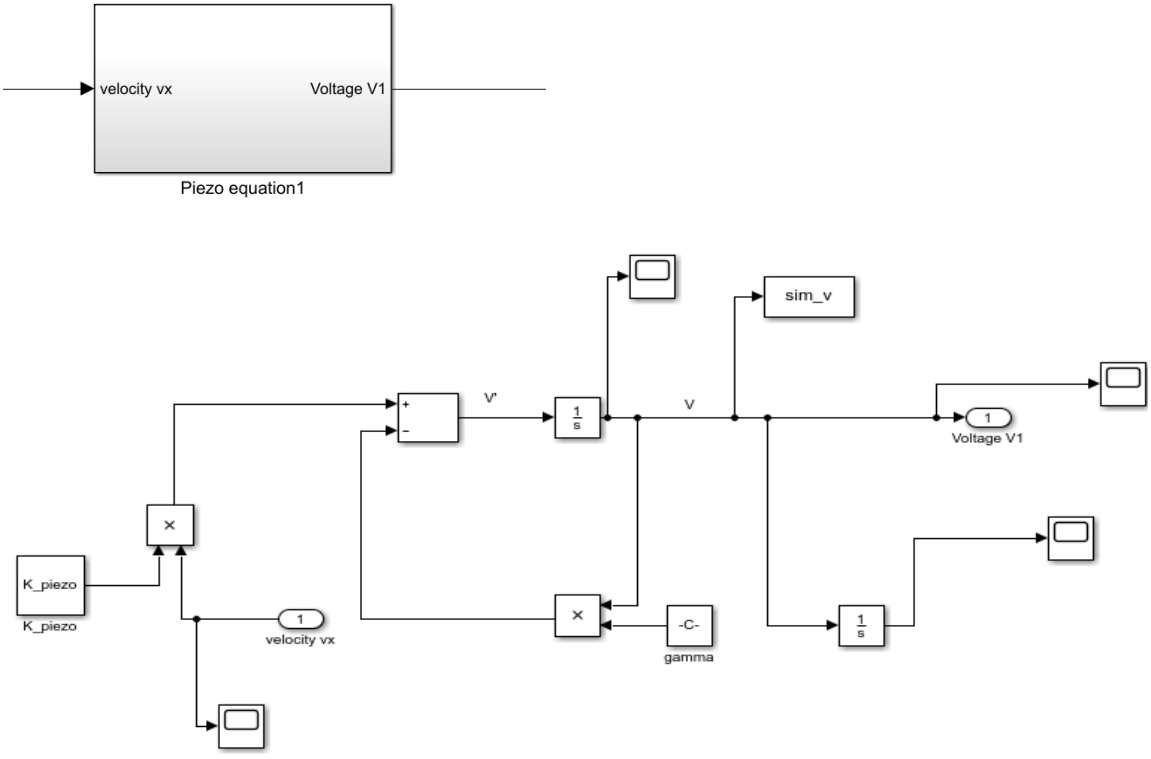

Fig. B.8: Simple U-shaped beam cantilever and Topology 1: Piezoelectric model.

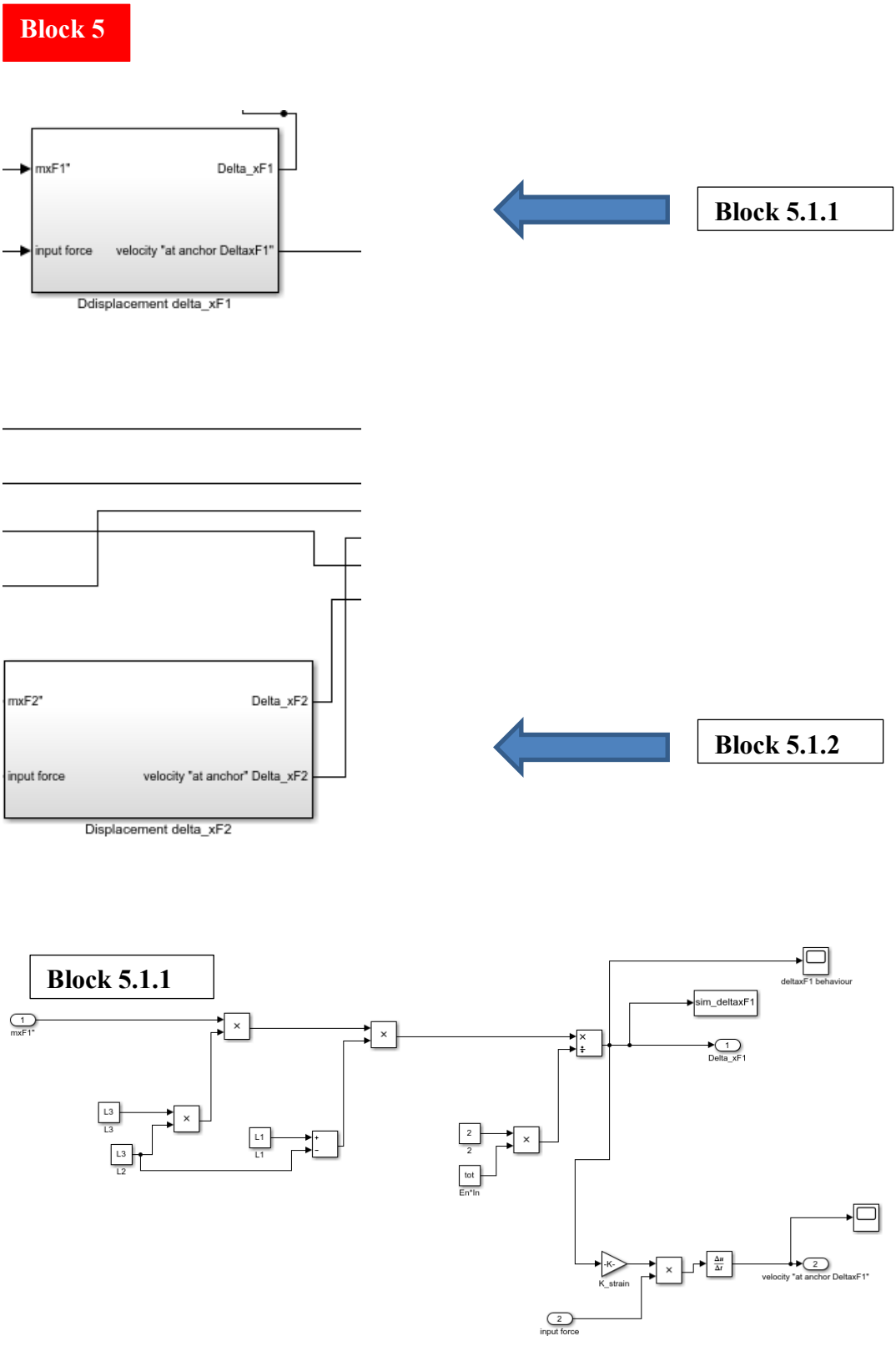

Fig. B.9: Topology 1: Mass-spring-damper system, displacement Δx_{F1}.

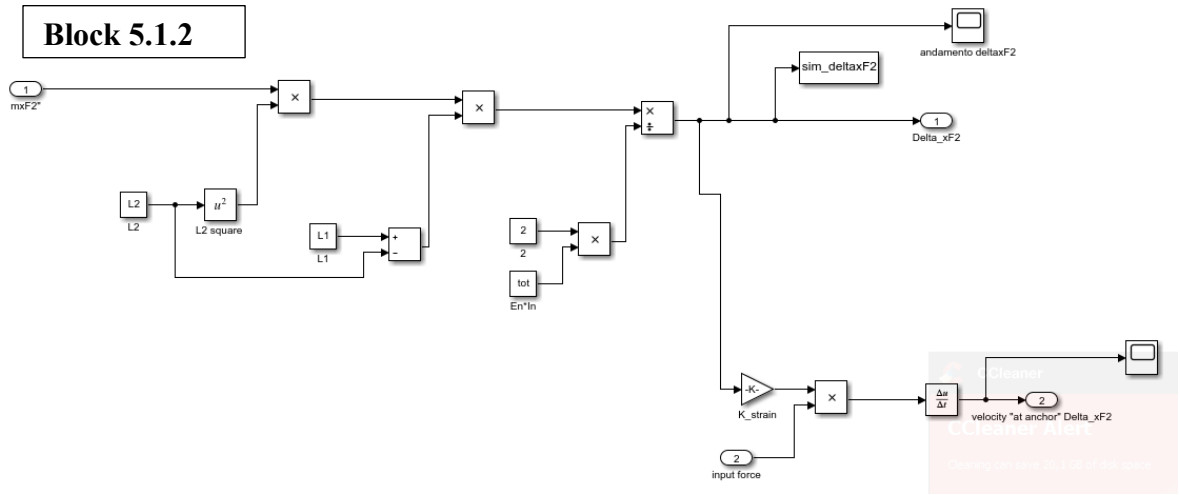

Fig. B.10: Topology 1: Mass-spring-damper system, displacement Δx_{F2}.

2.2. U-shaped beam cantilever VS Topology 2

A Matlab code has been implemented in order to obtain a parametric system and to determine all variables expressed in all equations which describe the static and dynamic model.

MATLAB CODE

```
%% U-shaped beam cantilever parameters
%% LENGTHS
 L10=6400e-6; % arm length [m]
 lm=4500e-6; % length pertinent to the inertial mass [m]
 w2=100e-6; % width pertinent to the inertial mass [m]
 w1=100e-6; % arm width[m]
 l_perp=lm+2*w1; % length where the Lorentz force operates [m]

%% Topology 2 parameters
%% LENGTHS
 L5=300e-6;
 L6=300e-6;
 L7=300e-6;

%% TICKNESS
 t_Si=10e-6; % Silicon [m]
 t_Al=1e-6; % Aluminum [m]
 t_AlN=0.5e-6; % Aluminum Nitride [m]
 t_tot=t_Si+t_Al+t_AlN;

%% LAYERS DENSITIES
```

```
 dens_Si=2.3e3; % expressed in [kg/m^3]
 dens_Al=2.7e3; % expressed in [kg/m^3]
 dens_AlN=3.3e3; % expressed in [kg/m^3]

 massa=lm*w2*(dens_Si*t_Si+dens_Al*t_Al+dens_AlN*t_AlN);   %   evaluation   of
inertial mass in kgr!!!

%% Parameters of Aluminum Nitride stack
 epsilon_33 = 7.9659*10^(-11); % product between epsi_0* epsi_rel (9) [F/m]
 e_31 = -0.58; % coming from the expression d_31/(s_11+s_12) [C/m^2]

%% Other parameters
 Rl =330*10^3; % load on AlN [Ohm]
 d =0.000001; % mechanical damping
 d_piezo =0.0069; % piezoelectric transduction damping
 miu_0 = 4*pi*10^(-7);

%% Parameters used to estimate the elastic constant
%% Simple U-shaped beam cantilever (total length)
 L=L10+w2;

%% Topology 2
 L8=5200e-6;
 L1=L8+4*w2+L5+L6+L7;
 L2=L8+3*w2+L6+L7;
 L3=L8+2*w2+L7;
 L4=L8+w2;

%% Other parameters
 gamma = t_AlN/(Rl*epsilon_33*w1*l_perp);
 K_piezo  =  e_31*t_AlN/(epsilon_33*w1*l_perp);  % coupling  constant  of  the
piezoelectric stack

%% Parameters used to create a magnetic field
 h_dist =1e-3; % radius of conductor [m]
```

%%%%%% EQUIVALENT SECTION METHOD

```
%% Young's Moduli
 E_Si=170*10^9; % Silicon
 E_AlN=310*10^9; % Aluminum Nitride
 E_Al=70*10^9; % Aluminum

 E=[E_Si E_AlN E_Al]; % Young's moduli vector
 T=[t_Si t_AlN t_Al]; % Thickness vector
 larghezza=[w1 w1 w1];
 E_max=max(E);

 for i=1:1:length(E)
  w_norm(i)=larghezza(i)*(E(i)/E_max);
 end

 for i=1:1:length(T)
  s_norm(i)=w_norm(i)*T(i);
 end

 tk=0;
 for i=1:1:length(T)
  h(i)=tk+(T(i)/2);
  tk=tk+T(i);
```

```
 end

 somma_sh=0;
 somma_s=0;
 for i=1:1:length(s_norm)
  somma_sh=somma_sh+(s_norm(i)*h(i));
  somma_s=somma_s+s_norm(i);
 end

 hn=somma_sh/somma_s;

 for i=1:1:length(T)
  Ix(i)=((T(i)^3)*w1*E(i)/E_max)/12;
 end

 for i=1:1:length(T)
  I_norm(i)=Ix(i)+(s_norm(i)*(hn-h(i))^2);
 end

 In=0;
 for i=1:1:length(I_norm)
  In=In+I_norm(i);
 end
 tot=0;
 for i=1:1:length(I_norm)
  c(i)=E(i)*I_norm(i);
  tot=c(i)+tot; %[N*m2]
 end

 K_strain = 3*((L)^2)/(E_max*w1*((t_tot)^2)); %parameter related to the axial
strain
%%%%%%

% Mechanical stiffness
 k=6*tot/(L^3); % Simple U-shaped beam cantilever [N/m]
% Topology 2
 k1=(6*tot)/((L1)^3);
 kF1=(12*tot)/((3*L1-L2)*(L2^2));
 kF2=(12*tot)/((3*L1-L3)*(L3^2));
 kF3=(12*tot)/((3*L1-L4)*(L4^2));

% Current into the conductor
 I_cond=5e-3;

 omega=sqrt(k/massa); % Related to the Simple U-shaped beam cantilever
 freq=omega/(2*pi);
 omega1=sqrt(k1/massa); % Related to the Topology 2
 freq1=omega1/(2*pi);

% Driving current into the Simple U-shaped beam cantilever
 I_cant=20e-3; % [App]

% Evaluation of magnetic induction
 B=miu_0*I_cond/(2*pi*h_dist); % ([H]*[A])/([m2])=[Wb]/[m2]=[T]

% Lorentz Force
 Fl=I_cant*B*l_perp;
```

SIMULINK SCHEMATIC

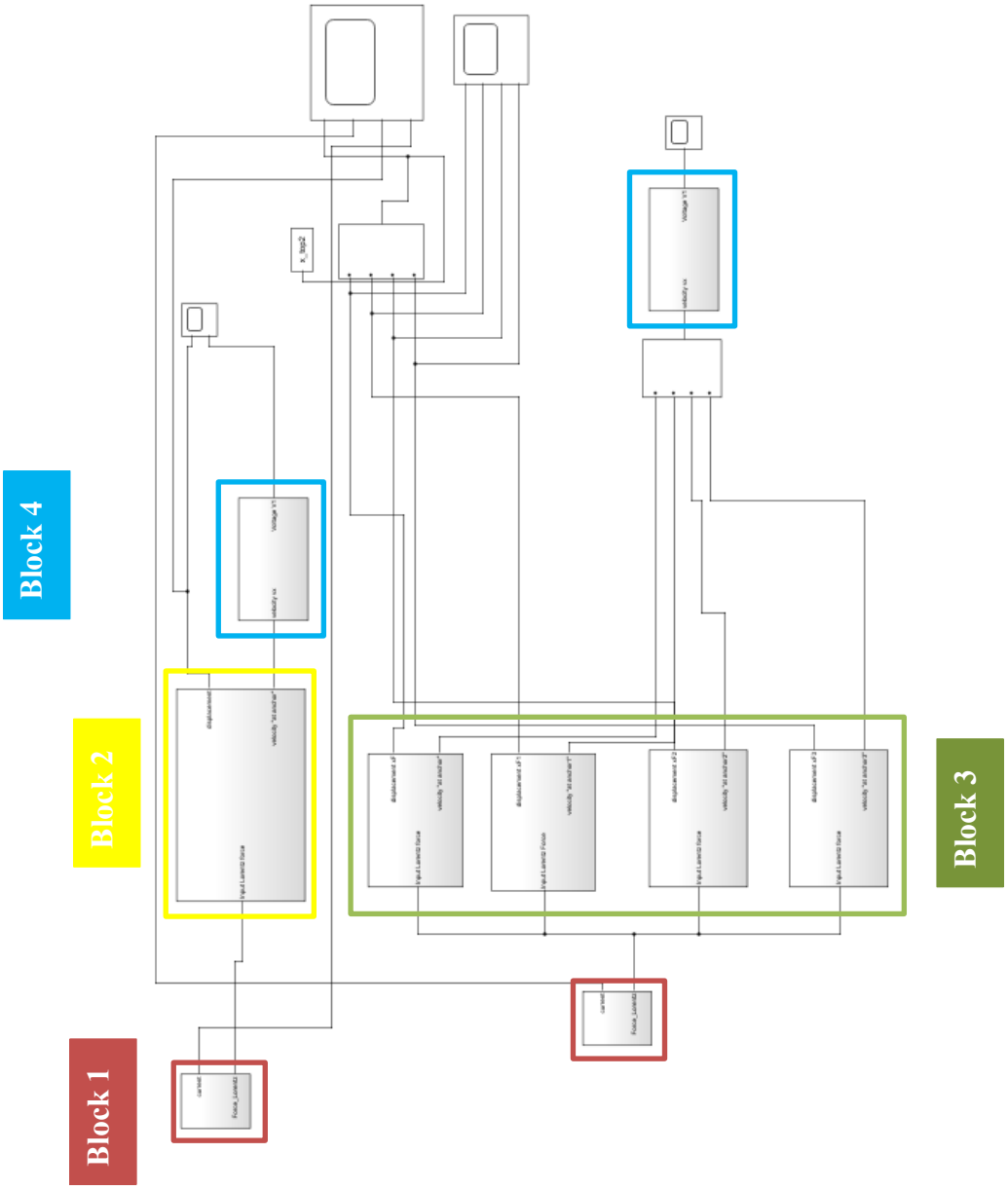

Fig. B.11: Simulink schematic: Simple VS Topology 2.

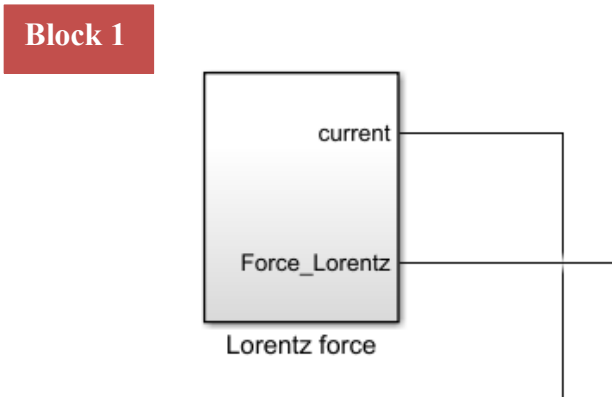

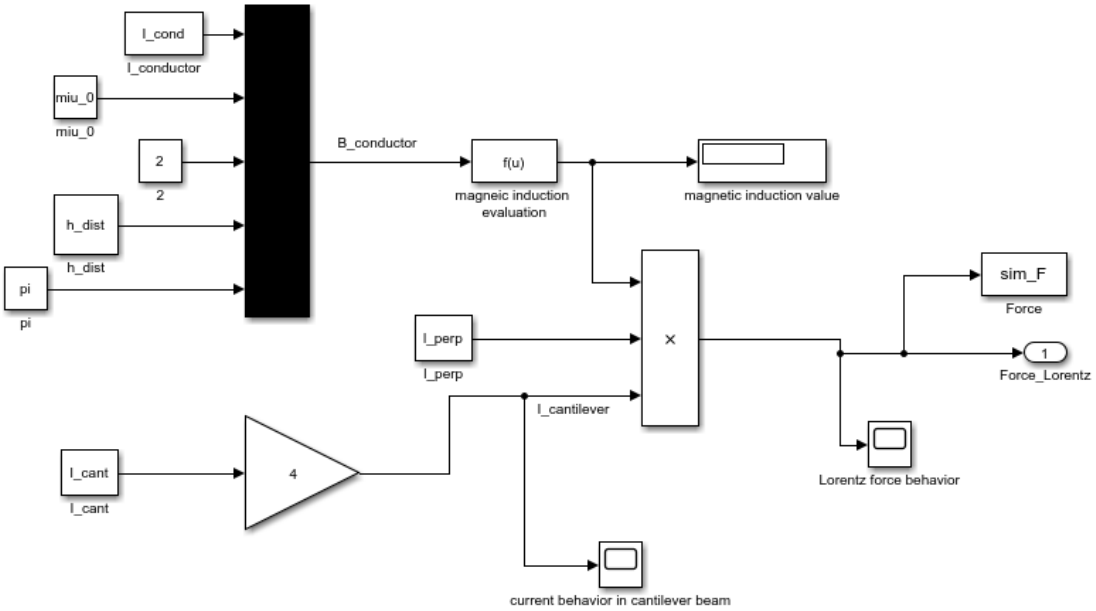

Fig. B.12: Simple U-shaped beam cantilever: Lorentz force in static analysis.

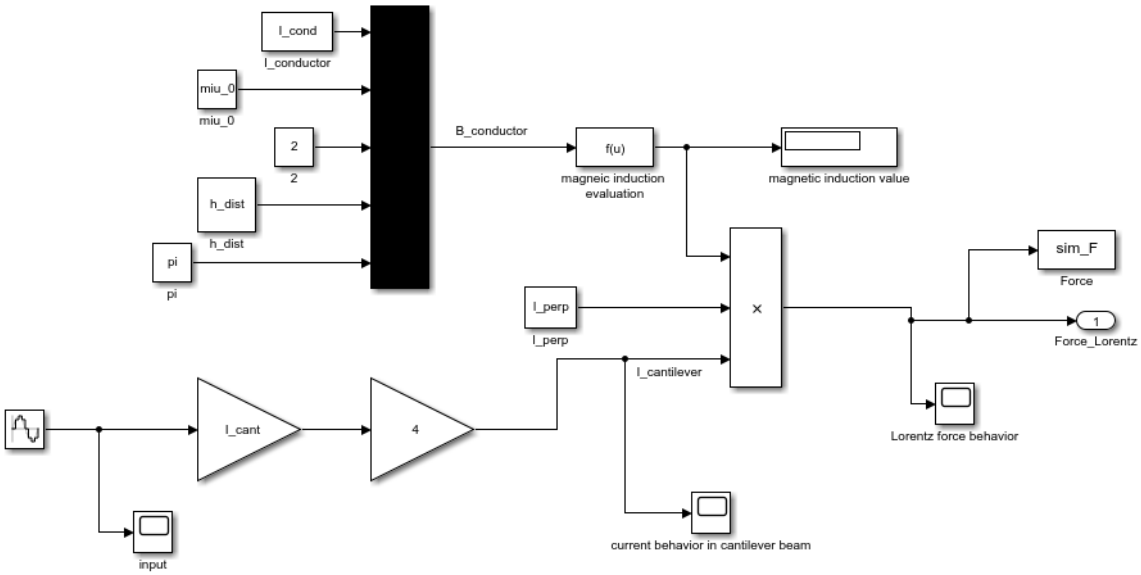

Fig. B.13: Simple U-shaped beam cantilever: Lorentz force in dynamic analysis.

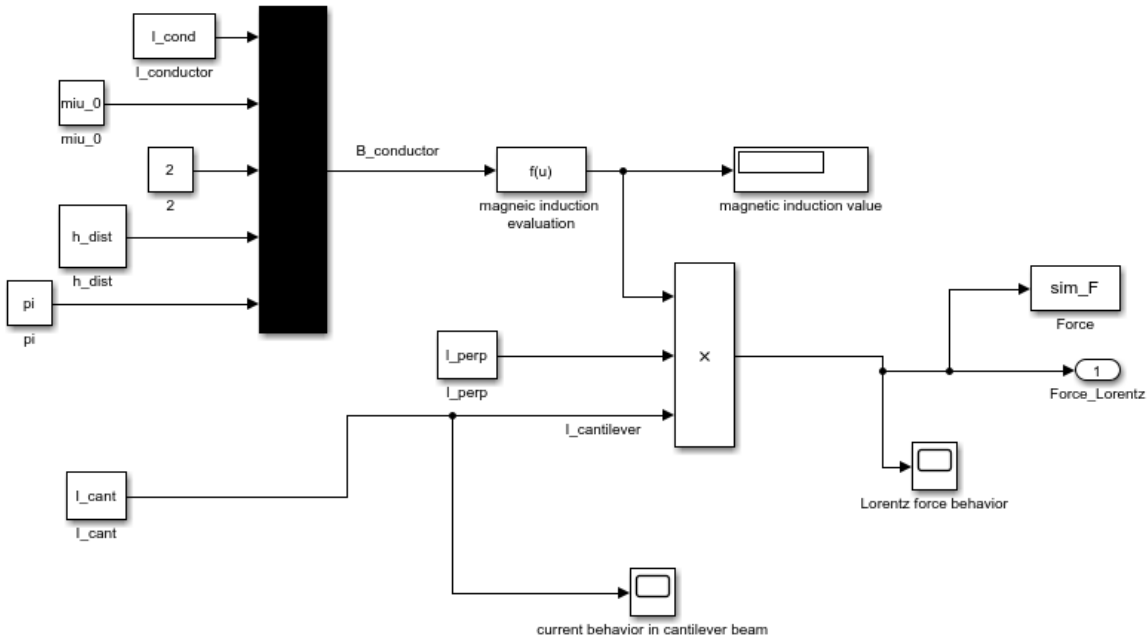

Fig. B.14: Topology 2: Lorentz force in static analysis.

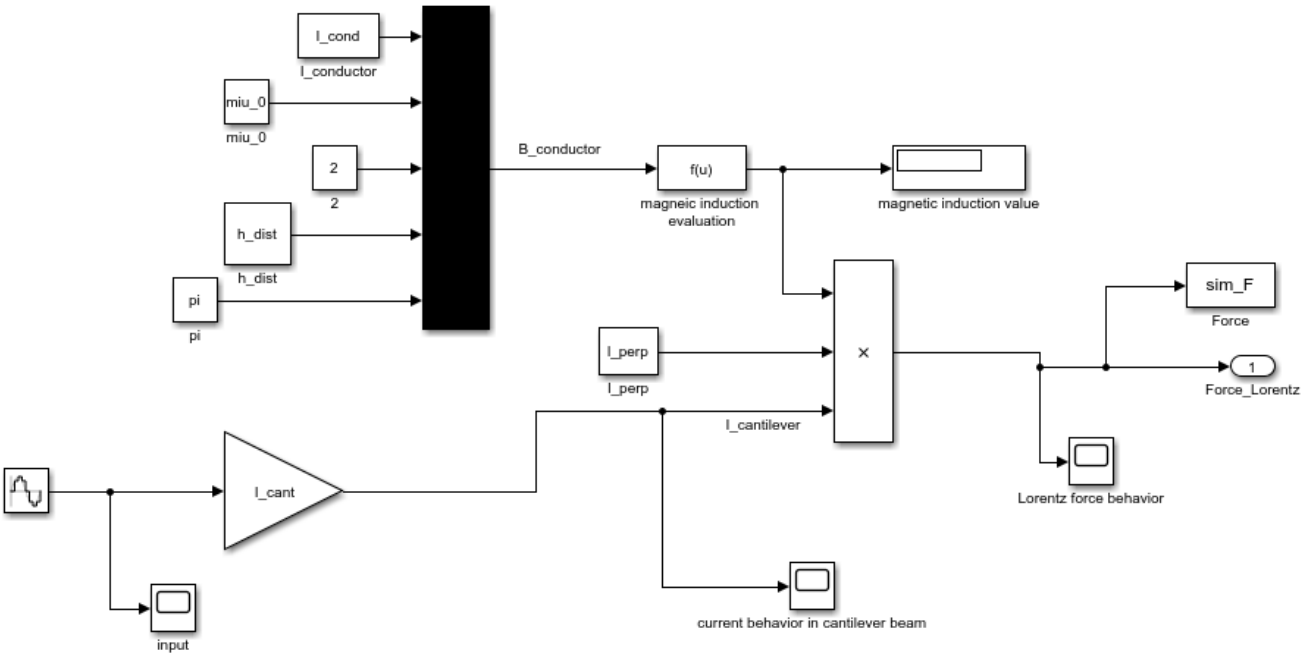

Fig. B.15: Topology 2: Lorentz force in dynamic analysis.

Block 2

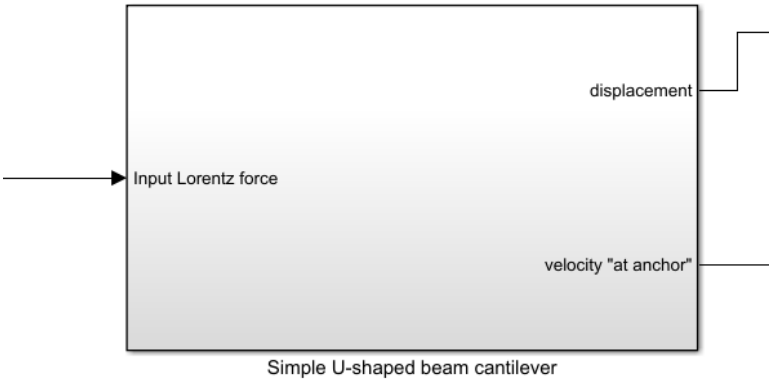

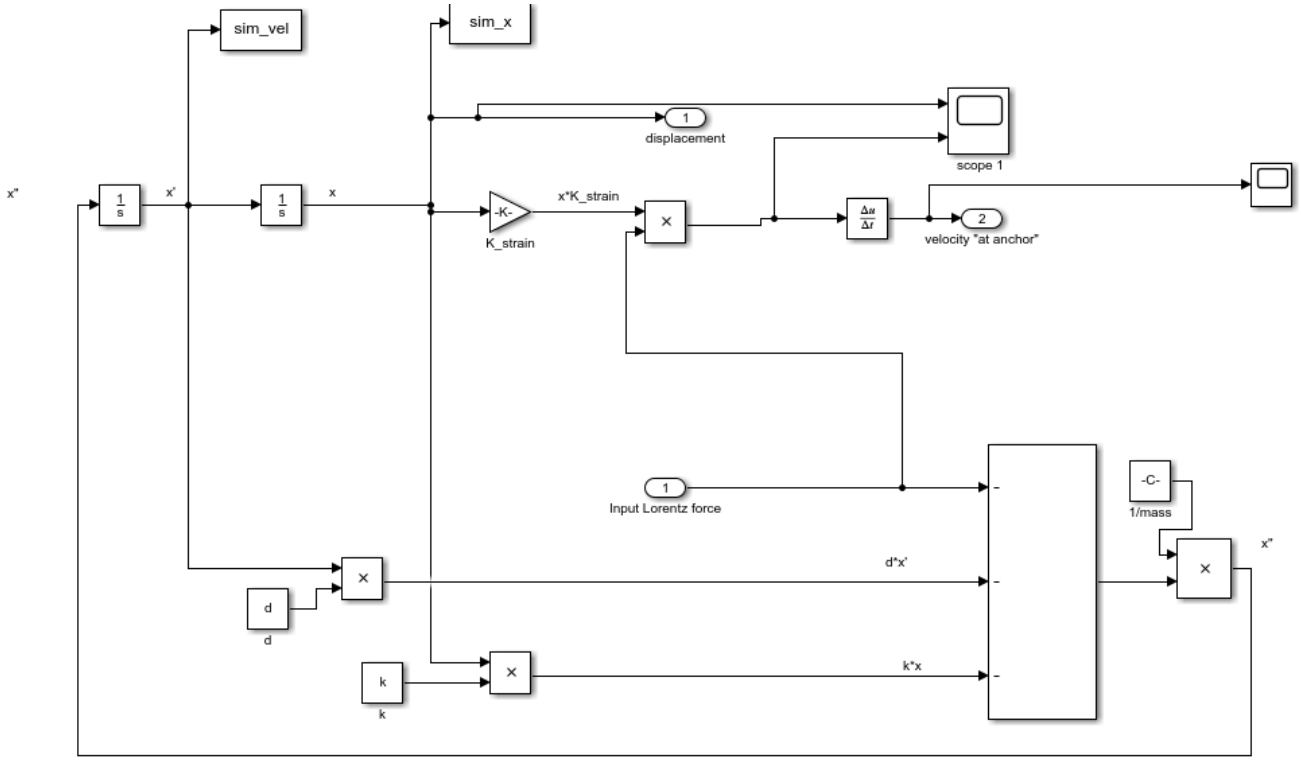

Fig. B.16: Simple U-shaped beam cantilever: Mass-spring-damper system.

Block 3

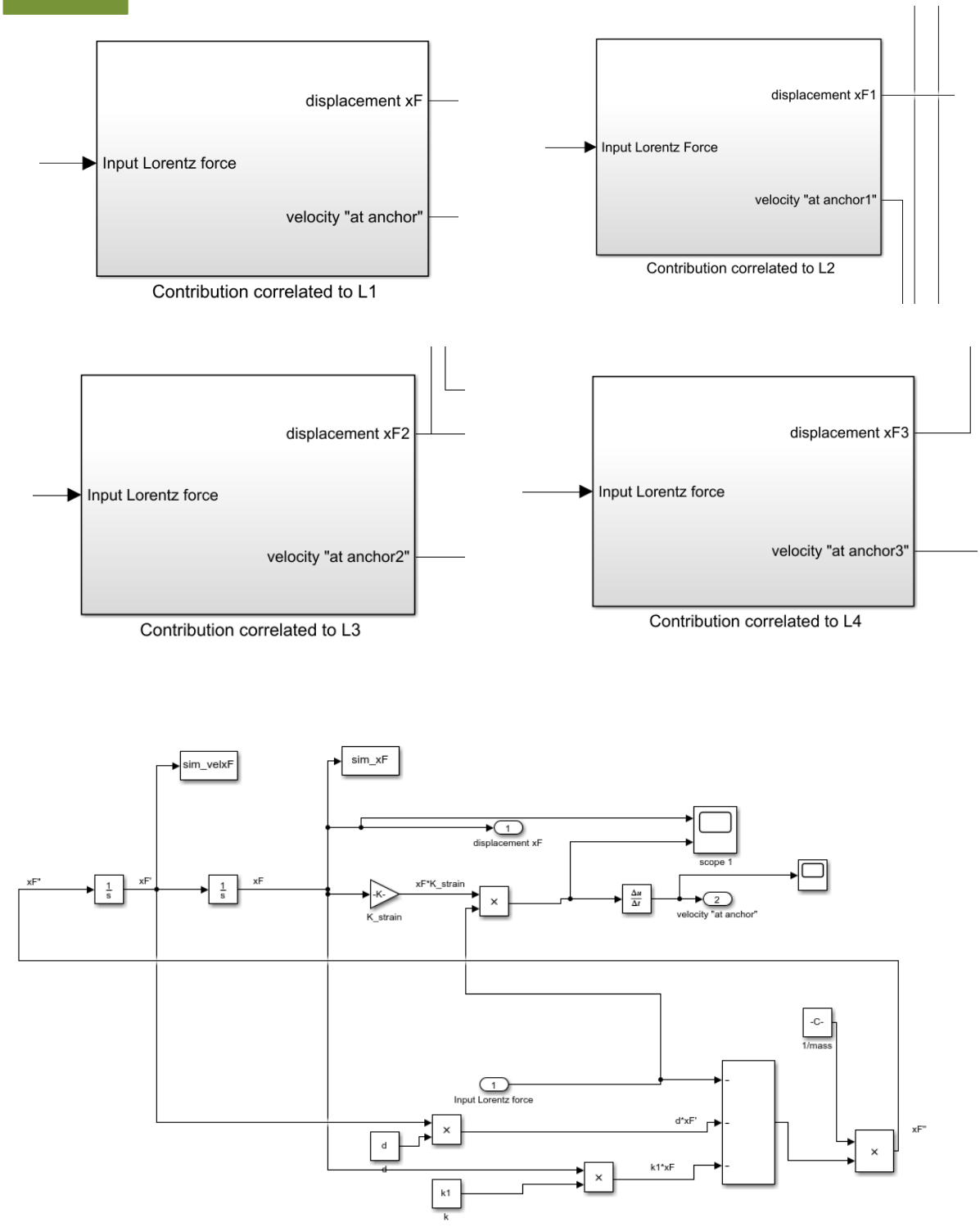

Fig. B.17: Topology 2: Mass-spring-damper system, associated to L_1.

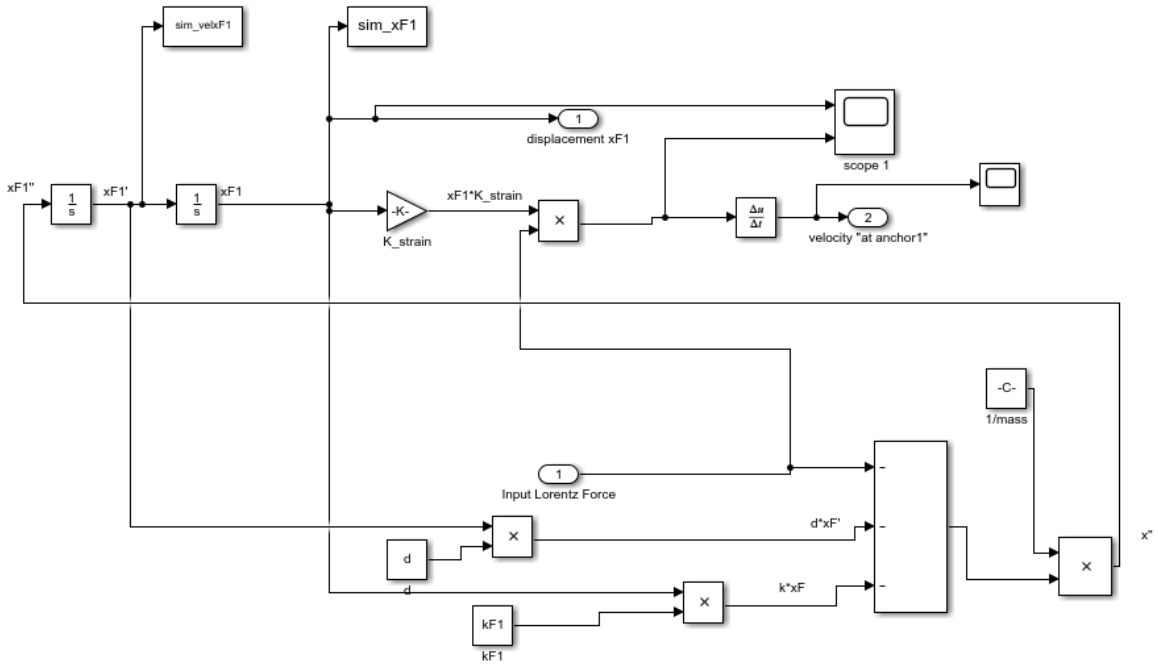

Fig. B.18: Topology 2: Mass-spring-damper system, associated to L_2.

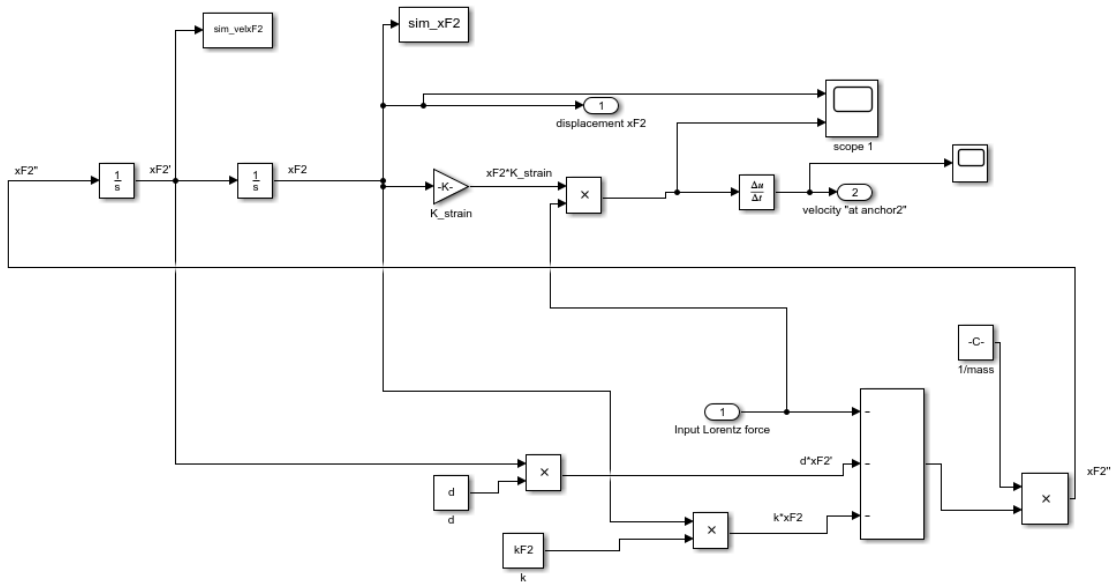

Fig. B.19: Topology 2: Mass-spring-damper system, associated to L_3.

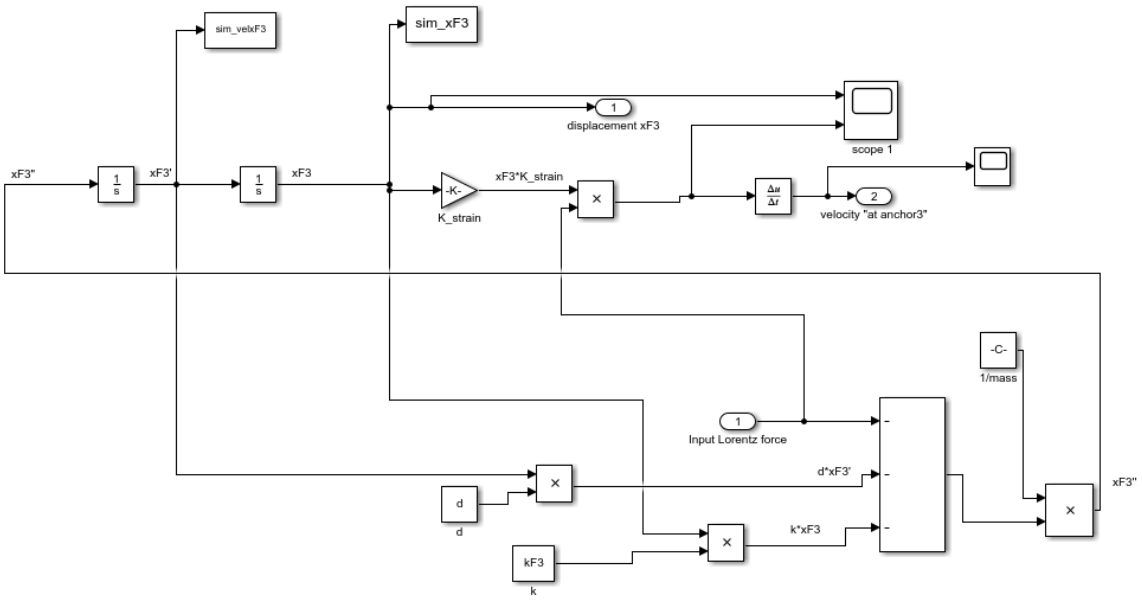

Fig. B.20: Topology 2: Mass-spring-damper system, associated to L_4.

Block 4

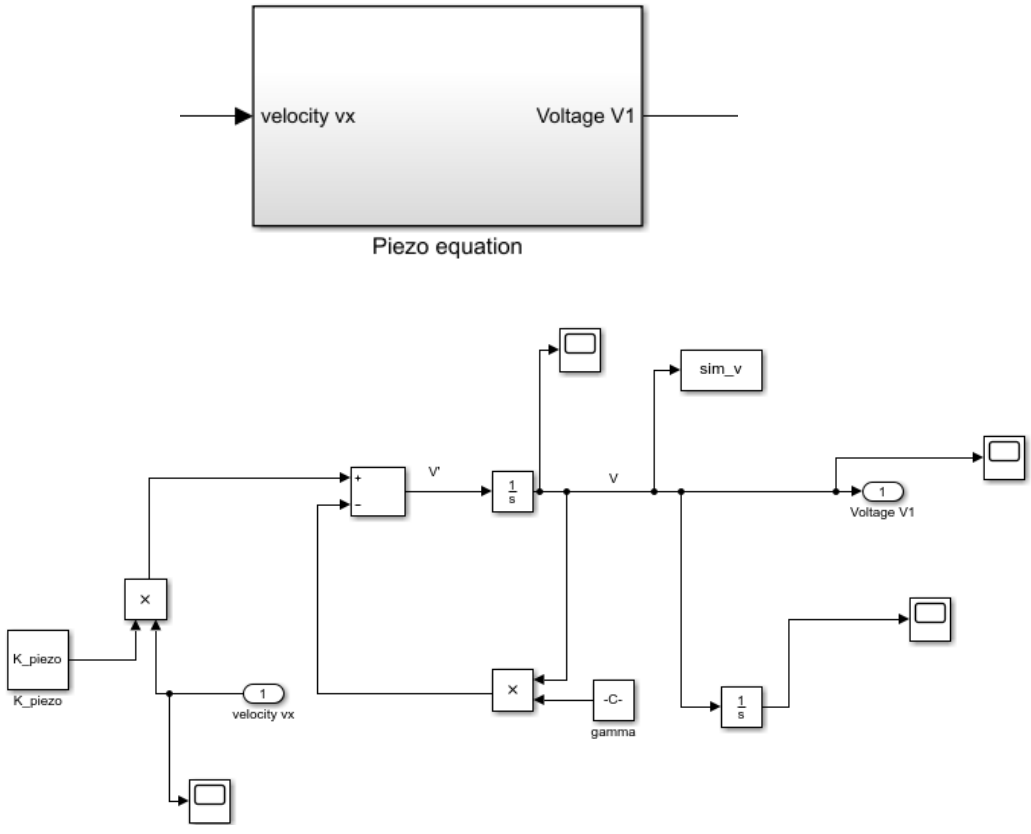

Fig. B.21: Simple U-shaped beam cantilever and Topology 2: Piezoelectric model.

2.3. U-shaped beam cantilever VS Topology 3

A Matlab code has been implemented in order to obtain a parametric system and to determine all variables expressed in all equations which describe the static and dynamic model.

MATLAB CODE

```
%% U-shaped beam cantilever parameters
%% LENGTHS
 lm=1500e-6; % length pertinent to the M inertial mass[m]
 w5=100e-6; % width pertinent to the inertial mass [m]
 w1=100e-6; % arm width related to M mass
 l_perp=lm+2*w1; % length where the Lorentz force operates [m]
 L10=6400e-6; % arm length

%% TOPOLOGY 3
%% WIDTHS
 w2=2*w1; % arm width related to M1 mass
 w3=3*w1; % arm width related to M2 mass
 w4=4*w1; % arm width related to M3 mass

%% TOPOLOGY 3
 L1=1500e-6;
 L2=1500e-6
 L3=1500e-6;

%% TICKNESS
 t_Si=10e-6; % Silicon [m]
 t_Al=1e-6; % Aluminum [m]
 t_AlN=0.5e-6; % Aluminum Nitride [m]
 t_tot=t_Si+t_Al+t_AlN;

%% LAYERS DENSITIES
 dens_Si=2.3e3; % expressed in [kg/m^3]
 dens_Al=2.7e3; % expressed in [kg/m^3]
 dens_AlN=3.3e3; % expressed in [kg/m^3]

 massa=lm*w5*(dens_Si*t_Si+dens_Al*t_Al+dens_AlN*t_AlN% evaluation of
inertial mass in kgr!!!
 massa1=2*massa; % inertial mass related to M1
 massa2=3*massa; % inertial mass related to M2
 massa3=4*massa; % inertial mass related to M3

%% Parameters of Aluminum Nitride stack
 epsilon_33 = 7.9659*10^(-11); % product between epsi_0* epsi_rel (9) [F/m]
 e_31 = -0.58; % coming from the expression d_31/(s_11+s_12) [C/m^2]

%% Other parameters
 Rl =330*10^3; % load on AlN [Ohm]
 d =0.000001; % mechanical damping
 d_piezo =0.0069; % piezoelectric transduction damping
 miu_0 = 4*pi*10^(-7);
```

```
%% Parameters used to estimate the elastic constant
%% Simple U-shaped beam cantilever (total length)
 L=L10+w5;
%% TOPOLOGY 3
 L4=1600e-6;

%% Other parameters
 L11=L1+w5;
 L21=L2+w5;
 L31=L3+w5;
 L41=L4+w5;

 Ltot=L11+L21+L31+L41;

%% Other parameters
 gamma = t_AlN/(Rl*epsilon_33*w1*l_perp); % time constant related to M
 gamma1 = t_AlN/(Rl*epsilon_33*w2*l_perp); % time constant related to M1
 gamma2 = t_AlN/(Rl*epsilon_33*w3*l_perp); % time constant related to M2
 gamma3 = t_AlN/(Rl*epsilon_33*w4*l_perp); % time constant related to M3
 K_piezo  =  e_31*t_AlN/(epsilon_33*w1*l_perp);  % coupling  constant  of  the
piezoelectric stack having mass M
 K_piezo1 = e_31*t_AlN/(epsilon_33*w2*l_perp); % coupling constant of the
piezoelectric stack having mass M1
 K_piezo2 = e_31*t_AlN/(epsilon_33*w3*l_perp); % coupling constant of the
piezoelectric stack having mass M2
 K_piezo3 = e_31*t_AlN/(epsilon_33*w4*l_perp); % coupling constant of the
piezoelectric stack having mass M3

% Parameters used to create a magnetic field
 h_dist =1e-3; % radius of conductor [m]
```

%%%%%%% EQUIVALENT SECTION METHOD

```
%% Young's Moduli
 E_Si=170*10^9; % Silicon
 E_AlN=310*10^9; % Aluminum Nitride
 E_Al=70*10^9; % Aluminum

 E=[E_Si E_AlN E_Al]; % Young's moduli vector
 T=[t_Si t_AlN t_Al]; % Thickness vector
 larghezza=[w1 w1 w1]; % related to the block with mass M1
 larghezza1=[w2 w2 w2]; % related to the block with mass M2
 larghezza2=[w3 w3 w3]; % related to the block with mass M3
 larghezza3=[w4 w4 w4]; % related to the block with mass M4
 E_max=max(E);

 for i=1:1:length(E)
  w_norm(i)=larghezza(i)*(E(i)/E_max); %related to the block with mass M1
  w_norm1(i)=larghezza1(i)*(E(i)/E_max); % related to the block with mass M2
  w_norm2(i)=larghezza2(i)*(E(i)/E_max); % related to the block with mass M3
  w_norm3(i)=larghezza3(i)*(E(i)/E_max); % related to the block with mass M4
 end

 for i=1:1:length(T)
  s_norm(i)=w_norm(i)*T(i); % related to the block with mass M1
  s_norm1(i)=w_norm1(i)*T(i); % related to the block with mass M2
  s_norm2(i)=w_norm2(i)*T(i); % related to the block with mass M3
  s_norm3(i)=w_norm3(i)*T(i); % related to the block with mass M4
 end
```

```
tk=0;
for i=1:1:length(T)
 h(i)=tk+(T(i)/2);
 tk=tk+T(i);
end

somma_sh=0;
somma_sh1=0;
somma_sh2=0;
somma_sh3=0;
somma_s=0;
somma_s1=0;
somma_s2=0;
somma_s3=0;

for i=1:1:length(s_norm)
 somma_sh=somma_sh+(s_norm(i)*h(i)); % related to the block with mass M1
 somma_sh1=somma_sh1+(s_norm1(i)*h(i)); % related to the block with mass M2
 somma_sh2=somma_sh2+(s_norm2(i)*h(i)); % related to the block with mass M3
 somma_sh3=somma_sh3+(s_norm3(i)*h(i)); % related to the block with mass M4
 somma_s=somma_s+s_norm(i); % related to the block with mass M1
 somma_s1=somma_s1+s_norm1(i); % related to the block with mass M2
 somma_s2=somma_s2+s_norm2(i); % related to the block with mass M3
 somma_s3=somma_s3+s_norm3(i); % related to the block with massM4
end

hn=somma_sh/somma_s; % related to the block with mass M1
hn1=somma_sh1/somma_s1; % related to the block with mass M2
hn2=somma_sh2/somma_s2; % related to the block with mass M3
hn3=somma_sh3/somma_s3; % related to the block with mass M4

for i=1:1:length(T)
 Ix(i)=((T(i)^3)*w1*E(i)/E_max)/12; % related to the block with mass M1
 Ix1(i)=((T(i)^3)*w2*E(i)/E_max)/12; % related to the block with mass M2
 Ix2(i)=((T(i)^3)*w3*E(i)/E_max)/12; % related to the block with mass M3
 Ix3(i)=((T(i)^3)*w4*E(i)/E_max)/12; % related to the block with mass M4
end

for i=1:1:length(T)
 I_norm(i)=Ix(i)+(s_norm(i)*(hn-h(i))^2); % related to the block with mass
M1
 I_norm1(i)=Ix1(i)+(s_norm1(i)*(hn1-h(i))^2); % related to the block with
mass M2
 I_norm2(i)=Ix2(i)+(s_norm2(i)*(hn2-h(i))^2); % related to the block with
mass M3
 I_norm3(i)=Ix3(i)+(s_norm3(i)*(hn3-h(i))^2); % related to the block with
mass M4
end

In=0;
In1=0;
In2=0;
In3=0;
for i=1:1:length(I_norm)
 In=In+I_norm(i); % related to the block with mass M1
 In1=In1+I_norm1(i); % related to the block with mass M2
 In2=In2+I_norm2(i); % related to the block with mass M3
 In3=In3+I_norm3(i); % related to the block with mass M4
End
```

```
 tot=0;
 tot1=0;
 tot2=0;
 tot3=0;
 for i=1:1:length(I_norm)
  c(i)=E(i)*I_norm(i); % related to the block with mass M1
  c1(i)=E(i)*I_norm1(i); % related to the block with mass M2
  c2(i)=E(i)*I_norm2(i); % related to the block with mass M3
  c3(i)=E(i)*I_norm3(i); % related to the block with mass M4
  tot=c(i)+tot; % [N*m2] % related to the block with mass M1
  tot1=c1(i)+tot1; % [N*m2] % related to the block with mass M2
  tot2=c2(i)+tot2; % [N*m2] % related to the block with mass M3
  tot3=c3(i)+tot3; % [N*m2] % related to the block with mass M4
 end
%%%%%%

 K_strain = 3*((L11)^2)/(E_max*w1*((t_tot)^2)); % related to the block with
mass M1
 K_strain1 = 3*((L21)^2)/(E_max*w2*((t_tot)^2)); % related to the block with
mass M2
 K_strain2 = 3*((L31)^2)/(E_max*w3*((t_tot)^2)); % related to the block with
mass M3
 K_strain3 = 3*((L41)^2)/(E_max*w4*((t_tot)^2)); % related to the block with
mass M4
 K_strain4 = 3*((L)^2)/(E_max*w1*((t_tot)^2)); % related to the simple U-
shaped beam cantilever

%% Mechanical stiffness
%% Topology 3
 k=6*tot/((L11)^3); % related to the block with mass M1
 k1=6*tot1/((L21)^3); % related to the block with mass M2
 k2=6*tot2/((L31)^3); % related to the block with mass M3
 k3=6*tot3/((L41)^3); % related to the block with mass M4

%% Simple U-shaped beam cantilever
 k4=6*tot3/((L)^3);

%% Current into the conductor
 I_cond=5e-3;

 omega=sqrt(k4/massa); % related to the simple U-shaped beam cantilever
 freq=omega/(2*pi);
 omega1=sqrt(k/massa); % related to the block with mass M1
 freq1=omega1/(2*pi);

%% Driving current into the Simple U-shaped beam cantilever
 I_cant=20e-3; % [App]

%% Evaluation of magnetic induction
 B=miu_0*I_cond/(2*pi*h_dist); % ([H]*[A])/([m2])=[Wb]/[m2]=[T]

%% Lorentz Force
 Fl=I_cant*B*l_perp;
```

SIMULINK SCHEMATIC

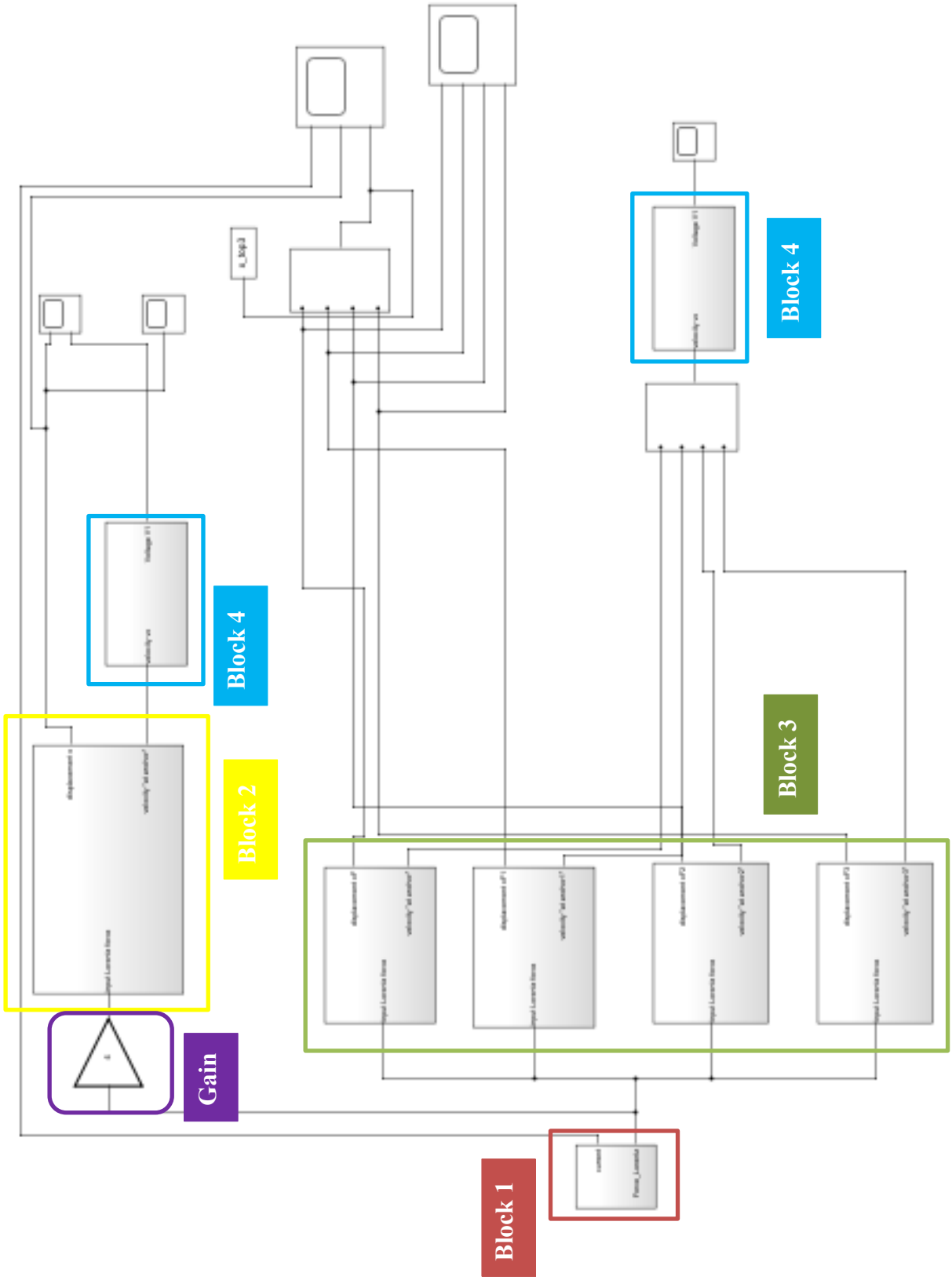

Fig. B.22: Simulink schematic: Simple VS Topology 3.

Block 1

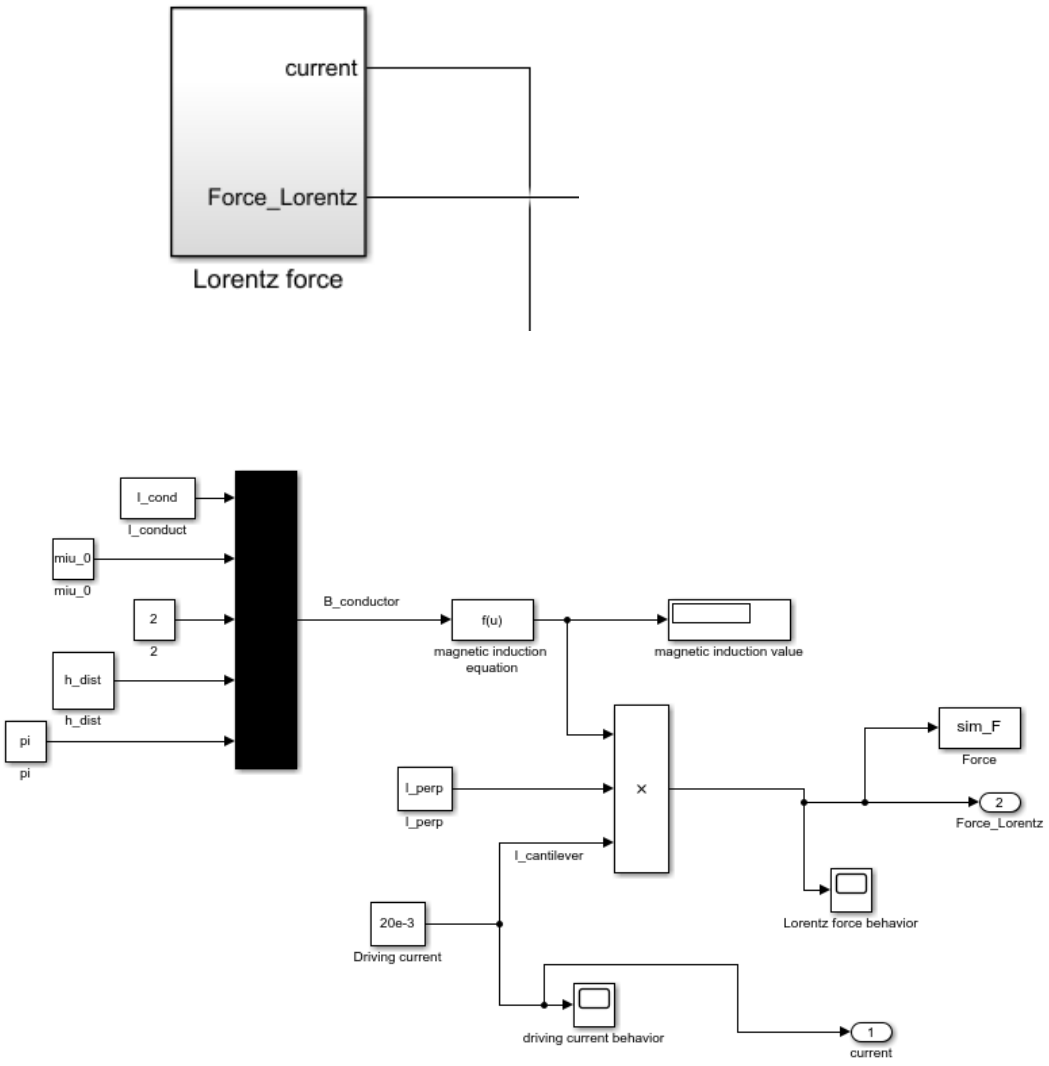

Fig. B.23: Lorentz force in static analysis.

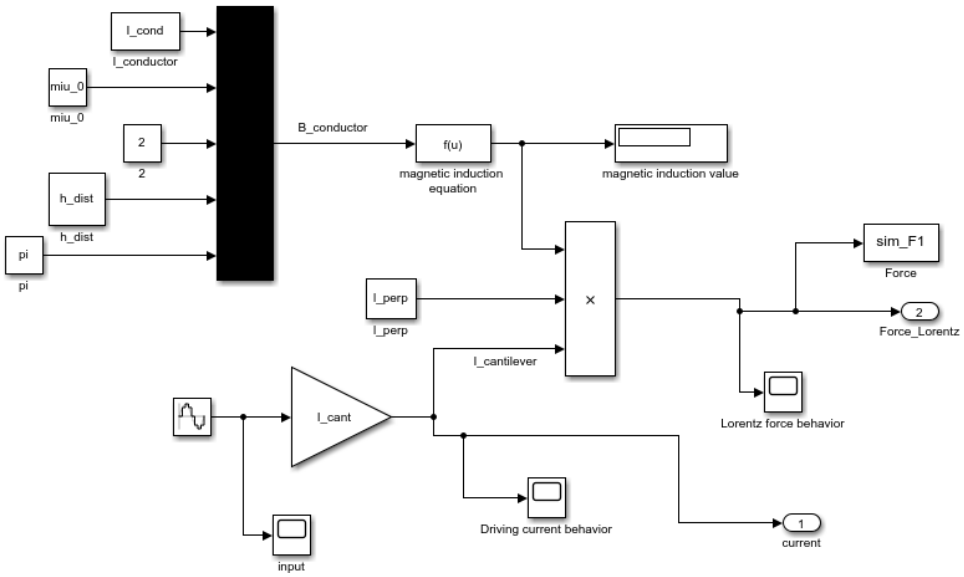

Fig. B.24: Lorentz force in dynamic analysis.

Block 2

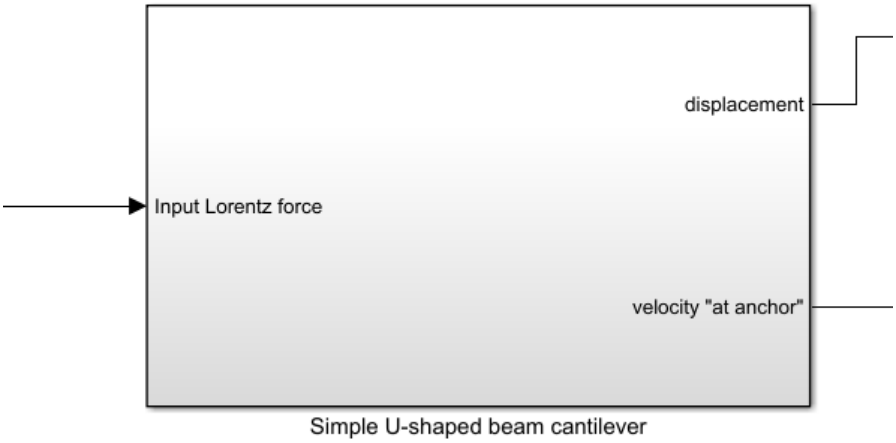

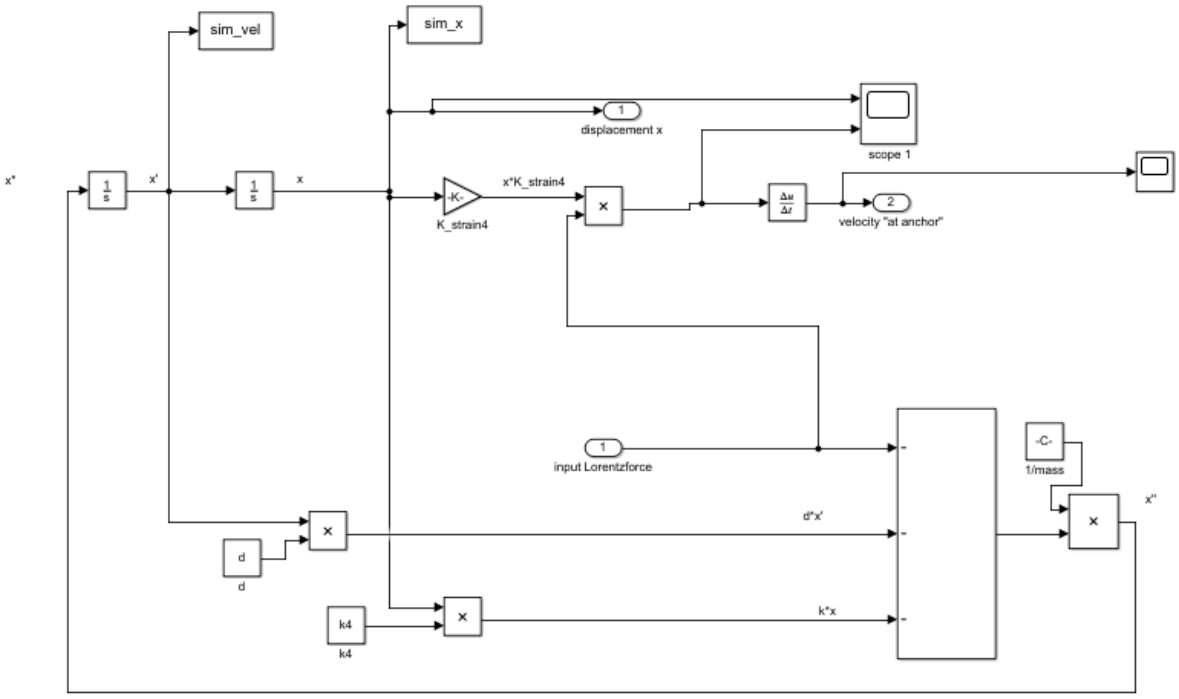

Fig. B.25: Simple U-shaped beam cantilever: Mass-spring-damper system.

Block 3

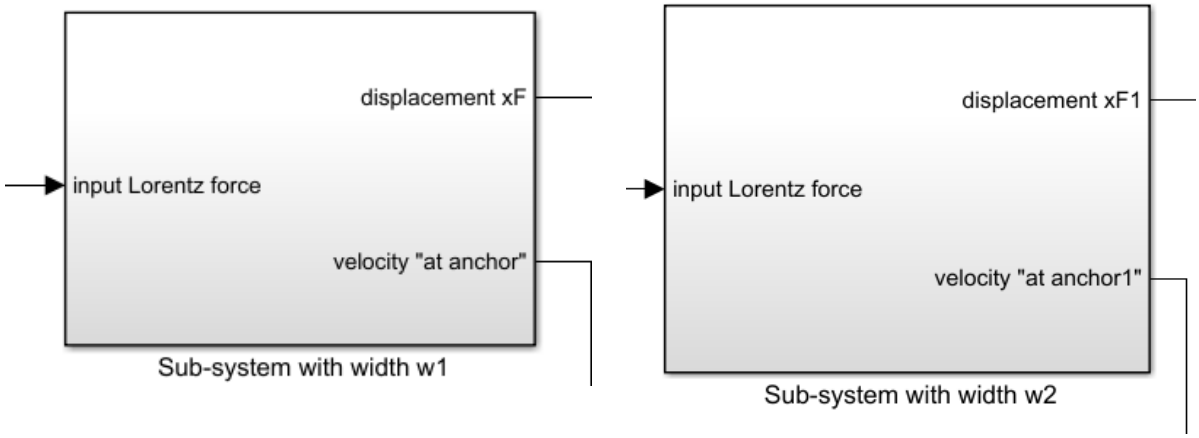

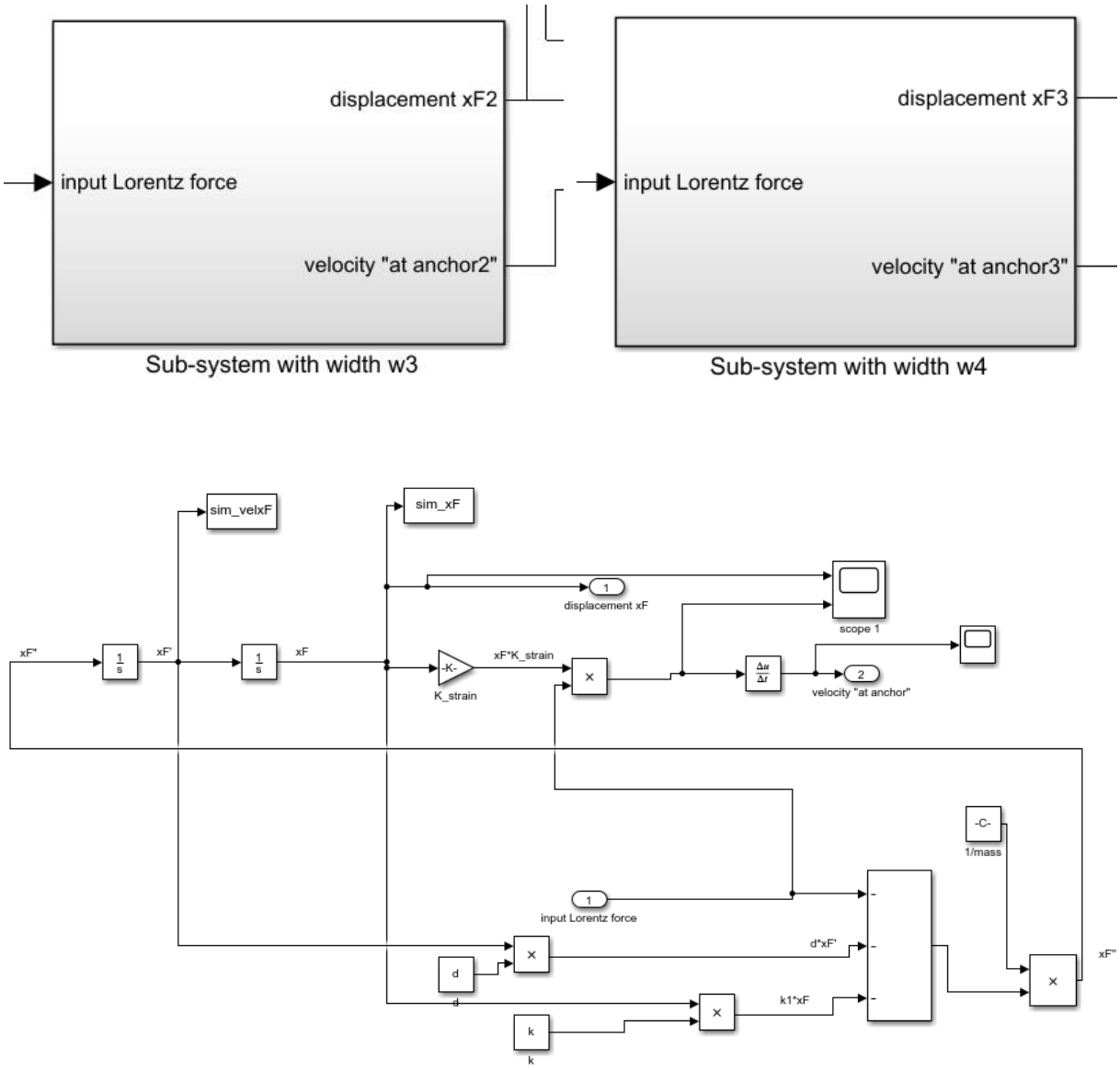

Fig. B.26: Topology 3: Mass-spring-damper system, associated to width w_1.

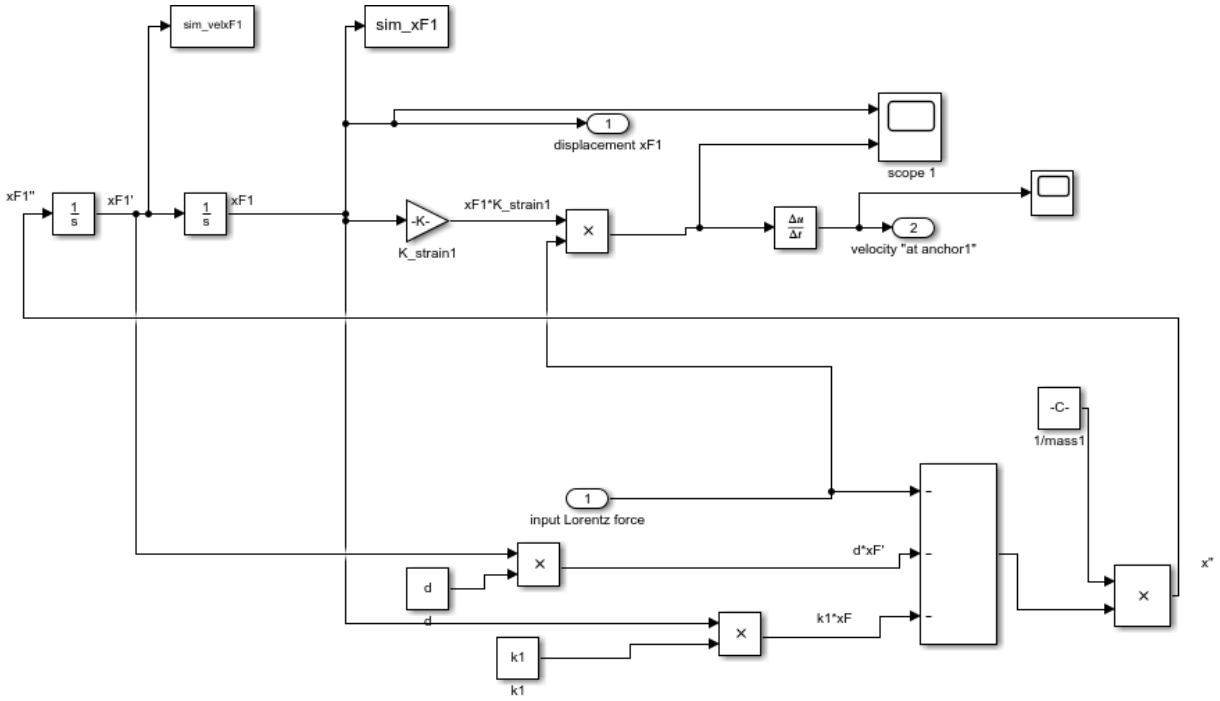

Fig. B.27: Topology 3: Mass-spring-damper system, associated to width w_2.

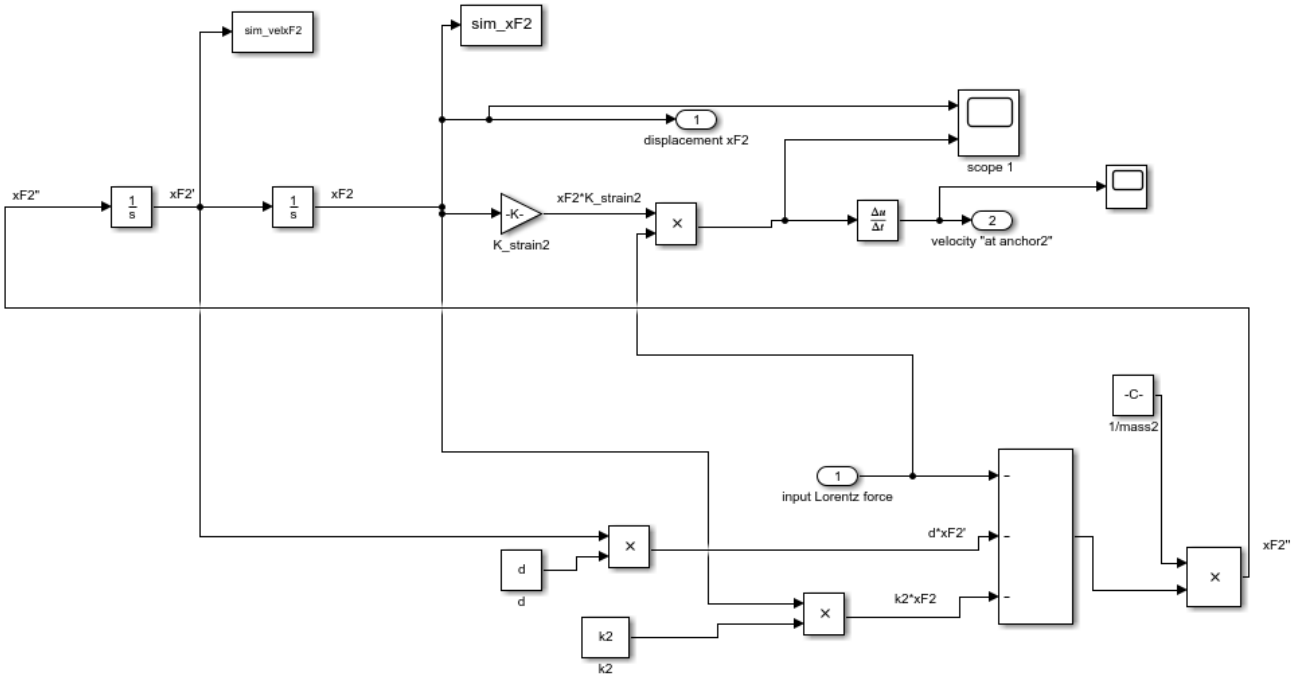

Fig. B.28: Topology 3: Mass-spring-damper system, associated to width w_3.

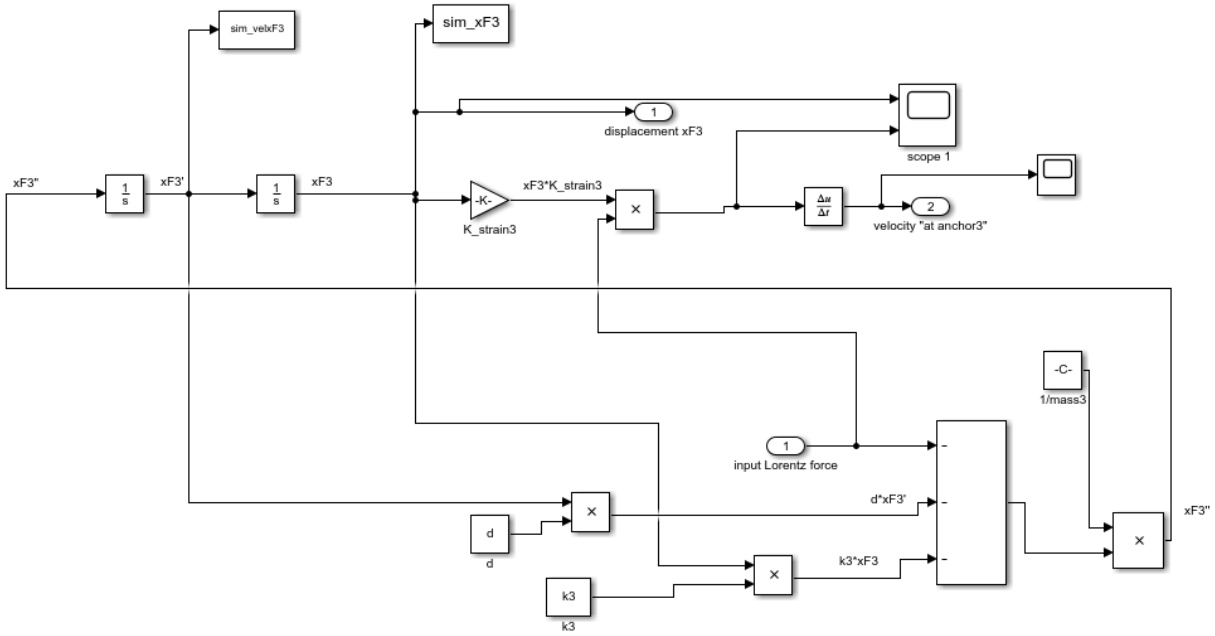

Fig. B.29: Topology 3: Mass-spring-damper system, associated to width w_4.

Block 4

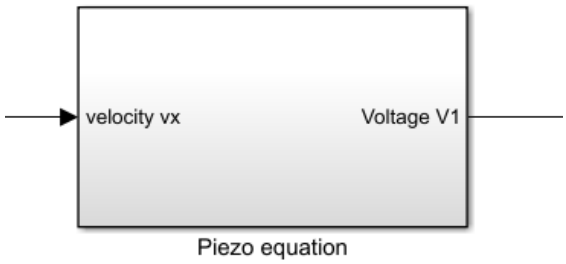

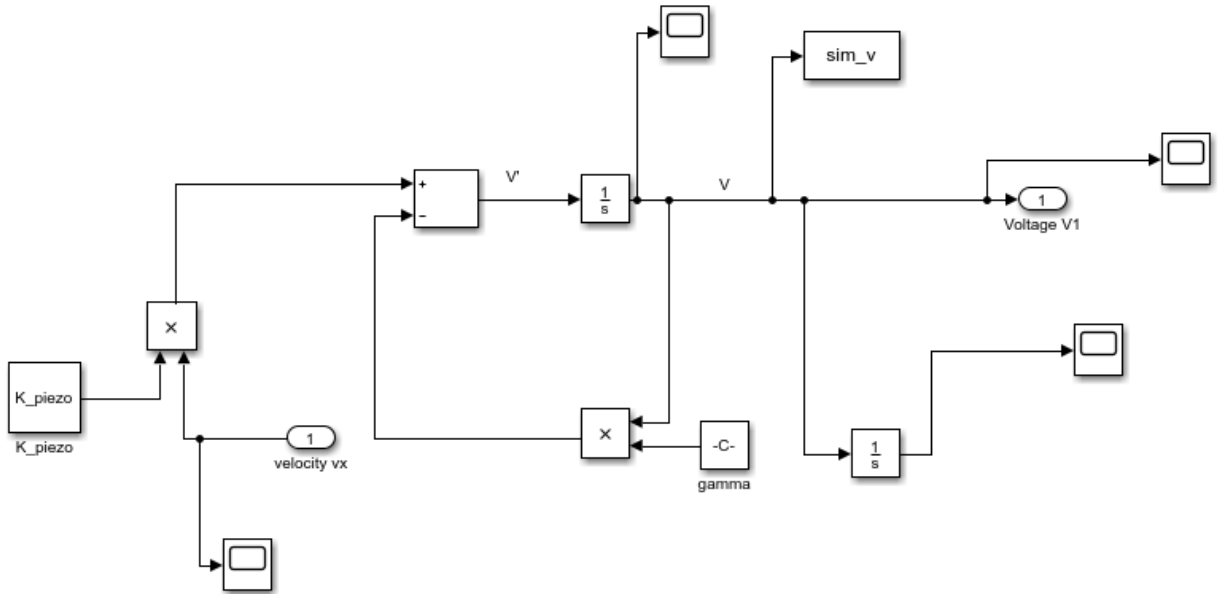

Fig. B.30: Simple U-shaped beam cantilever and Topology 3: Piezoelectric model.

2.4. U-shaped beam cantilever VS Topology 4

A Matlab code has been implemented in order to obtain a parametric system and to determine all variables expressed in all equations which describe the static and dynamic model.

MATLAB CODE

```
%% U-shaped beam cantilever parameters
%% LENGTHS
 lm=4500e-6; % length pertinent to the M inertial mass [m]
 w2=100e-6; % width pertinent to the inertial mass [m]
 w1=100e-6; % arm width
 l_perp=lm+2*w1; % length where the Lorentz force operates [m]
 L10=6400e-6; % arm length

%% TOPOLOGY 4A
 L5=1500e-6;
 L6=100e-6;
 L7=1500e-6;
 L8=5200e-6;
 L9=L6+2*w1; %% parameter

%% TICKNESS
 t_Si=10e-6; % Silicon [m]
 t_Al=1e-6; % Aluminum [m]
 t_AlN=0.5e-6; % Aluminum Nitride [m]
 t_tot=t_Si+t_Al+t_AlN;

%% LAYERS DENSITIES
```

```
 dens_Si=2.3e3; % expressed in [kg/m^3]
 dens_Al=2.7e3; % expressed in [kg/m^3]
 dens_AlN=3.3e3; % expressed in [kg/m^3]

 massa=lm*w2*(dens_Si*t_Si+dens_Al*t_Al+dens_AlN*t_AlN);   %   evaluation   of
inertial mass in kgr!!!

%% Parameters of Aluminum Nitride stack
 epsilon_33 = 7.9659*10^(-11); % product between epsi_0* epsi_rel (9) [F/m]
 e_31 = -0.58; % coming from the expression d_31/(s_11+s_12) [C/m^2]

%% Other parameters
 Rl =330*10^3; % load on AlN [Ohm]
 d =0.000001; % mechanical damping
 d_piezo =0.0069; % piezoelectric transduction damping
 miu_0 = 4*pi*10^(-7);

%% Parameters used to estimate the elastic constant
%% Simple U-shaped beam cantilever (total length)
 L=L10+w2;

%% TOPOLOGY 4A
 L4=900e-6;
%% TOPOLOGY 4B
 L41=L4-L9;
%% TOPOLOGY 4C
 L42=L4-2*L9;
%%TOPOLOGY 4D
 L17=300e-6;
 L14=L5;
 L16=L5;
 L15=L6;
 L43=300e-6;

%% Other parameters
%% TOPOLOGY 4A
 L1=L4+L9+L8+w2;
 L2=L8+L9;
 L3=L8+w1;
%% TOPOLOGY 4B
 L11=L8+2*L9+L41+w2;
 L21=L8+2*L9;
%% TOPOLOGY 4C
 L12=L8+3*L9+L42+w2;
 L22=L8+3*L9;
%% TOPOLOGY 4D
 L13=L8+2*L9+L17+L43+w2;
 L23=L8+L9;
 L18=L8+2*L9+L17;
 L19=L8+L9+L17;

%% Essential parameters to estimate the mechanical stiffness
%% TOPOLOGY 4A
 Ltot=L8+L9+L7+L5+L4+w2;
%% TOPOLOGY 4B
 Ltot1=L8+L7+2*L9+L5+L41+w2;
%% TOPOLOGY 4C
 Ltot2=L8+L7+3*L9+L5+L42+w2;
%% TOPOLOGY 4D
 Ltot3=L8+L7+L5+2*L9+L17+L16+L14+L43+w2;

%% Other parameters
```

```
 gamma = t_AlN/(Rl*epsilon_33*w1*l_perp);
 K_piezo  =  e_31*t_AlN/(epsilon_33*w1*l_perp);  % coupling  constant  of  the
piezoelectric stack

%% Parameters used to create a magnetic field
 h_dist =1e-3; % radius of conductor [m]
```

%%%%%% EQUIVALENT SECTION METHOD

```
%% Young's Moduli
 E_Si=170*10^9; % Silicon
 E_AlN=310*10^9; % Aluminum Nitride
 E_Al=70*10^9; % Aluminum

 E=[E_Si E_AlN E_Al]; % Young's moduli vector
 T=[t_Si t_AlN t_Al]; % Thickness vector
 larghezza=[w1 w1 w1];
 E_max=max(E);

 for i=1:1:length(E)
  w_norm(i)=larghezza(i)*(E(i)/E_max);
 end

 for i=1:1:length(T)
  s_norm(i)=w_norm(i)*T(i);
 end

 tk=0;
 for i=1:1:length(T)
  h(i)=tk+(T(i)/2);
  tk=tk+T(i);
 end

 somma_sh=0;
 somma_s=0;
 for i=1:1:length(s_norm)
  somma_sh=somma_sh+(s_norm(i)*h(i));
  somma_s=somma_s+s_norm(i);
 end

 hn=somma_sh/somma_s;

 for i=1:1:length(T)
  Ix(i)=((T(i)^3)*w1*E(i)/E_max)/12;
 end

 for i=1:1:length(T)
  I_norm(i)=Ix(i)+(s_norm(i)*(hn-h(i))^2);
 end

 In=0;
 for i=1:1:length(I_norm)
  In=In+I_norm(i);
 end
 tot=0;
 for i=1:1:length(I_norm)
  c(i)=E(i)*I_norm(i);
  tot=c(i)+tot; % [N*m2]
 end
```

```
 K_strain = 3*((L)^2)/(E_max*w1*((t_tot)^2)); %parameter related to the axial
strain

%%%%%%

%% Mechanical stiffness
%% Simple u-shaped beam cantilever
 k=6*tot/(L^3); % [N/m]

%% TOPOLOGY 4A
 kf=6*tot/((Ltot)^3);
 kf1=(12*tot)/((3*L1-L3)*L3^2);
 kf2=(12*tot)/((3*L1-L2)*L2^2);

%% TOPOLOGY 4B
 kf3=6*tot/((Ltot1)^3);
 kf4=(12*tot)/((3*L11-L3)*L3^2);
 kf5=(12*tot)/((3*L11-L21)*(L21)^2);

%% TOPOLOGY 4C
 kf6=6*tot/((Ltot2)^3);
 kf7=(12*tot)/((3*L12-L3)*L3^2);
 kf8=(12*tot)/((3*L12-L22)*(L22)^2);

%% TOPOLOGY 4D
 kf9=6*tot/((Ltot3)^3);
 kf10=(12*tot)/((3*L13-L3)*L3^2);
 kf11=(12*tot)/((3*L13-L23)*(L23)^2);
 kf12=(12*tot)/((3*L13-L19)*(L19)^2);
 kf13=(12*tot)/((3*L13-L18)*(L18)^2);

%% Current into the conductor
 I_cond=5e-3;

%% Simple U-shaped beam cantilever
 omega=sqrt(k/massa);
 freq=omega/(2*pi);

%% TOPOLOGY 4A
 omega1=sqrt(kf/massa);
 freq1=omega1/(2*pi);

%% TOPOLOGY 4B
 omega2=sqrt(kf3/massa);
 freq2=omega2/(2*pi);

%% TOPOLOGY 4C
 omega3=sqrt(kf6/massa);
 freq3=omega3/(2*pi);

%% TOPOLOGY 4D
 omega4=sqrt(kf9/massa);
 freq4=omega4/(2*pi);

%% Driving current into the Simple U-shaped beam cantilever
 I_cant=20e-3; %unità di misura [App]

%% Evaluation of magnetic induction
 B=miu_0*I_cond/(2*pi*h_dist); % ([H]*[A])/([m2])=[Wb]/[m2]=[T]
```

```
%% Lorentz Force
 Fl=I_cant*B*l_perp;
```

SIMULINK SCHEMATIC

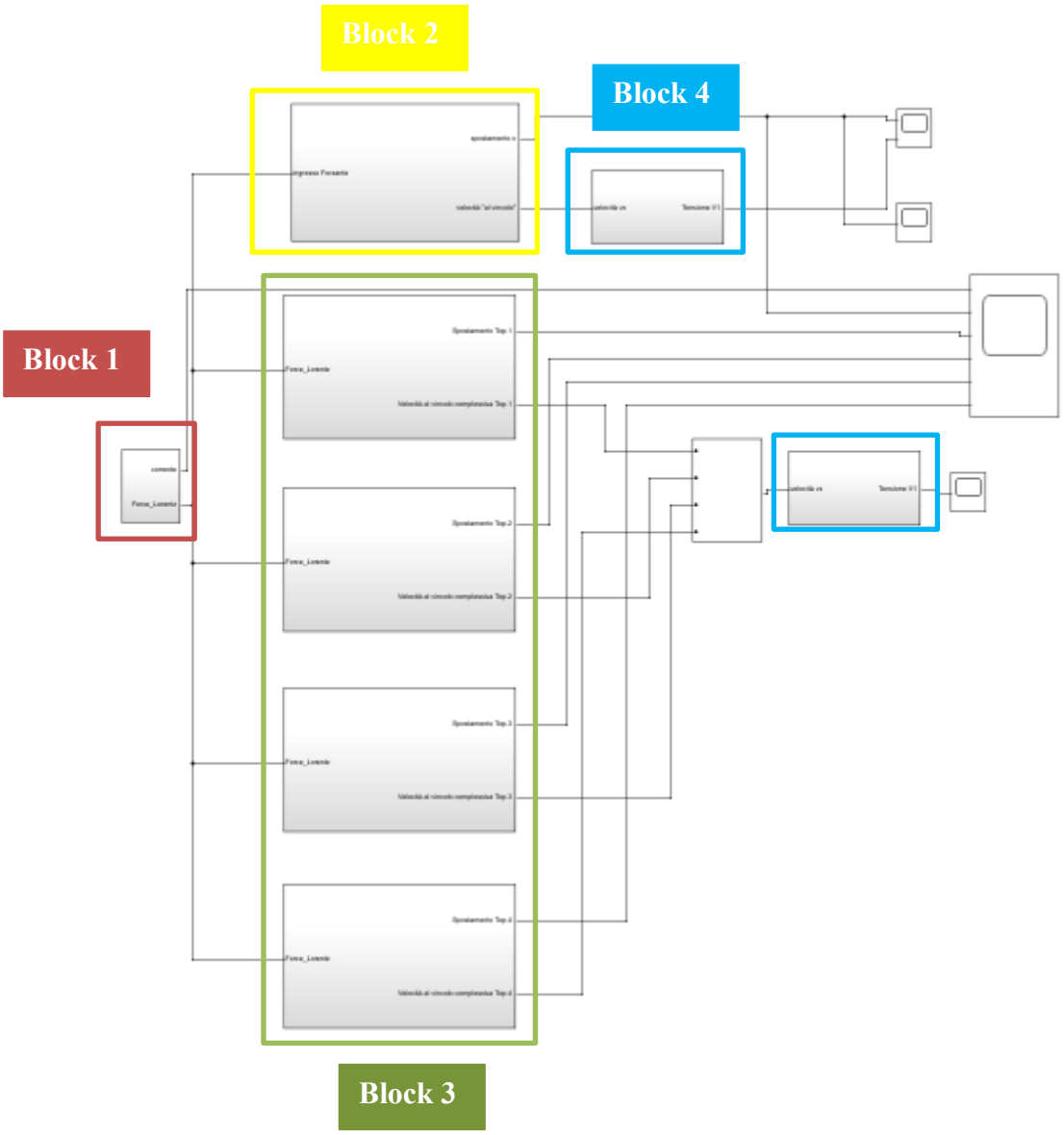

Fig. B.31: Simulink schematic: Simple VS Topologies 4A, 4B, 4C and 4D.

Block 1

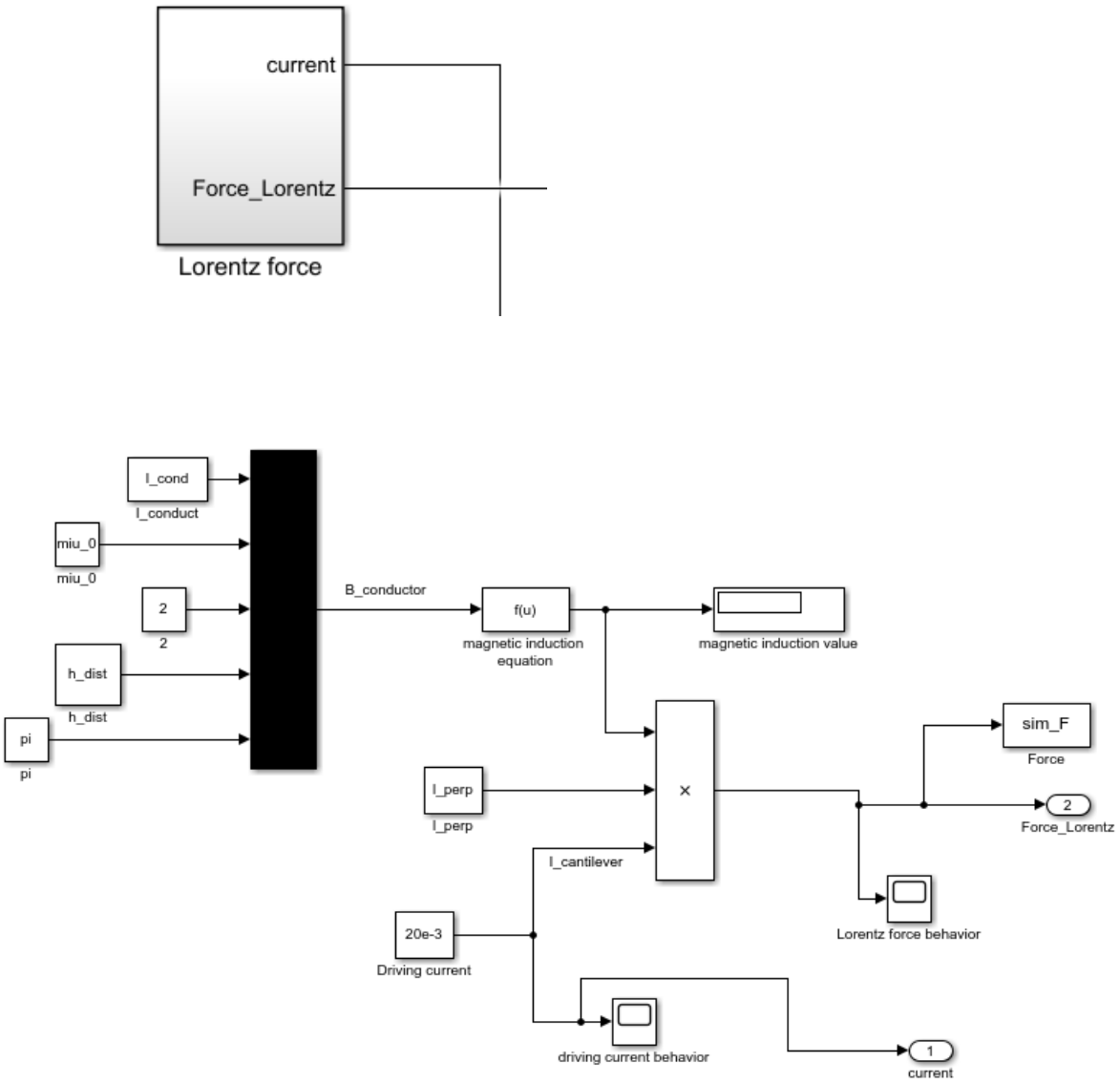

Fig. B.32: Lorentz force in static analysis.

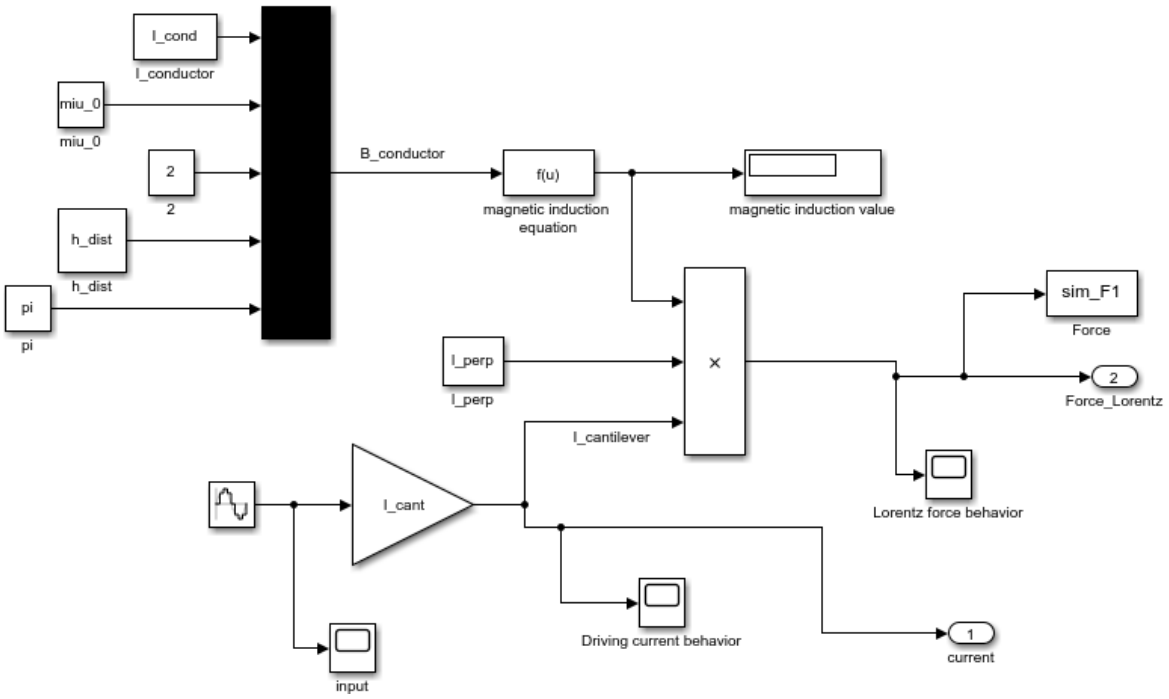

Fig. B.33: Lorentz force in dynamic analysis.

Block 2

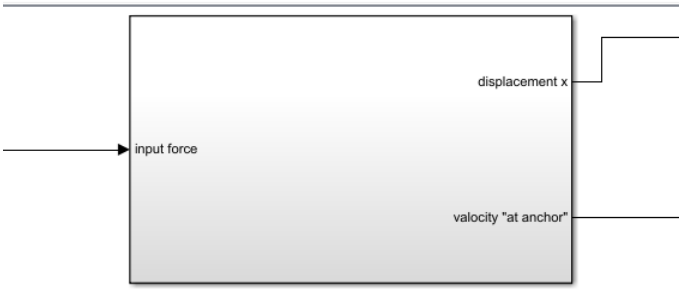

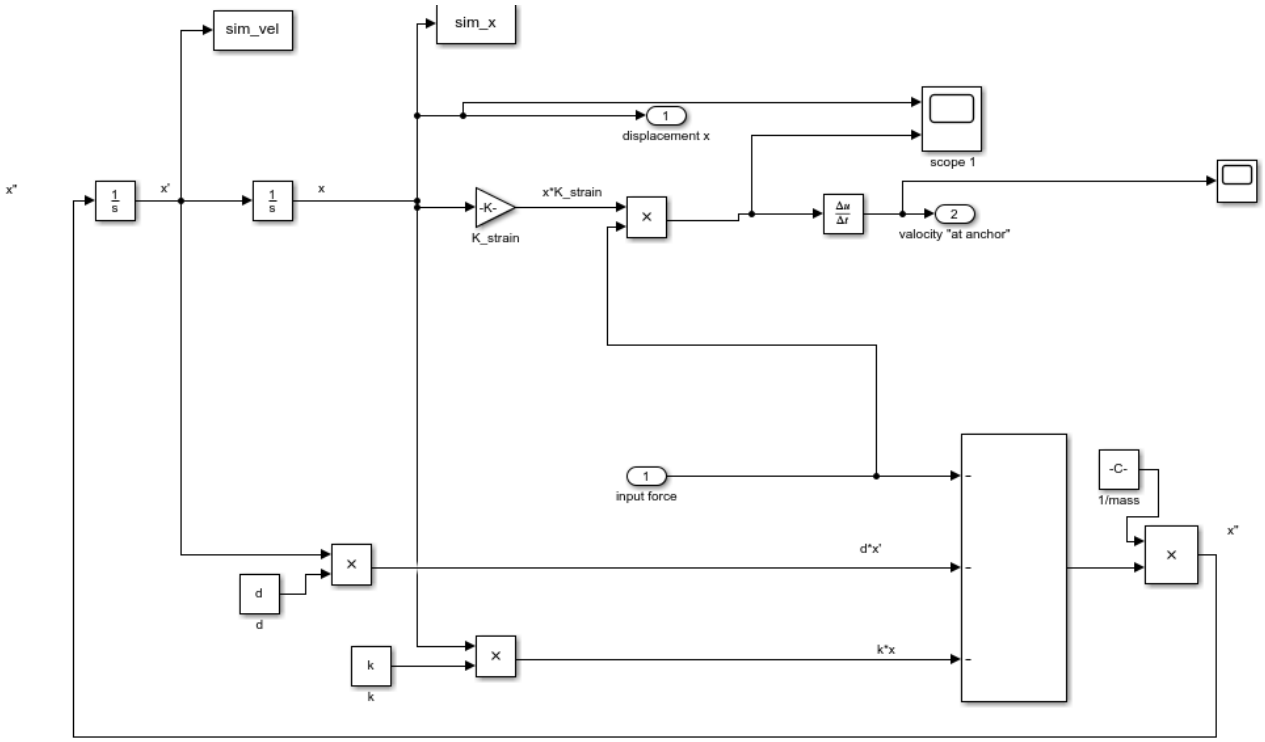

Fig. B.34: Simple U-shaped beam cantilever: Mass-spring-damper system.

Block 3

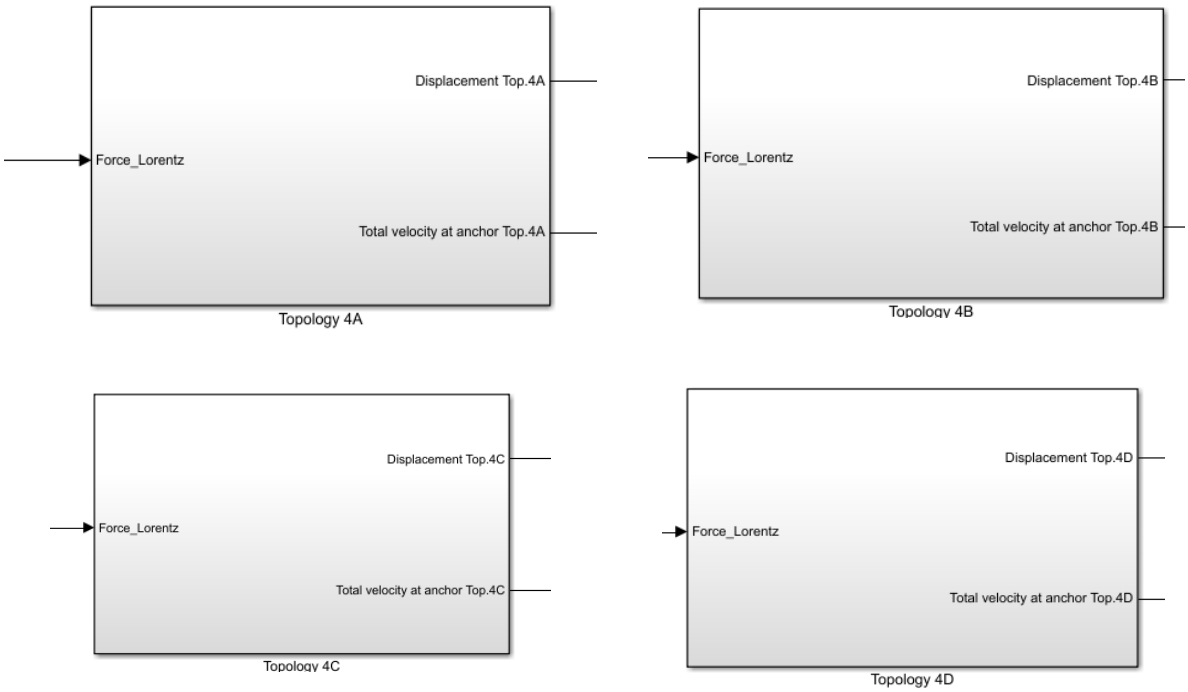

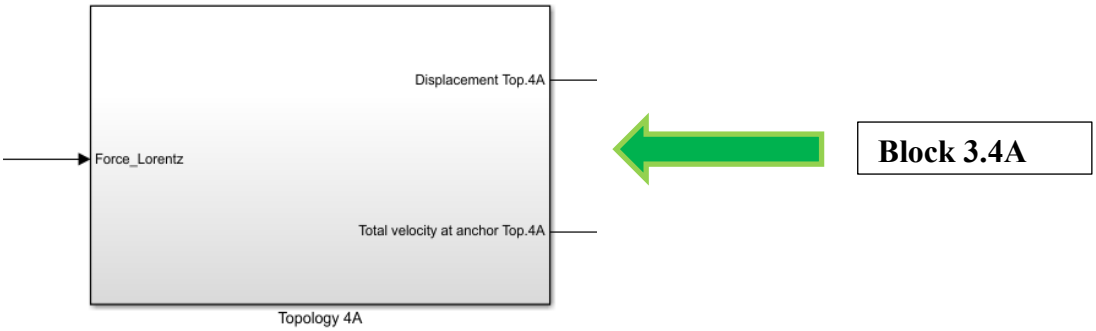

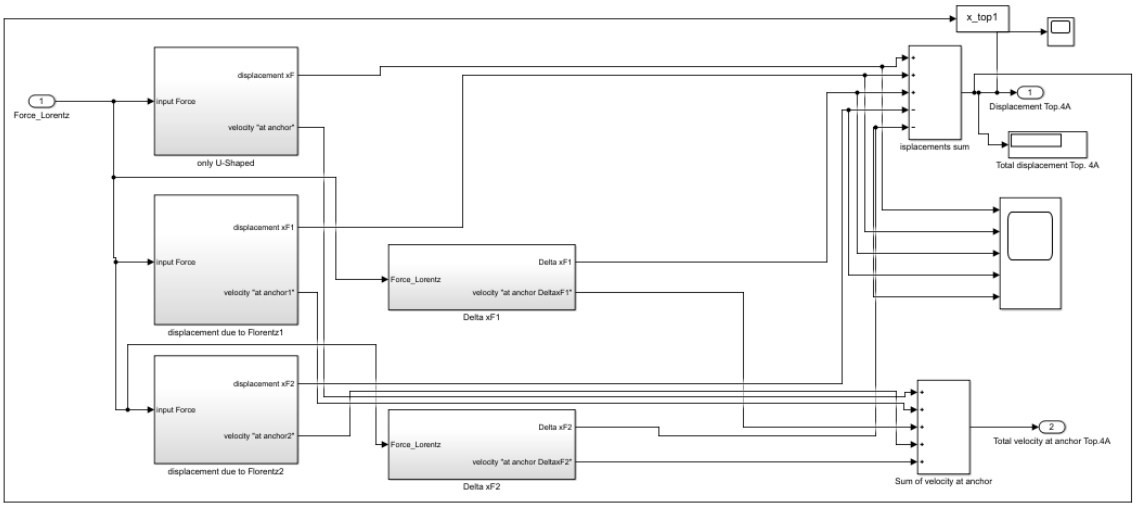

Fig. B.35: Topology 4A: The whole mass-spring-damper system.

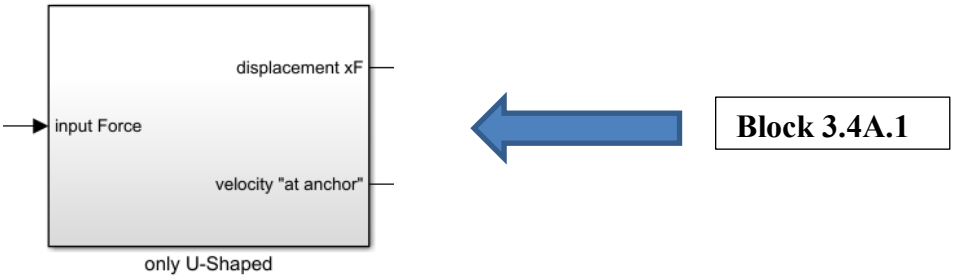

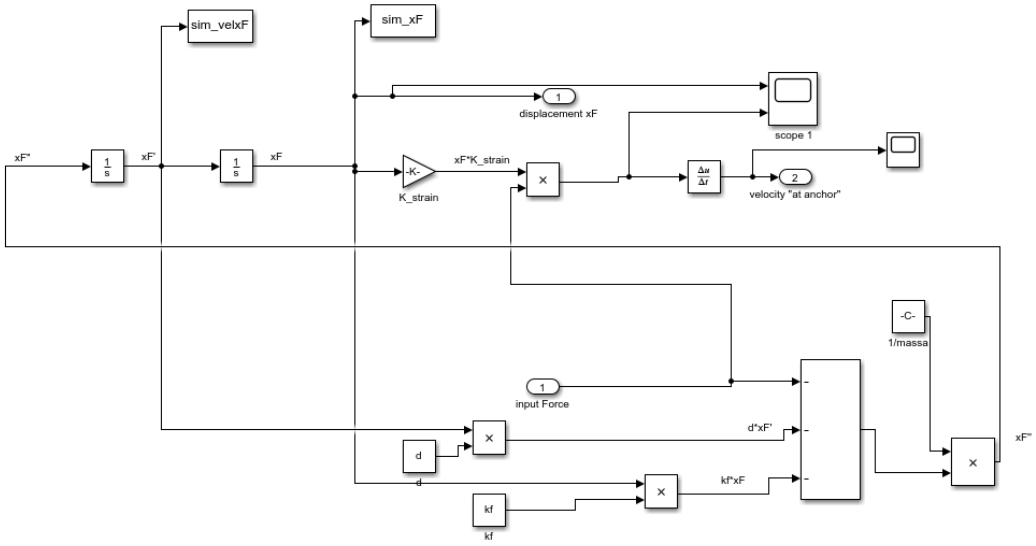

Fig. B.36: Topology 4A: Mass-spring-damper system.

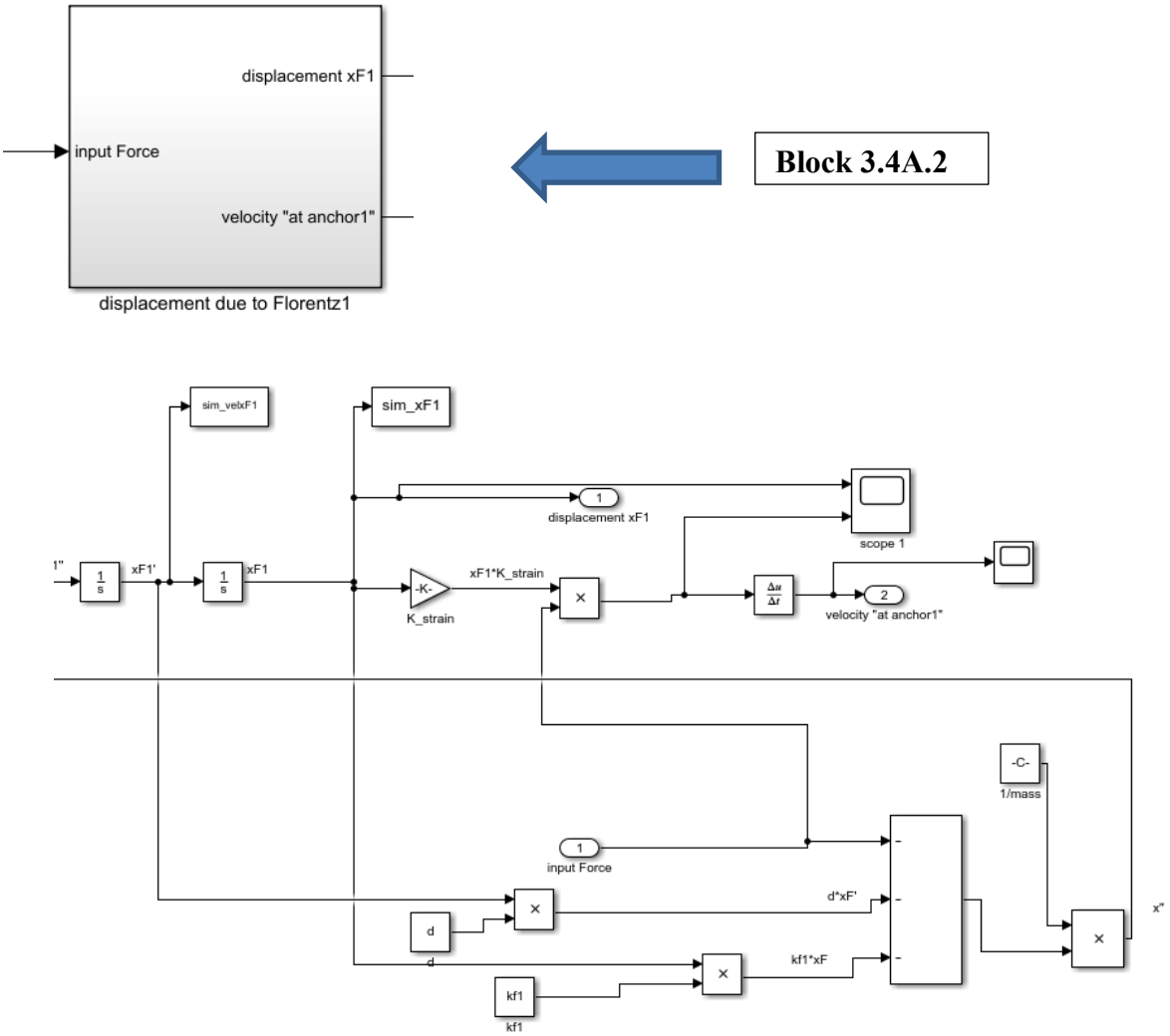

Fig. B.37: Topology 4A: Mass-spring-damper system, concordant with the tip displacement.

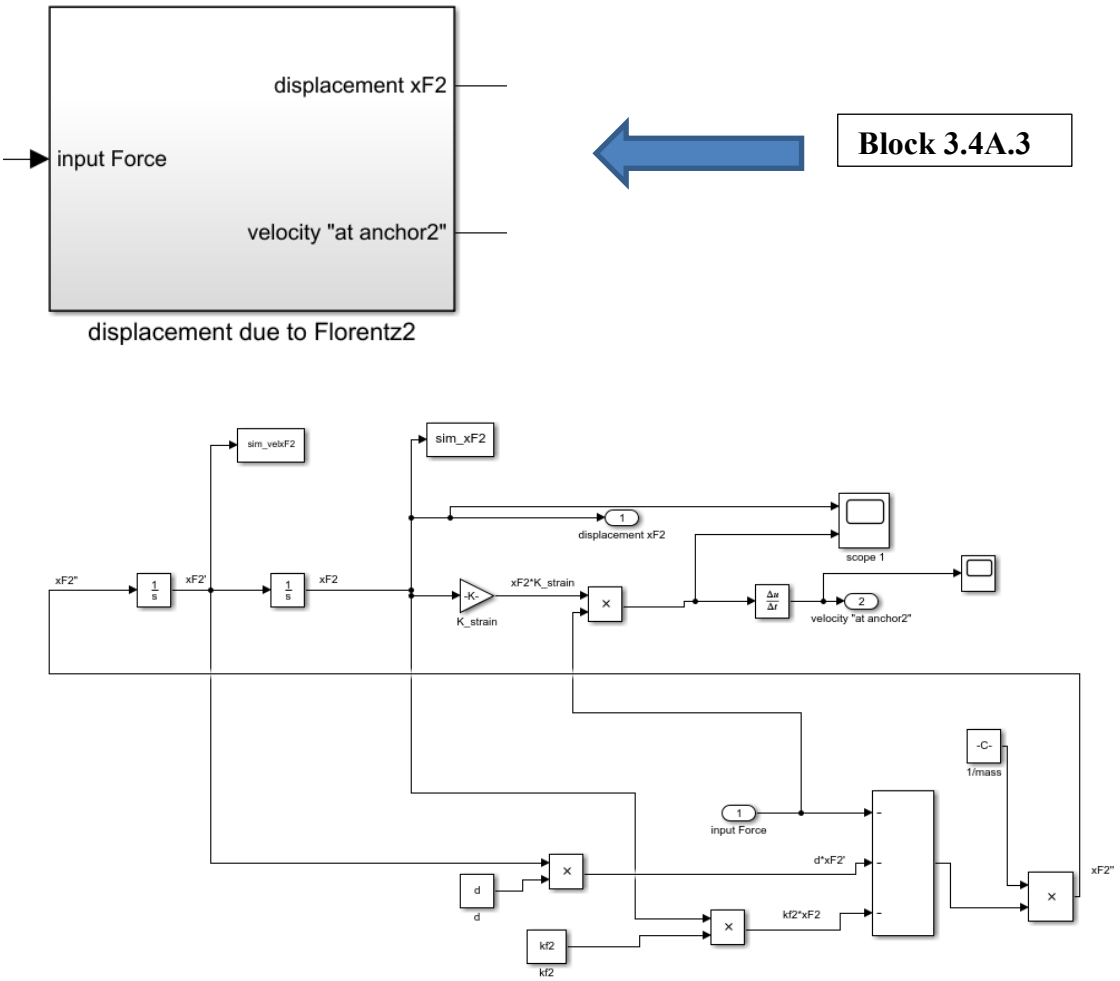

Fig. B.38: Topology 4A: Mass-spring-damper system, opposite displacement with the cantilever tip displacement.

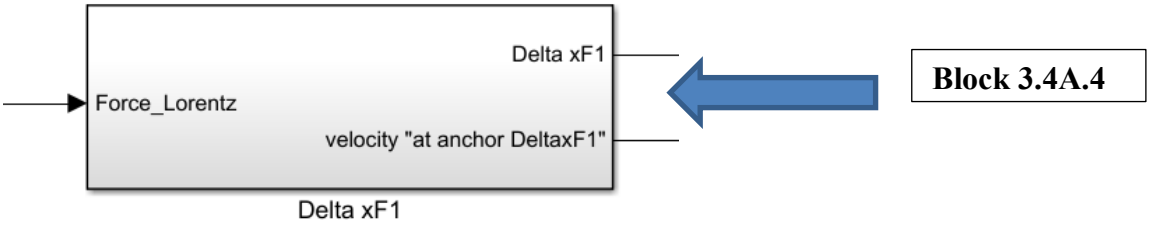

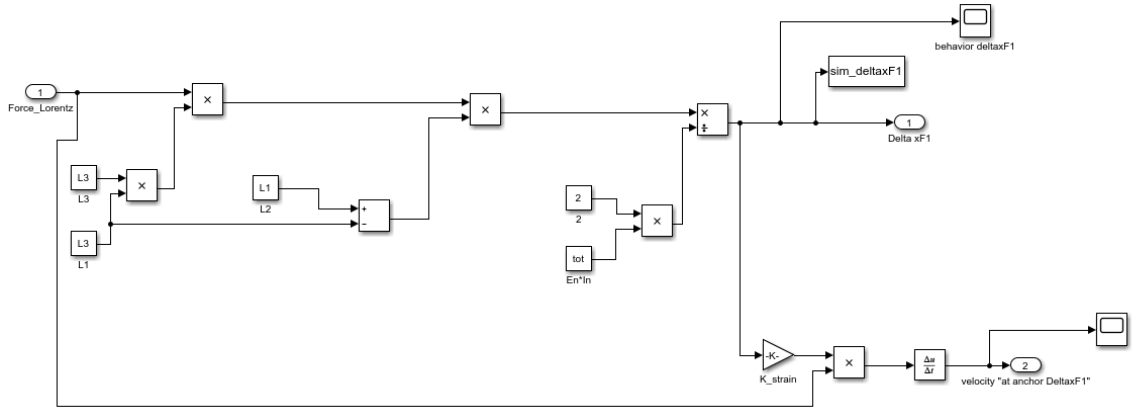

Fig. B.39: Topology 4A: Mass-spring-damper system, displacement Δx_{F1}.

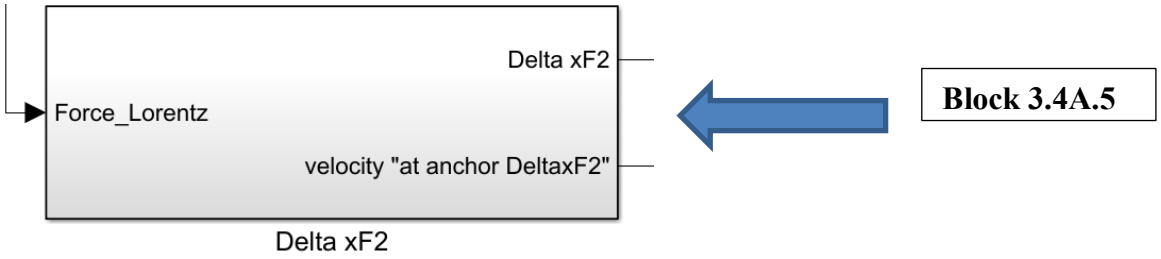

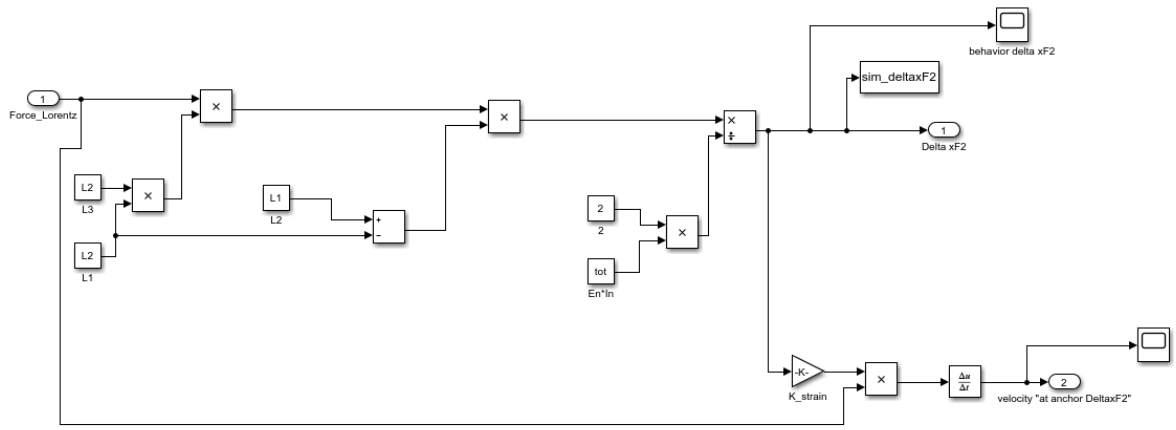

Fig. B.40: Topology 4A: Mass-spring-damper system, displacement Δx_{F2}.

P.S.: For the other Topologies the schematics are almost the same, except elastic constants and some L_i parameters, therefore, they can be reproduced easily without the necessity to repeat in this sub-section.

Block 4

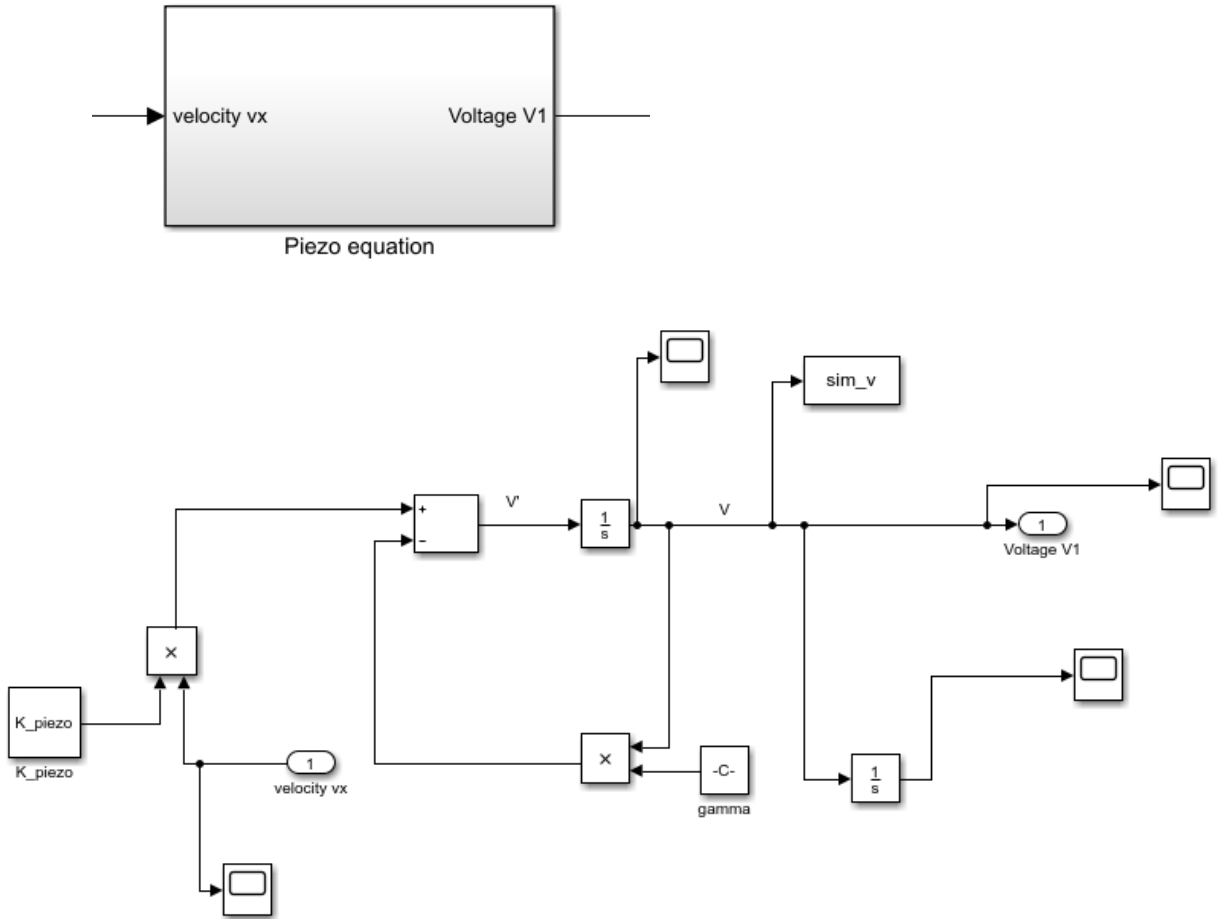

Fig. B.41: Simple U-shaped beam cantilever and Topologies 4A, 4B, 4C and 4D: piezoelectric model.

2.5. U-shaped beam cantilever VS Topology 5

A Matlab code has been implemented in order to obtain a parametric system and to determine all variables expressed in all equations which describe the static and dynamic model.

MATLAB CODE

```
%% U-shaped beam cantilever parameters
%% LENGTHS
 lm=5300e-6; % length pertinent to the M inertial mass [m]
 w2=100e-6; % width pertinent to the inertial mass [m]
 w1=100e-6; % arm width related to M mass
 l_perp=lm+2*w1; % length where the Lorentz force operates [m]
 L10=8500e-6; % arm length


%% TOPOLOGY 5 parameters
%% LENGTHS
 L5=1500e-6;
 L6=100e-6;
 L7=1500e-6;
 L8=5200e-6;
 L9=L6+2*w1; % parametric

%% TICKNESS
 t_Si=10e-6; % Silicon [m]
 t_Al=1e-6; % Aluminum [m]
 t_AlN=0.5e-6; % Aluminum Nitride [m]
 t_tot=t_Si+t_Al+t_AlN;

%% LAYERS DENSITIES
 dens_Si=2.3e3; % expressed in [kg/m^3]
 dens_Al=2.7e3; % expressed in [kg/m^3]
 dens_AlN=3.3e3;% expressed in [kg/m^3]

 massa=lm*w2*(dens_Si*t_Si+dens_Al*t_Al+dens_AlN*t_AlN);   %   evaluation   of
inertial mass in kgr!!!

%% Parameters of Aluminum Nitride stack
 epsilon_33 = 7.9659*10^(-11); % product between epsi_0* epsi_rel (9) [F/m]
 e_31 = -0.58; % coming from the expression d_31/(s_11+s_12) [C/m^2]

%% Other parameters
 Rl =330*10^3; % load on AlN [Ohm]
 d =0.000001; % mechanical damping
 d_piezo =0.0069; % piezoelectric transduction damping
 miu_0 = 4*pi*10^(-7);

%% Parameters used to estimate the elastic constant
%% Simple U-shaped beam cantilever (total length)
 L=L10+w2;

%% TOPOLOGY 5
 L44=2200e-6;
 L20=2*L7-w1;

%% Other parameters
%% TOPOLOGY 5
 L3=L8+w1;
 L24=L8+3*L9+2*L6+L44+w2;
 L26=L8+3*L9+2*L6;

 Ltot4=L8+L7+5*L9+4*L20+L5+L44+w2; %total length
```

```
%% Other parameters
 gamma = t_AlN/(Rl*epsilon_33*w1*l_perp);
 K_piezo  =  e_31*t_AlN/(epsilon_33*w1*l_perp);  % coupling  constant  of  the
piezoelectric stack

%% Parameters used to create a magnetic field
 h_dist =1e-3; % radius of conductor [m]
```

%%%%%% EQUIVALENT SECTION METHOD

```
%% Young's Moduli
 E_Si=170*10^9; % Silicon
 E_AlN=310*10^9; % Aluminum Nitride
 E_Al=70*10^9; % Aluminum

 E=[E_Si E_AlN E_Al]; % Young's moduli vector
 T=[t_Si t_AlN t_Al]; % Thickness vector
 larghezza=[w1 w1 w1];
 E_max=max(E);

 for i=1:1:length(E)
  w_norm(i)=larghezza(i)*(E(i)/E_max);
 end

 for i=1:1:length(T)
  s_norm(i)=w_norm(i)*T(i);
 end

 tk=0;
 for i=1:1:length(T)
  h(i)=tk+(T(i)/2);
  tk=tk+T(i);
 end

 somma_sh=0;
 somma_s=0;
 for i=1:1:length(s_norm)
  somma_sh=somma_sh+(s_norm(i)*h(i));
  somma_s=somma_s+s_norm(i);
 end

 hn=somma_sh/somma_s;

 for i=1:1:length(T)
  Ix(i)=((T(i)^3)*w1*E(i)/E_max)/12;
 end

 for i=1:1:length(T)
  I_norm(i)=Ix(i)+(s_norm(i)*(hn-h(i))^2);
 end

 In=0;
 for i=1:1:length(I_norm)
  In=In+I_norm(i);
 end
 tot=0;
 for i=1:1:length(I_norm)
  c(i)=E(i)*I_norm(i);
  tot=c(i)+tot; %[N*m2]
 end
```

```
 K_strain = 3*((L)^2)/(E_max*w1*((t_tot)^2)); % parameter related to the axial
strain

%%%%%%

%% Mechanical stiffness
%% Simple U-shaped beam cantilever
 k=6*tot/(L^3);

%% TOPOLOGY 5
 kf14=6*tot/((Ltot4)^3);
 kf15=(12*tot)/((3*L24-L3)*L3^2);
 kf16=(12*tot)/((3*L24-L26)*L26^2);
%% Current into the conductor
 I_cond=5e-3;

 omega=sqrt(k/massa); % Related to the Simple U-shaped beam cantilever
 freq=omega/(2*pi);

%% TOPOLOGY 5
 omega5=sqrt(kf14/massa);
 freq5=omega5/(2*pi);

%% Driving current into the Simple U-shaped beam cantilever
 I_cant=20e-3; % [App]

%% Evaluation of magnetic induction
 B=miu_0*I_cond/(2*pi*h_dist); % ([H]*[A])/([m2])=[Wb]/[m2]=[T]

%% Lorentz Force
 Fl=I_cant*B*l_perp;
```

SIMULINK SCHEMATIC

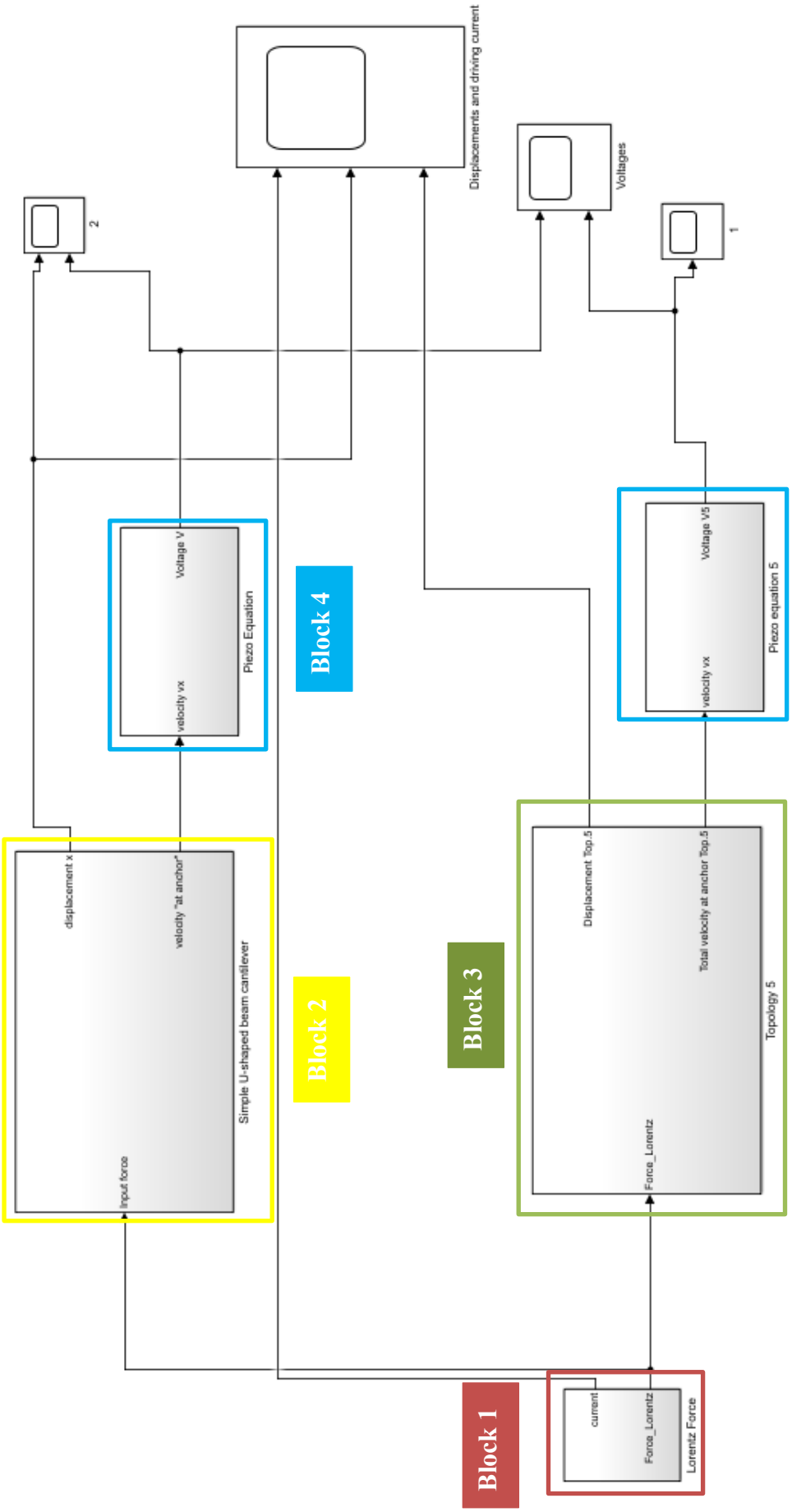

Fig. B.42: Simulink schematic: Simple VS Topology 5.

Block 1

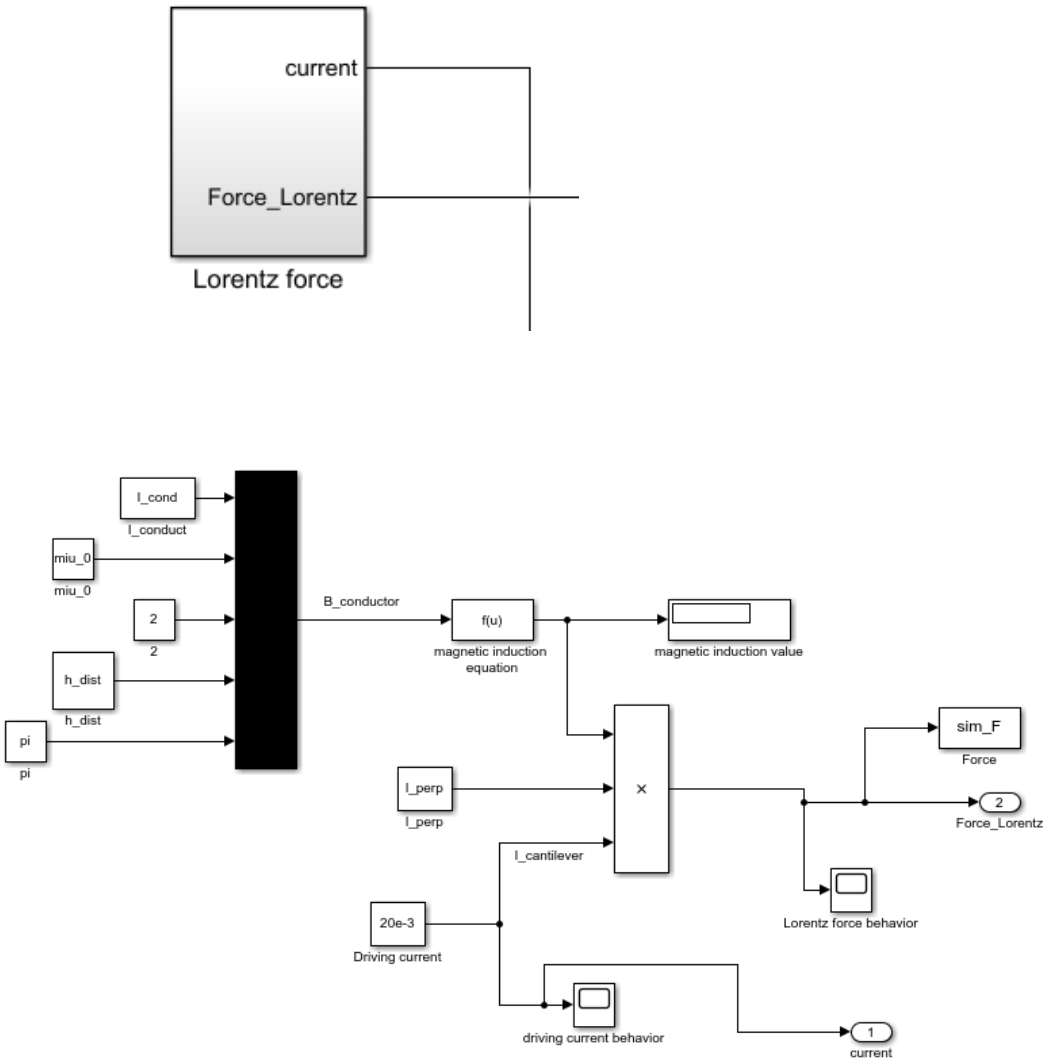

Fig. B.43: Lorentz force in static analysis.

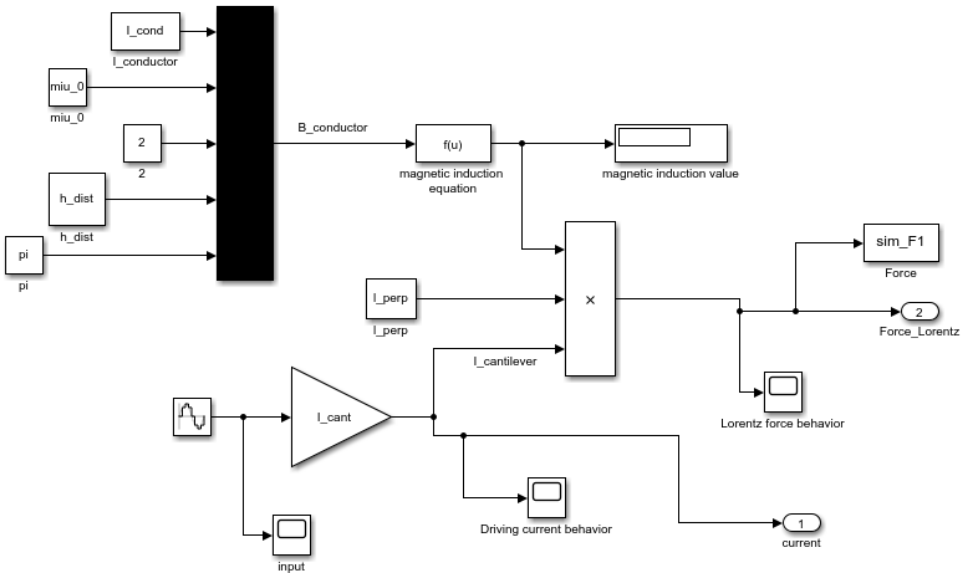

Fig. B.44: Lorentz force in dynamic analysis.

Block 2

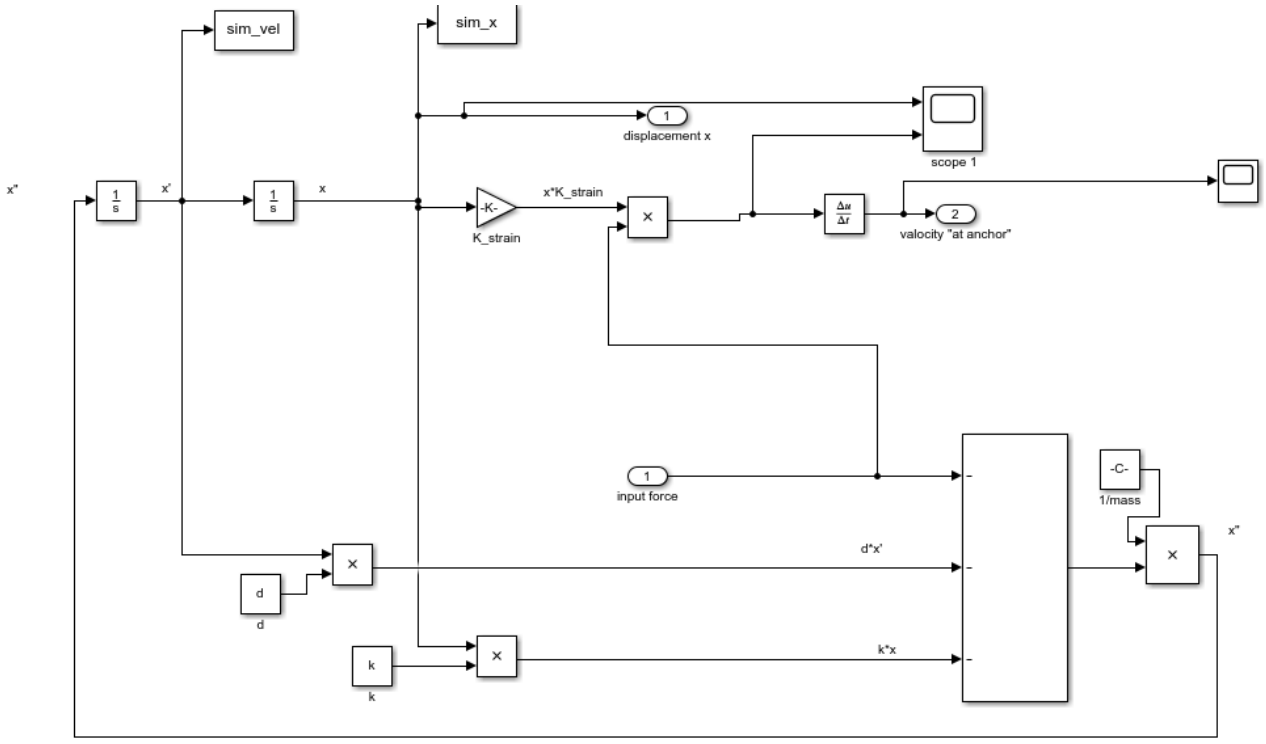

Fig. B.45: Simple U-shaped beam cantilever: Mass-spring-damper system.

Block 3

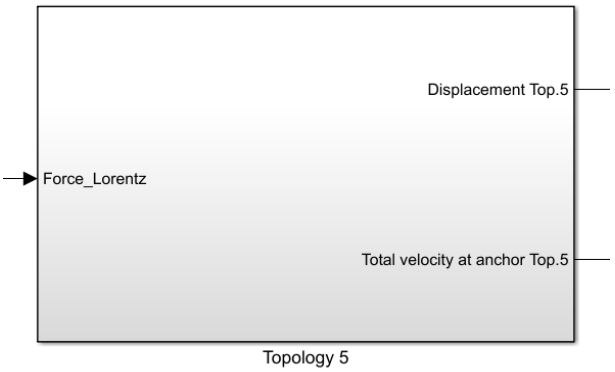

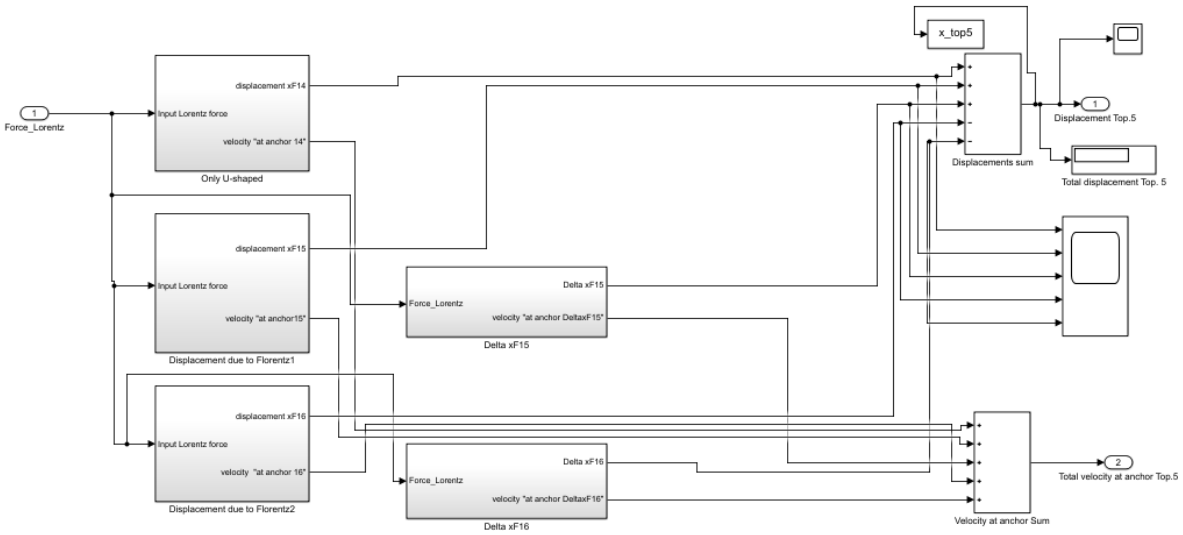

Fig. B.46: Topology 5: The whole mass-spring-damper system.

P.S.: In relation to the details on sub-systems presented in Fig. B.46 see previous figures from Fig. B.36 to Fig. B.40.

Block 4

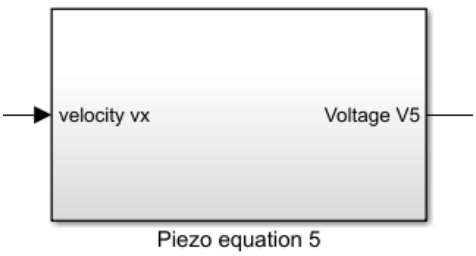

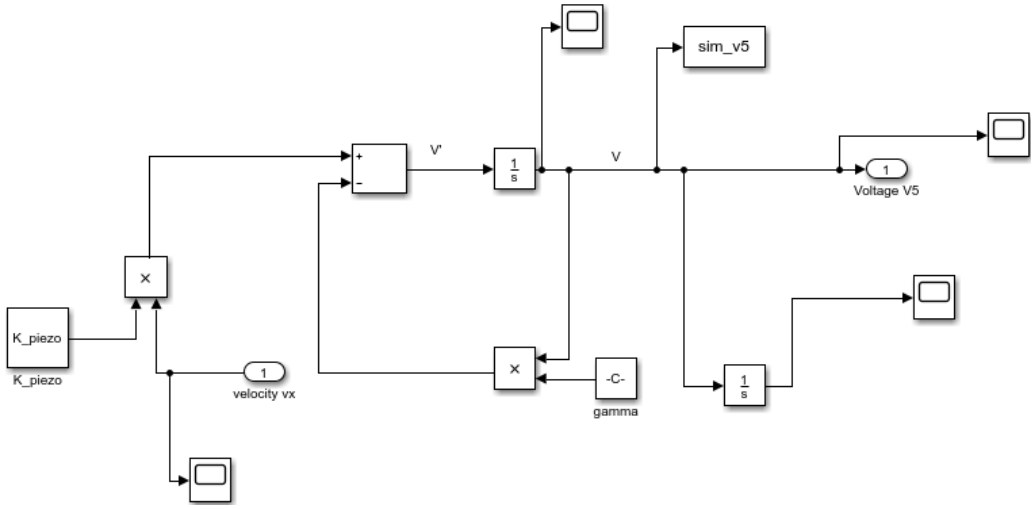

Fig. B.47: Simple U-shaped beam cantilever and Topology 5: Piezoelectric model.

2.6. U-shaped beam cantilever VS Topology 6

A Matlab code has been implemented in order to obtain a parametric system and to determine all variables expressed in all equations which describe the static and dynamic model.

MATLAB CODE

```
%% U-shaped beam cantilever parameters
%% LENGTHS
 lm=8200e-6; % length pertinent to the M inertial mass [m]
 w2=500e-6; % width pertinent to the inertial mass [m]
 w1=300e-6; % arm width related to M mass
 l_perp=lm+2*w1; % length where the Lorentz force operates [m]

 L10=8000e-6; % arm length

%% TOPOLOGY 6 parameters
%% LENGTHS
 L5=1700e-6;
 L6=300e-6;
 L7=1700e-6;
 L8=1500e-6;
 L9=L6+2*w1; % parametric

%% TICKNESS
 t_Si=10e-6; % Silicon [m]
 t_Al=1e-6; % Aluminum [m]
 t_AlN=0.5e-6; % Aluminum Nitride [m]
 t_tot=t_Si+t_Al+t_AlN;

%% LAYERS DENSITIES
```

```
 dens_Si=2.3e3; % expressed in [kg/m^3]
 dens_Al=2.7e3; % expressed in [kg/m^3]
 dens_AlN=3.3e3; % expressed in [kg/m^3]

 massa=lm*w2*(dens_Si*t_Si+dens_Al*t_Al+dens_AlN*t_AlN);  % evaluation of
inertial mass in kgr!!!

%% Parameters of Aluminum Nitride stack
 epsilon_33 = 7.9659*10^(-11); % product between epsi_0* epsi_rel (9) [F/m]
 e_31 = -0.58; % coming from the expression d_31/(s_11+s_12) [C/m^2]

%% Other parameters
 Rl =330*10^3; % load on AlN [Ohm]
 d =0.000001; % mechanical damping
 d_piezo =0.0069; % piezoelectric transduction damping
 miu_0 = 4*pi*10^(-7);

%% Parameters used to estimate the elastic constant
%% Simple U-shaped beam cantilever (total length)
 L=L10+w2;

%% TOPOLOGY 6
 L44=700e-6;
 L50=700e-6;
 L51=L7;
 L20=2*L7-w1;

%% Other parameters
%% TOPOLOGY 6
 L3=L8+w1;
 L24=L8+4*L9+4*L6+w1+L50+L44+w2;
 L28=L8+4*L9+4*L6+w1;
 L27=L8+4*L9+4*L6+w1+L50;

 Ltot5=L8+L7+8*L9+7*L20+L5+L50+L51+L44+w2; % Total length

%% Other parameters
 gamma = t_AlN/(Rl*epsilon_33*w1*l_perp);
 K_piezo  =  e_31*t_AlN/(epsilon_33*w1*l_perp);  % coupling constant of the
piezoelectric stack

%% Parameters used to create a magnetic field
 h_dist =1e-3; % radius of conductor [m]
```

%%%%%% EQUIVALENT SECTION METHOD

```
%% Young's Moduli
 E_Si=170*10^9; % Silicon
 E_AlN=310*10^9; % Aluminum Nitride
 E_Al=70*10^9; % Aluminum

 E=[E_Si E_AlN E_Al]; % Young's moduli vector
 T=[t_Si t_AlN t_Al]; % Thickness vector
 larghezza=[w1 w1 w1];
 E_max=max(E);

 for i=1:1:length(E)
  w_norm(i)=larghezza(i)*(E(i)/E_max);
 end
```

```
 for i=1:1:length(T)
  s_norm(i)=w_norm(i)*T(i);
 end

 tk=0;
 for i=1:1:length(T)
  h(i)=tk+(T(i)/2);
  tk=tk+T(i);
 end

 somma_sh=0;
 somma_s=0;
 for i=1:1:length(s_norm)
  somma_sh=somma_sh+(s_norm(i)*h(i));
  somma_s=somma_s+s_norm(i);
 end

 hn=somma_sh/somma_s;

 for i=1:1:length(T)
  Ix(i)=((T(i)^3)*w1*E(i)/E_max)/12;
 end

 for i=1:1:length(T)
  I_norm(i)=Ix(i)+(s_norm(i)*(hn-h(i))^2);
 end

 In=0;
 for i=1:1:length(I_norm)
  In=In+I_norm(i);
 end
 tot=0;
 for i=1:1:length(I_norm)
  c(i)=E(i)*I_norm(i);
  tot=c(i)+tot; % [N*m2]
 end

 K_strain = 3*((L)^2)/(E_max*w1*((t_tot)^2)); % parameter related to the axial
strain

%%%%%%
%% Mechanical stiffnes
%% Simple U-shaped beam cantilever
 k=6*E_max*In/(L^3); %  [N/m]

%% TOPOLOGY 6
 kf17=6*E_max*In/((Ltot5)^3);
 kf18=(12*E_max*In)/((3*L24-L3)*L3^2);
 kf19=(12*E_max*In)/((3*L24-L28)*L28^2);
 kf20=(12*E_max*In)/((3*L24-L27)*L27^2);

%% Current into the conductor
 I_cond=5e-3;

 omega=sqrt(k/massa); % Related to simple U-shaped beam cantilever
 freq=omega/(2*pi);
%% TOPOLOGY 6
 omega6=sqrt(kf17/massa);
 freq6=omega6/(2*pi); % Related to Topology 6
```

```
%% Driving current into the Simple U-shaped beam cantilever
 I_cant=20e-3; % [App]

%% Evaluation of magnetic induction
 B=miu_0*I_cond/(2*pi*h_dist); % ([H]*[A])/([m2])=[Wb]/[m2]=[T]

%% Lorentz Force
 Fl=I_cant*B*l_perp;
```

SIMULINK SCHEMATIC

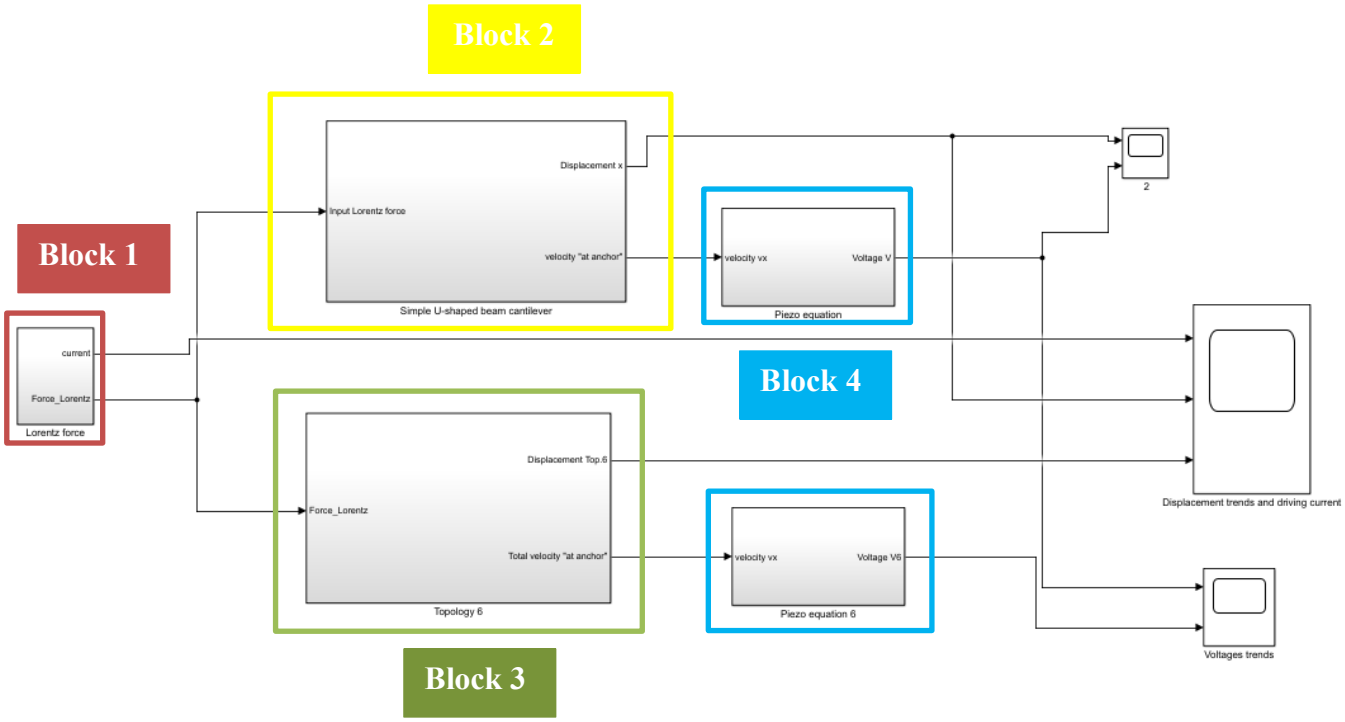

Fig. B.48: Simulink schematic: Simple VS Topology 6.

Block 1

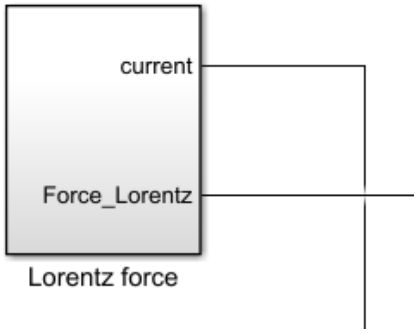

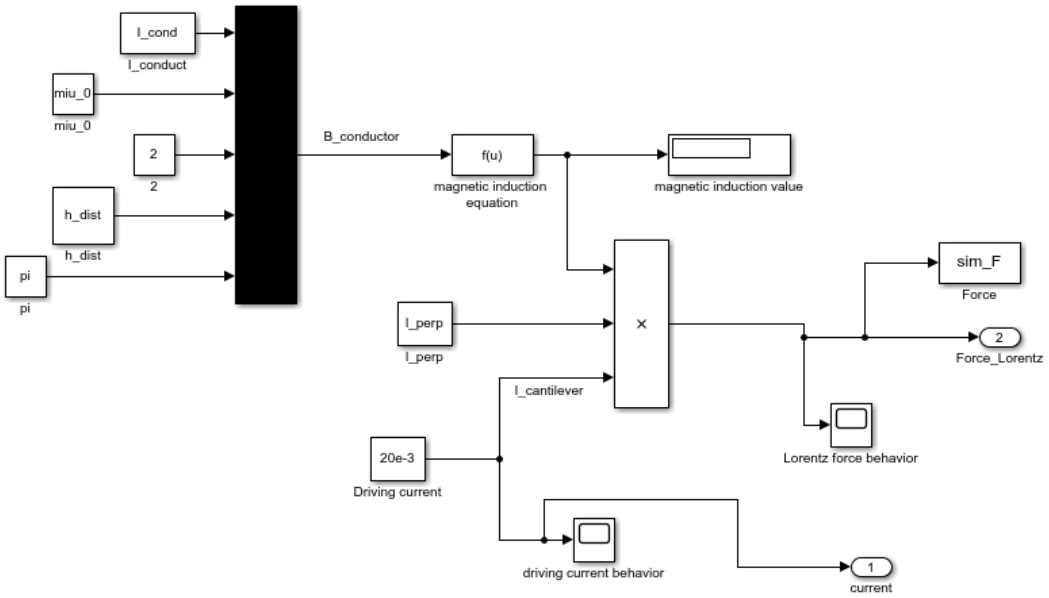

Fig. B.49: Lorentz force in static analysis.

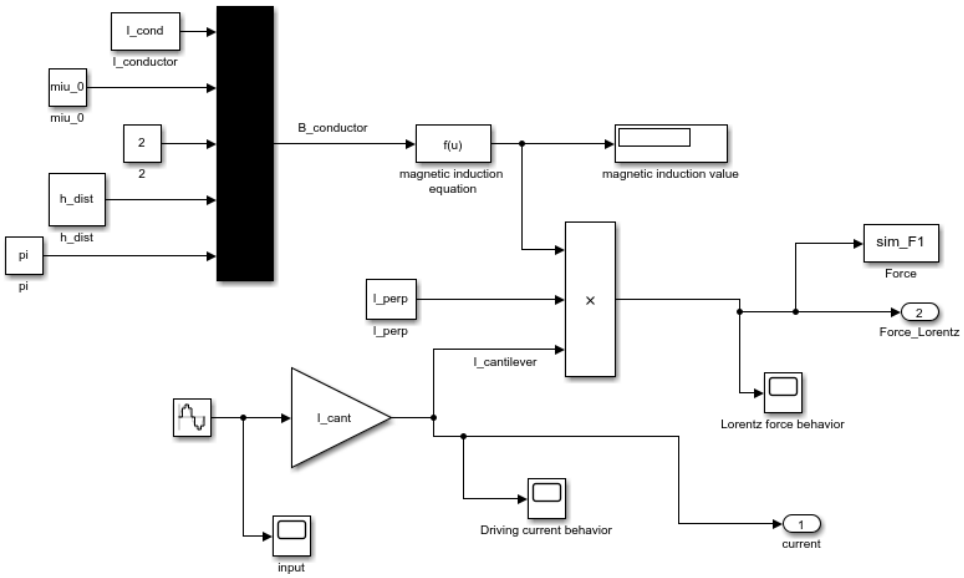

Fig. B.50: Lorentz force in dynamic analysis.

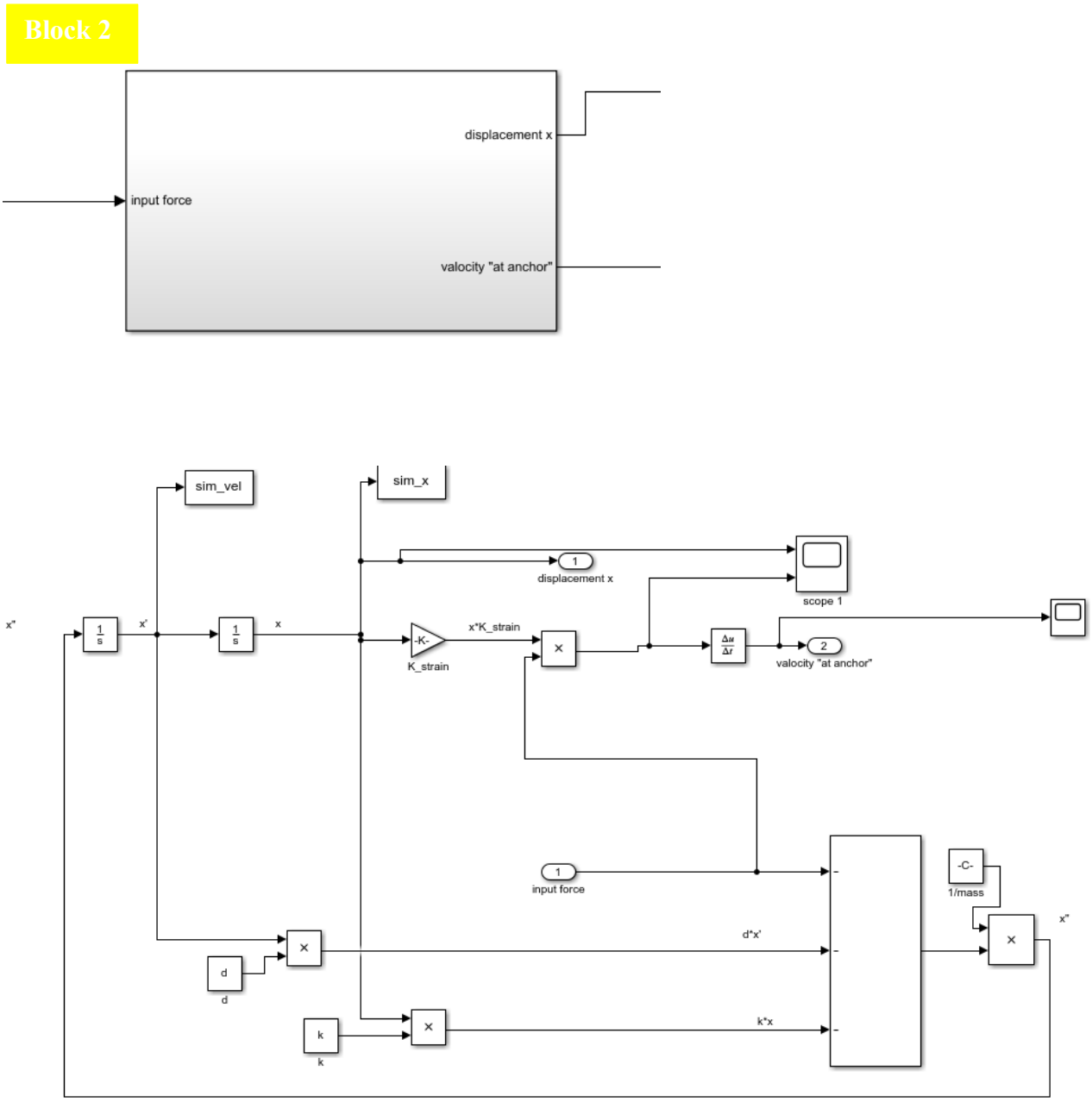

Fig. B.51: Simple U-shaped beam cantilever: Mass-spring-damper system.

Block 3

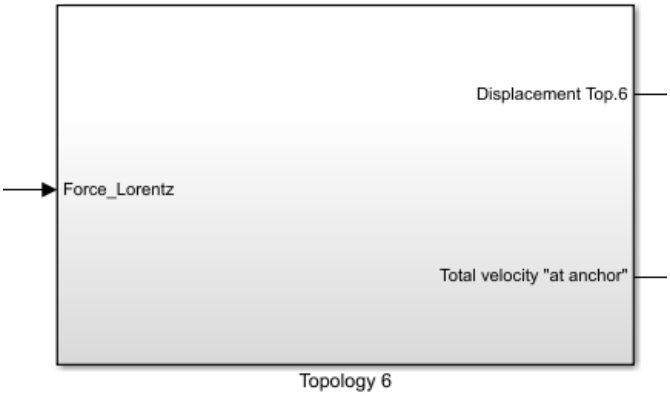

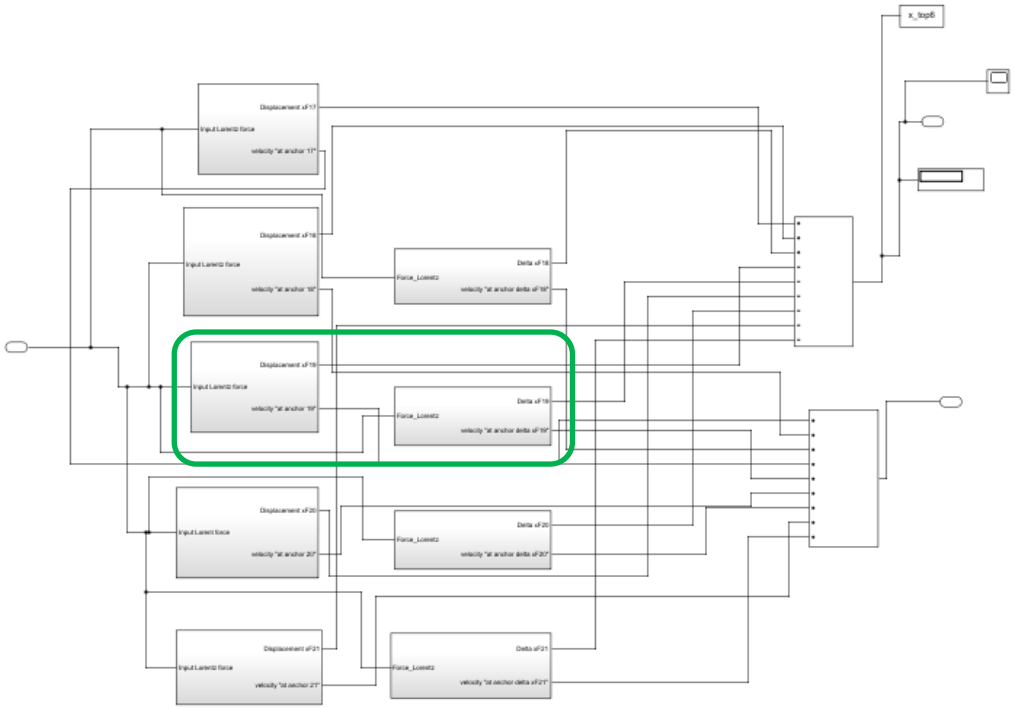

Fig. B.52: Topology 6: The whole mass-spring-damper system.

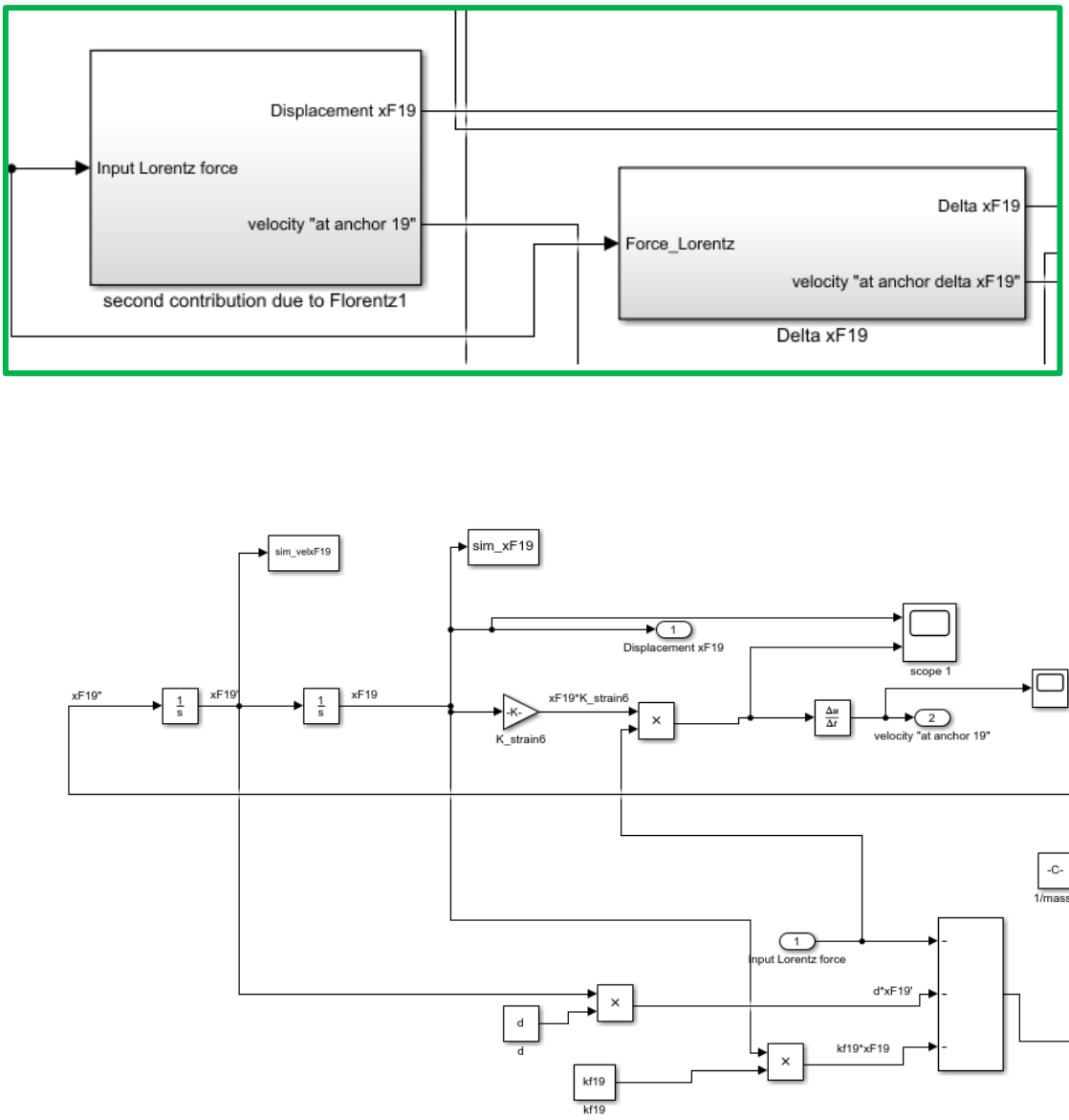

Fig. B.53: Topology 6: Focus on sub-system portion (displacement xF19).

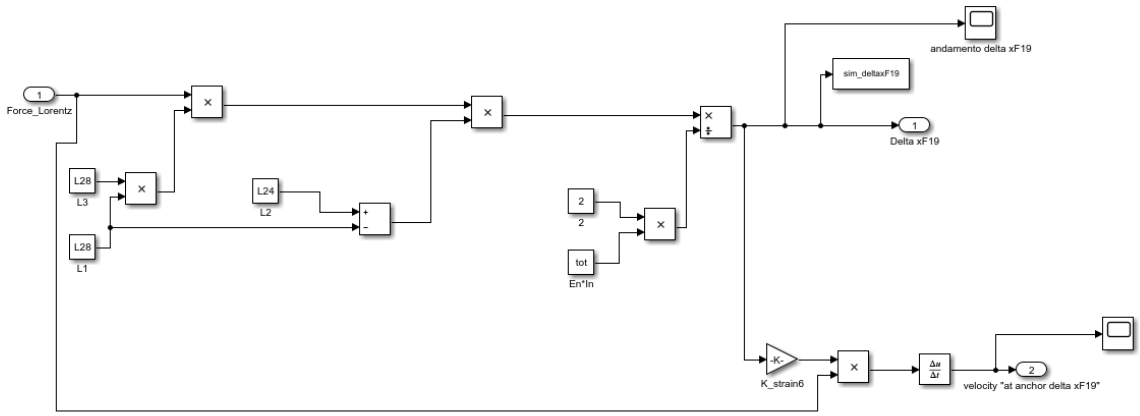

Fig. B.54: Topology 6: focus on sub-system portion (displacement ΔxF19).

Block 4

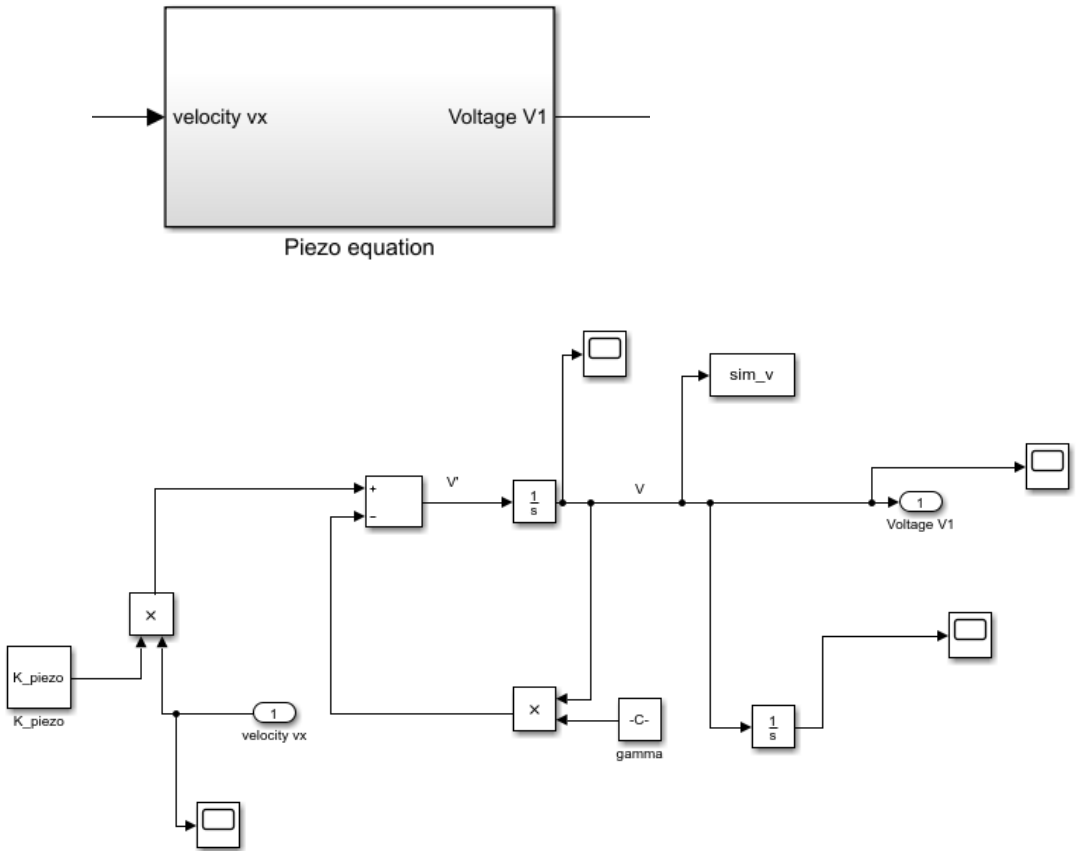

Fig. B.55: Simple U-shaped beam cantilever and Topology 6: Piezoelectric model.

List of figures

Chapter 1

Chapter 2

Chapter 4

Appendix

List of tables

Chapter 1

Chapter 2

Chapter 3

Chapter 4

La borsa di dottorato è stata cofinanziata con risorse del
Programma Operativo Nazionale Ricerca e Innovazione 2014-2020 (CCI 2014IT16M2OP005),
Fondo Sociale Europeo, Azione I.1 “Dottorati Innovativi con caratterizzazione Industriale”

UNIONE EUROPEA
Fondo Sociale Europeo